MAGNETIC ORDERING PHENOMENA IN THE HEXAGONAL ABX$_3$ HALIDES, A NEUTRON SCATTERING STUDY

by

Andrew Ross Monteith

A doctoral thesis submitted in the partial fulfilment of the requirements
for the award of Doctor of Philosophy
at University College London

Feburary 2000

For Mum

Index

Abstract

Most ABX_3 materials (where A is a 1A group cation, B is a divalent first row transition metal cation and X is a halide ion) possess a hexagonal perovskite structure where chains of face sharing BX_6 octahedra align along the c – axis separated by the A ions. This results in an *inter*chain separation that is much larger than the *intra*chain separation leading to a quasi one-dimensional magnetic behaviour at low temperature. The magnetic character of the compounds is strongly dependent on the nature and strength of the superexchange pathways and the environment around the B^+ ion, manipulation of which leads to new and interesting physics. The structural properties of the ABX_3 materials allow them to be used as model systems for a variety of conjectures. The chain like structure allows compounds such as $CsNiCl_3$ and $RbNiCl_3$ to be used as model systems for the Haldane conjecture, whilst the triangular arrangement of the spins on the B^{2+} ions allows compounds such as $CsMnBr_3$ to be used as model systems for the Chiral Universality class conjecture of Kawamura.

This thesis is concerned with the investigation of the crystallographic and magnetic properties of some the ABX_3 family of compounds by means of neutron scattering; specifically to observe the effects of extreme sample environment on the systems, such as applied hydrostatic pressure, applied magnetic and electric field etc. Magnetostructural correlations have been made for $CsFeCl_3$ and $CsFeBr_3$ on the basis of inelastic and powder neutron diffraction studies on the systems under pressure. Characterisation of the β and γ-phase of $KNiCl_3$ have been performed using inelastic neutron diffraction measurements and the magnetic and structural phase diagrams of $TlFeCl_3$ have also been mapped out. The magnetic phase diagram of $CsNiCl_3$ has been studied and a proof of the existence of a magnetoelectric effect in $CsMnBr_3$ has been obtained from elastic neutron scattering experiments.

List of Figures

List of Tables

Acknowledgements

First and foremost I would like to thank Dirk Visser for his day to day supervision in a role of external supervisor. His extraordinary experimental and crystallographic skills and his dedication and work rate, combined with his belief in my abilities has certainly ensured that my time spent as a PhD. student has been extremely rewarding.

I would also like to thank both my supervisors; Peter Day at The Royal Institution for giving me the opportunity to expand my scientific knowledge and providing the financial assistance necessary to attend scientific conferences and the like, and Quentin Pankhurst at University College London, whose help has ensured a smooth passage through my studies.

Due to the experimental nature of this thesis there are many, many colleagues that I should like to express my gratitude to for their expert assistance during the experimental work.

At the Laboratoire Leon Brillouin I would like to thank my local contact, Daniel Petitgrand and technicians Patrick and Richard for their help with the Helium Pressure cell.

At the Hahn Meitner Institut I would like to thank the sample environment team of Michael Meiβner and Harold Schneider for enabling us to undertake experiments with extreme sample conditions and the local contacts, Thomas Zeiske, Alex Krimmel, Hans Graf, Rainer Sonntag, Peter Voderwisch and Klaus Bartels for assistance in various neutron scattering experiments.

At the Institut Laue Langevin I would like especially to thank Garry McIntyre for his unstinting assistance in the face of overwhelming workload and local contacts Alan Hewat, Bachír Ouladdiaf and Francis Tasset for providing expertise in different aspects of neutron scattering work. I would also like to thank the PhD students at the

ILL, Rob, Darius, Trefor etc. who provided wine, women and song and made my stays there so enjoyable.

At the ISIS facility I would like to thank local contacts Steve Hull and Richard Ibberson for help with powder diffraction work.

Finally I would like to express my heartfelt gratitude to all my friends and family who have given me encouragement over the last three years. I would especially like to thank the boys and girls of the Royal Institution who have seen me at my worst (or best, as the case may be!) with a special mention for the RI boys of Goldhawk Road (Stiffy, Spence and Martin). Not forgetting of course my darling Marie who kept my spirits high, using threats, bribery and cups of tea!

Financial Assistance.

The funding for this thesis was provided by the Engineering and Physical Sciences Research Council (EPSRC).

These experiments contained herein were undertaken with the assistance of several funding bodies:

At the Laboratoire Leon Brillouin, CE-Saclay, France, neutron scattering experiments were performed financed by the European Commission under the 'Training and Mobility of Researchers, Access to Large Scale Facilities' Programme (Contract No. ERB FMGE CT 950043).

At the Hahn Meitner Institute, Berlin, Germany, neutron scattering experiments were also financed by European Commission under the 'Training and Mobility of Researchers, Access to Large Scale Facilities' Programme (Contract No. ERB FMGE CT 900060).

At the ISIS facility, Oxford, UK, neutron powder diffraction experiments were undertaken through funding from the Engineering and Physical Sciences Research Council (EPSRC).

1 Introduction

In the last few decades, the study of low-dimensional magnetic materials and especially their phase transitions and magnetic excitations has increased enormously. Since the 1975 review by de Jongh and Miedema entitled ‘Experiments on simple magnetic model systems’[1] many more materials have been synthesised possessing magnetic properties which could be described by the model magnetic Hamiltonian:

$$\mathcal{H}=\sum_{i,j}\frac{J^{xy}}{2}\left(S_i^+S_j^-+S_i^-S_j^+\right)+J^zS_i^zS_j^z \tag{1}$$

where J denotes the superexchange constant and S_x, S_y and S_z are the spatial spin components. We can distinguish between two types of interaction in the above Hamiltonian; the ferromagnetic exchange: where $J > 0$, and the antiferromagnetic exchange: where $J < 0$. The form of the interaction depends strongly on the number of spatial spin components. The fully isotropic case known as the Heisenberg model has $J_x = J_y = J_z$. Due to crystal field effects an anisotropy can be introduced, approximating a system with one or two spatial spin components: known as the Ising case and the XY case, respectively. As such, one can define a spin dimensionality n:

$n = 1(I)$,	$J_z \neq 0, J_x, J_y = 0$	Ising system
$n = 2(XY)$,	$J_x, J_y \neq 0, J_z = 0$	XY system
$n = 3(H)$.	$J_x, = J_y, = J_z \neq 0$	Heisenberg system

A full description of each type of system mentioned above is supplied later in Chapter 2.2. In real compounds intermediate systems are formed between those given above. Since the de Jongh and Miedema review, the research field of magnetic model systems has grown enormously[2,3,4]. The increased understanding of the statistical physics of the model Hamiltonians aided by increased computational power have resulted in the discovery of new aspects of low dimensional physics e.g. the magnetic ordering process in the different types of magnetic lattices and their co-operative magnetic excitation behaviour[5]. The development of neutron scattering techniques and the availability of high flux pulsed neutron sources have also made it possible to test and investigate the theoretical predictions by measuring the magnetic cross section S(Q,ω) over an extended part of reciprocal space, as can be seen below, where the dispersion curve of CsVCl$_3$, (a) and KCuF$_3$, (b) are given as examples.

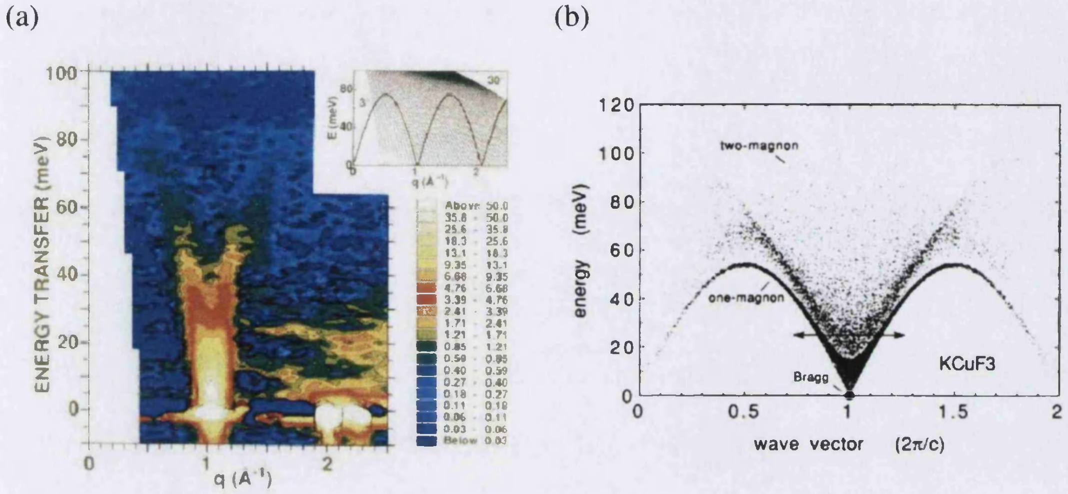

Figure 1: The magnetic dispersion curves for (a) the S=3/2 chain compound CsVCl$_3$[6] and (b) the S=1/2 chain compound KCuF$_3$[7].

In order to fully describe the magnetic behaviour of a system one must also take into account its structural dimensionality (*d*). Many more materials have been synthesised in which lattice dimensionality is used to create low dimensional magnetic behaviour, e.g. the early days of co-ordination chemistry provided many model systems, such as $M^{II}(Htrz)_2(CNS)_2$[8]. This field has evolved into the area of supramolecular systems with the aim of tailor made materials[9,10]. The discovery of high-T_c superconductivity led to the reinvestigation of the magnetism of materials with isostructural properties to those described by de Jongh and Miedema[1]. The field of research evolved further into the investigation of the giant magneto resistance ABX$_3$ systems. These properties were again found in a series of oxide materials already known from the early sixties. Their crystal structures are directly related to the ABX$_3$ cubic perovskite structure e.g. $La_{1-x}Sr_xMnO_3$ ($l = \infty$), $La_{1-x}Sr_xMnO_4$ ($l = 1$) and $La_{1-x}Sr_xMn_2O_7$ ($l = 2$)[11], where l is the number of layers. These crystal structures give rise to well organised long range 3D magnetism or short range 2D magnetic order. These phases are known as the Ruddelsden Popper phases[12].

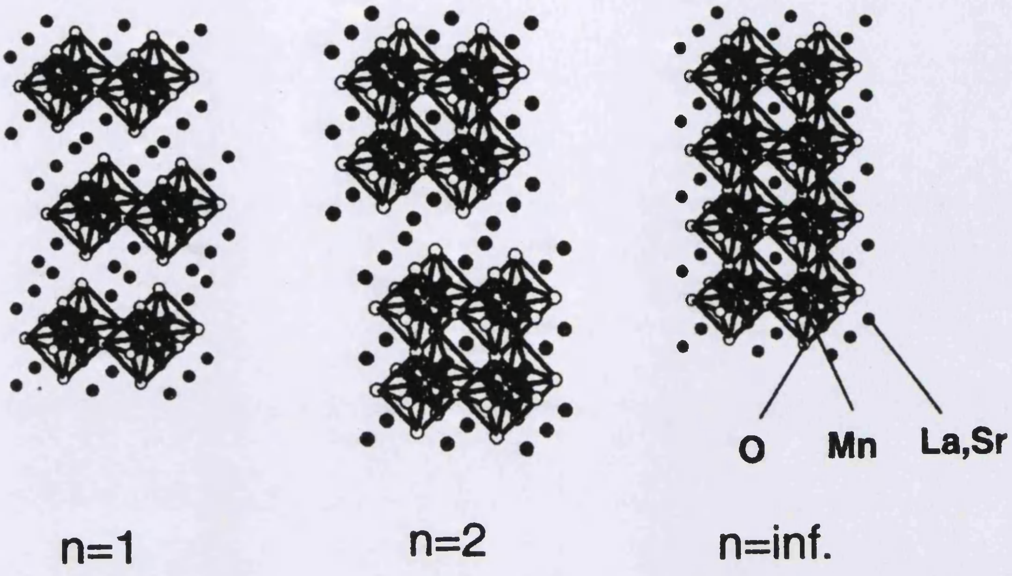

Figure 2: Structure of the $La_{1-x}Sr_xMnO_3$, $La_{1-x}Sr_xMnO_4$ and $La_{1-x}Sr_xMn_2O_7$ compounds[11].

More recently, it has been recognised that the magnetic long range order can be disturbed by the geometry of the crystal lattice. Also, depending on the magnetic character of the system, one can observe so called magnetic frustration effects[13]. These effects are present in the magnetic ordering of systems crystallising with magnetic lattices in the form of a triangular lattice with z = 6, for spin n = 1, 2, where z is the lattice coordination number of the nearest magnetic neighbours. Similar effects are found in the Kagome lattice[14], (z = 4) and a tetrahedron network e.g. the pyrochlore lattice[15] (z = 4).

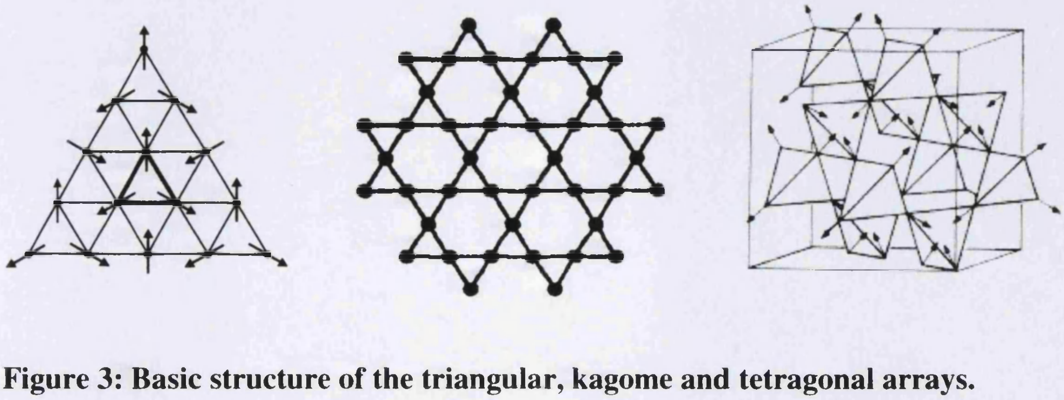

Figure 3: Basic structure of the triangular, kagome and tetragonal arrays.

The effects of the spin dimensionally, lattice dimensionality and additional frustration can be directly observed in the critical behaviour around the phase transition temperature. Phase transitions of the order - disorder type are characterised by an order parameter that decreases towards zero with increasing temperature. At a first order phase transition the order parameter changes discontinuously whereas at a second order phase transition the change in order parameter is continuous upon approaching the phase transition from the disordered phase. The magnetic susceptibility $\delta\mu$ /δH becomes infinite while the magnetic correlation length, ξ, diverges.

In a real system the singularity behaviour of a particular thermodynamic quantity is limited to a particular region of the phase transition known as the *critical region.* Within this critical region the thermodynamic function f(ε) often depends on the reduced temperature $\varepsilon(T - T_c) / T_c$ as $f(\varepsilon) = A\varepsilon^x(1+B\varepsilon^y + \ldots)$, where A and B are constants and x is the *critical exponent.* The concept and nature of the different critical exponents is elaborated upon in Chapter 2. We can say however, that near T_c, f(ε) can be described by a power law ~ $A\varepsilon^x$ and the value of x can be obtained from a 'log – log' plot of the intensity versus the reduced temperature. The critical exponents are dependent on the spin dimensionality *n*, and the system dimensionality *d.*

Each critical exponent can be expressed as a linear function of two other exponents through the laws of scaling[16,17], the seven scaling relations between the nine critical exponents are given below:

$$\gamma = \gamma'$$

$$\alpha = \alpha'$$

$$\nu = \nu'$$

$$\gamma = (2 - \eta)\nu$$

$$\alpha = 2(1 - \beta) - \gamma$$

$$\alpha = 2 - \nu d$$

$$\delta = (d + 2 - \eta) / (D - 2 + \eta)$$

Because the critical exponents are dependent on *n*, and *d*, equivalent relationships can be found for many dissimilar systems and are often found experimentally to have universal values such as the 2D Ising system where $\beta = 0.125$ and $\gamma = 1.75$ or the mean field predictions of $\beta = ½$ and $\gamma = 1$. These values give us a method of categorising systems into different *universality* classes, a topic which is further elaborated on in Chapter 2. This allows us to predict the behaviour of the system at its phase transition just armed with knowledge regarding its universality classification. In general, mean field theory is not valid to describe a phase transition because of the neglect of very short range fluctuations. It was shown by Ginzberg, that it was generally inadmissible to neglect fluctuations with wavelength $< \xi$. The importance of short wavelength fluctuations assumes greater importance for reduced lattice dimensionality, since the energy content of the fluctuations will be confined to less degrees of freedom. The modern renormalisation group theory description of critical phenomena takes the fluctuations of smaller wavelengths $< \xi$ into account[18].

However, it has also been demonstrated by simulation and experimental data that, depending on the symmetry and spatial geometry within a magnetically ordered phase, the actual symmetry can be lowered (e.g. by chiral ordering) and new universality classes may be identified. Thus, it also gives a way to investigate the changes in critical behaviour by observing the magnetic ordering of materials with specific geometry, symmetry and electronic state whilst inducing changes in these systems by applying electric field (E), magnetic field (H) and external pressure (P). The study of differences in the parameters in the Hamiltonian often results in the study of a series of isostructural materials where the changes are induced by the different crystallographic parameters of the materials in question. Similar changes can be induced by the application of hydrostatic or uniaxial pressure on a system.

The existence of spin chirality is still a hotly debated issue. Its existence has been investigated in this thesis by studying the ABX_3 halides using several different routes; e.g. the application of external parameters such as electric and magnetic field and hydrostatic pressure using elastic neutron diffraction as a probe. For the weak Ising compound $CsNiCl_3$ we show a transition to chiral ordering by an application of a magnetic field along the *ab* plane, (in the spin flop phase the magnetic structure is of the 120° type)

Using symmetry arguments Plumer *et al.*[19] suggested that the application of an electric field could remove the chirality ordering in the ABX_3 ternary halides. Experimental evidence for this magnetoelectric effect is presented for the compound $CsMnBr_3$. Plumer *et al.*[20] also suggested that a similar chiral ordering should be observed in the distorted triangular lattice. We have tested this prediction for the distorted hexagonal perovskite structures of the γ - phase of $TlFeCl_3$, in this case we introduced applied pressure to the system in order to influence the structural parameters. A test for the existence of chiral order has also been carried out in the β and γ - phases of the distorted hexagonal perovskite $KNiCl_3$.

Triangular 120° type magnetic ordering is also induced by an applied electric field: H // c axis, in the singlet ground state antiferromagnet material $CsFeBr_3$. The critical behaviour of the sublattice magnetisation along the phase boundary has been studied at mK temperatures with applied fields up to 6 Tesla.

Quasi one-dimensional magnetic materials also show interesting and unexpected magnetic excitations. For example, magnetic soliton motion been observed in ferro as well as in antiferromagnetic chains e.g. $CsNiF_3$ and $(CD_3)_4NMnCl_3$ (TMMC). For $CsNiCl_3$[21] it was shown that the spin wave description of the magnetic excitation did not explain the observed energies and intensities. Haldane conjectured that the magnetic excitations of spins on a 1-D array are different for half integer and integer spin systems[38,39]. The dispersion of half integer (S = 1/2, 3/2...) spin chains are gapless, while the integer spin chains (S = 1, 2...) have a gap at the zone centre. This gap is related to a singlet → triplet transition and has been observed in $CsNiCl_3$[22] and $Ni(C_2H_8N_2)NO_2ClO_4$ (NENP)[24]. A schematic of the general phase diagram of the anisotropy (Heisenberg → Ising) versus superexchange (Δ) for the integer S = 1 spin chains is given below[23]. It shows the possible position for a number of interesting quasi one-dimensional S = 1 chain systems.

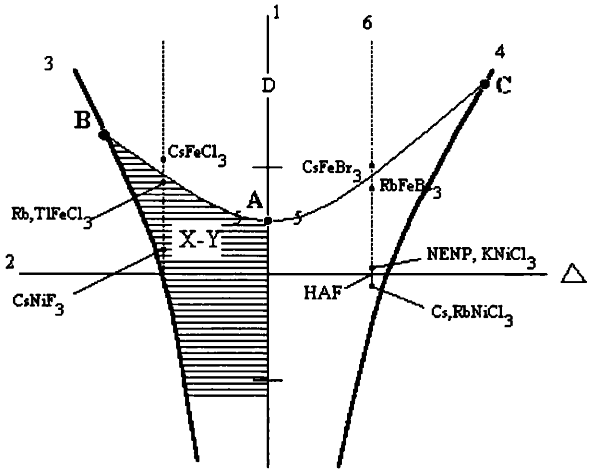

Figure 4: Simplified schematic of the phase diagram for the Ising – Heisenberg chain.

Line 6 in Figure 4 shows the energy of the gap of the 1-D system versus anisotropy. The gap energy rises steeply around D = 0. The gap energy in this region corresponds to the Haldane gap. At high D values this gap goes to zero, as D increases to greater than 1, the gap opens up again (see Figure 13, Chapter 2.2.1.1). Around the D = 1 point, line 5 in Figure 4 refers to a transition from a singlet ground state to an induced moment state.

On the antiferromagnet exchange side (right side) of the phase diagram novel groundstates were predicted and subsequently found in materials such as NENP and the $ANiCl_3$ halides. Experiments have shown that NENP, an S = 1 quasi 1-D system, shows a gap in the excitation spectrum around the zone centre at Q = 0, which persists down to low temperatures[24]. In this system the total superexchange (ΣJ) is smaller than the crystal field anisotropy (D). The observed gap energies are well explained by Haldane's predictions. However, for other systems shown in Figure 4, there are further complications, as in the case of $CsNiCl_3$ where magnetic order takes place. In this case the superexchange is much larger than the anisotropy of the system. It was shown that the spinwave description of the magnetic excitations does not explain the observed energies and intensities of these excitations. $CsNiCl_3$ has two modes present in the dispersion curve of the magnetic excitations; a linear mode which decreases to E = 0 at Q = 0, and a gap mode which is related to the longitudinal fluctuations which have a quantum mechanical origin. Very few materials are available to investigate the effect of different amounts of anisotropy on the S = 1 linear chain compounds. However a tuning of the gap mode is made possible by applying an external pressure on the system. In Appendix A, the dispersion of the magnetic excitations of the weak Ising like systems $CsNiCl_3$ and $RbNiCl_3$ under an applied hydrostatic pressure of 5kbar are presented, these have not been treated and are given 'as is'. The dispersion of the magnetic excitations in the XY like quasi one-dimensional linear chain compound $KNiCl_3$ has also been investigated in its β and γ - phases. These results are presented in Chapter 4.5.

The position of the quasi one-dimensional $AFeX_3$ compounds is also indicated on the phase diagram in Figure 4. In these materials one finds that the magnetism at low temperatures is governed by the singlet ground state and the low-lying doublet state. This can be described by an *effective* $S = 1$ Hamiltonian. The full spin moment is actually $S = 2$. The anisotropy in the $AFeX_3$ systems is much higher than that in the $ANiX_3$ ones[25]. Singlet ground state (SGS) behaviour is observed in the $CsFeX_3$ (X = Cl, Br), whereas the $RbFeX_3$ compounds have an induced moment behaviour and the systems order magnetically at low temperature. This is due to the fact that in the $CsFeX_3$ compounds, $D > \Sigma J$ and for the $RbFeX_3$ compounds, $D < \Sigma J$. The small differences apparent in the values of the anisotropy and *intra-* and *inter*chain superexchange is caused by the small variation in the structural parameters of the systems.

Applied hydrostatic pressure on the $CsFeX_3$ compounds has been explored as a means of inducing magnetic order in the system. A magneto-structural study of the systems is presented in Chapter 5. The dispersion of the magnetic excitations of $CsFeCl_3$ and $CsFeBr_3$ are measured as a function of applied hydrostatic pressure (up to 5kbar) at low temperature (< 2K). The corresponding crystal structures are also determined by means of time-of-flight neutron diffraction measurements. Magnetic order can also be induced in these compounds by application of a magnetic field along the chain direction. In this case the low-lying doublet ($m = \pm1$), is Zeeman split and for a sufficiently large field the lower doublet state ($m = -1$), will approach and eventually cross the singlet state and thus the system will order magnetically in a 120° type structure. The dispersion of the magnetic excitations are studied for the Singlet Ground State (SGS) antiferromagnet $CsFeBr_3$ for very low temperatures (60mK) in the presence of a magnetic field (5T) and presented in Chapter 5.3. Up to the phase transition an accurate description of the dispersion is given by the theory of Lindgård while in the ordered state the Dynamical Correlated Effective Field Approach (DCEFA) of Suzuki is preferred[26,27,28].

The thesis is arranged in the following order; Chapter 2 is presented as the theory chapter. Within this chapter structural and magnetic information is given on the diverse ABX_3 family of compounds and reasons for studying them are elaborated upon. The chapter also contains the necessary neutron scattering theory for the reader to understand experimental evidence given in later chapters. As this thesis deals specifically with experiments on the ABX_3 compounds, and as such, is an experimental thesis as opposed to a theoretical one, Chapter 3 gives information on the crystal growth and experimental methods employed in this thesis as well as individual specification of spectrometers and diffractometers used to collect data on the systems. The actual experimental results are presented and discussed in Chapters 4 and 5. Chapter 4 deals with chirality order in the ABX_3 compounds and Chapter 5 looks at the SGS compounds $CsFeCl_3$ and $CsFeBr_3$. A summary of results and a statement of further work is outlined in Chapter 6. Finally, Appendix A deals with recent experimental findings from the magnetic excitations of the easy axis compounds $CsNiCl_3$ and $RbNiCl_3$ under applied hydrostatic pressure, as well as those in the β and γ-phase of $KNiCl_3$ at ambient pressure.

2 Theory

This Chapter introduces the ABX_3 halides and classifies them according to the strength of their chainar anisotropy. Each classification is elaborated upon and information is given on their structural and magnetic properties. The theory behind universality, critical phase transitions and the production and diffraction of neutrons is also given herein.

2.1 Second Order Phase Transitions.

In this thesis a series of magnetic materials are studied which show magnetic ordering upon the application of magnetic field, electric field or applied pressure or by the lowering of the temperature of the system. Systems which undergo a second order phase transition, i.e. a transition where the second derivative of the Gibbs free energy changes discontinuously are said to have undergone a critical phase or continuous phase transition. To explain the concept of critical behaviour at phase transitions it is probably best to consider the phase transition of a simple ferromagnetic system. The typical magnetisation, M, of a simple ferromagnet, under different temperature conditions follows the form of that given below. The behaviour can be described by simple molecular field theory, which can be found in many general physics textbooks. The relative magnetisation of the system ($\sigma = M/M_o$ where M_o is the magnetisation at T = 0K) is modelled by the equation:

$$\sigma = B_J\left(\frac{g\mu_B(H+\lambda\sigma)}{k_BT}\right) \tag{2}$$

where the Brillouin function B_J is given by:

$$B_J(x)=\frac{2J+1}{2J}\coth\left(\frac{2J+1}{2J}x\right)-\frac{1}{2J}\coth\left(\frac{x}{2J}\right) \tag{3}$$

Close to the phase transition σ is small and B_J can be expanded in a power series of $g\mu_B\lambda\sigma / k_BT$. In the first approximation:

$$B_J(x) = \frac{(J+1)x}{3J} \tag{4}$$

we see from this expansion that the transition to the paramagnetic phase ($\sigma = 0$) takes place at:

$$T = T_c = \frac{Ng^2\mu_B^2 J(J+1)\lambda}{3k_B} \tag{5}$$

Just below T_C the magnetisation behaves according to:

$$\sigma = A((T_c - T) / T_c)^{\beta} \tag{6}$$

where mean field theory predicts that $\beta = 0.5$. Similarly one can calculate the magnetic susceptibility, $\chi = M / H$, above T_c, giving us:

$$\chi = A'(T - T_c)^{-\gamma} \tag{7}$$

where mean field theory predicts that $\gamma = 1.0$. A full breakdown of the critical exponents and their meaning is given below in Table 1.

Table 1: Definition and range of values for critical exponents encountered in Table 2 and Table 3.

Thermodynamic Variable	Symbol	Power	Comments	Typical values of exponents
Specific Heat at Constant field	C_H	$(T-T_c)^{-\alpha}$	$T > T_c, H=0$	-0.3 – 0.3
		$(T_c-T)^{-\alpha'}$	$T < T_c, H=0$	-0.3 – 0.3
Magnetisation	M	$(T_c-T)^{\beta}$	$T < T_c, H=0$	0.1 – 0.4
		$H^{1/\delta}$	$T = T_c$	3.0 – 6.0
Susceptibility	χ	$(T-T_c)^{-\gamma}$	$T > T_c, H=0$	1.3 – 1.4
		$(T_c-T)^{-\gamma'}$	$T < T_c, H=0$	
Correlation Length	ξ	$(T-T_c)^{-\nu}$	$T > T_c, H=0$	0.6 – 0.7
		$(T_c-T)^{-\nu'}$	$T < T_c, H=0$	0.6 – 0.7

The values of the critical exponents for magnetisation (β and δ) and for correlation length (ν) can be obtained by neutron scattering and the critical exponents for susceptibility (γ) can be obtained from AC measurements. As has been mentioned in the Introduction, the critical exponents are linked by scaling laws. The values of the critical exponents allow us to establish the universality class of the system.

According to the universality hypothesis, second order phase transitions may be classified as belonging to a small number of universality classes. The class to which the system belongs depends on a small number of basic properties of the system:

- The spatial dimension of the system, (d = 1,2 or 3 dimensional)
- The spatial dimension or symmetry of the order parameter, (Ising, XY and Heisenberg for n = 1, 2 and 3 dimensions respectively)
- Whether the order parameter is short or long range.

This is rather astonishing as it represents quite a large generalisation. It implies that the nature of the microscopic interaction is irrelevant (aside from the last point). It also implies that for continuous transitions such as magnetic transitions, the critical exponents will be identical regardless of crystal structure.

Therefore armed with the above knowledge, one can classify the universality of a system and thus define the universal qualities such as critical components, amplitude ratios and equations of state. If one concentrates on a standard bulk magnet, one sees that the universality of the system is basically determined by the symmetry of the order parameter. The critical properties associated with these *n*-component, O(*n*), universality classes have been extensively studied and are well understood. The values for the critical exponents for the different standard models are given below.

Table 2: Critical exponent values for the standard universality classes

Standard Model	Universality Class	α	β	γ	ν	A^+/A^-
Ising	Z2	0.1098(29)	0.325(1)	1.2402(9)	0.6300(8)	0.55
XY	S1	-0.0080(32)	0.346(1)	1.3160(10)	0.6693(10)	0.99
Heisenberg	S2	-0.1160(36)	0.3647(12)	1.3866(12)	0.7054(11)	1.36

However, there are systems which fail to be represented by the standard O(*n*) universality classes, systems such as random magnets with quenched disorder (e.g. spin glasses). Other systems include those standard magnets with frustrated magnetism. The nature of frustrated magnets leads to quite new and exciting phase transitions to those of conventional unfrustrated magnets, as will be demonstrated in what follows.

In order to understand the concepts of the standard magnets with frustrated magnetism, let us consider a triangular lattice with antiferromagnetically coupled spins at each vertex. It is immediately apparent that the spins cannot conform to a collinear antiferromagnetic alignment, the stable spin configuration depends on the type of spin symmetry or number of spin components. In the case of the spins being confined to one dimension (called the Ising case) the ground state is not uniquely determined as can be seen below.

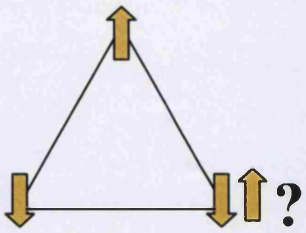

Figure 5: Ground state spin configuration of 3 Ising spins on a triangle. Frustration leads to a non-trivial degeneracy of the ground state.

The spin on the unoccupied vertex cannot align antiparallel with both other spins simultaneously. If we allow the spins to move in either two or three dimensions (*XY* and *Heisenberg* cases, respectively) the spins will become canted. An interesting consequence of this canting can be seen in Figure 6. In the XY case there are now two degenerate solutions for the ground state. This degeneracy corresponds to the 2 different *chiral* states. The concept of chirality was first introduced to magnetism by Villain[29], however, it was Kawamura[30,31] who first predicted that this extra degeneracy would lead to new and interesting physics.

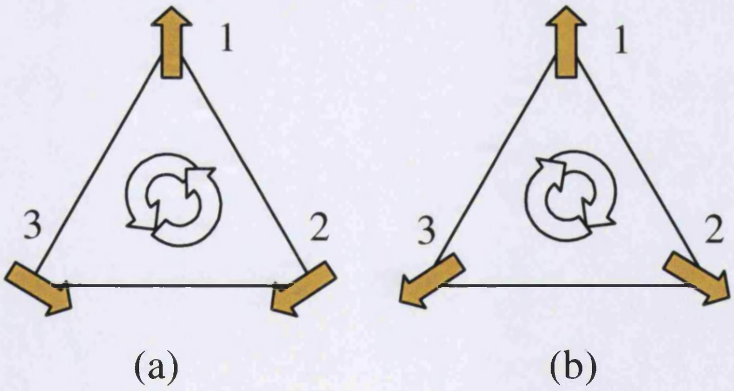

Figure 6: The twofold degenerate ground state for an XY antiferromagnet on a triangular lattice, showing the two different chiral states (a) and (b).

Kawamura conjectured that this chirality, in introducing an extra degeneracy would produce new *universality* classes, a conjecture that was (and still is) hotly disputed.

It can be seen from Figure 6, that a given chiral state cannot be transformed to the other chiral state via a global spin rotation in the *XY* spin space. It is necessary to use global spin reflection to achieve this. One may assign a different chirality of plus (+) or minus (-) to (a) and (b) in the above figure. Thus the extra degeneracy provide by the chiral states manifests itself as a hidden Ising like degeneracy. In order to characterise these two chiral states it is convenient to introduce a *scalar* quantity, chirality[32],

$$\kappa_p = \frac{2}{3\sqrt{3}} \sum_{\langle ij \rangle}^{p} \left[\vec{S}_i \times \vec{S}_j\right]_z = \frac{2}{3\sqrt{3}} \sum_{\langle ij \rangle}^{p} \left(S_i^x S_i^y - S_i^y S_i^x\right) = \left\langle \vec{C} \right\rangle \tag{8}$$

where the summation runs over the 3 spins depicted above. $\kappa_p = \pm 1$ for the two spin configurations.

Looking at the Heisenberg case, we see that there is no longer a discrete chiral degeneracy as the different spin configurations can be transformed into one another by continuous spin rotation via the third dimension. However, a chirality *vector* can be defined as,

$$\kappa_p = \frac{2}{3\sqrt{3}} \sum_{\langle ij \rangle}^{p} \vec{S}_i \times \vec{S}_j \tag{9}$$

A similar chiral degeneracy may be observed in systems such as helimagnets and 2D and 3D stacked triangular lattice antiferromagnets, the spin structures of which are shown below.

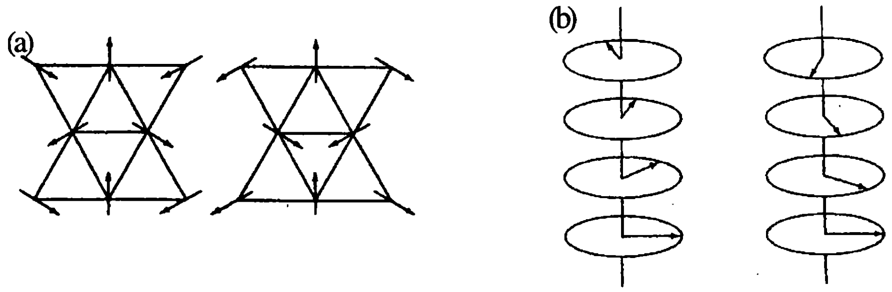

Figure 7: Chiral degeneracy in the ordered state of the *XY* antiferromagnet, (a) and the *XY* helimagnet (b) on the triangular lattice.

Kawamura first analysed the critical properties of systems known as stacked triangular lattice antiferromagnets (TLA's), this being the antiferromagnetic stacking of the triangular lattice seen in Figure 7. Kawamura used the theoretical techniques of symmetry analysis and Monte Carlo simulation to show that due to this extra chiral degeneracy, TLA systems may belong to a new universality class. The critical exponent values obtained by Kawamura for his new universality class are listed below and can be compared with the standard universality class critical exponents in Table 2.

Table 3: Critical exponent values for the chiral universality classes.

Chiral Model	Universality Class	α	β	γ	ν	A^+/A^-
XY	Z2 × S1	0.34(6)	0.253(10)	1.13(5)	0.54(2)	0.36(2)
Heisenberg	P3	0.24(8)	0.30(2)	1.17(7)	0.59(2)	0.54(2)

In order to investigate the Kawamura hypothesis it is necessary to find model systems with antiferromagnetic triangular lattice structures. Two such groups that satisfy this criteria are the BX_2 and ABX_3 halide families, where A is a 1A group cation, B is a divalent first-row transition metal cation and X is a halide anion. A wide variety of magnetic properties may be obtained by changing the B ion (due to the electronic changes induced) and the A and X ions (due to spatial changes). The different properties obtainable are due to the change in geometry and nature of the superexchange bridges, and the different electronic states induced by the crystal field levels for different types of B ion.

These systems generally crystallise in the hexagonal perovskite structure with space group $P6_3/mmc$. Chains of face-sharing BX_3^- octahedra aligned along the c-axis are separated by the A^+ ions. This results in the *inter*chain separation being much larger than the *intra*chain separation, leading to a quasi one-dimensional magnetic behaviour at low temperature.

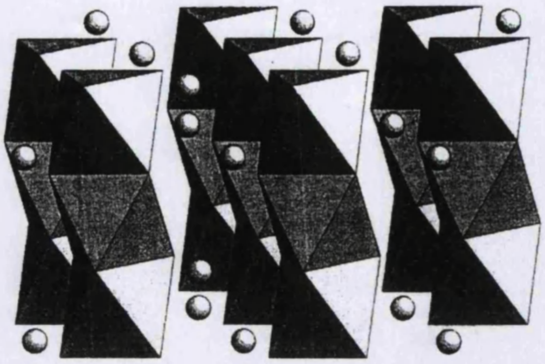

Figure 8: Schematic of the hexagonal perovskite structure, with the A^+ ions separating the infinite linear chains of BX_6^{2-} face-sharing octahedra, space group $P6_3/mmc$.

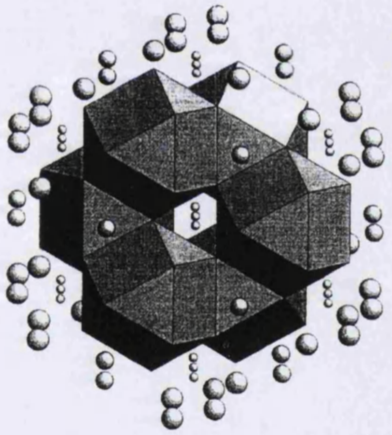

Figure 9: [0001] projection of hexagonal perovskite structure. The hexagonal stacking of the twinned-cuboctahedral AX_{12} coordination polyhedra, which separates the infinite BX_3^- chains is shown.

2.2 Heisenberg Triangular Antiferromagnets

This Chapter gives a brief overview of the family of Heisenberg triangular antiferromagnets. It introduces the systems reported on later in the thesis and acts as a reference point to the reader. It is by no means comprehensive and the interested reader is referred to the recent review by Collins and Petrenko[33]

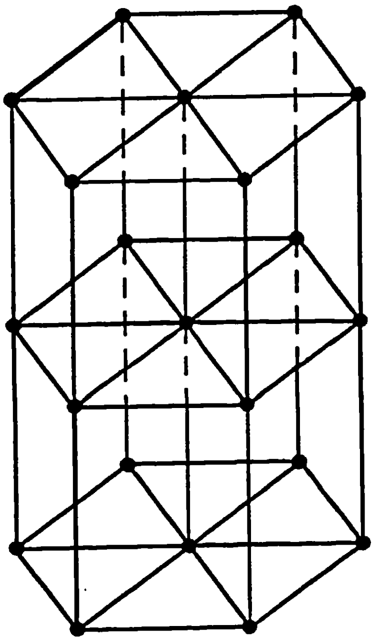

Figure 10: A schematic of the stacked triangular antiferromagnet lattice.

The stacked triangular antiferromagnet takes the form as that shown in Figure 10, it can be described with the following Hamiltonian:

$$\mathcal{H} = J\sum_{i,j} S_i S_j + J'\sum_{i,j} S_i S_j - D\sum_{i} \left(S_i^z\right)^2 - g\mu_B H\sum_{i} S_i \tag{10}$$

Where J is the exchange integral along the chains, J' is the exchange integral between the chains and D is the single ion anisotropy. The first term represents the superexchange parameter along the chain, the second term represents the superexchange parameter in the basal plane, the third term is the single ion anisotropy and the final term is a representation of the Zeeman term of the spins in the presence of an externally applied magnetic field, $\boldsymbol{H}$.

This Hamiltonian, depending on the value of the single ion anisotropy, D, can represent several different systems, each with its own unique character:

- If $D = 0$ then the system corresponds to the well known isotropic Heisenberg case. In actual fact no real triangular antiferromagnetic systems are perfectly Heisenberg in character, all have a degree of anisotropy inherent in the system. However, if D is small in comparison to both J and J' then the system can be represented by the above Hamiltonian (except at very low temperatures, $T < DS^2$, or near the critical point).

- If $D < 0$, the anisotropy makes it energetically favourable for the spins to align parallel to the z-axis. This is what is known as the *easy-axis* or Ising type. This alignment breaks the isotropic symmetry of the Heisenberg case and leads to new and interesting physics.

- Finally, if $D > 0$, the spins will align in the xy plane, known as the *easy-plane* type. The ordered state of this arrangement is the 120° type structure shown in Figure 6, this state has a chiral degenerate ground state and, as such, is a good model system for the testing of the conjecture of Kawamura.

These cases will be further elaborated on in subsequent Chapters. Chapter 2.2.1 deals with the easy axis anisotropy case, Chapter 2.2.2 deals with the easy plane anisotropy case and in Chapter 2.2.3 we elaborate on the case of the *distorted* triangular lattice antiferromagnet.

2.2.1 Easy Axis Anisotropy: D < 0

There are 5 compounds in the ABX_3 family that show easy axis anisotropy. These are: $CsNiCl_3$, $RbNiCl_3$, $CsNiBr_3$, $RbNiBr_3$ and $CsMnI_3$. All are characterised by the space group $P6_3/mmc$ at room temperature and all exhibit quasi one-dimensional behaviour due to the difference in the *intra*-chain and *inter*-chain superexchange integrals. In all cases the value of the single ion anisotropy, D, is of the same magnitude as the intra-chain exchange integral, J'. Both of the exchange interactions are antiferromagnetic in character. The (H, T) phase diagram of these systems is of the form shown in Figure 11.

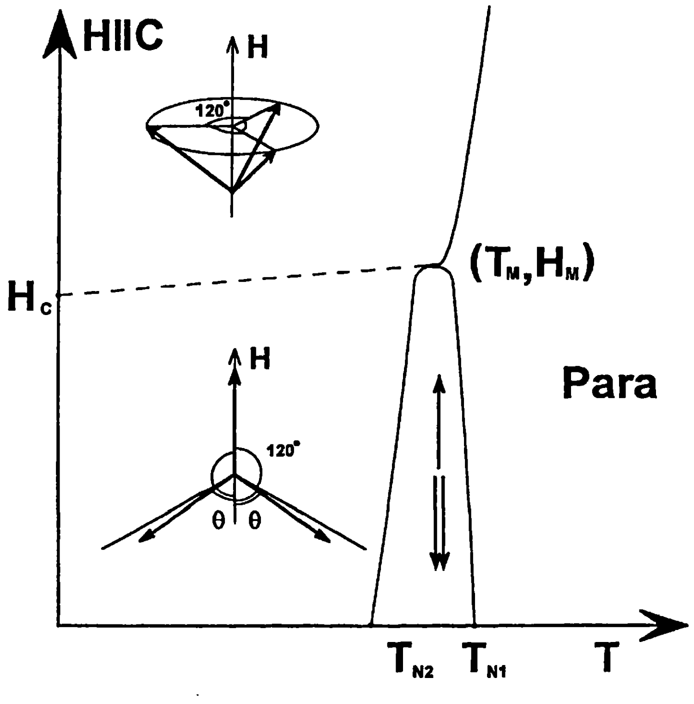

Figure 11: Magnetic phase diagram of the Heisenberg triangular antiferromagnet with easy axis anisotropy for $H \parallel c$ [33].

At low temperature and magnetic field the spins form the previously mentioned triangular structure, with the c-axis in the plane of the triangle, however, the magnetic anisotropy attempts to pull the spins into alignment in the basal plane, thus giving a slightly distorted 120° type structure. For a classical system the angle θ, which the spins make with the Ising (c) axis, is given by the formula:

$$\cos\theta = \frac{1}{2(1+D/6J')}, \qquad -D < 6J' \qquad (11)$$

It can be seen that at $-D = 6J'$ the system changes to a collinear structure where all spins are parallel to the *c*-axis. Between T_{N2} and T_{N1} there exists the collinear structure which disintegrates to the paramagnetic phase above T_{N1}. Applying a magnetic field parallel to the *c*-axis causes the spin to flip into the *ab* plane at a critical field H_c (the *spin-flop* field). This spin-flop phase takes place as soon as the Zeeman energy exceeds the Ising anisotropy energy, see for example Figure 135. Thus the spin-flop field is a measure of the Ising anisotropy as $T \rightarrow 0$.

Although not ideal, the systems in this family can be used as physical models of the Kawamura conjecture, see Chapter 2.1 for more details. The critical exponents and amplitude ratios determined from several different experiments for $RbNiCl_3$ and $CsNiCl_3$ are shown below. Also included are the theoretically predicted values for the different universality classes.

Table 4: Experimental values of the critical exponents in the easy axis systems, compared to model values [34].

	α	β	γ	ν	A^+/A^-
Expt.	0.37(8) [35]	0.243(5) [36]	---	---	0.30(11) [35]
	0.342(5)[37]	---	---	---	---
XY	-0.008	0.35	1.316	0.669	0.99
n=2 chiral	0.34(6)	0.253(10)	1.13(5)	0.54(2)	0.36(20)
O(4)	-0.22	0.39	1.47	0.74	
Mean field	0.5	0.25	1.0	0.5	0

As can be seen from Table 4, the experimental values obtained support the concept of the new chiral universality class. It should be noted however, that the value of the critical exponent β is close to the mean-field tricritical value but the values of the specific heat exponent, α, and the amplitude ratio, A^+/A^-, are closer to the chiral $n = 2$ case.

Perhaps the most exciting thing about these systems is that due to the small Ising anisotropy energy, they can be thought of as Heisenberg antiferromagnetic systems, this allows them to be used as model systems for theories involving Heisenberg antiferromagnetic spin chains. Indeed, these systems represent good physical models for one of the most controversial theories in magnetism in the recent past, the *Haldane* conjecture.

2.2.1.1 The Haldane conjecture.

It was in 1983 that Haldane[38,39] first conjectured that the low-lying excitations of integer and half-integer spin Heisenberg antiferromagnetic chains would have different behaviour. He predicted that the integer chains would have a finite gap in the excitation spectrum and only the half- integer spin chains are gapless. The conjecture is based on the large-S mapping of the Hamiltonian in (12) to quantum field theory – the O(3) non-linear σ model.

$$\mathscr{H} = 2J\sum_{n} S_{n}^{x}S_{n+1}^{x} + S_{n}^{y}S_{n+1}^{y} + \lambda S_{n}^{z}S_{n+1}^{z} + D\sum_{n}\left(S_{n}^{z}\right)^{2} \qquad (12)$$

λ represents the exchange anisotropy, such that, if $\lambda = 1$ the Heisenberg system is recovered. If $\lambda > 1$ the system corresponds to the uniaxial Ising system and if $0 \leq \lambda < 1$ the system is defined as an easy-plane one. D is the single ion anisotropy defined in Chapter 2.2.

The explanation of the large-S mapping of the Hamiltonian in (12) to quantum field theory is beyond the scope of this thesis. However, for elaboration on this and other mathematical descriptions of the Haldane conjecture the reader is referred to a review article on 'Quantum spin chains and the Haldane gap', by Affleck[40].

The conjecture of a finite gap for the Heisenberg integer spin chain is puzzling in that both the quantum $S = ½$ and classical $S \rightarrow \infty$ chains have vanishing excitation energies and infinite correlation length in the isotropic limit. Early attempts at a numerical solution to this problem were thwarted due to a lack of convergence in the $S = ½$ gapless case. More recent studies have helped to shed light on the nature of the Haldane conjecture. The destruction of long range order and the generation of a Haldane gap has been attributed to the condensation of *solitons.* If λ and D are varied between the Ising limit ($\lambda \to \infty$, $D \to -\infty$) and the Heisenberg point ($\lambda = 1$, $D = 0$)[39]. these solitons are different in nature for the $S = 1$ and $S = ½$ cases[41], this is due to the absence of $S_i^z = 0$ states in the integer case. Another topological excitation has been proposed by Affleck[42], he proposed that the gap was caused by vortex-like 'meron-antimeron' pairs. For the half-integer case these pairs cancel each other, but in the integer case pairs are formed which destroy the long range order. Again the difference can be traced back to the lack of a $S_i^z = 0$ state in the integer case.

The Lieb, Schultz, Mattis (LSM) rigorous proof of zero gap for an $S = ½$ system[43], has been extended to arbitrary half-integer S, but has been shown to fail for the integer case[44], however, spin wave theory and the mapping onto the non-linear σ model are not rigorous. Therefore the implications of the LSM theory are ambiguous. It would be useful to have solvable models of the quantum spin chains, even though these Hamiltonians are not realistic. Thus a different class of solvable (*valence bond*) models was theorised. When $S = 1$ in these systems, it could be rigorously proven that a non-zero gap existed[45,46].

This valence bond state can be explained as follows, each $S = 1$ site is split up into two $S = ½$ components, these then form singlet pairs with a neighbouring $S = ½$ component, a valence bond. The spins are symmetrised, in order to maintain spin 1 per site.

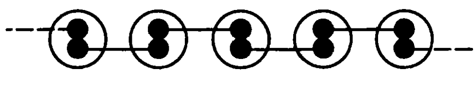

Figure 12: Schematic representation of the Valence Bond State (VBS).

To see that the VBS is indeed a ground state, take the 4 $S = ½$ variables associated with the bonding of two $S = 1$ sites. It is easy to see that at least 2 will be contracted to form a singlet. Symmetrising or antisymmetrising the other pair gives either spin 1 or spin 0, but never spin 2. Thus the ground state energy is 0.

This ground state was first presented by Affleck, Kennedy, Lieb and Tasaki and is thus known as the AKLT ground state. The exact ground state is represented by the Hamiltonian:

$$\mathrm{H} = 4J\sum_{n}\frac{1}{2}\vec{S}_{n}\,\vec{S}_{n+1} + \frac{1}{6}\left(\vec{S}_{n}\,\vec{S}_{n+1}\right)^{2} + \frac{1}{3} \qquad (13)$$

This ground state is translationally invariant, the excitation spectrum has a gap and the ground state correlations decay exponentially, as is predicted by the Haldane conjecture.

Of course the relevance of these models must be considered for real physical systems. Although $CsNiCl_3$ is not a pure Heisenberg system, due to its small Ising anisotropy it can be thought of as Heisenberg-like. The question is, will the Haldane conjecture still be relevant in integer spin systems where $\lambda \neq 1$ and $D = 0$ in equation 12.

Fortunately, numerical calculations have shown that the Haldane gap is found to persist for a finite range of exchange[47] and single ion anisotropy[48] values. The variation of the gap with exchange anisotropy only, (D = 0) is shown schematically for both integer and half-integer chains in Figure 13.

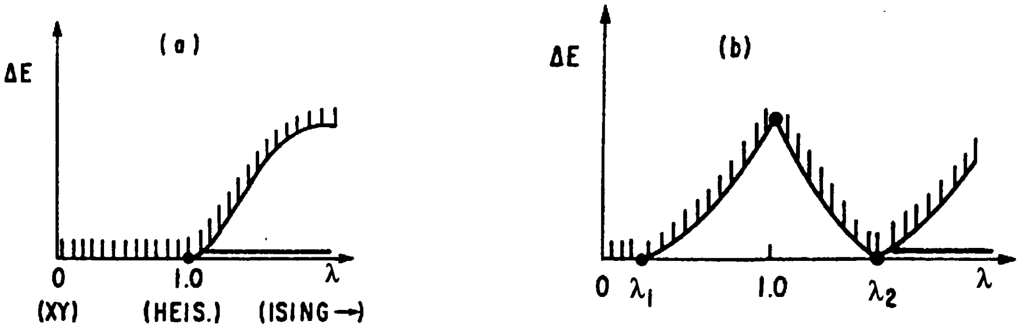

Figure 13: Schematic plot of the Haldane prediction for exchange anisotropy only, (D = 0), for (a), half-integer and (b), integer spin chains[49].

In the half-integer case, a gap opens up above the Heisenberg point at λ = 1, the excitations have an exponential dependence. In the integer case a stable Haldane gap is predicted between $\lambda_1 \leq \lambda \leq \lambda_2$. Calculated values of λ_1 and λ_2 are given below in Table 5.

Table 5: Boundaries of the Haldane phase for D = 0[57].

λ_1	λ_2	ν	β	η
0	1.18(1)	1.3(2)	0.17(5)	0.23(3)
0	1.175	< 1		
	1.184	1	0.125	0.25
	1.167(7)	0.98(2)	0.126(7)	0.253(2)
-0.01(3)	1.188(7)	1.02(5)		

Due to this persistence of the Haldane gap in an anisotropic system, much work has been undertaken on the compounds $CsNiCl_3$ and $RbNiCl_3$ in order to establish their validity as physical models for the Haldane conjecture. The two three-dimensional phase transitions (T_{N1} and T_{N2} in Figure 11) of $CsNiCl_3$, observed with specific heat[50] and nuclear magnetic resonance[51] measurements are 4.85 and 4.46 K respectively. The 1-D magnetic properties of $CsNiCl_3$ have been studied with magnetic susceptibility measurements[52] which mapped out the full phase diagram, and thermal expansion[53], heat capacity[51] and acoustic attenuation[54] methods but accurate values for the Hamiltonian could not be obtained using these measurements. The first experimental evidence for the Haldane gap in a spin 1, nearly isotropic antiferromagnetic chain came from inelastic neutron scattering measurements by Buyers *et al.*[55] on $CsNiCl_3$. They established the values of J, J' and D and showed that the gap existed in the 1D phase above 4.85K and that it was too large ($\Delta(T) = 0.32$ THz) to be caused by the known single-ion anisotropy. More recently the Haldane gap has been observed with inelastic neutron scattering in the closely related system $RbNiCl_3$[56] ($\Delta(T) = 0.63$ THz). A thorough comparison of the $S = 5/2$ system $CsMnI_3$, and the $S = 1$ system $CsNiCl_3$[57] shows several important differences in the magnon dispersion curves of the two isomorphic systems. Whilst conventional spin wave theory provides a consistent description of the $S = 5/2$ compound, it fails to describe the $S = 1$ system. Rather, the magnon dispersion curve of $CsNiCl_3$ is well described by spin wave calculations based on a field theory of the Haldane state by Affleck[40]; this provides further experimental evidence for the existence of the Haldane gap. The

Haldane gap has also been observed in other compounds such as $Ni(C_2H_8N_2)_2NO_2ClO_4$, (NENP)[58]. Recent heat capacity measurements on the pressure effect on NENP[59] show an increase in the gap mode with increasing hydrostatic pressure. It would thus be of interest to observe also the behaviour of the magnetic excitations and Haldane gap of $CsNiCl_3$ and $RbNiCl_3$ under the influence of external pressure for comparison purposes. Such experiments have been undertaken by the author and are reported on in Appendix A.

2.2.2 Easy Plane Anisotropy, $D > 0$

When the single ion anisotropy in Hamiltonian (1) is positive, the spins favour alignment in the *xy*-plane, perpendicular to the chain direction. The ground state of the structure is the chiral 120° type structure shown in Figure 6. Thus these systems are a good physical model for the testing of the Kawamura conjecture. In the presence of a magnetic field, the systems characteristics are defined by a competition between the interchain exchange energy, J', and the single ion anisotropy, D. The interchain energy prefers alignment of the spins in the 120° type structure perpendicular to the field direction, with the spins slightly canted towards the field direction. The single ion anisotropy prefers to align the spins in the *xy*-plane. The behaviour of the system with increasing field is dependant on the relative values of J' and D. There are two cases to consider, one, if $D > 3J'$ and the other if $D < 3J'$. These cases are elaborated on below and the respective phase diagrams can be seen in Figure 14 and Figure 15.

2.2.2.1 Large Easy Plane Anisotropy

Looking at the phase diagram in the case where $D > 3J'$, Figure 14, we see that upon the application of a field ⊥ to *c*, the chain direction, the spins remain in the plane but collapse into a collinear structure. There is only one example of an undistorted triangular easy-plane antiferromagnet which satisfies the condition $D > 3J'$, this is $CsMnBr_3$.

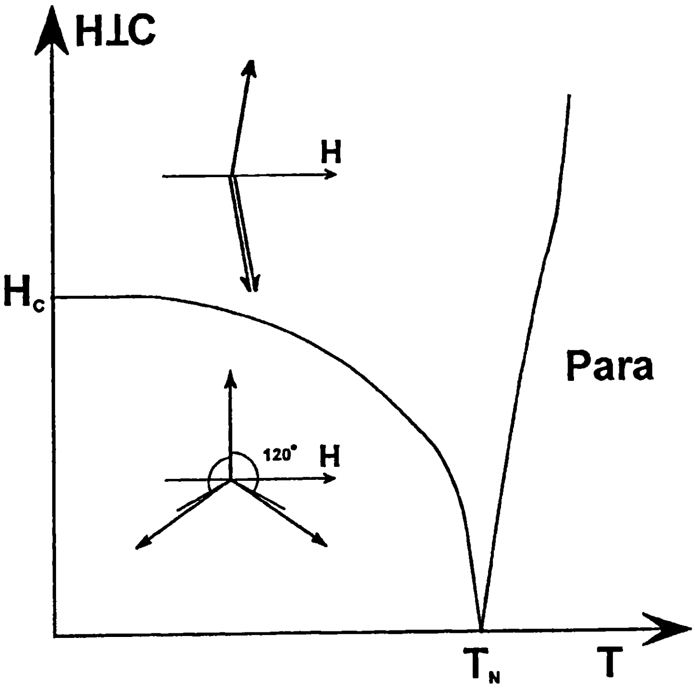

Figure 14: Magnetic phase diagram of a Heisenberg triangular antiferromagnet with large easy plane anisotropy.

The first experiments performed on $CsMnBr_3$ were done using neutron scattering techniques by the McMaster group[60,61] and the Japanese group of Ajiro[62,63], Both found critical exponent values close to that of the predicted new chiral university class. This was followed by high precision specific heat measurements by the Santa Cruz group[64] and the Karlsruhe group[65]. In later neutron scattering experiments Gaulin revealed that the zero field transition point corresponds to a *tetracritical* point in the magnetic phase diagram[66]. This is the first indication that the magnetic phase diagram of $CsMnBr_3$ does not conform to the usual, regular *XY* universality class. In order to reduce the ambiguity surrounding the new critical and novel multicritical points, theoretical scaling analysis was undertaken and subsequent predictions made[67]. Plumer, Kawamura and Caillé[19], have used symmetry arguments to show that the application of an electric field in the basal plane can break the chirality order of the 120° spin type structure. This is induced by magnetoelectric coupling (i.e. the coupling between the spin vector, S, and the electric field induced polarisation vector, P). For the hexagonal lattice these symmetry arguments show that the magnetoelectric coupling term takes a form identical to that of the Dzyaloshinsky – Moriya (DM) exchange interaction and that an applied electric (*E*) field along the basal [110] plane direction would stabilise a slightly incommensurate magnetic ordering.

The results obtained from the experiments outlined above are collated below, with the corresponding values for the critical exponents for the chiral and regular *XY* universality classes, also quoted is the mean field tricritical exponent value.

Table 6: Experimental values of the critical exponents in the easy plane system, $CsMnBr_3$ compared to model values[34].

	α	β	γ	ν	A^+/A^-
Expt.	0.39(9) [68] 0.40(5) [65]	0.22(2) [60,61] 0.25(1) [62,63] 0.21(2) [60,61] 0.24(2) [66]	1.10(5) [62,63] 1.01(8) [60,61]	0.57(3) [62,63] 0.54(3) [60,61]	0.19(10) [68] 0.32(20) [65]
XY	-0.008	0.35	1.316	0.669	0.99
n=2 chiral	0.34(6)	0.253(10)	1.13(5)	0.54(2)	0.36(20)
O(4)	-0.22	0.39	1.47	0.74	
Mean field	0.5	0.25	1.0	0.5	0

As with the results for the stacked triangular lattices with easy-axis anisotropy in Table 4, the values obtained for the large easy-plane anisotropy systems seem to support the Kawamura conjecture. Further proof could be obtained by applying an electric field in the basal plane of the system, as outlined above, and observing the net result. Work of this nature has been undertaken by the author and is reported in Chapter 4.1.

2.2.2.2 *Small Easy Plane Anisotropy*

Four systems are known to be in this category, all with the same divalent B ion, these are $CsVCl_3$, $CsVBr_3$, $CsVI_3$, and $RbVCl_3$, however, little work has been done on these compounds. The phase diagram and critical properties of the small easy plane anisotropy systems are as yet unmapped. It is expected that the phase diagram will be of the form predicted by Plumer *et al.*[69] as shown in Figure 15. Phase I is the plane triangular antiferromagnetic structure, Phase II is the collinear structure and Phase III is the spin flopped triangular structure. Work has been done on the magnetic excitations on the Cs compounds by Feile[70] who fitted the dispersions to a simple spin wave theory. However, later accurate absolute cross-section measurement work by Kadowaki[71] on $CsVCl_3$ shows that the intensity of the acoustic branch could not be accounted for by either linear spin wave theory or by magneto vibrational scattering. This is obviously a family of the stacked triangular lattice systems which has been neglected and is in need of further attention.

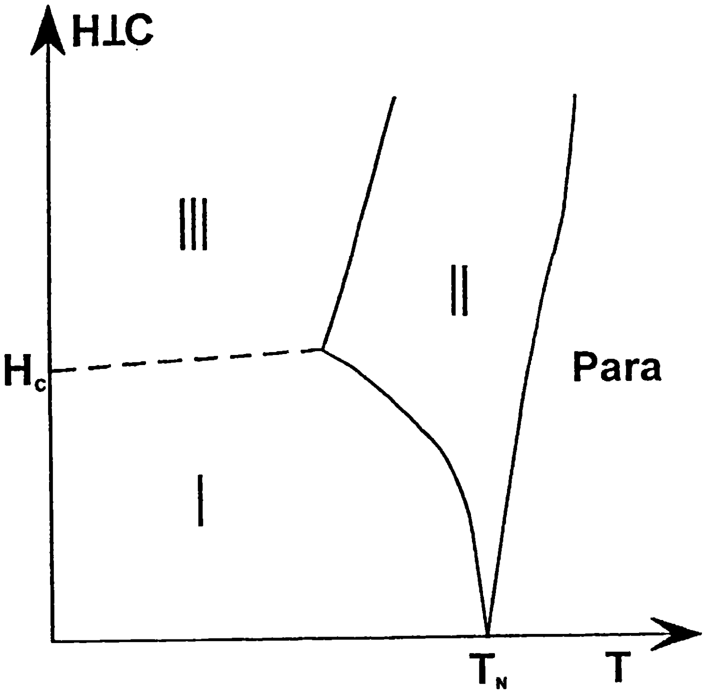

Figure 15: Magnetic phase diagram of a Heisenberg triangular antiferromagnet with small easy plane anisotropy.

2.2.3 Distorted Lattice

Not all of the ABX_3 family crystallise with space group $P6_3/mmc$. In a number of these systems structural phase transitions are observed. Systems where a structural phase transition has been observed include $KNiCl_3$, $TlFeCl_3$, $RbFeBr_3$ and $RbMnBr_3$. For the sake of clarity, the case of $RbFeBr_3$ is grouped with the singlet groundstate systems and is elucidated upon further in Chapter 2.3. Turning our attention to the other systems we observe that the typical phase transition involves the movement of two of three adjacent chains upwards while the other chain remains in the plane. The phase transition can be understood in terms of the r_A^+ and r_X^- radii. As the ratio r_A^+/r_X^- decreases, the A ion environment becomes unstable, leading to structural phase transition and to the space group P6$_3$cm.

The distorted crystal structure for KNiCl$_3$ is given below in Figure 16 as an example. It is seen that the unit cell increases from $a \times a \times c$ to the larger unit cell $\sqrt{3}a \times \sqrt{3}a \times c$ preserving the hexagonal symmetry.

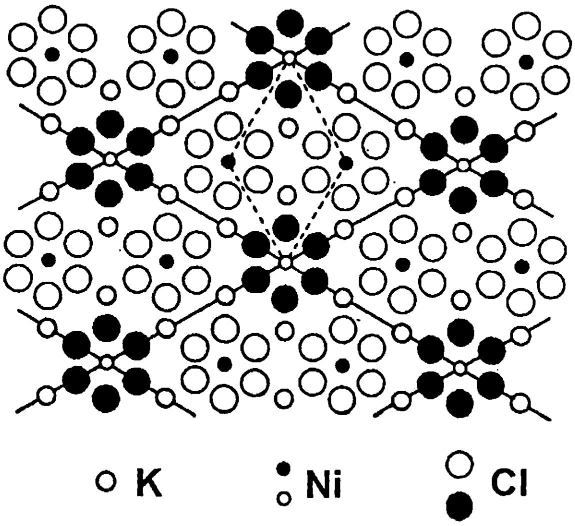

Figure 16: Room temperature structure of the distorted triangular antiferromagnet KNiCl$_3$[72].

Because the chains move as a unit there is no distortion to the chain structure and the *intra*chain superexchange energy, J, remains the same as in the undistorted case. What **is** affected by the movement of the chains, is the *inter*chain exchange energy, J'. The transition from P6$_3$/mmc → P6$_3$cm changes the symmetry of the system, reducing the co-ordination of the A ion from 12 to 9 and J' is split into two different interactions, $J'_{AA} = J'$ and $J'_{AB} = J'_1$ as shown below in Figure 17. Bearing in mind that both CsNiCl$_3$ and RbNiCl$_3$ retain the P6$_3$/mmc space group at room temperature, it is reasonable to assume that the structural phase transition is caused by the smaller size of the K^+ ion and the relative difference in the size of this and the Cl^- ion.

This reduction in the coordination number of the A ion obviously breaks the symmetry of the system and can lead to a partial lifting of the frustration. It seems that these systems are not in fact an intermediate case between frustrated and unfrustrated systems. Rather, they are predicted to exhibit novel physical properties of their own[73,74] and are thus worthy of investigation.

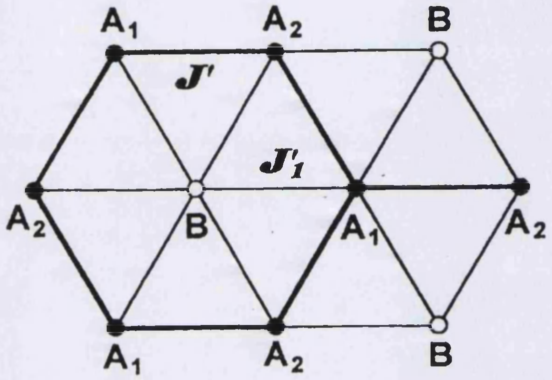

Figure 17: Magnetic interactions on the distorted triangular lattice model.

The situation as described above is observed in the room temperature structures of $KNiCl_3$ and $RbMnBr_3$, it is also observed in the *low* temperature structure of $RbFeBr_3$. The situation is further complicated in both $KNiCl_3$ and $RbMnBr_3$ by the presence of further structural phase transitions both above and below room temperature. For $KNiCl_3$ these occur at 274, 285, 561 and 762 K[75], both neutron[76] and X-ray[77] scattering have shown the existence of two crystal phases at *low temperature*. One of the phases is hexagonal and does not differ greatly from the RT structure, the other phase is orthorhombic[77].

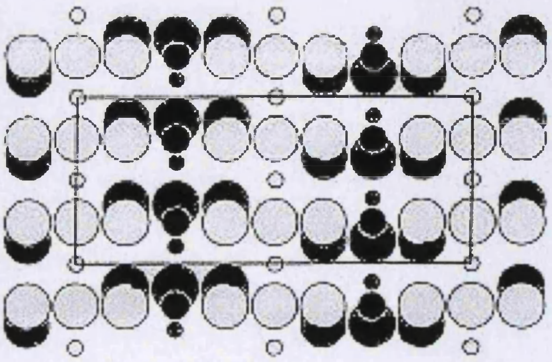

Figure 18: The row model of $KNiCl_3$.

Due to the existence of two different crystallographic structures, different magnetic structures have also been observed, with T_N = 12.5K and 8.6 K in the hexagonal and orthorhombic phases respectively. It is thought that different crystal preparation methods (i.e. annealing times, pulling rates, quenching etc.) cause these different phase transitions. With this in mind elastic and inelastic neutron scattering measurements were undertaken on several single crystal samples of $KNiCl_3$ which had undergone various heat treatments. These experiments are elaborated upon in Chapter 4.5.

Very little research has been done on the induced moment, distorted triangular lattice antiferromagnet $TlFeCl_3$. To remedy this powder diffraction studies were performed on the system, (Chapter 4.4.1) in conjunction with single crystal elastic neutron scattering studies, (Chapter 4.4.2.).

2.3 Singlet Ground State Antiferromagnets

There are 4 compounds that fall into this category with the $AFeX_3$ type structure $CsFeCl_3$, $CsFeBr_3$, $RbFeCl_3$ and $RbFeBr_3$. All crystallise with space group $P6_3/mmc$ at room temperature. It is a feature of these systems that there is a large value of magnetic anisotropy compared to the magnetic superexchange. In some instances, this large anisotropic factor will prevent the onset of long range order, even at T = 0K. The electronic structure of the Fe^{2+} ion in these systems is as shown below.

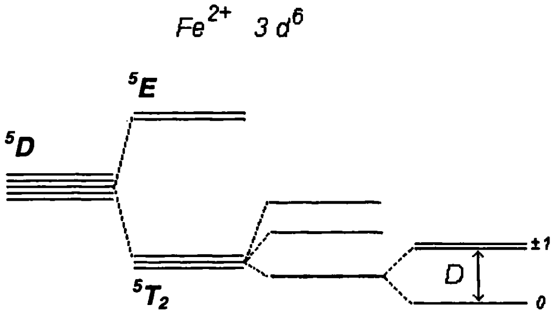

Figure 19: Electronic perturbations acting on the free ion 5D term of Fe^{2+} ion in the $AFeX_3$ family. The successive splitting arises from the *cubic component of the ligand field*, *spin orbit coupling* and the *trigonal distortion of the ligand field*, respectively.

The free ion in the ^5D ground state is split into an upper orbital doublet (^5E) and lower orbital triplet ($^5T_2$) by the cubic crystal field, separated by 10,000cm^{-1}. The lower triplet is then further split by spin orbit coupling according to the effective total angular momentum J = 1, 2, and 3, into the states $^5T_{2a}$, $^5T_{2b}$, and $^5T_{2c}$, spaced according to the Landé interval rule by 2λ and 3λ respectively. The lowest J = 1 is then split by a trigonal component of the crystal field Δ to produce a singlet ground state and an excited doublet with a separation of the order of 100cm^{-1}. At low temperatures only the lowest singlet and doublet are significantly populated, thus probing the transition between these states with neutron scattering allows us to gain knowledge of the system.

As T → 0, there are two regimes, (in the absence of magnetic field), which can be observed in these systems.

- For $D < 8\,|J| + 12\,|J'|$ the system has a magnetic ground state with an easy plane type anisotropy. This is the case for $RbFeCl_3$ and $RbFeBr_3$.

- For $D > 8\,|J| + 12\,|J'|$ the system has a singlet ground state meaning that it does not magnetically order even at T = 0K. This is the case for $CsFeCl_3$ and $CsFeBr_3$.

The application of an external magnetic field along the *c*-axis leads to magnetic order in the SGS materials. If the magnetic field is applied in the basal plane no transition to magnetic order is observed. In $CsFeCl_3$ the application of a magnetic field parallel to the c-axis induces a commensurate 120° type structure after transition through two intermediate incommensurate phases. In $CsFeBr_3$ the application of field leads directly to commensurate order.

2.3.1 *True singlet ground state antiferromagnets, ($CsFeBr_3$, $CsFeCl_3$).*

In the system $CsFeBr_3$ the *intra*chain exchange interaction is antiferromagnetic, this is in contrast to the intrachain exchange interaction in $CsFeCl_3$ which is ferromagnetic[78]. This is due to the different spatial characteristics of the Br and Cl ion, leading to different Fe – X – Fe distances and bridging angles.

The studies on $CsFeBr_3$ have mainly concentrated on the magnetic excitations of the system. Low temperature inelastic neutron scattering studies have shown that the magnetic excitations in $CsFeBr_3$ soften with decreasing temperature, stabilising at 0.11 THz at T = 2.5K down to T = 80mK[79,80]. This suggests that $CsFeBr_3$ is a SGS for T → 0K. Low temperature inelastic neutron scattering studies in an external magnetic field have shown that, at T =1.6K and H = 4.1T, a well defined magnetic Bragg peak appears at the reciprocal lattice point Q = (2/3 2/3 1). This indicates a phase transition to the long range commensurate 120° type structure[81].

As with $CsFeBr_3$, low temperature neutron scattering studies of $CsFeCl_3$ show that the system is a SGS system for $T \rightarrow 0K$. The values for exchange interaction and magnetic anisotropy have been estimated from the dispersion relations. However, the exact values depend on the theoretical model used to fit the data. Values have been obtained for correlated effective field analysis[96], self-consistent random-phase approximation[82] and dynamical correlated effective-field approximation[83]. Each theory gives substantially different values of the exchange interaction and magnetic anisotropy. Inelastic neutron scattering studies have showed that the minimum of the magnetic dispersion curve does not fall at the *K*-point as expected, rather it is slightly offset[84]. This can be accounted for by the inclusion of magnetic dipolar forces[85,100]. Neutron scattering studies on $CsFeCl_3$ in an external magnetic field demonstrate the transition to the 120° magnetically ordered state at T = 0.7K with H_3 = 4.5T, previous commensurate transitions take place at H_1 = 3.85T and H_2 = 3.92T. This transition to a magnetically ordered state has been observed with specific heat[86], Mössbauer[87], and magnetisation measurements[88]. The five possible transitions between the ground state and the excited doublet in the presence of external magnetic field ($H_{||}$ and $H_{\perp}$), have been observed with submillimetre wave ESR measurements[89]. Other work has been undertaken on the magnon dispersion branches of $CsFeCl_3$ and $CsFeBr_3$ under hydrostatic pressure by the author during his MPhil. degree and is re-analysed in Chapter 5. Also presented are full powder neutron diffraction studies on the above compounds as a function of applied pressure.

2.3.2 *Induced moment antiferromagnets, ($RbFeBr_3$, $RbFeCl_3$).*

$RbFeBr_3$ can be thought of as a combination of an induced moment antiferromagnet and a Heisenberg antiferromagnet with *XY* anisotropy. Measurements by Eibschütz *et al.* on the system show that, unlike the $CsFeX_3$ family, the exchange interaction is strong enough to produce magnetic long range order at T = 5.5K[90]. At 108K the system undergoes a structural phase transition from the hexagonal perovskite $P6_3/mmc$ space group, to the distorted phase with space group $P6_3cm$[91], as is described in Chapter 2.2.3. This distortion leads to two different nearest neighbour exchange interactions within the basal plane. The low temperature crystal phase is found to be ferroelectric[92], however this phase is not yet fully understood. Specific heat measurements on the system show two successive magnetic phase transitions at T_{N1} = 5.61K and T_{N2} = 2.00K[93], it is possible that this may be caused by the splitting between the two different basal plane exchange interactions. However, inelastic neutron scattering measurements have not shown this splitting due to inadequate resolution[94]. The measured excitations are well described by the dynamical correlated effective-field approximation.

As with $RbFeBr_3$, $RbFeCl_3$ also shows long range magnetic order, below T =2.55K[95]. Inelastic neutron scattering studies have clearly demonstrated the softening of the magnetic excitations as T → 2.55K[96,97]. Elastic neutron scattering studies have revealed that $RbFeCl_3$ undergoes three magnetic phase transitions in zero field, at T_{N1} = 2.5K, T_{N2} = 2.35K and T_{N3} = 1.95K. Between T_{N1} and T_{N2} and between T_{N2} and T_{N3} incommensurate magnetic phases exist. Below T_{N3}, $RbFeCl_3$ locks into the 120° type magnetic structure[95,96,98]. These values have also been confirmed using specific heat[86] and susceptibility methods[99], looking at the anomalies observed in these experiments a magnetic phase (*H, T*) diagram can be constructed.

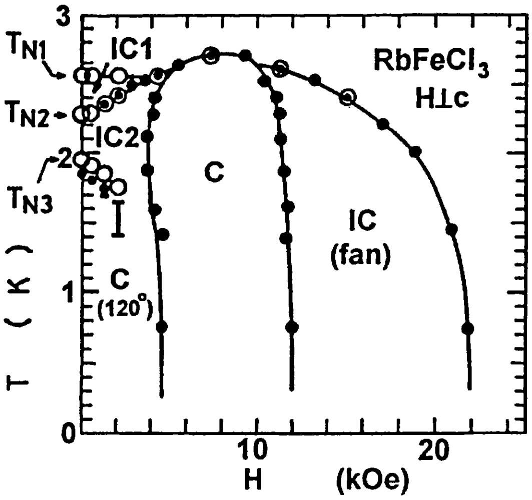

Figure 20: Magnetic phase diagram of $RbFeCl_3$, for H ⊥ *c* [99]. Open circles refer to anomalies in specific heat measurements, closed circles to anomalies in susceptibility measurements.

The phase diagram is explained from the point of dipole-dipole interactions inducing conical point instability[100]. Shiba conjectures that a small dipole-dipole interaction transforms the 120° structure to an incommensurate structure at intermediate temperatures, whilst the low temperature phase should still remain at 120°. This phase diagram has also been investigated using inelastic neutron scattering, producing good agreement for the magnetic transitions[101]. The calculated values of the exchange parameters are highly dependent on the theory use to fit the experimental data. The superexchange parameters have been estimated from various experiments. Using molecular field approximation[102] and pair approximation[103], the superexchange parameters were calculated for susceptibility measurements. Mössbauer and susceptibility data[104] was analysed using the correlated effective-field approximation[105]. Neutron scattering measurements were analysed using the three sublattice spin-wave approximation and the exciton model. Each model gives its own unique values for the superexchange parameters. Suzuki has attempted to understand the magnetic properties on the basis of a single set of parameters[26], using the dynamical correlated effective-field approximation (DCEFA) to model the experimental data. The calculated values of D, $J_{\perp}$, $J_{||}$, $g_{\perp}$ and $g_{||}$ gave reasonable agreement with experiment. This was only applicable to the paramagnetic phase as the theory only considered a single chain of Fe^{2+} ions for simplicity. More recently Suzuki has added interchain coupling and derived a consistent set of exchange parameters that accurately describe the behaviour of $RbFeCl_3$ both above and below T_N[27,28].

2.4 Neutrons: their properties and applications.

All experimental work contained in this thesis is the result of neutron scattering experiments performed at a variety of steady state and spallation neutron sources. Thus the following chapters give a brief introduction to the neutron, its fundamental properties, its production at steady state and spallation sources and the theory governing its interaction with condensed matter.

2.4.1 Fundamental properties of the neutron.

The neutron is composed of one up and two down quarks with charges of 2/3 and –1/3 respectively. In spite of the fact the neutron carries no net charge it does possess a magnetic moment. This is due to an electric charge distribution caused by its internal structure. It is believed that the neutron spends part of its time dissociated into a proton and a negatively charged π-meson according to the equation:

$$\mathrm{n} \Leftrightarrow (\text{proton})^{+} + (\pi\text{-meson})^{-}$$

During this dissociated time the positive and negative centres of the proton and meson coincide, but the negative charge is more diffuse. This charge distribution gives the neutron its magnetic moment and also an electric polarizability.

The energy and spin characteristics of the neutron further enhance its effectiveness in probing condensed matter. Summarising, we can say that the fundamental properties of the neutron make it a highly effective probe of condensed matter and these are outlined below.

- The neutron has no charge therefore its interactions with condensed matter are confined to the short range and magnetic interaction.

- Due to the fact that the kinetic energy of the neutron is close to that of the energy range of elastic and inelastic processes in condensed matter it is the ideal and the only tool to measure dispersion throughout the Brillouin zone.

- The magnetic moment of the neutron makes it an ideal tool to probe the magnetisation of condensed matter. Neutrons may be scattered from the magnetic moment associated with unpaired electrons in the magnetic material.

- The neutron has spin 1/2 and as such when a neutron is scattered from a nucleus with a non-zero spin, the strength of the interaction depends on the relative orientation of the neutron and nuclear spins. The orientation of the neutron may be manipulate by the application of 'spin flippers' on the neutron beam coming from the source, thus allowing one to deduce the relative nuclear spin of the nucleus.

2.4.2 Production of neutrons.

There are various means to produce neutrons, not all are efficient or effective. In this Chapter we will look at the two most widely employed techniques for neutron production, that using nuclear reaction used at steady state sources and that employing the proton spallation process, used at spallation sources. As with all techniques each has its own advantages and disadvantages and these are outlined below.

Virtually all neutrons used for scattering experiments at modern steady state reactor sources are obtained by slowing energetic neutrons produced in nuclear reactions by passing them through a moderating material containing light atoms. Thus the majority of atoms will have energies of the order of k_BT where T is the temperature of the moderator and k_B is Boltzman's constant. Using simple wave mechanics it is relatively easy to demonstrate that:

$$k_B T = \frac{\hbar^2}{2m\lambda^2} \tag{14}$$

where $\hbar = h/2\pi$, where h = Plank's constant and λ and m are the wavelength and mass of the neutron respectively.

Substituting the known values and assuming that T = 300K (room temperature), we see that $\lambda = 2\text{x}10^{-8}$ m. This is comparable to the interatomic separation of atoms in a solid or dense fluid, thus neutrons are ideally suited for the study of atomic structure.

The velocity spectrum of neutrons emerging from a reactor follows a Maxwellian distribution described by the equation

$$\phi(v) \propto v^3 \exp\left[-\frac{mv^2}{2k_B T}\right] \tag{15}$$

where $\phi(v)dv$ is the number of neutrons with energy between v and $v+dv$, m is the mass of the neutrons, k_B is Boltzman's constant and T is the temperature of the moderator.

The maximum of the function occurs where:

$$v = \left[\frac{3k_B T}{m}\right]^{\frac{1}{2}} \tag{16}$$

Thus we can see from the equation above that the only variable is T, the temperature of the moderator. This gives us an easy way of manipulating the energies of the neutrons. If higher energies are required then the neutrons are passed through a heated source, such as a heated graphite block, conversely the energies of the neutrons can be shifted to lower energies by passing them through a cooled moderator, such as liquid deuterium or helium. In this manner a full range of energies are obtainable from a single reactor source. Modern reactor sources, such as the Institut Laue Langevin, are capable of producing a neutron flux of around $1.2 \text{ x } 10^{15}$ $\text{ns}^{-1}\text{cm}^{-2}$.

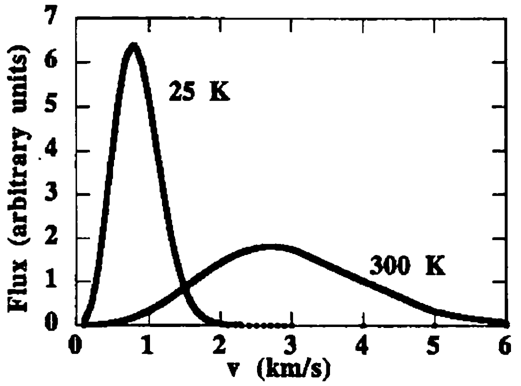

Figure 21: Flux distribution in the beam of neutrons from a moderator at 25K and from a moderator at 300K. The distributions are normalised to have the same total flux[106].

There are a number of disadvantages to steady state reactor sources, numbering amongst others, the radioactive waste produced by the nuclear reaction and the complicated technical problems of cooling such a reactor. It is widely assumed that the next generation of neutron sources will be based around the spallation technique employed at the ISIS facility (e.g. the proposed new European Spallation Source[107]). The term spallation originates from geology and literally means 'chipping off'. It describes the process by which an energetic charged particle, normally in this case, a proton, impinges on a stationary target material of heavy nuclei. The net effect is the 'spalling' of the target material into a large number of nucleons and other fragments. Protons accelerated to an energy of 600MeV can produce 10 – 12 neutrons of average energy of 2 – 3 MeV, per reaction, from a target such as lead or tungsten and about 25 neutrons per reaction from a ^{238}U target. The ISIS target consists of a set of thin tantalum sheets surrounded by a coolant of flowing water. The target is used to convert the proton beam energy (160 kW) into neutrons through the spallation process. Such target stations produce an average neutron production of 4×10^{16} n $s^{-1}cm^{-2}$ which compares favourably with steady state sources. Advantages of this type of source include less heat, thus less cooling and also less waste to contend with.

2.4.3 *Diffraction.*

Having produced the neutrons the next step in the experimental chain involves scattering them from a powder or crystalline sample. Like x-rays, neutrons can be thought of in terms of waves with a De Broglie wavelength of,

$$\lambda = \sqrt{\frac{\hbar^2}{2mE}} \tag{17}$$

where m is the neutron mass = 1.675 x 10^{-24} g and E being the kinetic energy of the neutron = ½ mv^2, v being the velocity of the neutron. In order to explain the rather complicated mechanics involved in neutron scattering it is probably advisable to start with scattering from a fixed atom, this is what is known as *elastic* scattering.

2.4.3.1 *Elastic scattering*

It is the case with x-rays that they scatter from the electrons surrounding the atom, with the intensity of scatter diminishing with increasing scattering angle. However neutrons are scattered by the nucleus of the atom, this being much smaller it can be regarded as a point target. By impinging a plane wave of neutrons of the form $\Phi = e^{ikx}$ onto an atom, one sees that the scattered wave has the form,

$$\Phi = -\frac{b_n}{r} e^{ikr} \tag{18}$$

where r is the distance from the nucleus and b_n is the neutron scattering length. The important thing to consider is the scattering cross section of the nucleus, this is the ratio of scattered neutrons to the incident neutrons and is given by the formula,

$$\sigma = 4\pi b_n^2 \tag{19}$$

Thus we can see that the scattering cross section is directly related to the neutron scattering length. The value of b_n varies widely from element to element through the periodic table and b_n may even be negative in some circumstances. This is important if we consider that the x-ray form factor increases linearly with increasing atomic mass, thus elements next to each other will have very similar scattering lengths and thus be difficult to distinguish in x-ray scattering experiments, this is not the case with neutrons. Also it can be deduced that light elements will scatter x-rays relatively weakly and thus be almost impossible to discern in your sample. Again this is not the case with neutrons as the light elements, such as Helium, have comparable neutron scattering lengths to the other elements in the periodic table.

The purpose of neutron scattering experiments is to measure the intensity of the neutrons scattered by matter as a function of the variables Q and ξ, where ξ is the energy transfer of the neutron. This scattered intensity often denoted as $I(Q, \xi)$, is known as the 'scattering intensity law' of the sample. It was in 1954 that Van Hove showed that the scattering law could be written exactly in terms of time-dependent correlations between the position of *pairs* of atoms in the sample. It is expressed in the form,

$$I(Q,\xi)=\frac{1}{h}\frac{k_i}{k_f}\sum_{m,n} b_n b_m \int_{-\infty}^{\infty} \left\langle e^{-iQ\cdot r_n(0)} e^{iQ\cdot r_m(t)} \right\rangle e^{-i\epsilon t}\, dt \tag{20}$$

Note that the sum here is over *pairs* of nuclei *m* and *n*, and that the nucleus labelled *m* is at position $r_m(t)$ at time t, whereas the nucleus labelled *n*, is at position $r_n(0)$ at time $t = 0$. The angular brackets $\langle ... \rangle$ denote an average over all possible starting times for observations of the system which is equivalent to an average over all the possible thermodynamic states of the sample.

Summing over all the atomic sites in 20 gives us,

$$\sum_{m,n} b_m b_n \left\langle e^{-iQ\cdot[r_n(0)-r_m(t)]} \right\rangle = \sum_{m,n} b_m b_n \int_{-\infty}^{\infty} \delta \langle (r-[r_n(0)-r_m(t)]) \rangle e^{-iQ\cdot r} d^3 r \tag{21}$$

Where δ is the Dirac delta function, expressed in terms of **r** and a difference vector between the position of nucleus *m* at time *t* and that of *n* at time zero. If we assume that $b_m = b_n = b$, this allows us to remove the scattering lengths in the above equation with the right hand side becoming,

$$Nb^2 \int_{-\infty}^{\infty} G(r,t) e^{-iQ\cdot r} d^3 r \tag{22}$$

where

$$G(r,t) = \frac{1}{N} \sum_{m,n} \langle \delta(r - [r_n(0) - r_m(t)]) \rangle \tag{23}$$

and *N* is the number of atoms in the sample. The delta function in the definition of *G(r,t)* is zero, except when the position of *n* at time zero and the position of *m* at time *t* are separated by vector **r**. Because the delta functions are summed over all possible pairs of atoms to obtain *G(r,t)*, this function is equal to the probability of an atom being at the origin of a coordinate system at time zero and an atom being at position **r** at time *t*. *G(r,t)* is generally referred to as the *time dependant pair correlation function* as it describes how correlation between two particles evolves over time. Van Hove's equation (20) can now be written as,

$$I(Q,\xi) = \frac{Nb^2}{h} \frac{k_i}{k_f} \int_{-\infty}^{\infty} G(r,t) e^{-iQ\cdot r} e^{-i\varepsilon t} d^3 r dt \tag{24}$$

This allows us to see that ***I****(Q*,ξ) is proportional to the space and time Fourier transforms of the time dependent pair-correlation function. Thus we see that Van Hove's result implies that ***I****(Q*, ξ) is simply proportional to the Fourier transform of a function that gives the probability of finding two atoms a certain distance apart. Thus by measuring the intensity of scattered neutrons as a function of *Q* and ξ, one may use the Van Hove result to relate the intensity of the scattered neutrons to the relative positions and motions of atoms in your sample. Van Hove's result may be manipulated to reveal scattering effects of two different types. The first type is *coherent* scattering in which the neutron wave interacts with the whole sample as a unit so that the scattered waves from different nuclei interact with each other. This type of scattering depends on the relative distances between the constituent atoms and thus gives information about the structure of materials. Elastic coherent scattering gives us information regarding the equilibrium structure whereas inelastic coherent scattering can tell us about the collective motions of the atoms in the sample.

The second type of scattering is called *incoherent* scattering and, as the name suggests, in this method the neutron wave interacts independently with each nucleus in the sample so that the scattered waves from different nuclei do not interfere, rather the intensities from each nucleus simply sum up. Incoherent scattering could take place, for example, when a neutron wave interacts with the *same* atom but at different times. Thus this method can be used for gaining information about atomic diffusion.

When neutrons of a suitable wavelength impinge on a crystal (which can be thought of classically, as a lattice of regularly spaced atoms), they are scattered by that lattice. This is a direct result of the wave-like nature of the neutron. Bragg's law states that diffraction will occur when the phase difference between scattered rays from a set of atomic planes is of an integral number of wavelengths, or more simply,

$$n\lambda = 2d sin\theta \qquad (25)$$

Thus constructive interference occurs where n, the lattice plane, is an integer. d is the lattice spacing and θ is the angle of incidence of the beam, this is shown graphically below.

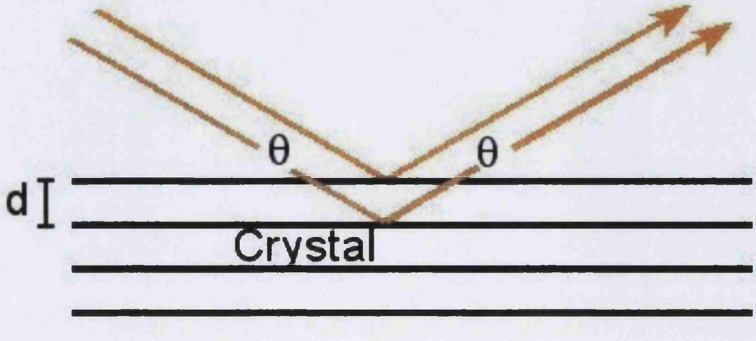

Figure 22: Bragg diffraction at an angle θ from a set of crystal planes separated by distance d.

The best way to analyse the results of neutron scattering experiments is by means of the reciprocal lattice. The reciprocal lattice is a rather convenient concept and involves the mapping the vectors of the real space unit cell *a*, *b* and *c* to a new set of basis vectors.

$$\vec{a}^* = 2\pi\frac{\vec{b}\times\vec{c}}{\vec{a}\cdot\vec{b}\times\vec{c}} \qquad \vec{b}^* = 2\pi\frac{\vec{c}\times\vec{a}}{\vec{a}\cdot\vec{b}\times\vec{c}} \qquad \vec{c}^* = 2\pi\frac{\vec{a}\times\vec{b}}{\vec{a}\cdot\vec{b}\times\vec{c}}$$

Thus the new units of distance will be $Å^{-1}$ and we can visualise that any Bragg reflection that corresponds to a set of lattice planes can now be regarded as a point in reciprocal space (x, y, z). This point may be described by a vector Q also, where $Q = xh + yk + zl$, from the origin of the reciprocal lattice. If we consider the case of elastic scattering, whereby the wavevectors of the initial ($|k_i|$) and scattered ($|k_f|$) beam are equal in magnitude, we see that the locus of points defined by the wavevectors $|k_i|$ and $|k_f|$ constructs a circle. This is commonly known as the Ewald sphere and as seen in Figure 23, elastic coherent scattering will be possible where a reciprocal lattice point falls on the sphere. It should be noted that this is an infrequent occurrence, thus in order to maximise the probability of elastic scattering occurring the sample is rotated. This construction in Figure 23 makes it simple to see the effect of rotation of the crystal in real space. As the crystal rotates, the reciprocal lattice rotates with it so that each of its points moves on an arc centred at the origin. As each point passes through the Ewald sphere, diffraction occurs for that Q at the corresponding scattering angle θ. This is the basis for conventional single crystal diffraction experiments.

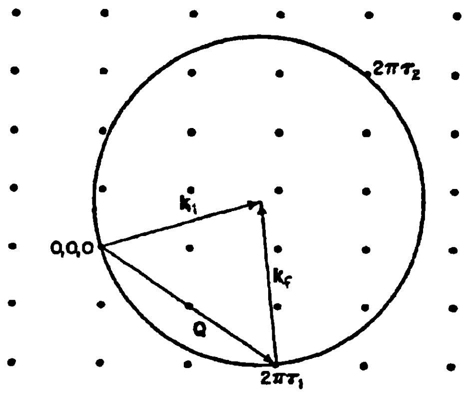

Figure 23: A representation of a crystal lattice in reciprocal space, showing the Ewald sphere condition for elastic scattering[108]**.**

Elastic scattering can be achieved with x-rays as well as neutrons but it is often more rewarding to utilise the former due to the availability of extremely intense synchrotron sources, such as the ESRF at Grenoble, which afford excellent resolution. It should be remembered that x-rays only penetrate a very small way into the sample (up to 1μm) whilst neutrons, due to their uncharged nature are scattered from the bulk of the material.

One would assume that the better quality of the scattering crystal, the more intense the diffraction. Paradoxically this is not the case, in perfect crystals *primary* extinction occurs and reduces the scattered beam. This is due to the attenuation the incident beam suffers upon passing through the perfect crystal domain. *Secondary* extinction occurs in less perfect crystals, when misorientations between the small mosaic blocks or domains that make up the crystal, are greater than the width of the reflected beam within each fragment. In normal cases the diffracted intensity is reduced by a combination of both *primary* extinction inside each mosaic block and *secondary* extinction between each mosaic block.

Elastic neutron scattering is measured as a *partial differential cross-section*, this is the function of the total scattered flux, σ, per unit angle $d\Omega$, per unit time. The elastic nuclear scattering cross section is the sum of the coherent and incoherent cross sections.

$$\frac{d\sigma}{d\Omega}=\left(\frac{d\sigma}{d\Omega}\right)_{coh}+\left(\frac{d\sigma}{d\Omega}\right)_{incoh} \qquad (26)$$

A good model for application to elastic scattering is the Fermi pseudopotential,

$$V(\underline{r})=\frac{2\pi\hbar^2}{m}b\delta(\underline{r}) \qquad (27)$$

where m is the mass of the neutron and b is the scattering length of the nucleus at position $\underline{r}$. The coherent part of equation 24 can be represented by,

$$\frac{d\sigma}{d\Omega} = \frac{N(2\pi)^3}{v_o} \sum_{\tau} \left| F_N(\underline{Q}) \right|^2 \delta(\underline{Q} - \underline{\tau}) \tag{28}$$

and describes the Bragg scattering from the sample. Here N is the total number of unit cells in the crystal, v_o is the volume of one unit cell in reciprocal space and $\underline{\tau}$ is the reciprocal lattice vector in terms of a basis of unit vectors as described above, where, $\underline{\tau} = h\underline{a}^* + k\underline{b}^* + l\underline{c}^*$. The δ function ensures the selection of only those scattering vectors $\underline{Q}$, that equal $\underline{\tau}$ (the Bragg condition). The unit cell structure factor, $F_N(\underline{Q})$, is the thermal average of the scatting amplitude from each nucleus and is expressed in the form,

$$F_N(\underline{Q}) = \sum_{j,s} \overline{b_s} e^{i\underline{Q} \cdot r_j^s} e^{-W_j^s(\underline{Q})} \tag{29}$$

where the summation is over the different atoms s and their positions in space j. $\overline{b_s}$ is the average scattering length for atom s in the unit cell.

The Debye – Waller factor, $e^{-W_j^s(\underline{Q})}$ arises due to the fact that each atom is not actually rigidly fixed in position, rather is subject to thermal and zero point motion. Thus the scattering comes from a diffuse area which gradually decreases with increasing $\underline{Q}$. The exact form of $W_j^s(\underline{Q})$ is dependent on the structure of the material.

Looking at the *incoherent* part of equation 24, this scattering originates due to the different isotopes and nuclear spins that are randomly distributed throughout the crystal. This scattering contributes to the background and is homogeneous over the entire solid angle, $\Omega = 4\pi$.

$$\left(\frac{d\sigma}{d\Omega} \right)_{incoh} = \frac{1}{4\pi} \sum_{\tau} \overline{\left| b - \overline{b} \right|^2} e^{-2W_j^s(\underline{Q})} \tag{30}$$

In actual fact, the scattered intensity will not behave like a delta function as is suggested above. Rather, for any real crystal, $\underline{\tau}$ is a cone from the origin of reciprocal space to a small volume centred on the mean reciprocal lattice point. In practice, the variation of intensity with ω or with 2θ is well approximated by a Gaussian function, which also accounts for the resolution function of the neutron scattering instrument. However, this is not always the case with powder diffraction as opposed to single crystal diffraction. The peak shape for powder diffraction patterns can be quite complex and is usually machine specific, normally mimicking the pseudo-Voigt function.

Of course the diffraction of neutrons by matter is not the same as scattering from a fixed point (an elastic event), this is due to the inherent thermal motion of the lattice The process of scattering can alter momentum and energy of both the neutrons and the crystal. This is what is known as an inelastic event and is elaborated upon further in the next Chapter.

2.4.3.2 *Inelastic scattering*

One significant advantage of using neutrons comes from inelastic scattering, i.e. when the scattered vector does not equal the incoming vector. The momentum transfer of the neutron during collision can be written as $\hbar Q = \hbar(k_i - k_f)$, where $k_i \neq k_f$. The relationship between Q, k_i and k_f can be represented, as above in Figure 23, with the aid of scattering triangles.

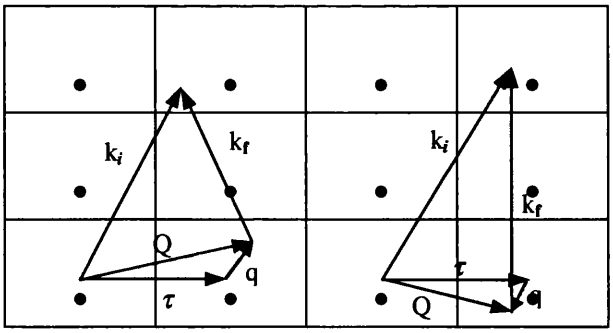

Figure 24: The scattering triangles in reciprocal space for an inelastic scattering event. Depicting energy loss and gain of the neutron on the left and right respectively.

The scattered neutrons will have energy of $\frac{\hbar^2 k_\mathrm{f}^2}{2m}$,

that is different to the energy of the incident beam. Instead, the picture is as shown in Figure 24, where $k_i \neq k_\mathrm{f}$. The mathematical representation of Figure 24 is given as a function of the *double differential cross section*, this is similar to the differential cross section but it deals with the probability of neutrons being scattered into $d\Omega$, with energy $E \pm \Delta E$. Due to the fact that the excited states involve large regions of the sample, rather than isolated atoms, and as the measurements select only a small fraction of the total scattered flux, large crystals and intense neutron beams are needed in order to study inelastic events. The inelastic one-phonon scattering cross section is written as below. The 'plus' sign refers to phonon creation and the 'minus' sign to the scattering whereby the neutrons gain energy from the thermal phonons in the lattice. Phonon creation is possible at any temperature whereas the latter is more likely at high temperatures.

$$\frac{d^2\sigma}{d\Omega dE} = \frac{k_i}{k_\mathrm{f}} \frac{(2\pi)^3}{2V} \sum_{\underline{q},\underline{\gamma},\underline{\tau}} \left|F_\gamma(\underline{q},\underline{Q})\right|^2 \frac{1}{\omega_\gamma(\underline{q})} \left[n_\gamma(\underline{q}) + \frac{1}{2} \pm \frac{1}{2}\right] \times \delta\left[\omega \pm \omega_\gamma(\underline{q}) \times \delta(\underline{Q} \pm \underline{q} - \underline{\tau})\right] \tag{31}$$

V is the crystal volume and q, Q and τ are as defined in Figure 24. γ is the quantum number that labels the eigenfrequencies $\omega_\gamma(q)$ of the phonon. The δ functions specify the energies and position in reciprocal space where the measurement is being taken. $n_\gamma(q)$ is the Boltzman factor and is describes the distribution function of phonons of different energies. The inelastic structure factor can be defined as,

$$F_\gamma(\underline{q},\underline{Q}) = \sum_{\underline{l}} \overline{b_l} \frac{\underline{Q} \cdot \underline{V}^l(\underline{q})}{\sqrt{M_{\underline{l}}}} e^{i\underline{Q}\cdot r_l} e^{-W_l(\underline{Q})} \tag{32}$$

and may be compared with the nuclear coherent elastic equivalent from equation 24. The extra parameters in the above are M_l, the mass of the atom at position l and $Q \cdot V^l(q)$, the dot product of the wavevector Q, and the polarisation vectors V for a particular q, summed over the set of normal vibrational modes.

2.4.3.3 Magnetic Scattering

In order to describe magnetic scattering of neutrons, it may be prudent to discuss first the principles of x-ray scattering by atoms. The basic interaction in this case is that of an electromagnetic wave with the electric charge of the atom. The scattered wave, from a small volume dV at position $\mathbf{r}$, should be proportional to the charge collected in this volume i.e. $\rho_c(\mathbf{r})dV$, times the phase factor $\exp(-i\kappa\cdot\mathbf{r})$, where $\kappa = k_f - k_i$. The total scattering by an atom is obtained when all such contributions are added together, which means that the scattering amplitude of x-rays by an atom must be proportional to,

$$Zf_c(\theta) = \int \rho_c(\mathrm{r})e^{-i\kappa\cdot\mathrm{r}}dV \qquad (33)$$

where Z is the total charge of the atom and $f_C(\theta)$ is the *charge form factor*, normalised to unity at $\kappa = 0$.

Because the electron distribution in an atom spreads out to something which we can imprecisely call the atomic radius, R_{at}, the function $f_C(\theta)$, is strongly θ - dependent. This is a direct consequence of the fact that the x-ray wavelengths and R_{at} are of the same order of magnitude. The form of the function is shown below, labelled f_C as a function of $\sin(\theta) / \lambda$.

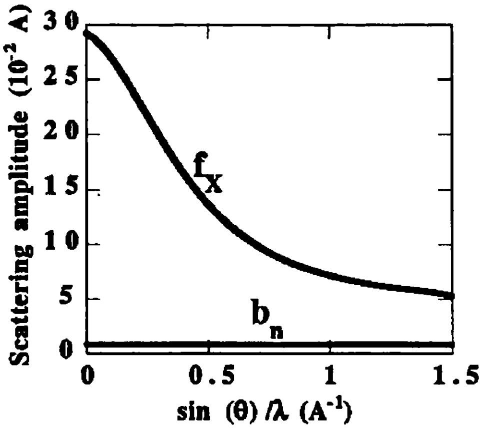

Figure 25: The variation of the form factors for x-ray (f_C) and magnetic neutron scattering (f_M)[106].

The short resume given above should be helpful in forming an idea of what happens when a neutron interacts with an atom with magnetic moment μ. The neutron is also in possession of a magnetic moment and thus can 'feel' the magnetic field created by the atomic moment. The scattering which results from the interaction of the neutron and atom must be proportional to the neutron's magnetic moment and also proportional to the spatial distribution of the magnetic moment μ of the atom, in much the same way as x-rays react to the spatial distribution of charge. The magnetic scattering should have the form, similar to (33),

$$\tilde{p}(\theta) = const \cdot \int \rho_M(\mathrm{r}) e^{-i\kappa \cdot \mathrm{r}} dV \qquad (34)$$

where $\rho_M(\mathbf{r})$ is the magnetisation density of the atom and the multiplicative constant must contain the neutron fundamental constants. Due to the fact that the magnetic scattering also depends on the mutual orientation of the neutron and atom magnetic moment and possibly on the scattering vector κ this constant should contain information on these as well. Indeed, it has been shown by Halpern and Johnson[109] that,

$$\tilde{p}(\theta) = 0.2659\ \sigma \cdot \mathrm{q} \mu f_M(\theta) = \sigma \cdot \mathrm{q} p(\theta) \qquad (35)$$

where f_M is the *magnetic form factor.*

$$f_M(\theta) = \frac{1}{\mu} \int \rho_M(\mathrm{r}) e^{-i\kappa \cdot \mathrm{r}} dV \qquad (36)$$

This function describes the spatial distribution of magnetisation within the atom and is also normalised to unity at $\kappa = 0$. The function is shown in Figure 25 with f_C for comparison. We know that magnetic scattering arises from the uncompensated magnetic moment of electrons occupying 3*d*, 4*d* or 5*d* shells (transition metals) or the 4*f* (lathanides) or 5*f* shells (actinides). These electrons are usually located outside the 'core' formed by the majority of the electrons, thus one can see that the spatial distribution of these electrons will be more diffuse than the overall charge distribution of the atom. Due to the properties of the Fourier transforms this must be reflected in a magnetic form factor which is narrower than the charge form factor of the atom. This is shown above in Figure 25, where the relatively fast decrease of $f_M(\theta)$ with scattering angle must immediately result in one difficulty, namely a rapid loss of the intensity of magnetic scattering.

Looking at equation 35, we see that $\vec{p}(\theta)$ also depends on $\vec{\sigma}$ and on $\vec{q}$, $\vec{\sigma}$ is simply the unit vector along the neutron spin. The $\vec{q}$ vector, or the Halpern vector is defined as, $\vec{q} = \vec{e}(\vec{e}\cdot\vec{m}) - \vec{m}$ where $\vec{m}$ is a unit vector along the atom magnetisation direction and where $\vec{e} = \vec{\kappa}/|\vec{\kappa}|$. If we allow $\vec{m} = \vec{e}$, then the $\vec{q}$ vector vanishes thus there is no magnetic scattering in such a case. Therefore we see that the magnetic neutron scattering arises solely from the magnetisation component *perpendicular* to the scattering vector. So, we see that when an atom has its moment oriented in any direction, for example in neutron scattering on a paramagnet, the magnetic scattering cross-section will be,

$$\frac{d\sigma_p}{d\Omega} = \frac{2}{3}|p(\theta)|^2 \tag{37}$$

that is, one third of the possible orientations will not contribute to the scattering.

Because magnetic diffraction can be regarded as an extra component of the coherent elastic scattering cross section, there is no interference between the nuclear and magnetic terms, they are merely superimposed. Thus by measuring the intensities of many different magnetic reflections, both the configuration and the orientation of the magnetic moments in a sample can be determined. For example, in a ferromagnet, the magnetic and nuclear unit cells are identical, so the magnetic peaks will simply add to the scattering at temperatures below T_C. For an antiferromagnet, the magnetic unit cell will be twice the nuclear cell in at least one direction. Thus when cooled below T_N, the antiferromagnetic reflections do not appear at the nuclear positions because at these points the reflections from successive planes with moments directed oppositely are out of phase and cancel. Instead, extra magnetic reflections appear at half the spacing along each axis where the magnetic unit cell has doubled. When the magnetic unit cell is not an integer multiple of the nuclear cell the system is described as incommensurate. Other magnetic systems include helimagnets such as Pd or spin glasses.

Just as phonons are the excitations observed by use of inelastic nuclear scattering, the magnetic equivalent, magnons, can be observed with the aid of inelastic magnetic scattering. Like the phonon the magnon is a quantised spin wave that represents the deviation from perfect magnetic spin order. The incoming neutrons interact with the quantised wave and can be scattered or exchange energy with it. Thus by taking measurements over temperature ranges, energy ranges and different reciprocal lattice positions, one can obtain a full description of the energy levels, magnetic dispersion curves and anisotropy of the system.

3 Experimental Methods

This Chapter gives details on the crystal growth of the systems used for experimental work in this thesis and also gives comprehensive information on each of the neutron scattering diffractometers/spectrometers used for data collection. Information is also given on the sample environment hardware that were used to subject the systems to different experimental conditions.

3.1 Crystal Growth Methods

The growth of large single crystals of air and moisture sensitive materials is usually accomplished using crystallisation from the melt. The most usual types are the Czochralski and the Bridgman-Stockbarger methods. The latter was employed in the production of single crystals for this thesis. The Bridgman-Stockbarger technique works by the process of pulling a molten sample through its freezing point thus promoting crystallisation. The molten charge is held in a sealed silica tube with a sharp or 'wiggly' tip. The tube is mounted in a Bridgeman furnace with temperature approximately 20K above the crystallisation temperature of the sample. The tube is gradually pulled through a temperature gradient ($\Delta T = 40K$) and as the tip of the tube passes the crystallisation temperature, nucleation occurs. The shape of the tip of the silica tube is designed to aid the growth of a small seed crystal.

The temperature gradient employed is of the utmost importance. The crystallisation point should be well defined in the furnace; this calls for a high degree of thermal and mechanical stability to ensure that the pull rate is constant and that the temperature profile is not smeared out. If this is not the case the crystallisation plane will be disturbed and the likelihood of the production a polycrystalline sample will increase. The melting point and pull rate is unique to each furnace and is gauged using trial and error.

Virtually all of the single crystal samples used in the experimental work in this thesis were grown by Dr. D. Visser, at Warwick University. The ternary halides were synthesised using stoichiometric amounts of the binary halides AX and BX_2, (e.g. $CsFeBr_3$ is prepared using CsBr and $FeBr_2$). It has been noted[110] that in order to produce a large single crystal sample by Bridgeman technique great importance should be placed on the purity of the starting materials. Normally the BX_2 precursor can be obtained commercially as a hydrate, e.g. $FeCl_2 \cdot 4H_2O$, this can then be dehydrated by heating steadily under a stream of HX gas.

Equal molar amounts of the pure powder precursors are mixed together and loaded into a silica tube, the tube is then sealed. This preparation takes place in the inert atmosphere of a dry box, due to the hygroscopic nature of the precursors thus preventing degradation of the starting materials. As a safety measure the silica tube containing the powder sample is placed in a muffle furnace and the contents melted, usually at 100K above the melting temperature of the sample. This helps prevent explosion of the precursors in the Bridgman furnace. The silica tube was loaded into the three-zone Bridgeman furnace available at the Physics department of Warwick University, manufactured by T.E. Brown and Barrington of Harston, Cambridge and procedure followed as above.

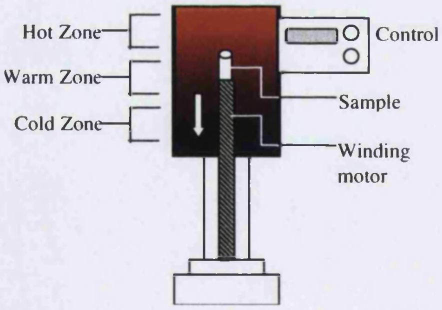

Figure 26: Schematic of a Bridgeman Furnace.

One of the fortunate aspects of working with the ABX_3 halides is that they have a cleavage plane along the [001] – [110] direction. This means that by simply pressing on the crystal with a sharp object such as a scalpel, it will cleave, leaving a flat face. This makes it relatively easy to distinguish and align the crystals for neutron scattering experiments.

3.2 The Neutron Scattering Spectrometers/Diffractometers.

There are currently many different types of neutron scattering spectrometers and diffractometers available to the scientific community, from the original and relatively 'simple' Triple Axis Spectrometer (TAS) to the more modern and complex Neutron Spin Echo (NSE) machines. The ever increasing number of different types of machines has considerably widened the typical profile of a neutron scatterer. Spectrometers such as Small Angle Neutrons Scattering (SANS) spectrometers have been developed which allow, for example, the characterisation of biological samples and opened up neutron scattering to the biological community, whilst development of stress & strain rigs have allowed non-destructive testing of mechanical devices and weld joints and thus have involved the engineering community. What follows is a description of the machines that have been utilised for neutron scattering experiments in this thesis. A brief comment on the nature and function of each spectrometer/diffractometer is given along with a commentary on the specific experiments undertaken.

3.2.1 Triple Axis Spectrometer

This classic instrument is now seen at virtually all neutron beam reactor facilities, sometimes outnumbering all other spectrometers put together. Historically, the first spectrometer developed was of TAS type by the Noble Laureate Bert Brockhouse at the Chalk River facility, Canada. It is so called due to the three principal components of which it consists. These are the monochromator drum, the sample table and the analyser crystal. All may be varied independently, hence, triple axis. This provides great flexibility within one machine and the TAS can be operated in many different configurations.

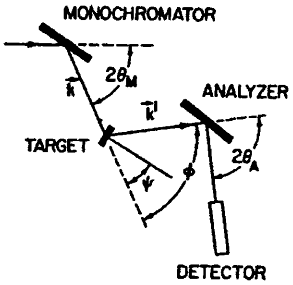

Figure 27: Schematic of a Tripe Axis Spectrometer for inelastic neutron scattering.

The triple axis spectrometer can be operated in either inelastic or elastic scattering mode. The only difference being that for elastic scattering either the analyser is excluded altogether or it is positioned such that it matches the scattering of the monochromator. Both monochromator and analyser usually consist of single crystals of either Ge or pyrolytic graphite. The crystal are orientated in such as way as to fulfil the Bragg condition with a particular *hkl* plane, e.g. the (1, 1, 1) plane in Ge or the (0, 0, 2) plane in pyrolytic graphite. Normally the TAS consists of a flat monochromator and analyser, as shown schematically above, but curved monochromators and analysers that allow both horizontal and vertical focussing have become more popular, mainly for the increased flux they provide at the sample. The detector is usually a ^{3}He filled counter with an applied voltage of approximately 1500V between cathode and anode. Neutrons that enter the detector chamber react with the He gas via the equation,

$$ {}^3_2He + {}^1_0n \rightarrow {}^1_1H + {}^3_1H + 0.76MeV $$

The energetic electrons produced by this reaction are accelerated to the anode and produce a voltage pulse that is proportional to the number of incident neutrons. Filters are often used to reduce the second order contamination from the beam. If one looks at the Bragg equation, $n\lambda = 2d\sin\theta$, one see that there are many different plane levels in the monochromator or analyser which contribute to scattering. In order to reduce this contamination, filters such as pyrolytic graphite, which works by transparency to certain wavelengths but not to others, are employed.

The flexibility of a TAS lies mainly in its ability to chose any point in (**Q**, ω) space with one extra degree of freedom left to chose from, such as incident energy E_o. If we take this option and fix E_o whilst scanning in energy, it is known as the constant-**Q** method and is normally used for phonon/magnon dispersion measurements [Figure 28]. Constant-**E** scans are used in special situations when the frequency response varies very rapidly as a function of **Q**, it is then the practise to fix ω and scan **Q** along some convenient linear path in reciprocal space.

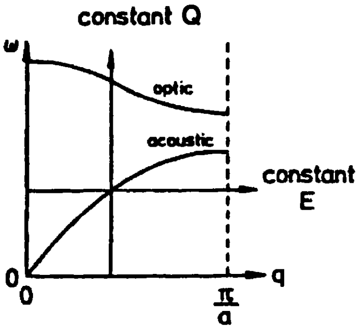

Figure 28:Phonon dispersion with an acoustic and an optic branch. Scanning directions for Constant-Q(or K) and Constant-E (energy) scans are indicated.

Constant- **Q** scans may be performed using three different methods:

- *Fixed initial energy* (2θ$_M$ fixed, 2θ$_A$ is scanned), for each 2θ$_A$, ψ and ϕ are changed to keep **K**= **G** ± **q** constant. Here |**k**| is fixed and lies on a circle of constant radius. A disadvantage associated with this method is the inherent $k_1 cot\theta_A$ distortion of the scatted intensities due to scanning the analyser. This can, however, be corrected for in the final analysis.

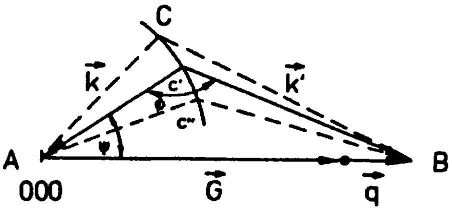

Figure 29: Scattering triangle for fixed incoming energy, in up-scattering mode (neutron energy gain).

- *Fixed final energy* ($2\theta_M$ is scanned, $2\theta_A$ is fixed), ψ and ϕ are changed as above to keep **K** constant. This does not have the associated distortions of the above technique but it is a physically slower technique due to the movement of the TAS.

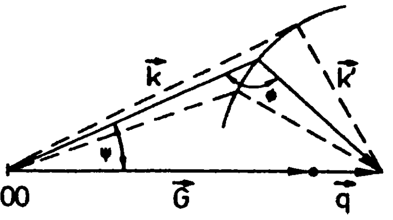

Figure 30: Scattering triangle for fixed final energy, in down-scattering mode (neutron energy loss).

- *Constant sample scattering angle* (Both $2\theta_M$ and $2\theta_A$ are scanned), this technique is sometimes used in pressure dependant experiments when a severe limitation is place on the incoming and outgoing pathways.

Significant other factors should be taken into account before a successful neutron scattering experiment may be undertaken. Depending on the configuration of the TAS it may be more advantageous to look at mirror images of the Bragg peak that you wish to measure. For instance one may possibly gain better resolution by measuring the Bragg peak at (-2/3, -2/3, 1), rather than (2/3, 2/3, 1). The Cooper-Nathans model of the resolution function of a TAS was first published in 1967. It is now incorporated into neutron scattering measurement software at all neutron scattering facilities throughout the world (albeit modified for each spectrometer). The resolution function $R(\Delta Q, \Delta\omega)$, is defined as the probability of detecting neutrons with energy $\omega \pm \Delta\omega$ and wavevector $Q \pm \Delta Q$ at position (Q, ω). It arises from the mosaic spread of the analyser and monochromator and the transmission function of the collimator. The function $R(\Delta Q, \Delta\omega)$ is four dimensional, but is normally considered with the component Q_z out of the scattering plane and thus it reduces to an ellipsoid in Q_x, Q_y ω; the resolution ellipsoid.

The intensity measured at the detector is given by convolution of the scattering function with the resolution function for that point. In the case of a dispersion surface, such as phonons etc., a constant-*E* or constant-*Q* scan consists of moving the resolution ellipsoid vertically or horizontally and integrating where the two functions intersect. This is demonstrated below.

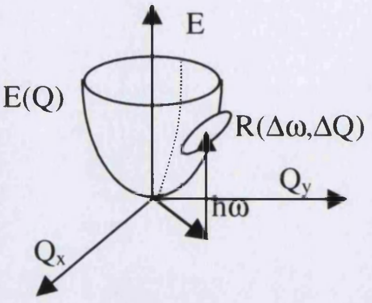

Figure 31: Schematic of a dispersion curve and resolution ellipsoid in (Q, ω) space.

The normal configuration of a TAS is that of the 'w' formation, whereby the monochromator, analyser and detector line up in the shape of a 'w', as shown below. It can be seen that the best resolved peak will occur when the resolution ellipsoid and the dispersion surface are aligned to have the same gradient.

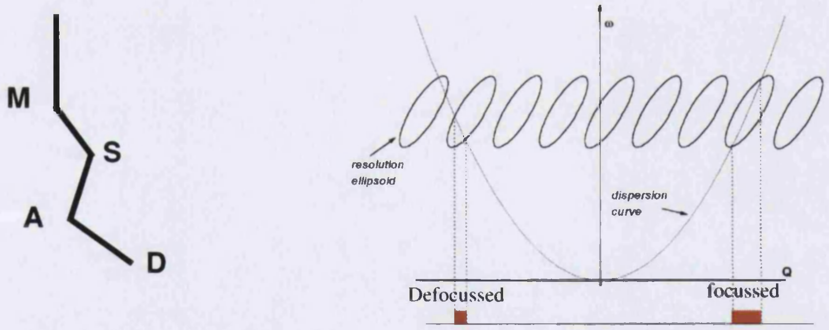

Figure 32: (a) The 'W' configuration for a Triple Axis Spectrometer, where M is the monochromator, S is the sample, A is the analyser and D the detector. (b) Constant – E scans on the focussed and defocused sides of the dispersion curve.

Many different Triple Axis Spectrometers have been used for data collection for experimental work presented in this thesis. For clarity, the descriptions of the individual characteristics of each spectrometer have been grouped below and the interested reader is referred to those Chapters for further information.

3.2.1.1 The TAS E1 at the HMI, Berlin.

The spectrometer is located on the D1N beamline of the BER – II reactor at the Hahn Meitner Institut. The monochromator and analyser can either be pyrolytic graphite (PG 002) or a Heusler crystal (Heusler 111). Both monochromator and analyser have variable curvature in the horizontal and vertical directions. The whole spectrometer is made of non-magnetic materials, this allows polarisation analysis to be undertaken without spurious signals from the spectrometer. A second turntable, below the sample table with its axis collinear to the sample axis, can be used for mounting and orienting ancillary equipment, such as Helmholtz coils used to produce a horizontal magnetic field. The analyser and detector are constructed into a single "Tanzboden" unit, this is unusual in that normally the analyser and detector are separate units. The detector is mounted on a cantilever arm, which can be rotated freely around the analyser axis after decoupling it from a beam tube device leading through the analyser shielding. By rotating both the cantilever arm and the detector by 180°, it is possible to quickly change to a two-axis mode of operation, this feature was utilised during the experiment elaborated upon in Chapter 4.1. The analyser shielding has an unconventional design: a horizontal segment of the polyethylene shielding is replaced by a rubber tire filled with water, over which a specially formed polyethylene block containing the beam channel can be moved. This beam tube device is coupled to - and automatically rotates with - the detector arm’[111].

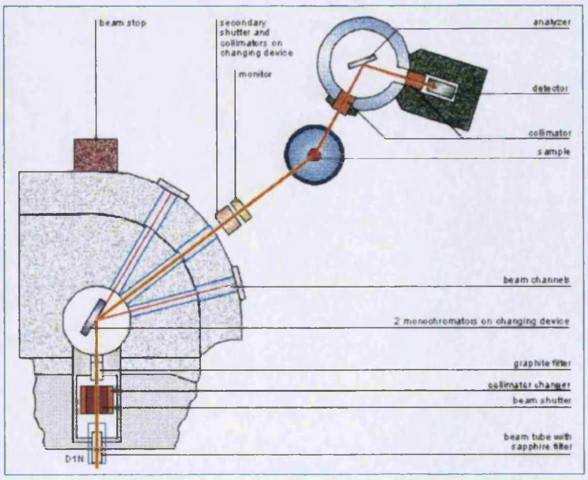

Figure 33: Schematic Representation of the TAS E1 at the HMI[112]

This spectrometer was used in conjunction with the vertical magnet, VM3 (temperature range 300K-2K and maximum field of 5T), to establish the critical exponent, β, of $CsNiCl_3$ under magnetic field and electric field (Chapter 4.1). It was also used, again in conjunction with the vertical magnet, VM3, to establish the critical exponent β, of $CsMnBr_3$ under magnetic and electric field (Chapter 4.1)

3.2.1.2 The TAS V2 (FLEX) at the HMI, Berlin.

FLEX (V2) is located at the cold neutron guide NL 1B at the BER-II reactor of the HMI. A schematic of the spectrometer is shown below,

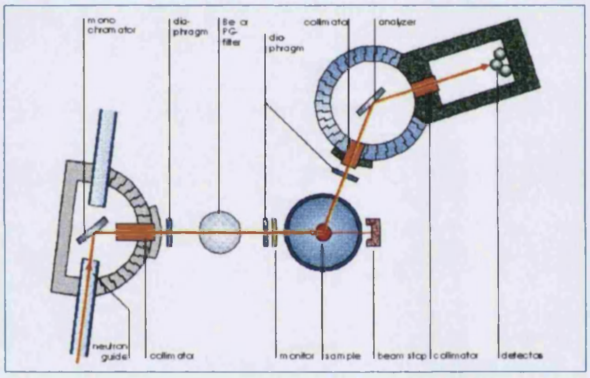

Figure 34: Schematic Representation of the Triple Axis Spectrometer V2 at the HMI[113].

All distances, i.e. those between monochromator and sample, sample and analyser, and analyser and detectors can be varied. This is so that optimal scattering geometry for best intensity at the required angular and energy resolutions can be obtained. In order to further increase the flux, a tuneable curved monochromator and analyser are used, both of which are fabricated from strips of Pyrolytic Graphite (002). The geometry of FLEX allows incident neutron wavelengths of between 1.7Å (27meV) and 6.5Å (1.9meV). In order to reduce second order contamination of the beam, a tuneable pyrolytic graphite filter is used for $\lambda \leq 4Å$ and a cooled Be filter for $\lambda \geq 4Å$. This spectrometer was used in conjunction with a dilution refrigeration unit and a 6 Tesla, Horizontal Field magnet, in order to establish the magnetic phase diagram, magnon dispersion curves and critical exponent β of $CsFeBr_3$ at mK temperatures (Chapter 5.3).

3.2.1.3 The TAS 4F1 and 4F2 at the LLB, Saclay, Paris.

These are more conventional Spectrometers than E1, described above, in that the analyser and detector are separate units. The 4F1 spectrometer was used in conjunction with a modified Orange cryostat and a He-pressure cell (Chapter 3.3.3) to enable us to establish the magnetic dispersion curves of $CsFeCl_3$ (Chapter 5.1.1) and $CsFeBr_3$ (Chapter 5.2.1) under hydrostatic pressure of 5.0kbar. 4F2 was used in combination with an Orange cryostat to measure the sublattice magnetisation of several different samples of $KNiCl_3$ and establish the critical exponent β. The spectrometers 4F1 and 4F2 are located on the left and right tangential channels of the beamline 4F at the Orphée reactor, Saclay.

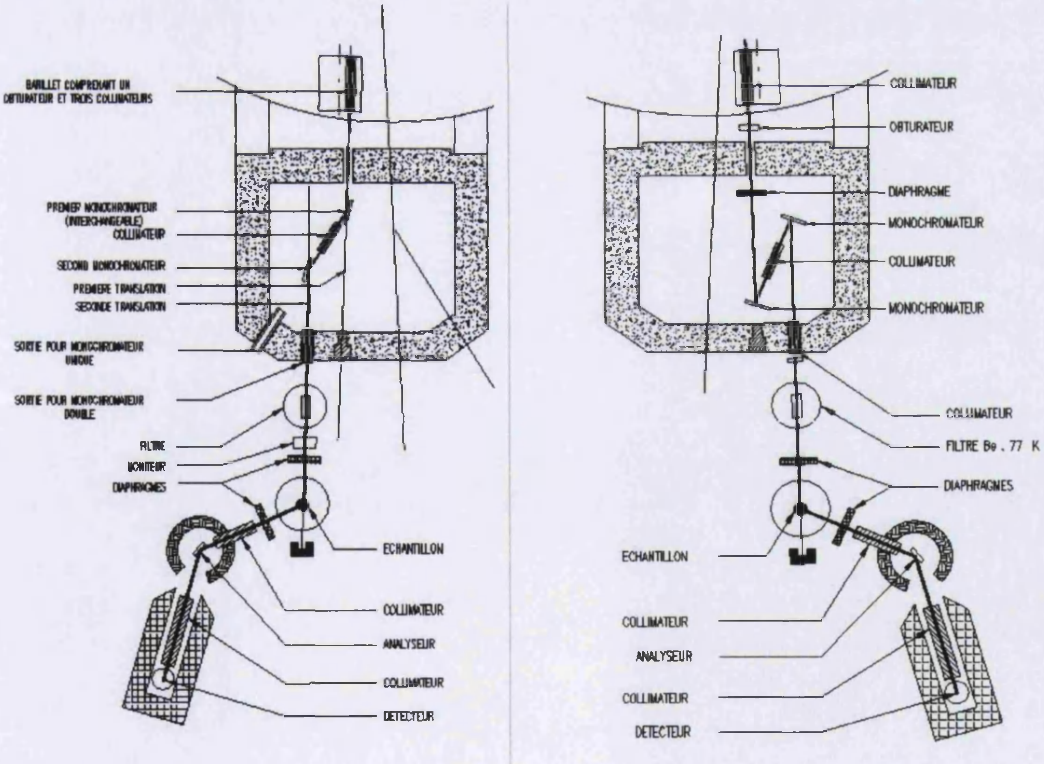

Figure 35: The Triple Axis Spectrometers, 4F1 and 4F2, at the LLB, Saclay[114].

Both have a pyrolytic graphite double monochromator setup, and both can have the ability to use either flat or curved pyrolytic graphite as an analyser. As is described in the experimental Chapter 5.1.1, for fixed incoming energies of k_i = 2.662 $Å^{-1}$ a PG filter were used to reduce the second order contamination of the neutron beam. At k_i = 1.55 $Å^{-1}$ a cooled Beryllium filter was used for the same purpose.

3.2.1.4 The Single Crystal Diffractometer, D15 at the ILL, Grenoble.

D15 is a single-crystal diffractometer of the Harwell MK VI design. It is installed on an inclined beam tube (IH4) at the ILL, Grenoble. To compensate for the inclination of the incident beam, the scattering vector of the monochromator is tilted to bring the monochromatic beam into the horizontal plane. It is possible to operate the instrument in four-circle mode but is more often used, as in the case in this thesis in the normal-beam mode. The monochromator, unusually, utilises Cu (331) as a reflection plane, as opposed to the usual PG(002).

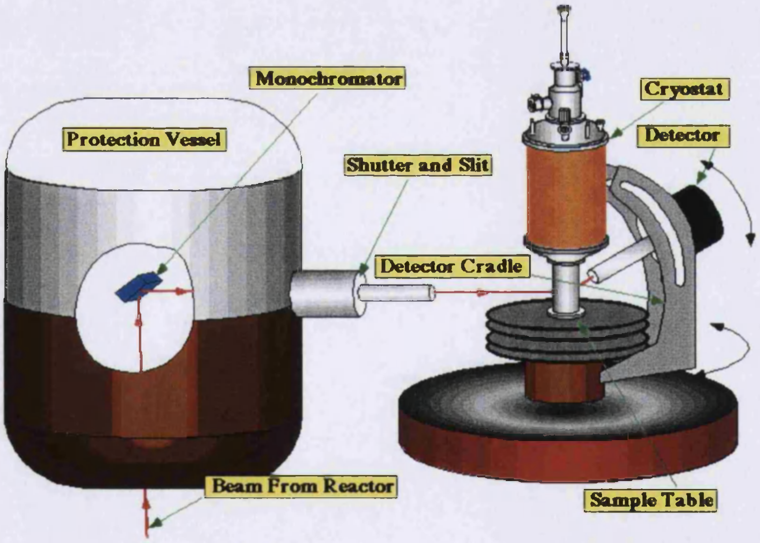

Figure 36: The single crystal diffractometer D-15 at the Institut Laue Langevin[115].

As can be seen above in Figure 36 the detector has a motorised motion allowing inclination of the detector to the plane of scattering from -10° to +35°. D15 can be used for a wide range of physical problems including the determination of magnetic phase diagrams or of pressure-temperature phase diagrams. We used D15 in conjunction with a He pressure cell and 'Orange' cryostat to establish the pressure – temperature phase diagram of $TlFeCl_3$,(Chapter 4.4.2).

3.2.1.5 The Membrane Diffractometer, V1 at the HMI, Berlin.

The diffractometer V1 is installed at the curved neutron guide NL 1A at the Ber –II, reactor at the HMI, Berlin. It has a vertically focusing graphite monochromator (PG 002) which provides adjustable wavelengths between 3Å and 6Å. The detector is a ^{3}He area detector with a sensitive area of 20 cm x 20 cm. This allows large areas of reciprocal space to be scanned with each single measurement. The detector may also be inclined out of the plane of the experiment in order to detect scattering from higher planes, similar to the diffractometer D15 outlined above. The monochromator to sample and sample to detector distances can be varied in order to produce the most suitable resolution for the particular experiment. A schematic of the Diffractometer is shown below.

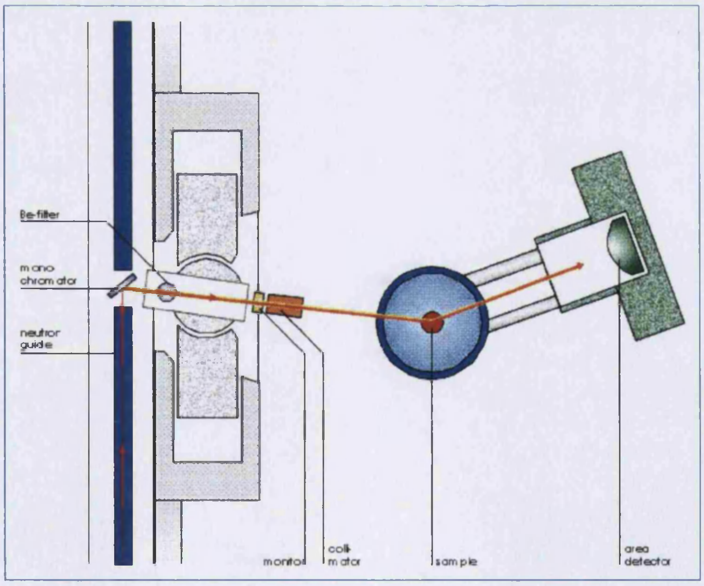

Figure 37: Schematic Representation of the Membrane Diffractometer V1 at the HMI[116].

Although V1 has been principally designed for use with biological samples such as biological membranes, polymers etc. we used it for a single crystal experiment on the large easy plane anisotropy system $CsMnBr_3$. This experiment was the first single crystal experiment undertaken on V1 and was performed in conjunction with an applied electric field. The experiment is elaborated upon in Chapter 4.1.1.

3.2.2 Powder Diffractometer.

There are two methods of obtaining a powder diffraction profile. The first is where the powder sample is exposed to a monochromatic beam and the crystallites with the necessary orientation to satisfy Bragg's law will produce scattering. If a powder diffraction instrument is based at a *reactor* source then the scattered beam will be measured as a function of the detector angle, 2θ, as below.

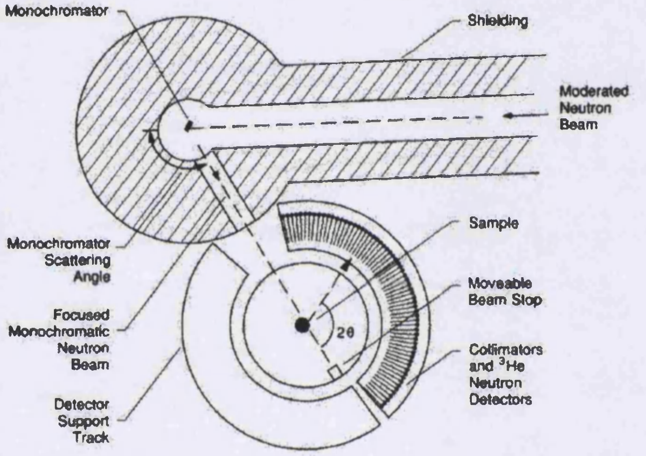

Figure 38: Schematic of a powder diffraction experiment at a reactor source. [Ref. Theory of Thermal Neutron Scattering, Clarendon Press, Oxford, 1971]

If the diffractometer is based at a *spallation* source then the sample is irradiated with a pulsed beam of neutrons having a varying range of energies. Banks of detectors located at different scattering angles measure the scattered neutrons. Figure 41 shows a schematic of the powder diffractometer POLARIS based at the ISIS facility with the different detectors (low, 90° and backscattering) visible. At a particular scattering angle the diffraction pattern will look similar to that of the steady state source, however in this case the independent parameter is now the neutron's time of flight rather than the scattering angle. Thus the time at which each neutron impinges on the detector is recorded. Because the neutron's time of flight is proportional to its wavelength and, for constant scattering angle, this wavelength is proportional to the *d* spacing between the atomic planes, $n\lambda = d\sin\theta$, the measured neutron scatter can be plotted against time, λ or *d*-spacing. The detector bank sitting at small scattering angles will provide information concerning widely space atomic planes, whilst the banks at large scattering angles will provide information concerning smaller *d*-spacing.

The second method of obtaining a powder diffraction profile is whereby the detector is fixed and the wavelength is varied. This is commonly used, as with the TAS method of fixed detector, when using apparatus with limited pathways for incoming and outgoing beam, such as magnets, pressure cells etc.

Powder samples consist of small crystallites lying in all possible orientations compressing the three dimensional reciprocal lattice into one dimension. Thus, the large number of intensities obtainable from a single crystal are projected in a powder sample and instead, a radially symmetric diffraction pattern is produced. In order to properly refine the data it is necessary to compare not only integrated intensities but also intensities calculated for every position 2θ of the detector. This approach was pioneered by Rietveld[117] and therefore, the comparison of experimentally measured and theoretically predicted dependencies of intensity on the scattering angle is know as *Rietveld refinement.*

The refinement involves three groups of parameters to account for the profile model, corrections to intensity and the structural model. Within the profile model are parameters to refine the positions and shapes of the Bragg peaks. Parameters that define the Bragg peak position include the diffractometer zero point, the unit cell constants, sample displacement and transparency terms. The intensity correction terms include parameters to allow for effects such as absorption, extinction and preferred orientation. The structural model contains the same parameters as that for single crystal refinement, namely atomic coordinates, occupancies and temperature factors.

No matter where the data originates from, X-ray, steady state or pulsed reactor source, the objective of Rietveld refinement is the same, that is the most accurate leastsquares fit to all of the individual observed data points (y_i) simultaneously. The quantity minimised is the residual S_y.

$$S_y = \sum_i w_i (y_i - y_{ci})^2 \tag{38}$$

where the sum is over all the data steps and where,

$w_i = 1/y_i$,
y_i = observed (gross) intensity at the i^{th} step ,
y_{ci} = calculated intensity at the i^{th} step ,

For the reasons outlined above, many Bragg reflections will contribute to the intensity y_i, observed at a point, i. The calculated intensities y_{ci} are determined from the $|F_K|^2$ values calculated from the structural model. This is achieved by the summing of the calculated contributions from neighbouring Bragg reflections and the background. Thus,

$$y_{ci} = s \sum_K L_K |F_K|^2 \phi(2\theta_i - 2\theta_K) P_K A + y_{bi} \tag{39}$$

where,

s is the scale factor, K represents the Miller indices for a Bragg reflection, L_K contains the Lorentz, polarisation and multiplicity factors, ϕ is the reflection profile function, P_K is the preferred orientation function, A is an absorption factor, F_K is the structure factor for the K^{th} Bragg reflection and y_{bi} is the background intensity at the i^{th} step.

The reflection profile function is machine specific and has special relevance to spallation source neutron scattering. Due to the nature of the production of the neutron pulse from a spallation source its shape is highly asymmetric in time. The peak shape calculated for HRPD at the ISIS facility is given below as an example. HRPD uses a modified Robinson-Taylor-Carpenter (RTC) peak shape, which is a rather complicated function consisting of epithermal and thermal components.

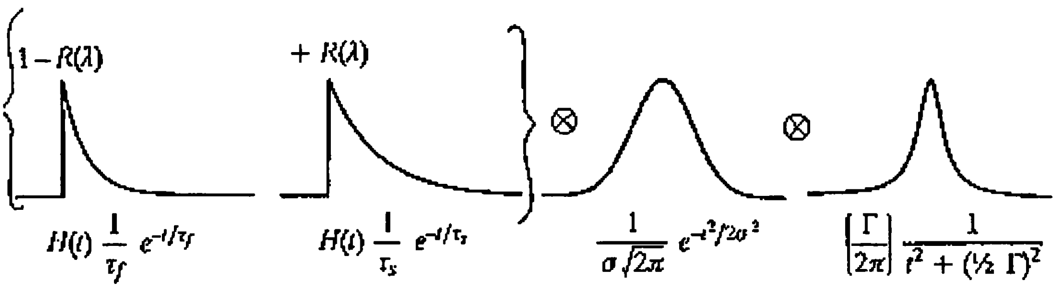

Figure 39: The contributing functions of the HRPD lineshape based on a modified RTC function[118].

The success of a refinement is judged from the following sums of the residual intensities, (R-factors):

The profile R-factor:

$$R_P = \frac{\sum \left| y_i(obs) - y_i(calc) \right|}{\sum y_i(obs)} \tag{40}$$

The weighted profile R-factor:

$$R_{WP} = \left\{ \frac{\sum w_i \left(y_i(obs) - y_i(calc) \right)^2}{\sum w_i \left(y_i(obs) \right)^2} \right\} \tag{41}$$

The structure factor R-factor:

$$R_{WP} = \left\{ \frac{\sum \left| \left(I_K('obs') \right)^{1/2} - \left(I_K(calc) \right)^{1/2} \right|}{\sum \left(I_K('obs') \right)^{1/2}} \right\} \tag{42}$$

and the Bragg R-factor:

$$R_B = \left\{ \frac{\sum \left| I_K('obs') - I_K(calc) \right|}{\sum I_K('obs')} \right\} \tag{43}$$

The *Goodness of fit* indicator, χ, is given by:

$$\chi = \sqrt{\frac{S_y}{N-P}} = \frac{R_{wp}}{R_e} \tag{44}$$

where R_e the expected R-factor is given by,

$$R_e = \sqrt{\frac{N-P}{w_i y_{oi}^2}} \tag{45}$$

N is the number of data points, *P* is the number of parameters.

A χ value of over 1.5 indicates that the model is a poor fit or that you have a false minima in the model. A value of less than 1 indicates that the model is overparameterized.

3.2.2.1 The Powder Diffractometer, HRPD, at the ISIS facility, Oxford.

The design and positioning of the High Resolution Powder Diffractometer at the end of a 100m beam line makes it one of the highest resolution neutron diffractometers in the world and thus gives it unique power in the study of structural information and small structural changes. HRPD has 3 different detectors, positioned at 28-32°, 90° and Backscattering, these can be seen below in Figure 40.

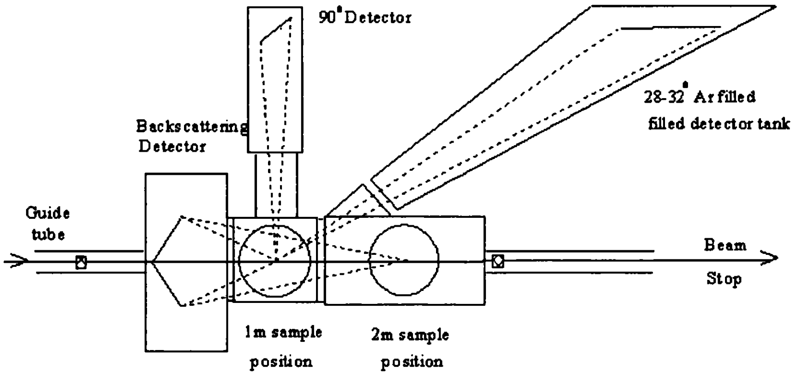

Figure 40: Schematic plan view of the HRPD detector configuration[119].

Each detector has characteristics which make it suitable for different tasks. The backscattering detector has, in total, 720 discrete detector elements which may be used, decoupled, as a radially pixelated position sensitive detector. These elements are software linked to form 60 rings, these rings are designed to mirror the Debye-Scherrer rings produced by powder diffraction. In this manner the geometric aberration may be minimised. The data obtained in backscattering detector is of inherently high resolution. The effective upper *d*-spacing limit of the backscattering detector is approximately 5Å. This limit is a direct consequence of the incident flux of the diffractometer which, at only modest intensity, extends to wavelengths of approximately 10Å. In order to measure longer *d*-spacing information, detectors at lower angles are vital. In these detectors, for a given *d*-spacing the Braggs' Law equation is satisfied by neutrons of shorter wavelength and therefore, on HRPD, of higher flux.

The 90° detector utilises a ZnS scintillator, which by virtue of its peak height response can discriminate between neutrons and γ radiation. This insensitivity to γ rays is significant, as the backscattering detector is quite insensitive to this radiation. The detector is comprised of 6 modules each with 66 elements. Each module is positioned on a constant radius from the 1m sample position. As with the backscattering detector just mentioned, data may be collected in each of the 396 discrete elements but more usually the detector is software configured into 66 radial segments.

The low angle detector utilities ½" ^{3}He tubes as a detector. The HRPD low angle bank, currently houses 72 tubes which lie on a constant radius parallel to the through beam direction and are configured in 3 rows of 24 tubes. Again, similar software linking strategies outline above may be applied. The long secondary flightpath of the low angle bank, necessary in order to minimise angular divergence, requires that the large tank housing the detector be filled with Ar gas. The tank is therefore discrete from the other sample and detector tanks which are evacuated during diffraction measurements. The incident and transmitted beam intensity is monitored by two Davidson (1985) monitors situated at 93.50m and 96.74m from the moderator.

The characteristics of each detector bank are summarised below:

	Backscattering	90°	Low Angle
Detector Specification	ZnS scintillator	ZnS scintillator	½" 10atm He^3 gas tubes
Geometry	60 rings: $7 \le r_1 \le 8.5$cm	Slab: 20 × 20cm	72 tubes: (20cm active length)
	$35.5 \le r_{60} \le 37$cm	66 × 3mm elements	8 tubes/module
	8 Octants: 4147cm^2	6 Modules: 2400cm^2	9 Modules: 1800cm^2
Fixed Scattering Angle	$160^\circ \le 2\theta \le 176^\circ$ (1m)	$87^\circ \le 2\theta \le 93^\circ$	$28^\circ \le 2\theta \le 32^\circ$
Solid Angle (Ω)	0.41 ster (1m)	0.08 ster	0.01 ster
Resolution ($\Delta d/d$)	~ 4-5 × 10^{-4}	~ 2 × 10^{-3}	~ 2 × 10^{-2}
d-spacing range (30-230ms)	~ 0.6 - 4.6Å	~ 0.9 - 6.6Å	~ 2.2 - 16.5Å

The powder diffractometer HRPD has been used in conjunction with a gas pressure cell (Chapter 3.3.3) and modified Orange cryostat to enable us to characterise the low temperature structure of TlFeCl$_3$ under hydrostatic pressure. More information on this experiment can be found in Chapter 4.4.1.

3.2.2.2 The Powder Diffractometer, POLARIS, at the ISIS facility, Oxford.

As with HRPD, POLARIS has a variety of detector banks available for data collection, these are, ‘very low angle’, ‘low angle’, 90° and ‘back scattering’, as shown below.

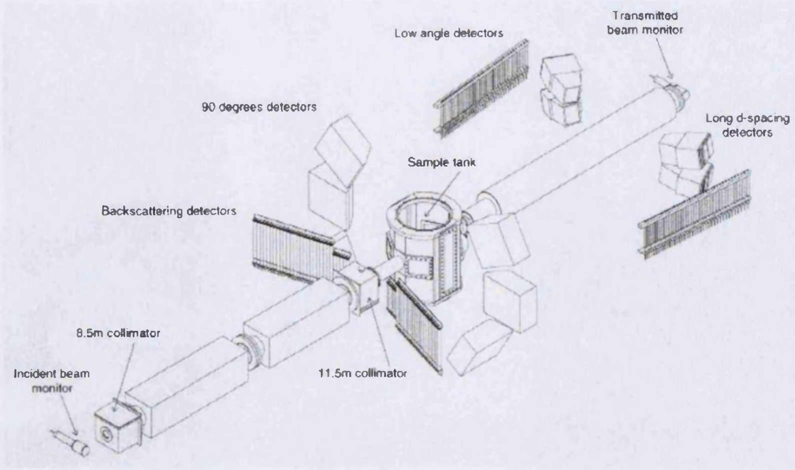

Figure 41: Schematic of the powder diffractometer POLARIS at the ISIS facility[120].

The POLARIS diffractometer is located on the D7 beamline at the ISIS facility, receiving a 'white' beam of neutrons from the ambient temperature water moderator. It has the possibility of incident wavelengths of 0.1 - 6.0 Å, with a corresponding incident energy range of ~ 2meV - 8eV. Motor driven collimators allow the incoming beam to be reduced, from a maximum size of 40mm high x 20mm wide, to match the sample size. This eliminates any background scattering contamination from the sample environment equipment.

The characteristics of the detectors present are given below in tabular format.

Position	Very low angle	Low angle	90 degrees	Backscattering
Type	ZnS scintillator	½" ^{3}He tubes	ZnS scintillator	1" ^{3}He tubes
No. of detectors	80	80	216	58
2θ range	13°-15°	28° - 42°	85° - 95°	130° - 160°
Ω(steradians)	0.009	0.046	0.48	0.29
$\Delta d/d$ (%)	3×10^{-2}	1×10^{-2}	7×10^{-3}	5×10^{-3}
L_2 (m)	~ 2.2	1.72 - 2.65	~0.8	0.60 - 1.30
d range (Å)	0.5 - 21.0	0.5 - 8.15	0.3 - 4.1	0.2 - 3.2

We utilised POLARIS for low temperature, structure determination studies, on the triangular lattice antiferromagnets $CsFeCl_3$ and $CsFeBr_3$ under hydrostatic pressure. A modified Orange cryostat was used in combination with a gas clamp cell to obtain the necessary sample environment.

3.2.3 Flat Cone Diffractometer.

The flat cone technique is a modified case of the Weissenberg technique which was developed for use with X-ray diffractometers in conjunction with photographic detectors. In the Weissenberg method a single crystal is rotated about an axis and thus the planes normal to this axis will diffract. The diffraction will take the form of a plane or cone shape i.e. all the reflections of one reciprocal plane or layer are recorded along straight lines on a cylindrical film. If only one line is selected by filtering the image by placing a layer-line screen before the film, then a two dimensional lattice plane can be mapped on the two dimensional film by coupling the crystal rotation and the film rotation. This same procedure can be realised with a one-dimensional electronic multidetector that is placed along one layer line. For each rotational movement of the single crystal a separate measurement is made, this results in a loss in resolution perpendicular to the layer line in comparison to the film method. However statistical analysis of the data allows this to be reduced to a minimum. There are distinct advantages to the flat cone technique, firstly and most obviously the data collection rate will be many times that of a conventional TAS due to the fact that the data is being collected by a multidetector which can scan many Bragg peaks simultaneously, compared to a TAS which may only measure one point of the scattering function at any one time. Thus this technique is well suited to the systematic search of the intensity distribution in reciprocal space. This is especially true for the determination of unknown lattices, e.g. in magnetically ordered crystals, or for the observation of diffuse scattering between Bragg points. The detector may also be tilted out of the plane of the experiment in order to establish scattering from different layers in reciprocal space. The principle of this method is described below.

The incoming neutron beam is reflected at the monochromator in the usual way and impinges onto the sample. The scattered neutrons are analysed by reflection at flat crystal plates. These are orientated such that the neutrons are reflected out of the horizontal (experimental) plane into the vertical plane. A schematic of the setup of the flat cone technique is shown below.

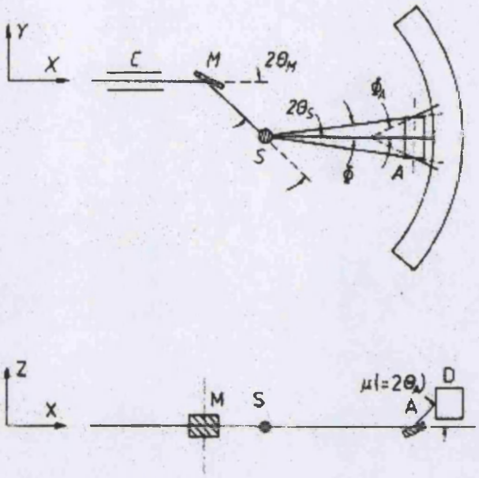

Figure 42: Schematic view of a the neutron beam path for a flat cone diffractometer, shown in plan view (above) and plane view (below) [Born, IAEA-CN-46/44P]

The analyser crystals are placed close to the curved one-dimensional multidetector, so that the diffracted beam does not change much in height for different energies. The scattering events which take place in the horizontal plane and with a given energy can be detected simultaneously in an angular range limited only by the dimensions of the multicounter or by the number of analyser crystals. The advantage over TAS measurements can be seen by looking at the Ewald sphere construction for the diffractometer. One measurement corresponds to a constant energy scan on a circle concentric to the Ewald circle in reciprocal space, as is shown below. The TAS can only scan one point along this curve at any one time increasing the experimental time enormously.

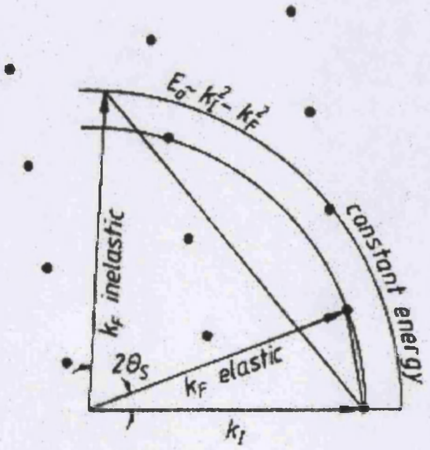

Figure 43: Ewald sphere construction for the flat cone technique, showing the concentric circle that can be simultaneously measured using this technique.

A realisation of this instrument is in place at the BER–II reactor, at the HMI, Berlin and a description of this diffractometer is given in the next Chapter.

3.2.3.1 The Flat Cone Diffractometer, E2 at the HMI, Berlin.

The diffractometer is located at the radial beam tube R1 of the BER II reactor at the HMI, Berlin. A schematic of the instrument is shown in Figure 44.

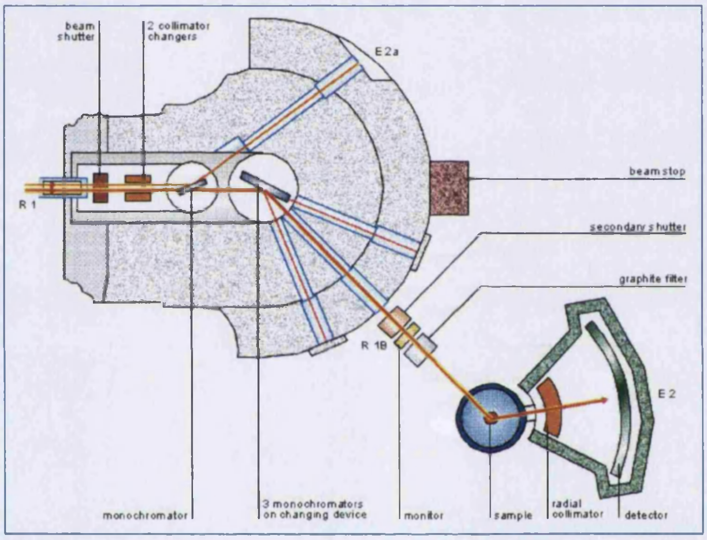

Figure 44: The Flat Cone Diffractometer E2, at the HMI, Berlin[121].

The monochromator and analyser are both fabricated from pyrolytic graphite, with each analyser composed of four plates each with dimensions of 50 x 75 mm^2, covering a scattering angle of 8°. The analyser units are mounted on motorised cradles with the rotation axis in the horizontal plane, thus the energy transfer can be adjusted to suit experimental conditions and sample. The detector is a BF_3 filled curved multicounter with 400 wires. The distance between the analyser and detector is quite small at 8cm, this is for the reasons explained above in that it means a small vertical translation of the detector (5cm) covers a wide range of energy transfers (8meV with k_i = 14.2meV). The analysers and detector are located in the same shielding block and can be tilted in order to observe scattering form the different layers in reciprocal space. Thus by combining this tilting with the fact that the analyser can select different energy transfers, one can, in principle, record all elastic and inelastic scattering events in a single crystal in a systematic way.

Many structurally or magnetically disordered crystals give rise to coherent diffuse scattering which gives information about the local structure of disordered atoms or spins and their correlations. This diffuse scattering takes place over a large range of reciprocal space and thus a multidetector is ideally suited to the task of characterising this scattering. If the disorder is static or quasistatic i.e., the time scale of the dynamic process is larger than that given by the inverse of the instrumental energy resolution, then the diffuse scattering is elastic or quasielastic. In this case the elastic or integrated quasielastic intensity can be collected with the use of the E2 diffractometer by putting the analyser crystals to an energy transfer of $E = 0$.

Using this method, we measured the diffuse magnetic scattering of the triangular lattice antiferromagnet $CsNiCl_3$ above and below the magnetic transition temperature. A full description of this experiment can be found in Chapter 4.2.2.

3.3 Sample Environment

Having given a full description of the neutron scattering spectrometers and diffractometers it would be advantageous to consider the sample environment techniques employed in this thesis. Sample environment assumes great importance for systems such as magnetic compounds that order at very low temperatures and also, as was suggested in the Introduction, sample environment allows the experimentalist to tune the various parameters of his system. Magnetic field can be used to induce order in the system and pressure can be used to accurately change its structural makeup, in this way a greater understanding of the physics of the systems can be gained. The apparatus used for each technique is outlined in the subsequent chapters.

3.3.1 The ILL Orange Cryostat.

The ‘Orange’ cryostat (known by its colour) was developed by scientists at the Institut Laue Langevin, specifically for use in neutron scattering environments and presently, the company ‘A.S. Scientific Ltd.’ manufacture it under licence.

The cryostat utilises the properties of liquid ^{4}He to obtain temperatures in the region of 1.8K. As can be seen from above, the sample is mounted on a stick, which has several baffles affixed to it to prevent convective heat transfer. The stick is positioned in the evacuated central core of the cryostat. This is surrounded by a jacket of liquid ^{4}He, which is in turn protected from the environment by a jacket of liquid nitrogen. To prevent unnecessary heat loss all jackets are protected with vacuum. The liquid nitrogen pre cools the system to ~70K, where the ^{4}He takes over. The ^{4}He will lower the temperature to 4.2K. A small amount of exchange gas is permitted to enter the central chamber and the vapour pressure is reduced in the chamber by pumping. This allows cooling down to temperatures approaching 1.5K.

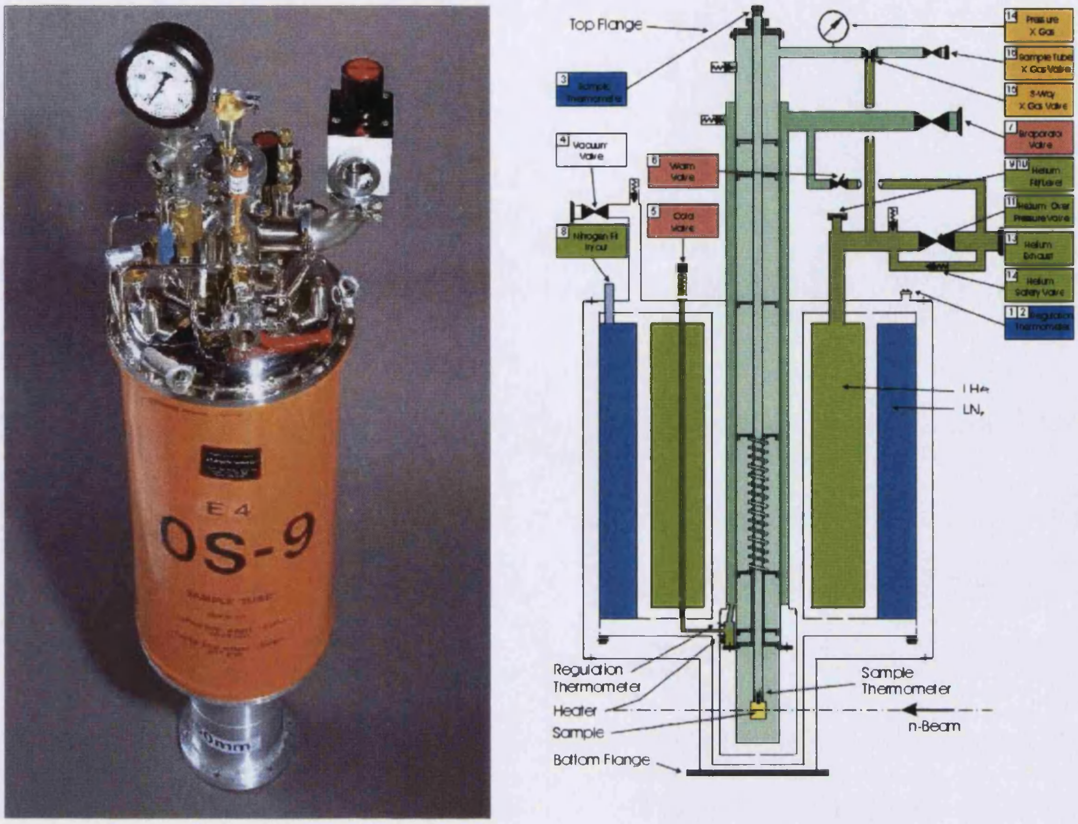

Figure 45: The typical ILL Orange cryostat, manufactured under licence by A.S. Scientific[122].

As can be seen from above, the liquid nitrogen and helium Dewars sit above the sample, allowing the neutron beam unhindered access to the sample. The aluminium which forms the 'tail' of the cryostat is as thin as possible to prevent any spurious signals which may contaminate the observed neutron diffraction pattern. The advent of the cryostat has allowed scientists to probe the low temperature magnetic structures of various new and exciting materials and also investigate the dynamics of materials at low temperatures.

3.3.2 Dilution Refrigeration Units

Temperatures of ~0.3K can be reached by the same evaporation method as described above but substituting ^{3}He for ^{4}He. To obtain temperatures below this value a technique known as dilution refrigeration is employed. The principle of dilution refrigeration was suggested by F. London around 1950, when it became evident that a liquid mixture of two helium isotopes ^{3}He and ^{4}He would undergo a phase transition at temperatures below 0.9K. If the mixture contains more than 6% then phase separation will occur at a certain temperature along the cooling curve. The ^{3}He (concentrated) phase will float on top of the more dense ^{4}He-rich (dilute) phase. Further cooling along the co-existence curve causes the concentrated phase to become almost entirely 100% pure ^{3}He, whilst the dilute phase tends to a limit of 6% ^{3}He in superfluid ^{4}He. It is this ^{3}He concentration in the dilute phase which makes the dilution cooling process possible. When the ^{3}He atoms move across the boundary from concentrate to dilute phase, a heat solution is taken from the liquids. This is analogous to the method explained in the previous chapter whereby evaporation of the ^{4}He extracts latent heat and causes cooling. The ^{3}He atoms in the dilute superfluid phase behave like the particles of a gas moving through the inert ^{4}He background as if it were a vacuum. The vapour pressure equivalent is the osmotic pressure for a solution of ^{3}He in ^{4}He. Thus in order to maintain a continuous flow of ^{3}He an osmotic-pressure gradient must be established in the system. This is achieved if the mixing chamber is connected to the still, which is maintained at a temperature of 0.7K. This is demonstrated schematically below.

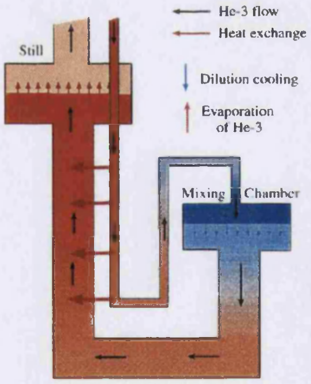

Figure 46: Schematic diagram of a ^{3}He - ^{4}He dilution refrigeration unit.

When the liquid in the sill is pumped, the vapour removed is almost entirely ^{3}He because it has a much higher vapour pressure than that of ^{4}He. Thus the required flow of ^{3}He for cooling the mixing chamber is established. The evaporated ^{3}He is collected, condensed and passed through a heat exchanger in which cooling by contact with the counter flowing dilute phase occurs. The actual arrangement of the dilution unit for neutron scattering experiments is shown below. The still and mixing chambers can be clearly seen and the sample is mounted just below the mixing chamber.

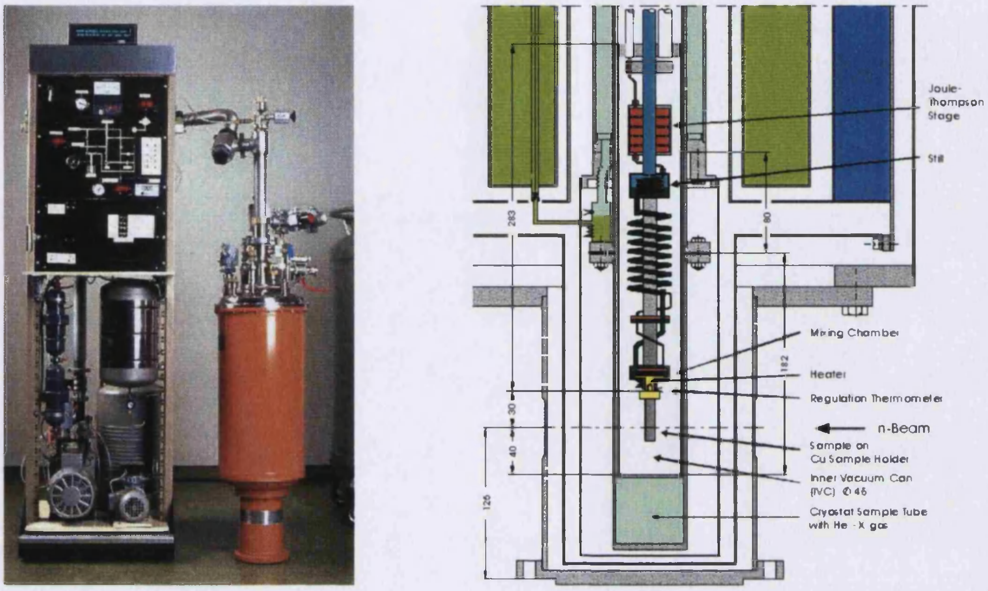

Figure 47: The dilution refrigeration unit used in conjunction with a 6 Tesla, Horizontal Field magnet for the experiment in Chapter 5.3. It is shown here inserted into a modified Orange cryostat (left) and schematically (right)[123].

3.3.3 Gas/Liquid Pressure Cells.

There are two different methods of applying pressure to a sample, which are applicable to neutron scattering, the clamp cell and the compressed gas cell. The clamp cell is used for higher pressures (up to Gpa), whilst the latter is useful for low pressure, low temperature measurements. It is the latter, which has been utilised for neutron scattering measurements in this thesis.

This method normally utilises the low temperature properties of Helium. The single crystal sample is immersed in a chamber filled with Helium liquid, pressurised, and the temperature lowered until solidification occurs. This gives a truly hydrostatic environment which is capable of obtaining pressures of 5 – 6 kbar and the ability to make measurements at low (liquid Helium) temperatures. There are several reasons why He is used for a pressure transmitting medium:

- Helium retains its fluid state down to a lower temperature than other elements. This provides a pure hydrostatic environment for a wide range of temperatures and pressures.

- When He is solidified in the chamber the pressure loss along the isochore is smaller than any other element. This is due to the fact that most of the internal pressure is caused by the zero point instability of He, thus it is relatively insensitive to temperature change.

- The shear stress of the rare gases when plotted as a function of T_N/T falls on a universal curve, thus He should have the lowest shearing stress of all substances.

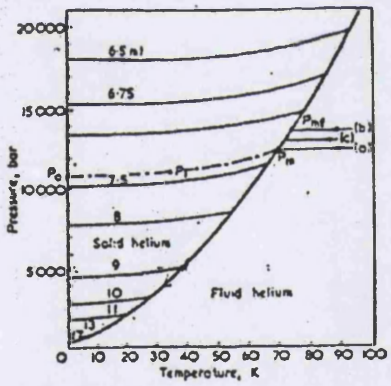

Figure 48: Extrapolated melting curve of He. Path (a) shows the cooling path with freezing occurring under constant pressure conditions at pressure P_m, followed by cooling along an isochore to a final pressure P_o. Path (b) indicates freezing under constant volume conditions from pressure P_{mf} in the fluid phase. Path (c) is an intermediate case, with change with both molar volume and pressure occurring during freezing (1bar = $10^5 Nm^{-2}$) (Schull, cryogenics 1970).

The He pressure cell method was used in the neutron scattering experiments performed at the Laboratoire Leon Brillouin, Saclay, France. This cell was built 'in house' and was specifically designed with low temperature, single crystal neutron diffraction in mind. The He pressure cell outlined above was utilised in experiments whose details can be found in Chapters 5.1.1 and 5.2.1.

3.3.4 Horizontal and Vertical Magnets

This section gives information on the two different magnets from the Hahn Meitner Institut that were used in experimental work elaborated upon in later chapters.

3.3.4.1 The Vertical Magnet, VM3, at the HMI, Berlin.

The vertical magnet VM3, manufactured by AS Scientific Ltd is shown below. One can see that its basic design is similar to that of the normal 'Orange' cryostat (Figure 45), in that it utilises liquid Nitrogen and liquid Helium dewars, as well as the properties of vacuum to enable temperatures of approximately 2K to be reached. The Helium cooled superconducting coils allow a vertical field of 5 Tesla to be applied to the sample.

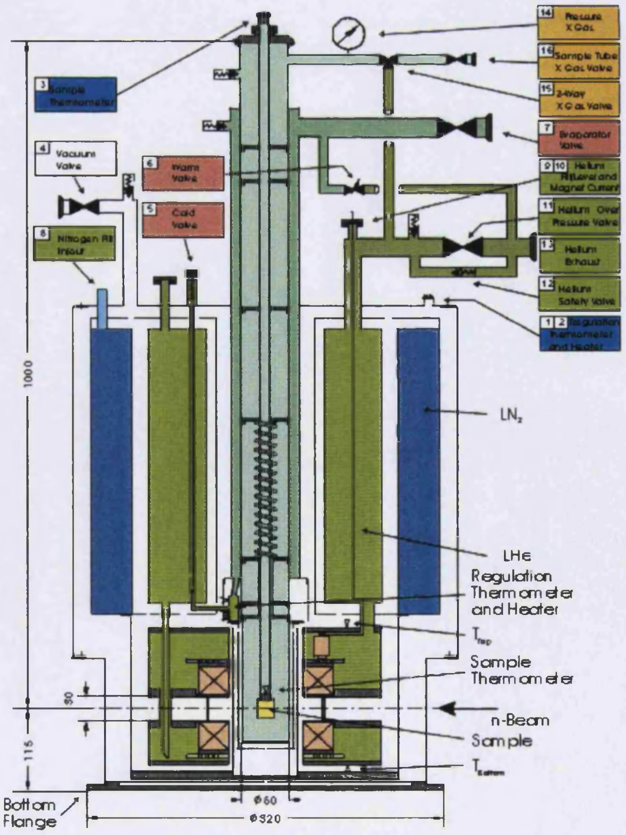

Figure 49: Schematic of the Vertical Magnet VM3 at the HMI[124].

This magnet was used in conjunction with the TAS, E1, at the HMI, in order to establish the critical exponent, β, of $CsNiCl_3$ under magnetic field. However, due to the construction of the magnet, only certain windows of scattering are allowed. This was to prevent the accurate measurements of β during the experiment. More information on this can be found in Chapter 4.2.1.

3.3.4.2 The Horizontal Magnet, HM1, at the HMI, Berlin.

The basic construction of HM1 is similar to that of VM3, due to the construction of the windings in the magnetic, the field can be applied horizontally to the plane of the experiment and allow one to look at different aspects of the magnetic ordering in the system in question.

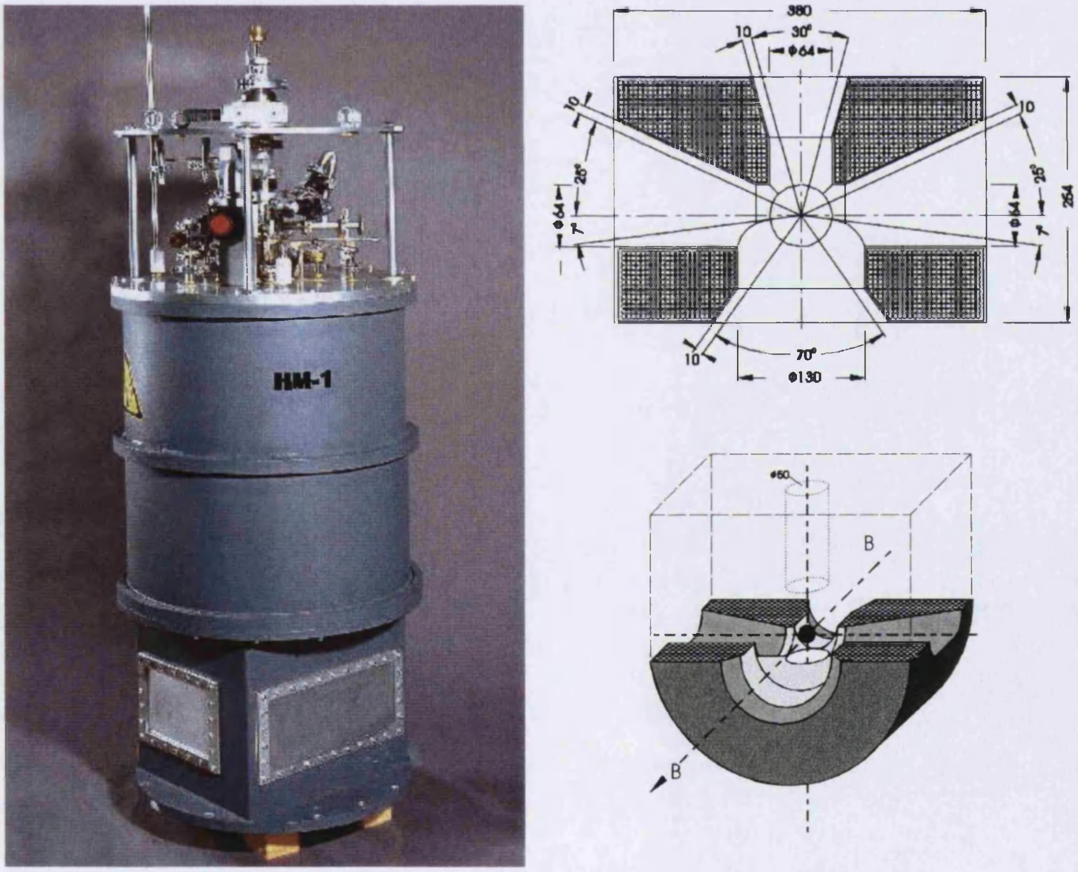

Figure 50: The Horizontal Magnet HM1, showing the plan and plane view of the available scattering windows[125].

This magnet was used in conjunction with a dilution refrigeration unit in order to establish the low temperature magnetic phase diagram and the critical exponent β of the SGS $CsFeBr_3$ at millikelvin temperatures, more information on these experiments can be found in Chapter 5.3.

4 Chiral Order in ABX_3 compounds

The information given in this Chapter relates to experimental work performed on the ABX_3 model systems. Chapter 4.1 deals with experiments performed on the easy plane anisotropy system $CsMnBr_3$, looking at the magnetic ordering of the system in the presence of an applied magnetic field. Chapter 4.2 deals with experimental measurements on the easy axis anisotropy system $CsNiCl_3$ which is a particularly good model material for the Haldane conjecture. Chapter 4.3 details magnetic sublattice magnetisation measurements on the isomorphous material $RbNiCl_3$. Chapter 4.4 gives a full description of the structural and magnetic, temperature – pressure, phase diagram of the distorted lattice compound $TlFeCl_3$ and finally the different phases another distorted system, $KNiCl_3$, have been characterised in Chapter 4.5.

4.1 $CsMnBr_3$ (E1, V1 - HMI)

To establish the validity of the predictions and conjectures made in Chapter 2.2.2, neutron scattering experiments were performed on $CsMnBr_3$ in the presence of an electric field. Plumer *et al.*[126] used symmetry arguments to demonstrate that an electric field applied in the basal plane of a stacked triangular antiferromagnet breaks the chiral degeneracy associated with the induced 120° spin structure which is achieved through magneto-electric coupling which introduces a Dzyaloshinsky – Moriya type of interaction.

It is known that the chirality of helically polarised magnetic structures, in crystals lacking a centre of symmetry, is determined by the sign of the Dzyaloshinsky – Moriya interaction[127,128,129]. The phenomenon known as the magnetoelectric effect refers to the appearance of a magnetic moment in response to an applied electric field, or vice versa[130]. For example, in the system $ZnCr_2Se_4$[131] the sense of the chirality of its helical ordering can be controlled by applied electric field. By means of a polarised neutron scattering study it was possible to prove that a magnetic structure of a definite helicity can be produced in this system in the presence of an electric and magnetic field. Plumer *et al.*[126] used symmetry arguments to construct the lowest order coupling term between a spin vector, $\vec{S}$, and an electric field, ($\vec{E}$), induced polarisation vector, $\vec{P}$, on a simple hexagonal lattice with planar anisotropy.

It has been shown that the terms which contribute to the magnetic Hamiltonian have to satisfy several criteria: time reversal (only even powers of $\vec{S}$ can occur) and invariance to the symmetry operations of the space group (in our case centrosymmetric). Thus, in our case of a hexagonal lattice with a centre of inversion symmetry, one is left with one term;

$$\mathscr{H}_c = {}^{1}\!/_{2V} \int d\vec{r}d\vec{r}'C(\vec{\tau})(P\times\tau)_z \cdot [\vec{s}(\vec{r})\times\vec{s}(\vec{r}')] \tag{46}$$

where $\vec{\tau} = \vec{r} - \vec{r}'$, $C(-\vec{\tau}) = C(\vec{\tau})$ and subscript z indicates the $\hat{z}$ component. The spin density of $\vec{s}(\vec{r})$ can be represented as

$$\vec{s}(\vec{r}) = \left({}^{V}\!/_{N}\right)\sum_{R} \vec{\rho}(\vec{r})\delta(\vec{r} - \vec{R}) \tag{47}$$

where $\vec{R}$ denotes the hexagonal lattice points and $\vec{\rho}$ the long range magnetic order. $\vec{\rho}(\vec{r}) = \vec{S}_1 e^{i\vec{Q}\cdot\vec{r}} + \vec{S}_2{}^{*} e^{i\vec{Q}\cdot\vec{r}}$, with $\vec{S}_1$ and $\vec{S}_2$ being real vectors.

The polarisation vector $\vec{P}$ in equation 46 is expected to be proportional to the applied E - field. This form is comparable to the Dzyaloshinsky – Moriya interaction, of the form:

$$\vec{D}\cdot\left\lfloor\vec{S}_i \times \vec{S}_j\right\rfloor \tag{48}$$

Taking only nearest-neighbour interactions into account the magnetoelectric coupling contribution to the groundstate energy is given by,

$$E_C = i\tilde{C}_Q P_{\hat{z}} \cdot \left(\vec{S}\times\vec{S}^{*}\right) \tag{49}$$

where,

$$\tilde{C}_Q = 2C_\perp[2bp_x \cos \tfrac{1}{2} q_x \sin q_y - ap_y(\sin q_x + \sin \tfrac{1}{2} q_x \cos q_y)] \qquad (50)$$

with, $C_\perp = (V/N)C(\vec{a})$, $\vec{P} = P(p_x\hat{x} + p_y\hat{y})$, $q_x = aQ_x$, $q_y = bQ_y$, and $b = (\sqrt{3}/2)a$.

The magnetic superexchange interactions are of the usual form,

$$\mathscr{H}_J = \frac{1}{2V}\int d\vec{r}d\vec{r}'\, J(\vec{\tau})[\vec{s}(\vec{r})\cdot\vec{s}(\vec{r}')] \qquad (51)$$

and contribute to the ground state energy $E_J = J_Q(\vec{S}\cdot\vec{S}^*)$ and where, regarding nearest neighbours only,

$$J_Q = 2J_{//}\cos(q_z) + 2J_\perp[\cos(q_x) + 2\cos(\tfrac{1}{2}q_x)\cos(q_y)] \qquad (52)$$

with,

$$J_{//} = (V/N)J(\mathrm{c}) \text{ and } J_\perp = (V/N)J(\mathrm{a}) \qquad (53)$$

The superexchange interaction causes a modulation of the spin density and results in a magnetic structure with $\vec{Q}_n = (4\pi/3a)\hat{a}_n + (\pi/c)\hat{c}$, where $\hat{a}_n$ is one of the six hexagonal basal plane crystallographic axes and with a helical polarisation where $\vec{S}_1 = (S/\sqrt{2})\hat{x}$ and $\vec{S}_2 = (S/\sqrt{2})\hat{y}$, as favoured by the interaction of Equation 50.

This results in the 120° type spin structure with two different chiral spin states:

- A positive chirality state with,

$$\vec{Q}_\perp = +(4\pi/3a)\vec{x}, \quad -(2\pi/3a)\vec{x} \pm (\pi/b)\vec{y} \qquad (54)$$

- and the negative chirality state where

$$\vec{Q}_\perp = -(4\pi/3a)\vec{x}, \quad +(2\pi/3a)\vec{x} \pm (\pi/b)\vec{y} \qquad (55)$$

These states are energetically equivalent. Both $\vec{S}$ and $\vec{Q}_\perp$ are confined to the basal plane.

The effect of the magnetoelectric coupling on the wavevector $\vec{Q}$ can be considered by minimisation of the energy $E_Q = \left(J_{\vec{Q}} + P\tilde{C}_{\vec{Q}}\right)S^2$. Since $\tilde{C}_{\vec{Q}} = 0$ for the 120° type spin structure, this type of magnetic ordering may be destabilised towards a slightly incommensurate magnetic ordering. The two cases are now considered, where

- $\vec{P} // \hat{x}$: i.e. parallel to the $\hat{a}_n$ axis, which is equivalent to the [100] direction,
- $\vec{P} // \hat{y}$: i.e. perpendicular to the $\hat{a}_n$ axis which is equivalent to the [110] direction. This direction also corresponds to the direction of the $\vec{k}$ - vector of the 120° type magnetic structure.

Considering the above states (and looking at only the cases where, in the limit $P \rightarrow 0$, $\vec{Q}_\perp = \pm(4\pi/3a)\vec{x}$, as the other four wavevectors give equivalent structures), we see that for $\vec{P} // \hat{x}$, $\tilde{C}_{\vec{Q}}$ is an even function of q_x and no chirality selection occurs, and the magnetic wavevector for a small magnetoelectric coupling is $q_x \cong \pm[4\pi/3 + (1\sqrt{3})\delta_b^2]$ and $q_y \cong \delta_b$, where $\delta_b = bPC_\perp / J_\perp$. For $\vec{P} // \vec{y}$, in the limit $P \rightarrow 0$, $\tilde{C}_{\vec{Q}}$ is an odd function of q_x and *chiral symmetry is broken*, this results in two senarios:

- A positive helical state $q_x \cong +4\pi/3$ is stabilised for $C_\perp > 0$. The minimum occurs for E_q at $q_x \cong 4\pi/3 - \delta_a$ where $\delta_a = aPC_\perp / J_\perp$ and $q_y = 0$. The magnetoelectric coupling energy is given by, $E_C \cong -3/2\, C_\perp aP(\delta_a + \sqrt{3}\delta_a^2 / 4)S^2$.

- A negative helical state occurs, $q_x \cong -4\pi/3$ for $C_\perp > 0$. The minimum energy occurs at $q_x \cong 4\pi/3 + \delta_a$ and equal energy.

A schematic drawing of the wavevector dependence of the groundstate energy in these two cases is given below in Figure 51. The broken curve shows chirality degenerate minima at $q_x = \pm 4\pi/3$ resulting from the antiferromagnet exchange. The solid curves show (as described above) the minima at $q_x \cong +4\pi/3$ for $C_\perp > 0$ and at $q_x \cong -4\pi/3$ for $C_\perp < 0$ as a result of including the magnetoelectric term.

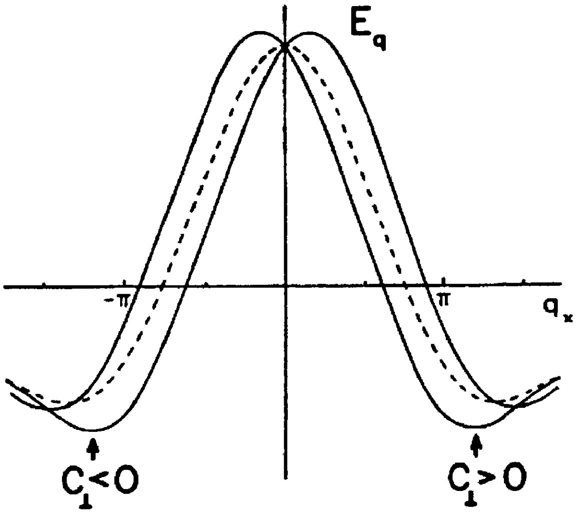

Figure 51: Wave vector dependence of the ground state energy[19].

Thus one would expect to observe a helical incommensurate structure with a $\vec{k}$-vector $k = (1/3 + \delta, 1/3 + \delta, 1)$ when the magnetoelectric effect is induced.

However, a more complicated picture emerges from the investigation of the electric field – temperature phase diagram. The Landau-type free energy for these systems can be expressed to low order as,

$$F = A_Q S^2 + \frac{1}{2} A_E P^2 + i\tilde{C}_Q P\hat{z} \cdot \left(\vec{S} \times \vec{S}^*\right) + B_1 S^4 + \frac{1}{2} B_2 \left|\vec{S} \cdot \vec{S}\right| + 2\tilde{B}_4 \left|\vec{P} \cdot \vec{S}\right| + \tilde{B}_5 P^2 S^2 - \vec{P} \cdot \vec{E} \tag{56}$$

where $A_Q = aT + J_Q$. The parameters a, $J_{//}$, $J_\perp$, A_E, $C_\perp$, B_1, B_2, $\tilde{B}_4$, $\tilde{B}_5$, are all specific to the material of interest. Following earlier work by Plumer[19], it is known that:

- A positive B_2 component stabilises the helical polarisation in the absence of an external field (magnetic).
- For $\tilde{B}_4 > 0$ a configuration with $\vec{S} \perp \vec{P}$, i.e. a linear polarised state, is preferred. The B_4 term must be relatively large to realise complete polarisation because the Dzyaloshinsky – Moriya term favours the helical state.

Thus, depending on the relative strength of the parameters one can obtain several scenarios from the minimisation of F when $E // \pm \hat{y}$. Plumer produced two phase diagrams from the numerical minimisation of F, and these are shown below. The parameters a, A_E, B_1 and B_2 were set to unity and the parameters $J_{//}$, $J_\perp$, $C_\perp$ and $\tilde{B}_4$ were varied. The results given were found for cases where $\tilde{B}_4$ was not large in comparison to $C_\perp$. Plumer found that a relatively strong interaction $\left|\vec{P} \cdot \vec{S}\right|^2$ stabilised the linear (commensurate) phase.

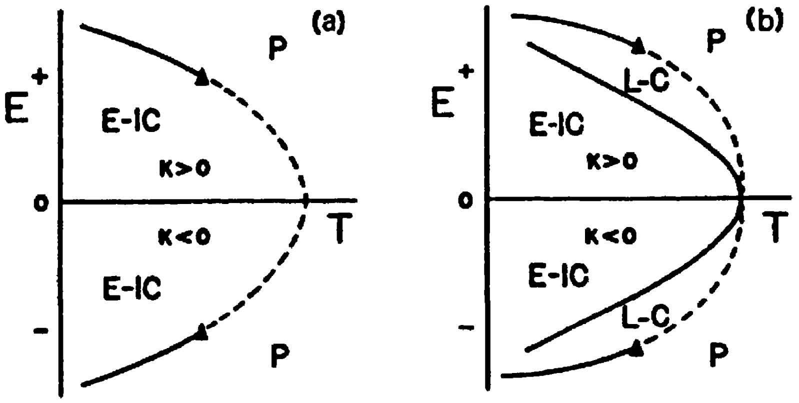

Figure 52: Schematics of electric field versus temperature phase diagrams with E along y and $C_\perp > 0$ for the cases of (a) small and (b) large coupling $\tilde{B}_4$ relative to $C_\perp$[19].

The ordered states can be further characterised by the chirality.

$\lvert\kappa\rvert = 1$	helical phase,
$\lvert\kappa\rvert < 1$	elliptical phase,
$\kappa = 0$	linear phase,

One may also visualise that for a particular temperature an increase of electric field may create a crossover between the different states.

The conjecture of Plumer *et al.*[126] concerning the magnetoelectric effect in the 120° type triangular antiferromagnet $CsMnBr_3$ was tested by Visser *et al*[132]. It was postulated that the application of an electric field should remove the chiral degeneracy by creating a mono-domain crystal of a single chirality when *E* // [110] direction. In this case one would expect to observe in the first instance a helical incommensurate structure, as has been observed for the IC_1 phase of $RbFeCl_3$. Furthermore, the removal of the chirality would induce a change in universality class from the $n = 2$ chiral class to the 3D *XY* class. With a predicted rise in the value of the critical exponent β from $\beta = 0.253$ to $\beta = 0.346$. However, the experiments performed by Visser *et al.*[132] on $CsMnBr_3$ in the presence of an electric field show a more complex picture.

The observed values for the critical exponent β with an applied electric field perpendicular to the [110] direction are shown in Figure 53. It can be seen that the value of β remains constant upto a critical value of applied *E* field and then drops via some intermediate values to $\beta = 0.165(10)$ around $E \geq 1.5$ kVcm^{-1}.

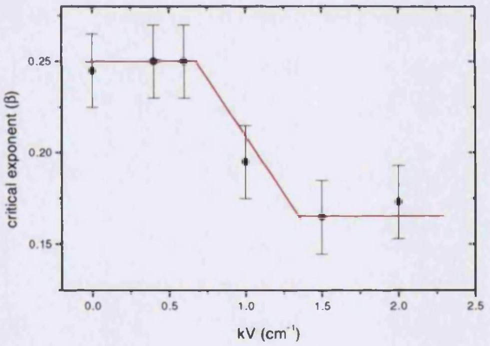

Figure 53: Critical Exponent β versus Electric Field for the Easy Plane Triangular Antiferromagnet $CsMnBr_3$[132].

These are very unusual values of the critical exponent, the only other system that shows such a low value of β is the 2D-Ising system where $\beta=0.125$. It should be noted also that a low value of β has been reported for the Ising triangular antiferromagnet $CsCoBr_3$ ($\beta = 0.22$). Thus, the initial simple picture of magnetoelectric coupling is not valid. The theoretical investigation of the electric field – temperature phase diagram shows that other options may be considered, depending on the relative strengths of the different coupling constants of the terms of the Landau free energy expansion. As indicated above one may observe a helical phase when the Dzyaloshinsky – Moriya term is strong, but when the $\tilde{B}_4$ coupling term is strong one obtains a $\vec{S}\perp\vec{P}$ configuration, that is, a linear polarised state. This means that either the spins are lifted out of the plane // *c*, or that the structure in the plane is changed. No additional intensity was found by Visser for reflections of the type [001] and [111] upon the application of *E* field. The presence of these peaks would indicate the formation of an Ising like structure. Low values of β may also be indicative of a weakly first order transition. Recent Monte Carlo simulations[133] indicate that the possibility still exists that the transition at T_N in a triangular antiferromagnet is of weak first order character. Experimentally, such a transition has not been observed, however this may be due to the lack of sufficient temperature resolution in the conventional experimental techniques of specific heat, susceptibility, neutron scattering etc. The application of electric field may enhance the first order character of this transition.

4.1.1 Temperature Dependence of the Magnetic Ordering in $CsMnBr_3$ in the presence of an Electric Field.

A large degree of diffuse magnetic scattering can be observed around the magnetic Bragg point Q(1/3 1/3 1) at $T > T_N$. Mason *et al.* have shown that this diffuse scattering extends along the [110] direction of reciprocal space and that its width is temperature dependent. The diffuse scattering adopts the same character as that found for $CsNiCl_3$, see for example, Figure 74. Measurements of the temperature dependence of the diffuse magnetic scattering in the basal plane of $CsMn_{1-x}Fe_xBr_3$ as a function of temperature, by Visser and McIntyre[134], on the diffractometers D10 and D16 at the ILL, show that above T_N the intensity smears out along the (K – M)/(A – H) line of the Brillouin zone.

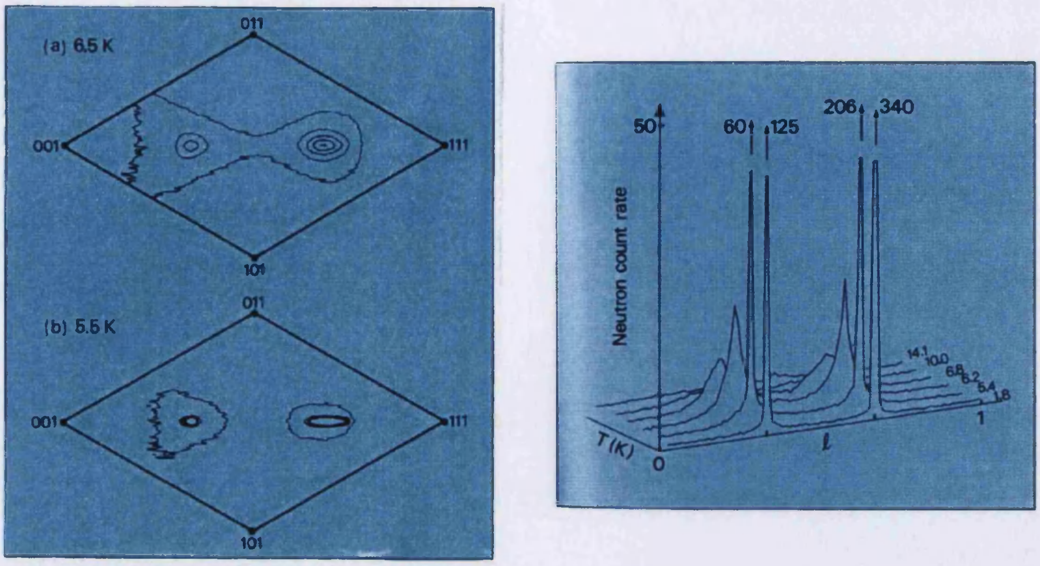

Figure 54: Diffuse scattering around the softmode point in $CsMn_{1-x}Fe_xBr_3$[134].

The K point Q(1/3 1/3 1) represents the 120° magnetic structure whilst the other extreme, the H point, Q(1/2 0 1), represents the pure 3-domain antiferromagnet structure, as shown in Figure 55.

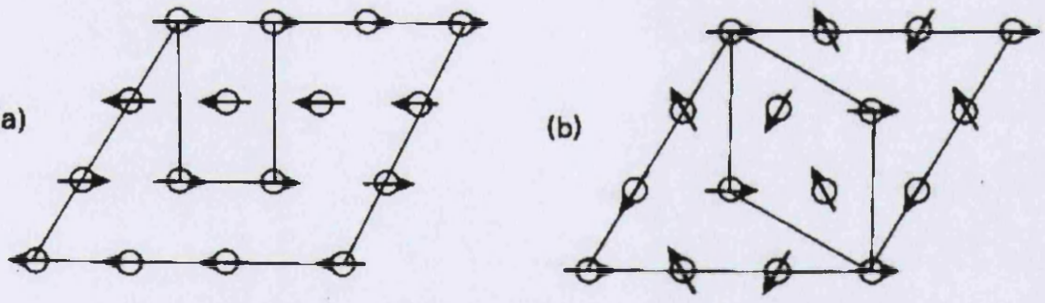

Figure 55: Schematics of the pure 3-domain and 120° antiferromagnet structures.

The magnetic intensity observed by Visser and McIntyre indicates that magnetic spin arrangements are present in $CsMnBr_3$, which are intermediate between the two extremes described above. If the structure would be static it would represent a helical incommensurate ordering. Simulations in connection with NMR studies indeed indicate the presence of such arrangements. Upon cooling of the system, the relative size of the ordering domains increase. In principle two types of chiral domains will be present, which in a real system will be connected by anti phase boundaries.

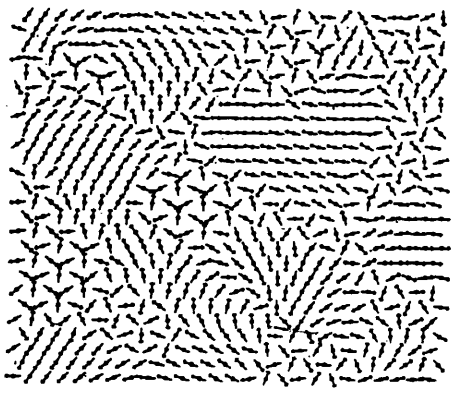

Figure 56: Monte Carlo simulation of the possible spin structures in CsMnBr$_3$.

However, the domain population density does not have to be equal for the two different chiral types. The population density could be influenced by the quality of the sample (defects etc.) and the influence of applied magnetic and/or electric field. In view of the observations made above, it was decided to undertake further experiments on the multicounter membrane diffractometer, V1, at the HMI, Berlin. Detailed information on this diffractometer can be found in Chapter 3.2.1.5. This was done in order to investigate the influence of electric field on the diffuse magnetic ordering in CsMnBr$_3$. The use of the multicounter enabled us to measure the total magnetic scattering as well as the extent of magnetic scattering in Q-space. It is expected that the diffuse scattering should reduce due to the removal of the domain walls between the chiral regions upon the application of *E* field.

The crystals of CsMnBr$_3$ were grown by the Bridgeman technique in a three-zone float furnace. The cleavage plane of this material lies in the [001]-[110] plane of reciprocal space, this corresponds to the *a*-axis and *c*-axis in real space. This means that one would ideally like to obtain diamond shaped crystals for the present experiment. In order to observe the effect, if any, of the application of *E*-field, it has to be applied along the [110] direction, thus the sample crystal has to be reshaped from a diamond form to that of a square one in order to have the two [110] faces parallel to each other. As CsMnBr$_3$ is hygroscopic in nature this reshaping has to be performed in the inert atmosphere of a drybox. It was deemed that the brittle nature of the material meant that the reshaping had to be done by hand as mechanical reshaping would have destroyed the sample. In order to apply electric field directly to the crystal, contacts were made on the crystal with Ag paint, other methods include evaporating Au onto the surfaces to make the contact. The single crystal used had dimensions of 2mm x 2mm x 7mm. Two contacts were made on each parallel face of the sample with Cu wire, one pair provided a means of applying the *E*-field and the other allowed us to measure the applied field across the sample. The 4 wires were fed into the cryostat via the sample stick and the sample itself was isolated from the stick by mounting it on a quartz rod. With this setup we found that we could achieve a maximum field of 700V/2mm at exchange gas pressures around 100mbar. Higher fields and lower pressures produced sparking across the crystal. In order to increase the effective applied *E*-field it is necessary to reduce the width of the sample crystal.

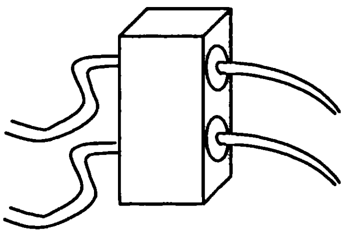

Figure 57: Schematic of the connection of the electric field wires to the single crystal of $CsMnBr_3$.

In all, four complete datasets were taken around the reciprocal lattice point Q(1/3 1/3 1). Data was collected at T=8.20K and 8.55K with no applied electric field and again at the same temperatures with an applied electric field of 700V/2mm (equivalent to 3.5kVcm^{-1}). One would expect that should the application of an electric field cause a reduction of the diffuse magnetic scattering, this would become apparent by subtracting the data under field from the data with no applied electric field. One should then observe a small residual diffuse magnetic scattering. This can be seen below in Figure 58 and Figure 59. It was impossible to discern the shape of the diffuse scattering from the available data, this was mainly due to small size of the sample crystal although the resolution limit of the multidetector also contributed to this.

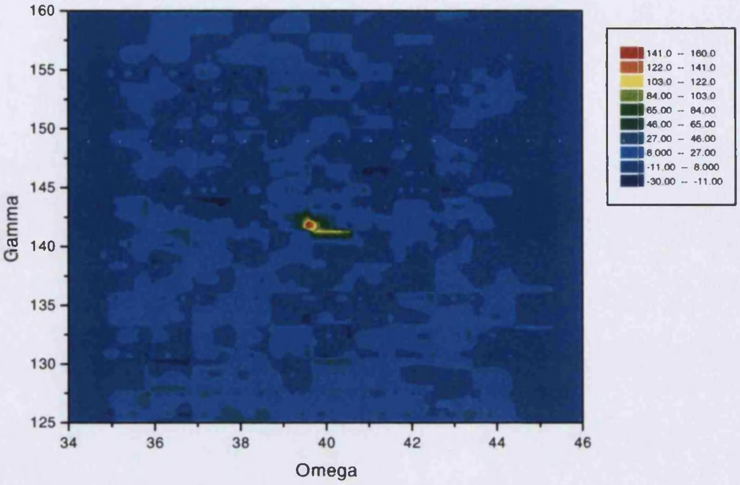

Figure 58: Difference in magnetic scattering of CsMnBr$_3$ at T=8.20K – E=0V and T=8.20K – E=700V at the magnetic Bragg reflection Q(1/3 1/3 1).

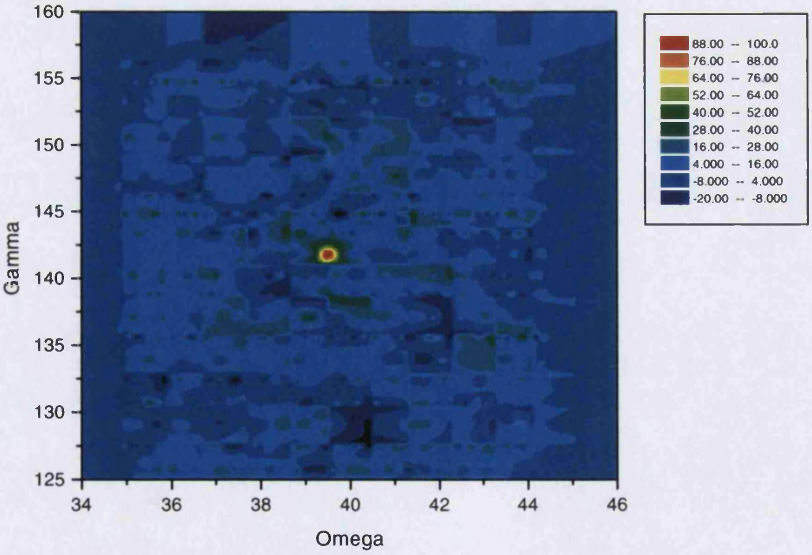

Figure 59: Difference in magnetic scattering of CsMnBr$_3$ at T=8.55K – E=0V and T=8.55K – E=700V at the magnetic Bragg reflection Q(1/3 1/3 1).

As has been suggested, the very small scattering from the sample observed above was due to the physical dimensions of the crystal used in the experiment, but it is clear from the data above that there is indeed a difference apparent between the scattering observed with and without the presence of applied electric field.

A second experiment was performed, (on the same diffractometer with the same sample conditions) in order to investigate the sublattice magnetisation of the system above T_N. This was achieved by fixing the multidetector at the position Q(1/3 1/3 1) and varying the temperature. The observed data are quite noisy but an effect is quite visible upon the application of electric field, the β value is reduced from β=0.243(10) to β=0.220(10) in agreement with the previous experiments[132]. The reduction of diffuse magnetic scattering can be seen below in Figure 60. It should be noted that during the experiment there were several problems with contacting the electrodes to the sample surface due to the high moisture levels in the air at the time the experiment was carried out. When the crystal was removed from the cryostat at the end of the experiment it was found that a part of the crystal had broken and become detached from the bulk of the material. These factors may explain the low value of β = 0.22 in the presence of an applied electric field: only a part of the crystal may have had the *E*-field applied to it. Other possibilities may be that the crystal faces may not be perfectly parallel or that the crystal may have extended defects.

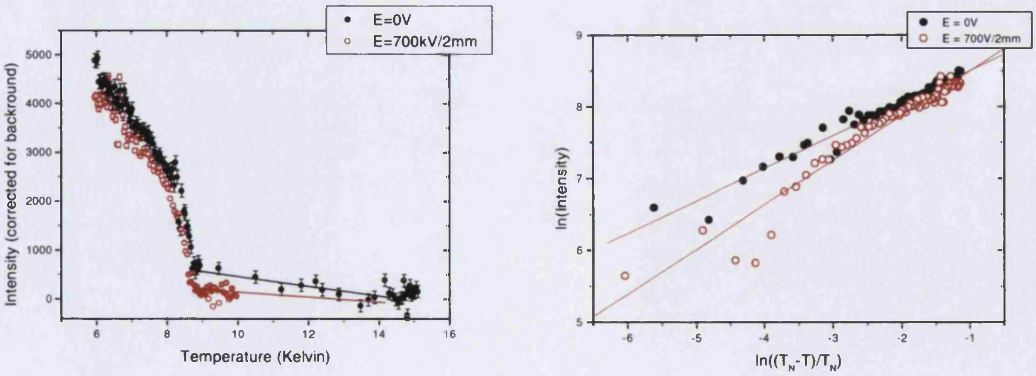

Figure 60: Sublattice Magnetisation of CsMnBr$_3$ showing different diffuse magnetic scattering for the system in and out of electric field.

The temperature dependence of the magnetic scattering shows also clearly that the diffuse scattering above T_N is dramatically reduced when an electric field is applied. This lends weight to the hypothesis that the application of electric field removes the 'domain walls' and increases the size of the ordered domains in the crystal. Thus $CsMnBr_3$ can be considered as a model system for the new XY chiral universality class of Kawamura.

4.1.2 Elastic Scattering on $CsMnBr_3$ in the presence of an Electric field and a Magnetic field.

As can be seen from Figure 14, Chapter 2.2.2.1, the phase diagram of $CsMnBr_3$ shows a tetracritical point along B = 0T. This point is formed by the amalgamation of the spinflop phase boundary and the collinear – paramagnetic phase boundary. At this special point which coincides with T_N, the critical exponent $\beta = 0.25$. The nature of this point is not well characterised and different predictions have been put forward. It may be that the value of the critical exponent is entirely due to the chiral ordering of the system. The point may be a mean field tricritical point or it may be that a simple first order transition takes place at T_N. Plumer *et al.*[135] investigated the structure of all phases in the presence of an applied magnetic field by means of a non local Landau type free energy calculation. It was predicted that the upper transition should belong to the conventional XY class and the lower to the conventional Ising class.

Neutron scattering experiments have shown that the critical exponent $\beta = 0.29(2)$ for $B_{\perp c} = 4T$ for the upper transition. However, this value is in between that of conventional and chiral universality classes. It has been shown in the previous Chapter that the magnetoelectric effect in $CsMnBr_3$ changes the critical behaviour of the system dramatically. This opens up the question about the shape and character of the phase diagram in the presence of an applied *E* and *B*-field. No Landau type predictions are available for this scenario; therefore a neutron scattering experiment was carried out to investigate these points.

The experiment was performed on the TAS E1 at the HMI, a full description of which can be found in Chapter 3.2.1.1. The magnetic field was applied using the 7T horizontal field magnet, HM3. Several practical problems had to be overcome before the successful implementation of the experiment. A slightly bigger single crystal of $CsMnBr_3$ (~4mm width) than the previous experiment was prepared in the same manner and again 2 pairs of wires were connect to the crystal in order to apply and measure the *E*-field at the crystal. The crystal faces had an Au coating deposited on them in order to make the contact. A schematic of the setup of the crystal and connecting wires can be seen in Figure 57. A maximum field of 800V was applied across the faces of the sample before sparking occurred. This sparking could be identified by a spike in the reading of the DC meter.

Full sublattice magnetisation measurements across the magnetic Bragg peak of (1/3 1/3 1) were taken at base level (B = 0T, E = 0V), and with an applied electric field of 800V/4mm at 0T, 2T and 4T. The resulting data is collated and plotted below. The corresponding critical exponent β was calculated from the 'log – log' plots shown adjacent to each sublattice measurement.

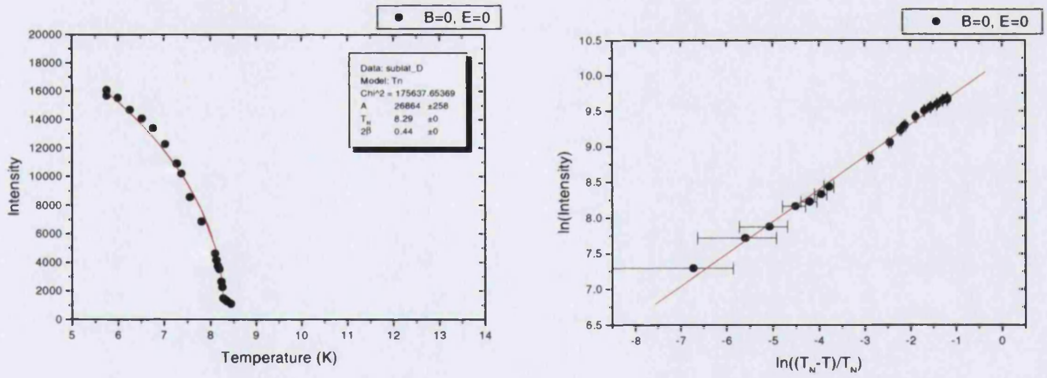

Figure 61: Sublattice magnetisation of $CsMnBr_3$ at B = 0T, E = 0V (line is best fit to power law $A\varepsilon^{2\beta}$ with β=0.22).

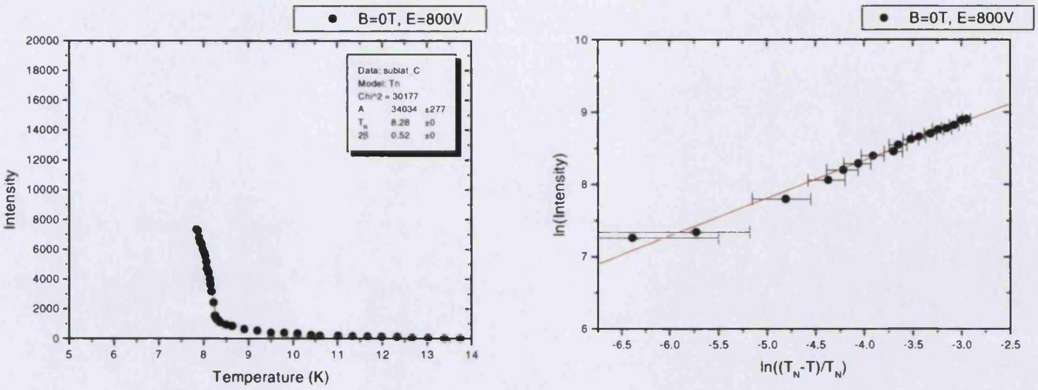

Figure 62: Sublattice magnetisation of CsMnBr$_3$ at B = 0T, E = 800V (line is best fit to power law $A\varepsilon^{2\beta}$ with β=0.26).

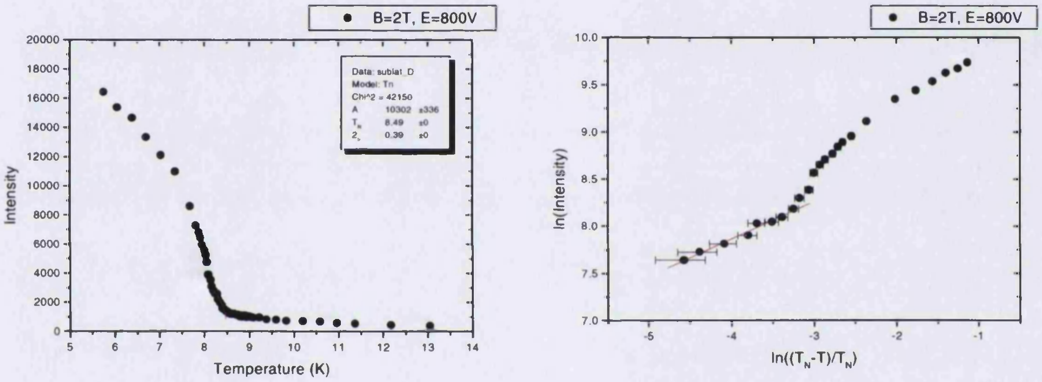

Figure 63: Sublattice magnetisation of CsMnBr$_3$ at B = 2T, E = 800V (line is best fit to power law $A\varepsilon^{2\beta}$ with β=0.195).

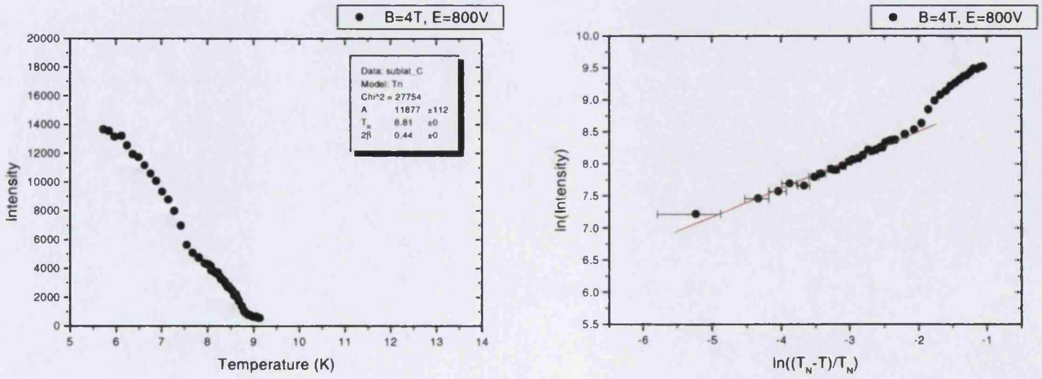

Figure 64: Sublattice magnetisation of CsMnBr$_3$ at B = 4T, E = 800V (line is best fit to power law $A\varepsilon^{2\beta}$ with β=0.22).

The calculated values of the critical exponent β and the corresponding transition temperatures T_N are collated below and shown in Table 7.

Table 7: Critical exponent β values for $CsMnBr_3$ under the influence of electric and magnetic field.

Magnetic Field (T)	Electric Field ($kVcm^{-1}$)	Critical Exponent (β)	Transition Temp. (T_{N2})	Transition Temp. (T_{N1})
0	0	0.22 (3)	8.29 (1)	--
0	800	0.26 (2)	8.28 (1)	--
2	800	0.195 (15)	8.15(2)	8.49 (1)
4	800	0.22 (1)	7.57(1)	8.81 (1)

From the observed values of the transition temperatures we can construct the phase diagram of $CsMnBr_3$ under the influence of an applied magnetic and electric field. The first observation that can be made is that the magnetic phase diagram of $CsMnBr_3$ under applied electric field is not dissimilar to the form for that of the magnetic phase diagram the same system without the application of field. This can be witnessed by the comparison of the general form of the figure below and that of Figure 14.

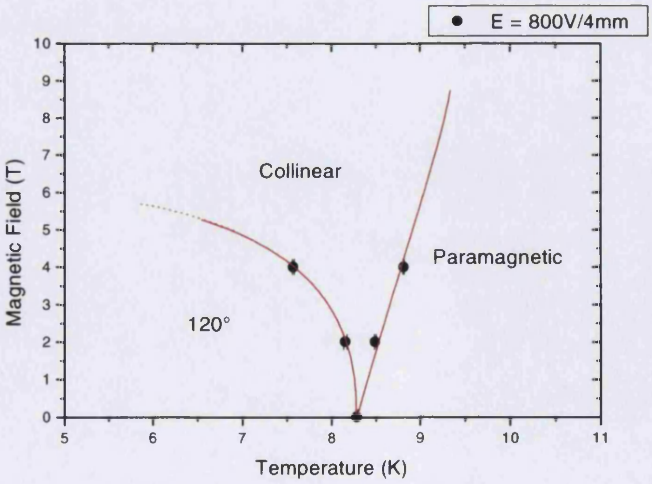

Figure 65: The magnetic phase diagram of $CsMnBr_3$ under and applied electric field of 800V / 4mm, lines are a guide to the eye only and given phases are most likely.

The present experiment establishes the phase boundary at B = 0 to be T_N = 8.29(1)K. This is slightly smaller than the accepted value of T_N found from C_p measurements. The difference can be accounted for by factors such as the placement of the thermometers and the type of sample support used in different experiments. Scaling the values of the specific heat measurements and previous neutron scattering measurements with our measurements we observe that the values of T_{N1} are all comparable within their error bars. However, the transition from the 'collinear phase' to the '120°' type phase (T_{N2}) occurs at higher temperatures with an applied E and B field than that with applied B field only. It is expected that this phase boundary will have the same trend at low values of applied B-field but we do not have enough data points to establish this.

The analysis of the magnetic sublattice magnetisation scans shows that no magnetoelectric effect is observed for the initial cooling of the crystal from room temperature in the presence of an electric field. We find that β = 0.26(1), which is very similar to the value calculated for β when the electric field is removed. The sublattice magnetisation scans for the sample cooled in the presence of both an electric and magnetic field where B = 2T and 4T show that a magnetoelectric effect takes place. The value of the critical exponent β changes from the reference value of β = 0.22 at B = 0T to a value of β = 0.195 at B = 2T and finally to β = 0.22 at B = 4T. This increase (β changing from 0.195 to 0.22) is similar to that observed for the value of β along the paramagnetic → collinear phase boundary in the absence of an electric field: β increases from 0.24 – 0.29 at B = 4T.

From these results we can conclude that the magnetic phase diagram only changes slightly upon the application of an applied E-field. The critical behaviour at the paramagnetic phase boundary is influence in an identical way as for fixed E-field and applied B-field. To understand the observed changes in detail a thorough theoretical investigation of the E, B phase diagram is required.

4.2 $CsNiCl_3$ (E1 / E2 - HMI)

As discussed in Chapter 2.2.1, $CsNiCl_3$ is a triangular lattice antiferromagnet with easy axis anisotropy. The (*H*, *T*) phase diagram in Figure 11 shows the two stage ordering of the system. At T_{N1} a partially magnetically ordered structure will be formed, while at T_{N2} the magnetic structure will be fully ordered in a modified 120° type structure which is rotated by 90° out of the hexagonal *ab* plane into the [111] plane. Recent specific heat studies by and Beckmann *et al.*[35] and birefringence experiments by Enderle *et al.*[37] have shown that $CsNiCl_3$ has a specific heat exponent of $\alpha = 0.32(5)$ and $\alpha = 0.342(5)$ respectively along the paramagnetic to spin flop boundary. These are much larger than the non-chiral universality classes of $\alpha = 0.1098(29)$ for Ising, $\alpha = -0.0080(3)$ for XY and $\alpha = -0.1160(36)$, on the other hand they agree with the $n = 2$ chiral value of $\alpha = 0.34(6)$. Close to the multicritical point, α was found to decrease to 0.25(8) and 0.23(4) respectively. This is in agreement with the $n = 3$ chiral universality class value of $\alpha = 0.24(8)$. Furthermore, according to Beckmann, the critical amplitudes follow the predictions for $n = 2$ and $n = 3$ chiral critical behaviour. The critical exponents suggest that $CsNiCl_3$ is an XY like system along the $H = 0$ line[51]. It is reasonable to expect the critical exponent β to exhibit the same characteristics as α. Thus in order to lend weight to the chiral universality class hypothesis we measured the critical exponent β, by means of neutron scattering.

4.2.1 *Elastic Scattering on $CsNiCl_3$ in the presence of a magnetic field.*

The neutron scattering experiment was undertaken on the TAS E1, at the HMI, Berlin. The spectrometer was operated in two-axis mode as described in Chapter 3.2.1.1. Since the magnetic interactions are quasi one dimensional, i.e. strong along *c* and weak in the perpendicular direction we mounted the large single crystal sample (~4 cm^3) with the [110] – [001] plane in the scattering plane. A magnetic field was applied // *c*-axis using the Horizontal field magnet, HM1, detailed information on this magnet can be found in Chapter 3.3.4. As can be seen from the description of HM1, the magnet does not afford unhindered access to the sample due to the magnet poles obscuring 195° of the scattering pathways. Simulations of the scattering pathways showed that we were unable to measure the strong magnetic Bragg peak at (1/3 1/3 1) with a k_i = 2.0Å, neither could we access the magnetic Bragg peak (2/3 2/3 1). Rather we were obliged to measure the (1/3 1/3 3) reflection using the $\lambda/2$ contribution from the PG 002 monochromator. The calculated scattering windows for the Horizontal field magnet HM1 with k_i = 2.0Å and 1.2276Å are given below in (a) and (b) respectively.

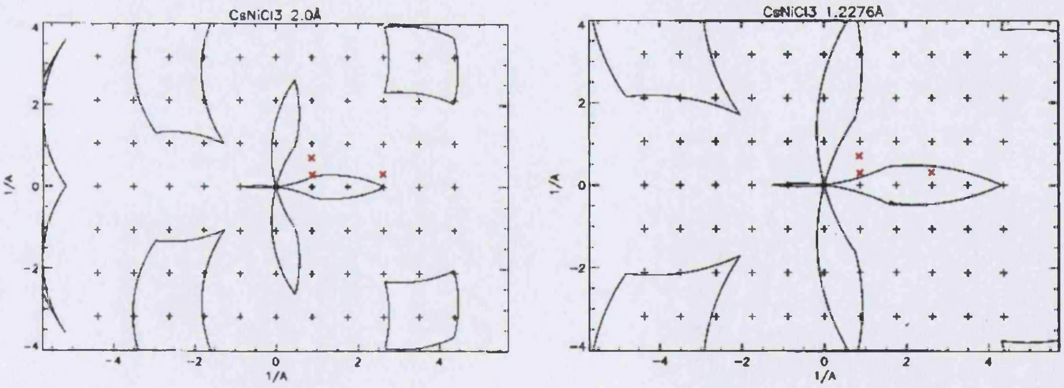
(a)

(b)

Figure 66: Comparison of the calculated scattering windows for the horizontal field magnet, HM1 for different incoming neutron wavelengths. The magnetic Bragg peak (1/3 1/3 1), (2/3 2/3 1) and (1/3 1/3 3) are shown as (x).

However, even when the sample was aligned with the *c*-axis // to the axis of the magnet no magnetic reflection was observed at the Q(1/3 1/3 3) position. It was discovered that the Bragg peak lay just outside the scattering window of the magnet.

In order to acquire a signal from the peak the sample stick within the magnet was rotated by 4°. This of course meant that the magnetic field was no longer directed // to the *c*-axis but instead was applied at an oblique angle. It was not known what effect that this would have on the results.

Thus the lack of flux, combined with the small structure factor of the (1/3 1/3 3) reflection and the high absorption of the crystal made it very difficult to obtain accurate data. However, we were able to obtain sufficient data to determine the critical exponent β at magnetic fields of B = 0T, 1.75T, 2T, 3T and 4T. The sublattice magnetisation scans and corresponding 'log – log' plots are show below.

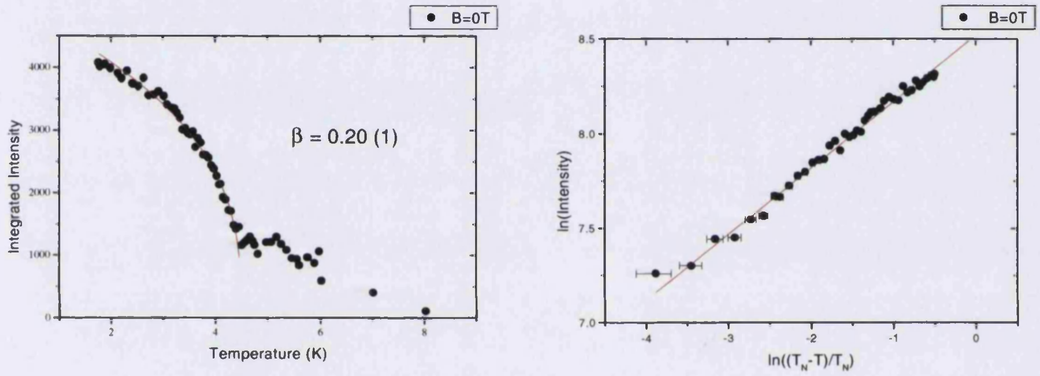

Figure 67: Sublattice magnetisation of CsNiCl$_3$ at Q(1/3 1/3 3) with B = 0T, (line is best fit to power law A$\varepsilon^{2\beta}$ with β=0.20).

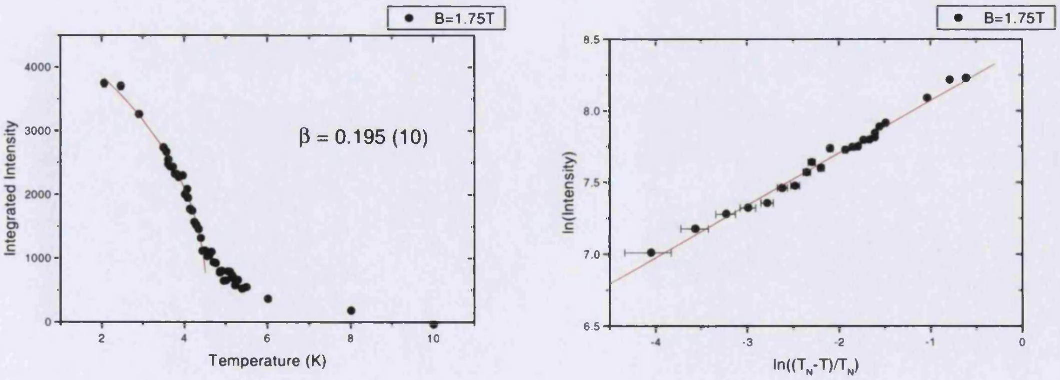

Figure 68: Sublattice magnetisation of CsNiCl$_3$ at Q(1/3 1/3 3) with B = 1.75T, (line is best fit to power law A$\varepsilon^{2\beta}$ with β=0.195).

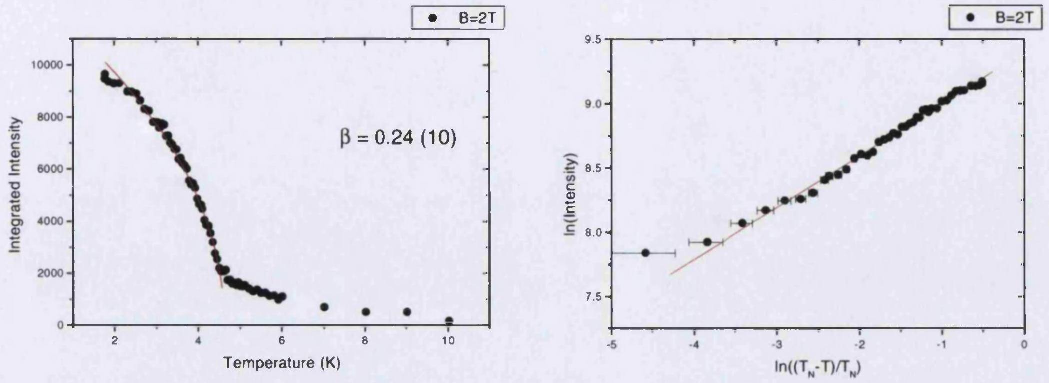

Figure 69: Sublattice magnetisation of CsNiCl$_3$ at Q(1/3 1/3 3) with B = 2.0T, (line is best fit to power law A$\varepsilon^{2\beta}$ with β=0.24).

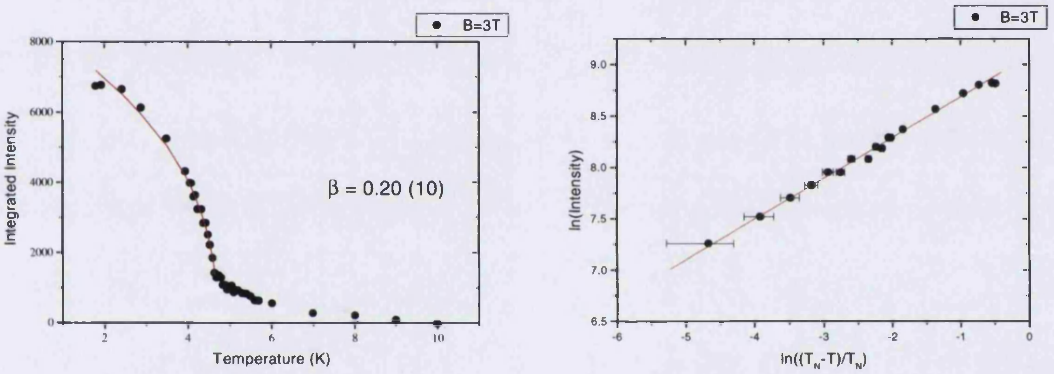

Figure 70: Sublattice magnetisation of CsNiCl$_3$ at Q(1/3 1/3 3) with B = 3.0T, (line is best fit to power law A$\varepsilon^{2\beta}$ with β=0.20).

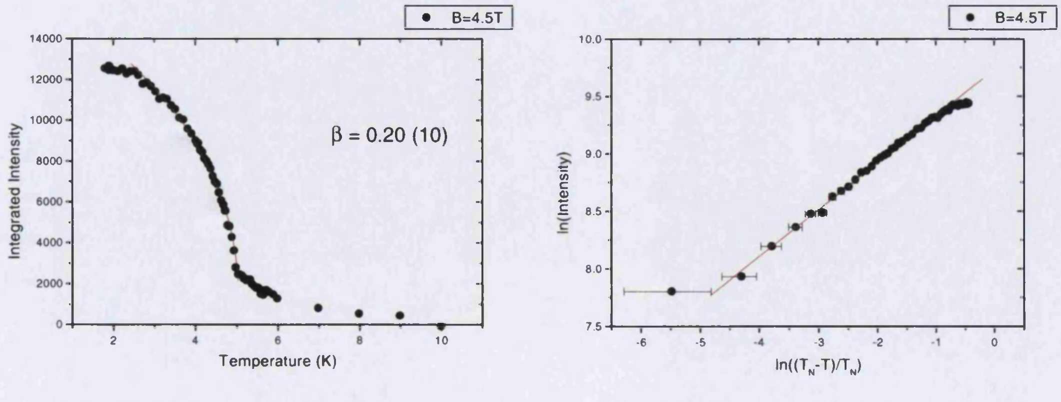

Figure 71: Sublattice magnetisation of CsNiCl$_3$ at Q(1/3 1/3 3) with B = 4.5T, (line is best fit to power law A$\varepsilon^{2\beta}$ with β=0.20).

The values of the critical exponent β and the transition temperature T_N are collated below in Table 8. It is seen that β changes from the value of β = 0.20 (10) at B = 0T to a value of β = 0.24 (1) at the spin flop transition, reducing to β = 0.20 (1) for higher magnetic fields.

Table 8: The transition temperatures and calculated critical exponents β of $CsNiCl_3$ under applied magnetic field // *c*.

Field (Tesla)	T_N (K)	β
0	4.50 (2)	0.20 (1)
1.75	4.55 (2)	0.195 (10)
2.0	4.61 (2)	0.24 (1)
3.0	4.69 (2)	0.20 (1)
4.5	5.06 (2)	0.20 (1)

The first observation to be made is that the calculated value of the critical exponent β does not correspond to the n = 2 chiral value of β = 0.25 at the paramagnetic to spin flop boundary (H_M ~ 2.2T). Nor does it correspond to the n = 3 chiral value of β = 0.3 at fields above H_M. As can be seen from the sublattice magnetisation scan at B = 0T the data cannot resolve the two previously measured phase transitions of $CsNiCl_3$ at ~4.40K and ~4.84K[51, 52], this is also the case for the data at 1.75T. Thus we should not be surprised that the data at 0T does not provide us with an exponent close to that of the normal XY class. We would expect that the critical exponent β should be in the region of ~0.35 for the 0T measurements, diminishing to ~0.3 at the multicritical point and finally coming to rest at ~0.25 along the spin flop to paramagnetic phase boundary.

The results obtained are quite different from those that were expected and there are several factors that have a role in this. As has been explained previously the magnetic field was 4° off from H // *c* so that the perpendicular component of the spin has begun to mix into the phase. The measurements have been performed on the (1/3 1/3 3) magnetic Bragg reflection where the <*XY*> component of the spin is larger than at the (*h h* 1) points. *N*uclear *M*agnetic *R*esonance (NMR) measurements indicate that the ordering process in $CsNiCl_3$ and $CsNiBr_3$ develops in two stages[136]. Firstly the z component of the spins begin to order at T_{N1}, followed at a lower temperature by the xy component at T_{N2}. This z component can be observed in the area $T_{N1} < T < T_{N2}$ at the reciprocal lattice points of Q(1/3 1/3 1) and Q(2/3 2/3 1), where the critical exponent is found to be $\beta = 0.30$. It can be seen from the sublattice magnetisation scans above, that the scattering profile from the (1/3 1/3 3) peak shows a great deal of diffuse scattering throughout the temperature range in which we have measured. As has been stated, no long range order contribution at T_{N1} can be distinguished, however this is comparable to observations made on the similar system $CsMnI_3$. So the observed β at T_{N2} for $H = 0$ is much lower than any of the known values for recognised universality classes. Only the Monte Carlo calculated value by Bramwell *et al.* of $\beta = 0.23$ for a finite 2D-XY system gives a point of reference[137,138]. Looking at the magnetisation measurements one can see that at H = 2.0T and above, a sharp kink is observed in the intensity profile indicating the transition temperature. At H = 2T at, or close to, the critical point we find $\beta = 0.24$ which could indicate an $n = 3$ chiral universality class. However at higher fields β decreases again to a value of $\beta = 0.20$ which is indicative of 2D – XY system.

Subsequent measurements by Enderle *et al.* on the same system were made, where the experimental conditions allowed the magnetic field to be applied // to the c-axis. The magnetic Bragg point (1/3 1/3 3) was measured and two transition temperatures were observed up to H = 2.2T. The critical exponent was calculated to be $\beta = 0.28$ at this field which indicates an $n = 2$ or $n = 3$ chiral class. At H = 3T and 5.5T the critical exponent was found to be $\beta = 0.25$ which is in agreement with the $n = 2$ chiral class, these values are in agreement with the classes found for the α critical exponents.

The specific heat studies of Weber[139] show that the phase diagram of $CsNiCl_3$ undergoes an alteration when an oblique magnetic field is applied to the system. As can be seen from the figures below the sharp transition at the critical point with H // c is 'smeared' out when an oblique field is applied at $\theta = 13°$.

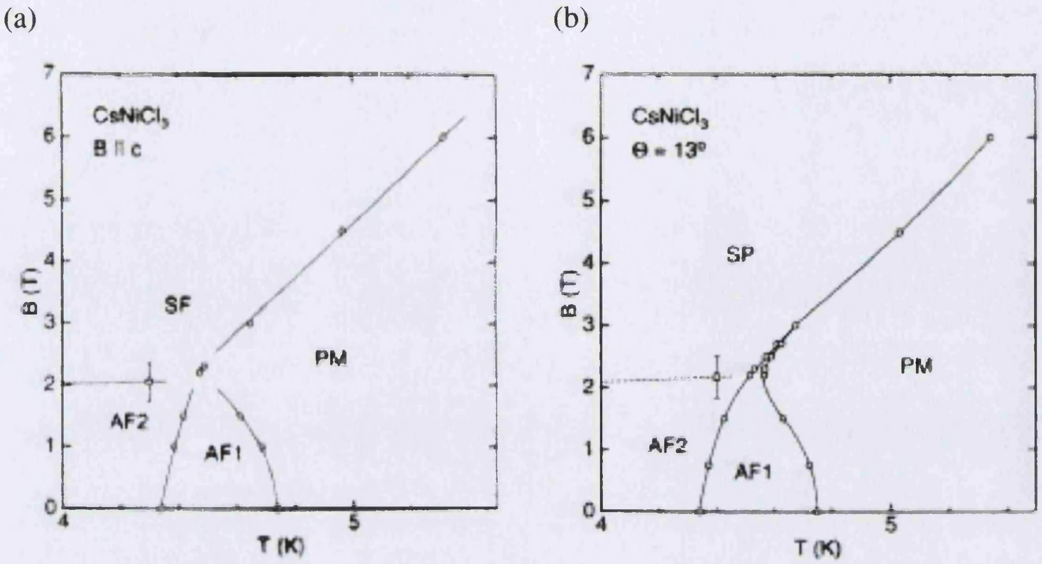

Figure 72: The effect of the application of an oblique magnetic field on the phase diagram of $CsNiCl_3$[139].

In this paper Weber shows that the critical part of the phase transition takes place at ~H = 2.2T, below this transition 2 anomalies have been observed representing the transitions T_{N1} and T_{N2} . When the field is applied at an oblique angle it can be seen that the critical point persists up to 2.7T. In this case the calculated value of the critical exponent α is lower than that of the aligned sample. The values calculated by Weber et al for α and $A^+/A^-$are given below.

Table 9: Critical parameter of $CsNiCl_3$ for different field directions[139].

	Θ = 0°		Θ = 13°	
B(T)	α	A^+/A^-	α	A^+/A^-
0 (T_{N1})	-0.05 (8)	1.21 (50)		
0 (T_{N2})	-0.06 (10)	1.18 (30)		
2.3	0.25 (8)	0.52 (10)		
3	0.29 (8)	0.39 (12)	0.25 (7)	0.47 (10)
4.5	0.31 (8)	0.38 (10)	0.29(9)	0.39(10)
6	0.37(8)	0.30 (11)	0.37 (6)	0.38 (11)

Weber shows that the magnetocaloric effect for the field applied at 13° indicating the first order phase transition around 2T is no longer a sharp transition, rather it has been smeared out. Even for B // *c* it is not clear if the transition is first order as no hysteresis effect has been observed. Enderle quotes 0.23T for the width of the spinflop transition where B // *c*. This compares to our value of 0.5T, which is observable below in Figure 73. The clear onset to the transition can be seen at 1.5T ending towards 2.2T. It is seen that the intensity of the Q(1/3 1/3 3) magnetic Bragg peak is a factor of 2 different in the two structure types. This phase diagram where B is applied at an oblique angle of 4° shows that transition takes place at around 2.0T – 2.2T.

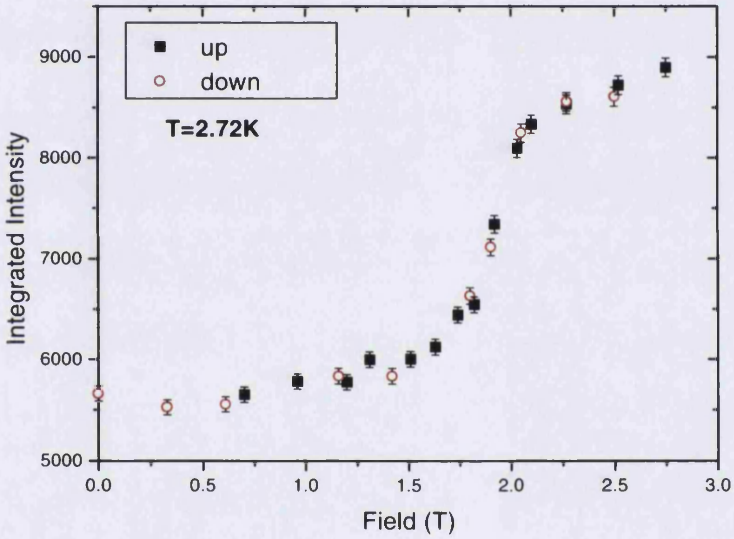

Figure 73: Spinflop Transition of $CsNiCl_3$ with magnetic field applied at 4° off-parallel to the *c*-axis.

The observed values of β follow the same trend as those found by Weber for the misaligned sample. Our values of β are lower than the predicted values and lower than the measured values of Enderle, where B // *c*. Thus we should not look at the exponent β as a real value for the system but rather an *effective* exponent of the system.

4.2.2 Diffuse Magnetic Scattering from $CsNiCl_3$ around the transition point.

The results above led us to question the nature of the ordering in $CsNiCl_3$. What is obvious from study of the sublattice magnetisation scans above is that there is a great deal of diffuse magnetic scattering around the transition point T_N. The diffuse magnetic scattering seems to remain for $T > 2T_N$. The pre-ordering process in a quasi 1-D system shows planes of magnetic scattering along the *c*-axis. The onset of 3-D magnetic ordering may be seen by modulation of the magnetic intensity in these sheets. However in $CsMnBr_3$ part of the magnetic scattering intensity starts to condense in the hexagonal planes l = 1, 3, 5 etc. perpendicular to the *c*-axis. Zaliznyak[140], showed the extent of the diffuse scattering along the [110] directions for $T>T_N$. In order to fully characterise this diffuse scattering it is necessary to use the diffractometer E2, at the HMI, Berlin. This diffractometer is based on a modified Weissenberg technique and more information about this technique and diffractometer can be found in Chapter 3.2.3. A full characterisation of the magnetic ordering of $CsNiCl_3$ in the [*hh*l] plane around the transition point was undertaken. Sweeps across approximately 65°-70° of reciprocal space were made at temperatures of T = 1.68K, 3.60K, 4.64K, 5.02K, 7.47K and 10.60K. These scans were expanded by symmetry into 360° 'sections' and are shown below. In the 10.60K slice we can still see diffuse scattering in the *ab* plane. It takes the form of a triangular structure which builds up around the magnetic Bragg points situated along the A – H line of the Brillouin zone. As the temperature is lowered the scattering becomes less diffuse and begins to concentrate around the magnetic Bragg points ($h/3$ $h/3$ 1). The diffuse scattering slowly disappears as the moment builds up, however even at T = 1.68K there is still diffuse scattering present in the system, in the same form as that at higher temperatures. It has to be noted that in a quasi one-dimensional system only half the magnetic moment is observable, the other 50% is accounted for by the quantum fluctuations of the system[141].

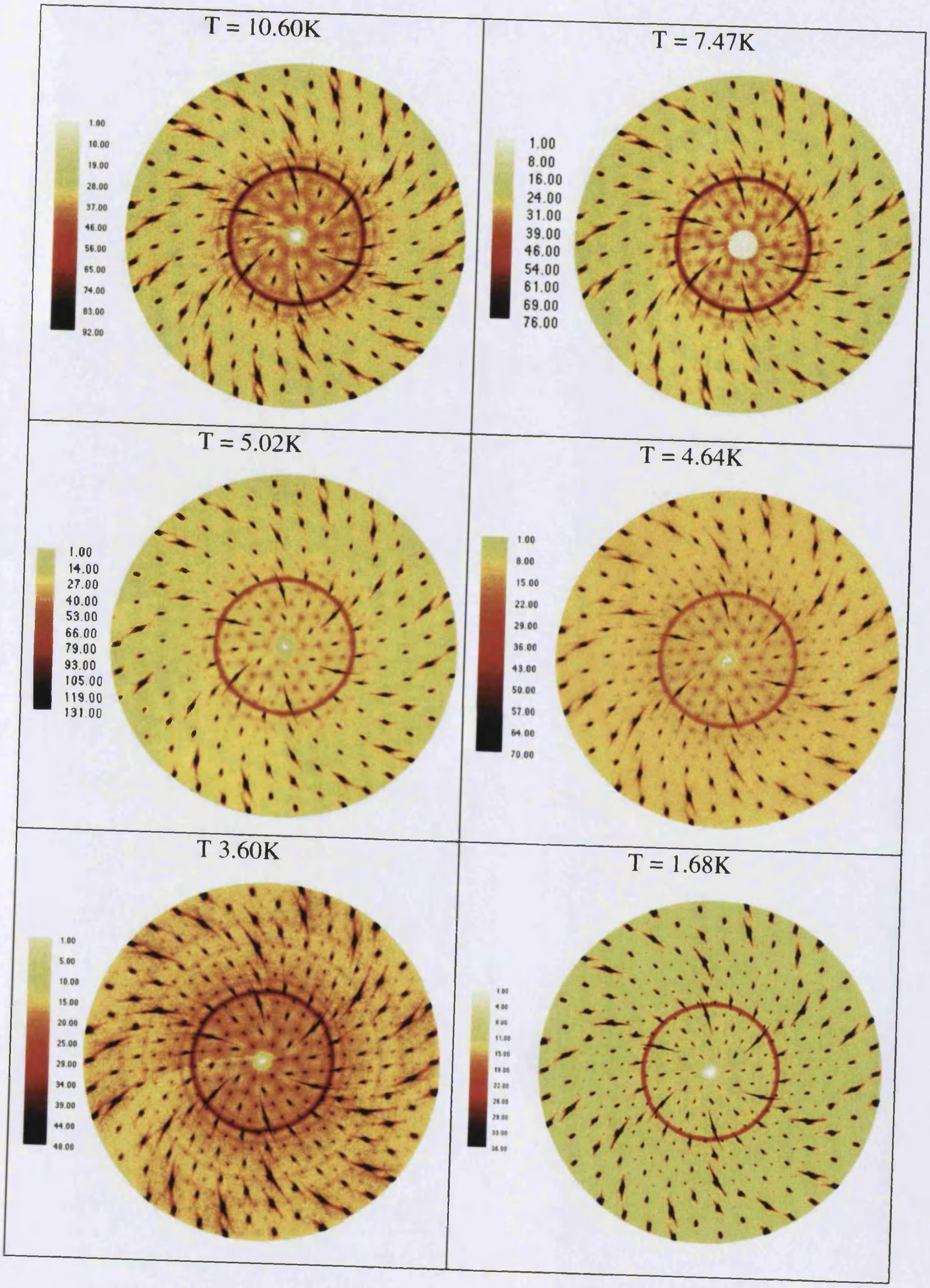

Figure 74: Diffuse magnetic scattering from $CsNiCl_3$ at various temperatures around the transition temperature (false colour image with plan view).

The dark band present in each dataset above is the background scattering as a result of using Al foil of too high a grade (i.e. too thick) to protect the sample. The increase in the intensity of the Bragg peaks is demonstrated more clearly in the graphs below for T = 1.68K, 3.60K and 4.64K for (a), (b) and (c) respectively.

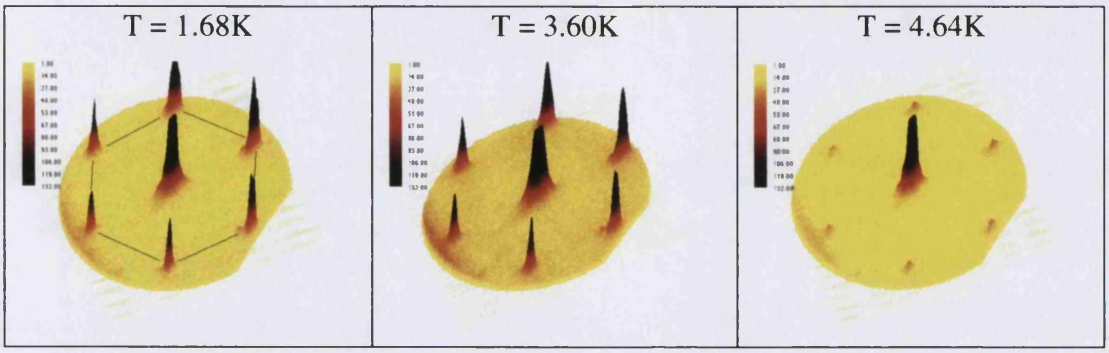

Figure 75: Decreasing magnetic scattering from CsNiCl$_3$ with increasing temperature around the transition point (false colour image with plane view).

The scattering along the [110] direction can be analysed in order to obtain the correlation length in the *ab* plane (interchain). The data was analysed using a package called NIH image, an Apple Macintosh image analysis freeware program from the National Institute of Health and the Windows ported version, Scion Image. The software allowed us to take 'vertical slices' through the data, enabling us to observe the increasing diffuse magnetic scattering around the transition point. Several cross sections were taken across many of the different Bragg peaks, the paths taken as shown below.

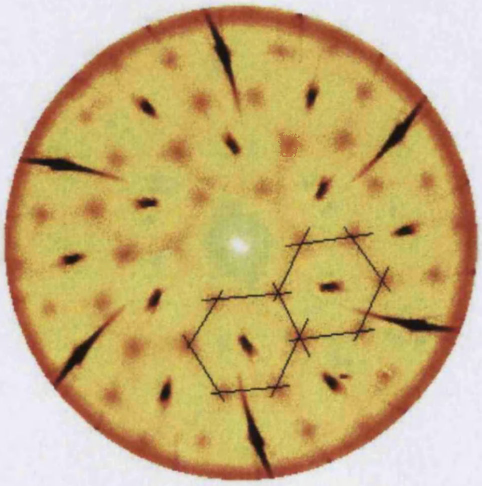

Figure 76: Typical paths (black lines) taken for data analysis purposes, shown here for the 5.02K data set.

Each peak was fitted to a Gaussian lineshape and the average half width of the peaks measured enabled us to determine the correlation length of the system at the given temperature. We assume that the line width at T = 1.68K was identical to the resolution of the instrument. Sample cross section data from the various temperatures is given below for illustrative purposes.

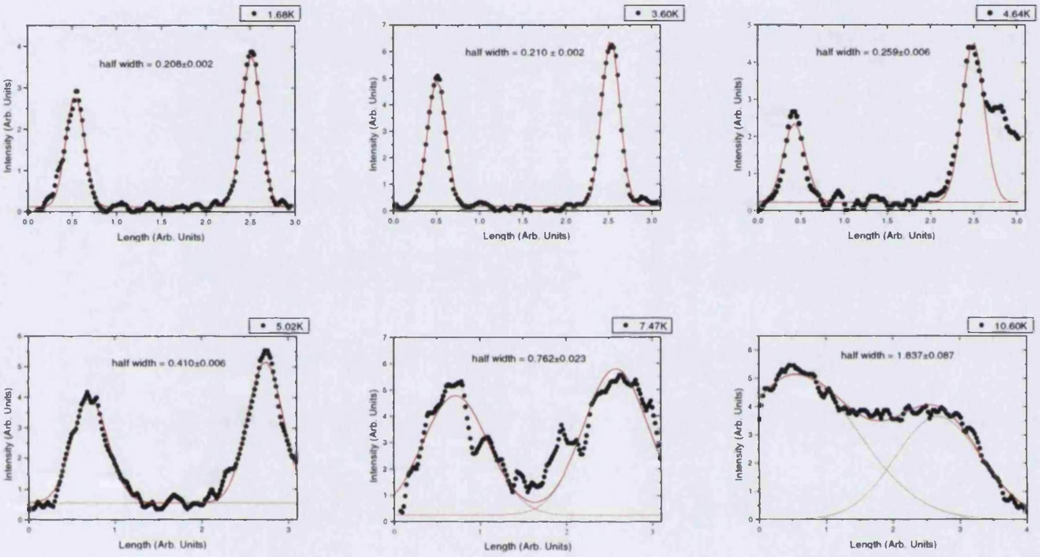

Figure 77: Typical results for the scan lines in Figure 76 showing the decreasing correlation length of CsNiCl$_3$ with increasing temperature

The fitted peaks are constrained to be equal in width in each plot and as can be seen the half width of the magnetic Bragg peak increases with increasing temperature, demonstrating the decrease in planar correlation length. The fitted data was collated and averaged for the different temperatures and is shown below.

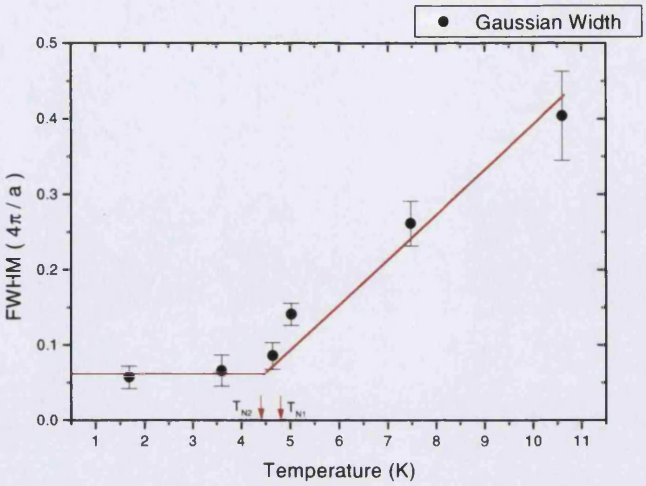

Figure 78: Gaussian half width of the magnetic excitations of CsNiCl$_3$.

Figure 78 shows the temperature dependence of the full width half maximum of the reflections along the [110] direction in units of $4\pi/a$. The corresponding correlation length, ξ, above T_{N2} is $\xi \sim 14.25$Å which decreases in a linear fashion to about $\xi \sim 2.5$Å at T = 11K. These values correspond well with data obtained by Zaliznyak *et al.*[140] from Triple Axis data. These measurements show clearly that a large part of the spin fluctuations condense in the basal plane at temperatures even larger than $2T_N$.

4.3 $RbNiCl_3$ (4F1)

As with the isostructural compound, $CsNiCl_3$ and as discussed in Chapter 2.2.1, $RbNiCl_3$ is a triangular lattice antiferromagnet with easy axis anisotropy. However, until recently $RbNiCl_3$ was found to exhibit only one observable phase transition at around 11K[142-144]. It was not until the sublattice measurements of Oohara *et al.*[145] that two successive phase transitions were resolved at T_{N1} = 11.25K and T_{N2} = 11.11K. The values of the critical exponents of the parallel and perpendicular sublattice moments were found to be $\beta_{//} = 0.27 \pm 0.01$ and $\beta_{\perp} = 0.28 \pm 0.01$. The $\beta_{//}$ and $\beta_{\perp}$ values were extracted from the intensity of the Q(1/3 1/3 1) and Q(2/3 2/3 1) magnetic reflections by dividing the intensity up into contributions of the <*xy*> and <*z*> component, respectively. These values did not conform to the values predicted by Kawamura *et al.*[67] who predicted that the transitions would be governed by the 3D – XY symmetry, giving a critical exponent of β = 0.345. It was thought that the discrepancy could be resolved by assuming a crossover behaviour in the system. Because $RbNiCl_3$ has a very small Ising anisotropy one could naively treat the system as an isotropic Heisenberg one. In this type of system the critical behaviour at temperatures far from the transition points is governed by the 3D – SO(3) symmetry. However, in the region close to the phase boundary the system will be governed by the 3D – XY symmetry, thus between these two regions a crossover effect will take place and the value of the critical exponent β will be modified accordingly.

Oohara *et al.*[145] also mentioned that $RbNiCl_3$ could exhibit another crossover effect. The Ising anisotropy confines the 120° type spin structure to the *ac*-plane and deforms it through competition with the interchain exchange interaction *J'*. In Ising like triangular lattice antiferromagnets with easy axis anisotropy which do not have a deformation of the 120° type spin structure the successive phase transitions coalesce and a new criticality of the chiral ordering characterised by 3D – $S_1 \times S_1$ symmetry will occur. Thus, because the anisotropy in $RbNiCl_3$ is very small the crossover effect from the 3D – $S_1 \times S_1$ symmetry to the 3D – XY symmetry may be observed. Further measurements on the system by Oohara *et al.*[146], using birefringence, add weight to this hypothesis.

It is known that the application of hydrostatic pressure on the triangular antiferromagnet lattice compounds will not only distort the physical structure of the system, but also modify the strength of the single ion anisotropy (*D*) and the interchain (*J*) and intrachain (*J'*) exchange energies (as demonstrated for the Singlet Ground State systems $CsFeCl_3$ and $CsFeBr_3$ in Chapter 5.1.1). Thus, by applying pressure to the system one may be able to change, and in an ideal case tune, the parameters of *D*, *J* and *J'*.

With this in mind an elastic neutron scattering experiment was undertaken on $RbNiCl_3$, using the TAS, 4F1 at the LLB, Saclay in order to establish the effect of hydrostatic pressure on the system.

4.3.1 Elastic Scattering on $RbNiCl_3$ under the Presence of Hydrostatic Pressure.

The measurement of the sublattice magnetisation was undertaken on the TAS, 4F1 at the LLB, Saclay. A $1cm^3$ single crystal, grown by Bridgeman technique and having a mosaic width of 0.3° was mounted in a He-pressure cell, which was itself mounted in a modified 'Orange' cryostat. The system was pressurised and then cooled to T=1.5K. The process of pressurising at room temperature and cooling to 1.5K takes about 7 hours, the majority of this time is used in cooling the mass of the pressure cell. The sample was mounted, as is the case with most measurements we have performed, with the [110]-[001] plane in the scattering plane of the instrument. The optimised lattice parameters for the system with 5kbar applied hydrostatic pressure were calculated to be $a = 6.8370Å$ and $c = 5.7787Å$.

The resolution ellipsoid of the spectrometer combined with the focussing analyser used, made the magnetic Bragg point Q(1/3 1/3 –1) the most favourable for measurements of the sublattice magnetisation. Scans were taken across the magnetic Bragg point for temperatures in the range 4.00K → 17.00K and the sublattice magnetisation can be seen below in Figure 79. The critical exponent β was determined from the slope of the log of the integrated intensity versus the log of the reduced temperature, shown adjacent to the sublattice magnetisation.

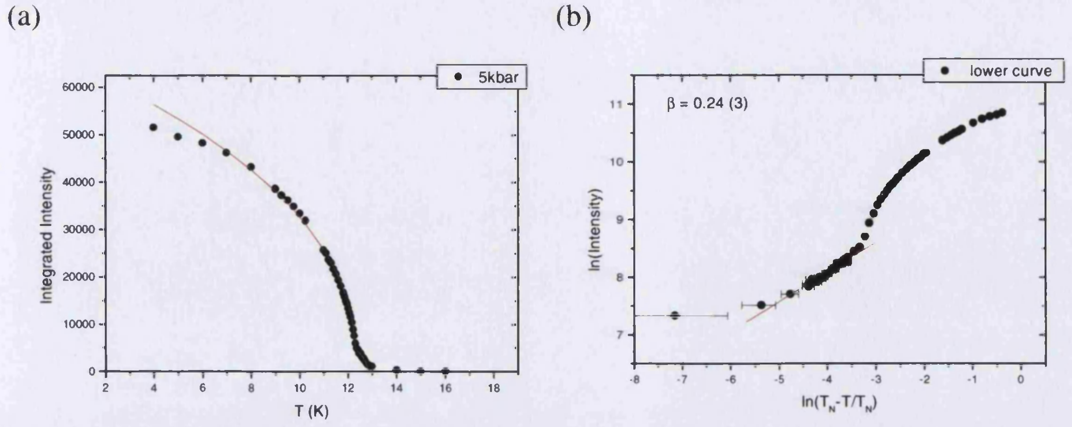

Figure 79: Sublattice magnetisation of $RbNiCl_3$ at Q(1/3 1/3 -1) with P = 5kbar, (lines are best fit to power law $A\varepsilon^{2\beta}$ with $\beta_{TN1} = 0.245(10)$ and $\beta_{TN2} = 0.24(2)$).

With an applied hydrostatic pressure of $P = 5.0$kbar the two transitions in $RbNiCl_3$ are observed at $T_{N1} = 12.37 \pm 0.01$ and $T_{N2} = 12.81 \pm 0.04$ with corresponding critical exponents of $\beta_{TN1} = 0.245 \pm 0.01$, and $\beta_{TN2} = 0.24 \pm 0.1$ respectively. The value of these critical exponents correspond to the predicted values for the chiral $n = 2$ universality class.

Yelon and Cox[143] found that $\beta = 0.25$ at ambient pressure for $T_N = 11.11$K rising to a value of $\beta = 0.30$ when a transition temperature of $T_N = 11.15$K was taken for the calculation of the critical exponent. Due to the fact that they only observed 1 transition their fit should compare to our fit of the sublattice magnetisation as given in Figure 79a, where T_{N2} is the ordering temperature and the intensity of the magnetic scattering at T_{N2} is taken to be the background level. We observed that the ratio of $(T_{N1} - T_{N2})/T_{N1}$ increased from the value found by Oohara of 0.012 at ambient pressure to 0.034 at 5kbar. From inelastic neutron scattering measurements performed by the author (Appendix A), it is obvious that the values of D, J and J' in $RbNiCl_3$ change upon the application of 5kbar hydrostatic pressure. Thus, a slightly distorted magnetic structure will be adopted by the system. The measurements of Oohara and those from the present experiment suggest that the exponent of β measured at T_{N1}, which is related to the freezing of the z-component of the spin, but which leaves the xy-component disordered in the xy-plane, may represent an effective β for a 'partially chiral' spin system. The influence of pressure manifests itself in the 'opening up' of the intermediate phase by an effective change of D, J and J' which changes β from 0.28 → 0.25. For a comparable magnetic system, $CsNiCl_3$, the magnetic order parameter, $\beta = 0.30$ at T_{N1} and the ratio $(T_{N1} - T_{N2})/T_{N1} = 0.09$.

4.4 TlFeCl$_3$

As was suggested in Chapter 2.2.3, the hexagonal perovskite TlFeCl$_3$ is an induced magnetic moment system. Due to the large positive single-ion anisotropy, D, in this type of system, the magnetic moments lie in the hexagonal basal plane. Therefore, the triangular arrangement of the magnetic moments in the basal plane make this material a candidate for chiral magnetic ordering. Previous work by McIntyre and Visser[147] has shown that the system undergoes two structural phase transitions, at 179K where the space group changes from P6$_3$/mmc to P6$_3$cm structure and at 79K where a further structural transition takes place in which the disorder of the P6$_3$cm structure is removed.

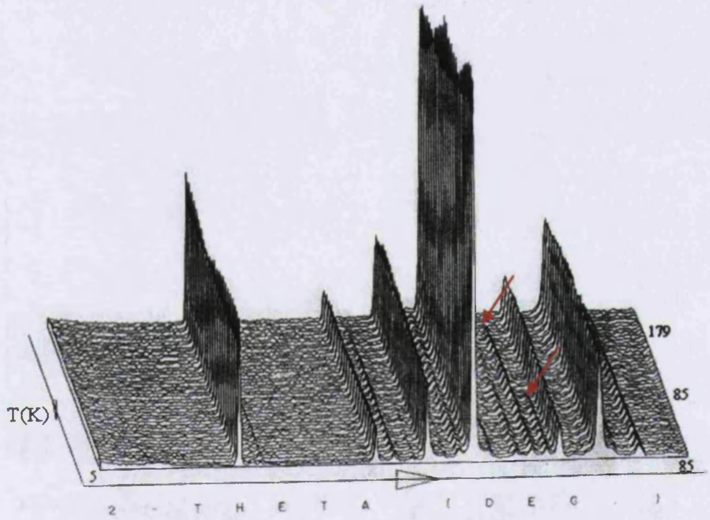

Figure 80: Structural phase transition of TlFeCl$_3$ with decreasing temperature, Visser *et al.*[147]

Medium resolution powder neutron diffraction studies at T =5K showed no indication the 79K phase transition. However, this transition can be observed in a thermo-diffractogram of TlFeCl$_3$ taken on the medium resolution powder diffractometer D1B, at the ILL, Grenoble. However, the quality of this data is quite poor, the number of observed extra peaks very limited and their intensities are low. Thus with the available data it has been impossible to characterise the structure of the lowest temperature phase. It has been shown by the present author that TlFeCl$_3$ orders with an incommensurate magnetic structure at T$_N$ = 2K and that the application of a hydrostatic pressure of 5kbar increases T_N dramatically[148], at this pressure the magnetic ordering is seen to take place in two stages. However, the character of the magnetic phase transition could not be determined from these measurements. The transitions may be related to a possible change in the crystal structure.

4.4.1 Structural Characterisation of $TlFeCl_3$.

In order to obtain more precise information about the crystallographic structure of $TlFeCl_3$ under pressure and at low temperature, a further characterisation of the system was undertaken using the high resolution powder diffractometer, HRPD, at the ISIS facility, Oxford. The situation of the diffractometer at the end of a 100m beam line makes it one of the highest resolution diffractometers in the world and further information is given in Chapter 3.2.2.1.

A 5g powder sample of $TlFeCl_3$ was prepared by grinding up several single crystals of this material. The powder was loaded in a He pressure cell which was itself inserted in a modified Orange cryostat. Such a setup should have allowed us obtain applied pressures of up to 5kbar at temperatures approaching 2K. Unfortunately due to safety requirements the maximum pressure allowed for the cell was of the order of 3.5kbar at a temperature of 5K. Two powder diffraction patterns were taken at ambient and applied pressure. Each pattern took approximately 12 hours to collect using the 90° detector bank and the collected raw data were firstly normalised, then corrected for absorption. The treated diffraction patterns were refined using the Rietveld method outlined in Chapter 3.2.2. The ISIS facility utilises the Cambridge Crystallographic Subroutine Library (CCSL)[149] in conjunction with the graphics and data handling package GENIE[150] to refine the data. The library and data analysis package have both been developed at the ISIS facility specifically for the analysis of diffraction data from Time Of Flight (TOF) diffractometers. The Rietveld refinement for ambient, $P = 0$kbar, and $P = 3.5$kbar at $T = 5$K are shown below.

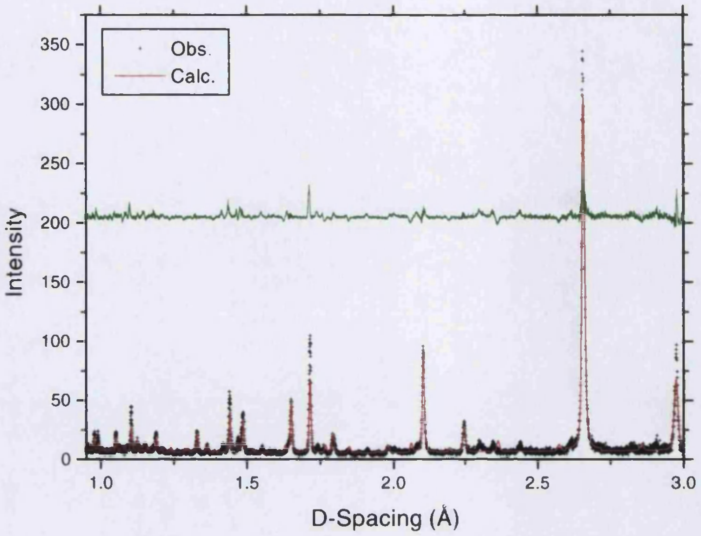

Figure 81: Observed, Calculated and Difference plot for $TlFeCl_3$ at P = 0kbar and T = 5K.

The diffraction pattern could be indexed on the *a√3 x a√3 x c* unit cell. The data at ambient pressure with T = 5K were fitted to a model with space group $P6_3cm$, resembling the room temperature structure of the $KNiCl_3$ phase. As can be seen this gives a reasonable agreement with the observed data. However, some systematic deviations remain. The calculated peaks are consistently less intense than those observed, also a small number of peaks have not been accounted for by the model.

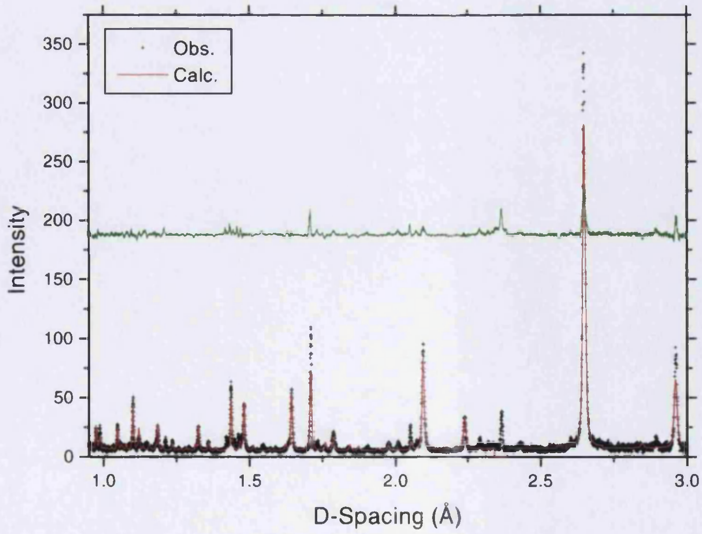

Figure 82: Observed, Calculated and Difference plot for $TlFeCl_3$ at P = 3.5kbar and T = 5K.

The data at P = 3.5kbar did not shown any major deviations from the ambient pressure data and was fitted to the same model. Again, the calculated intensities are systematically lower than the observed intensities. Several observed peaks have not been accounted for by the model, however these peaks may well be anomalous scattering from grains in the pressure cell. What is clear when we superimpose the two data sets, as below, is that there is no structural phase change between the ambient and 3.5kbar data. The only effect the pressure exerts on the system is the reduction of the unit cell of the system and a slight change in the structural parameters. The final tabulated values for $TlFeCl_3$ are collated and given below in Table 10.

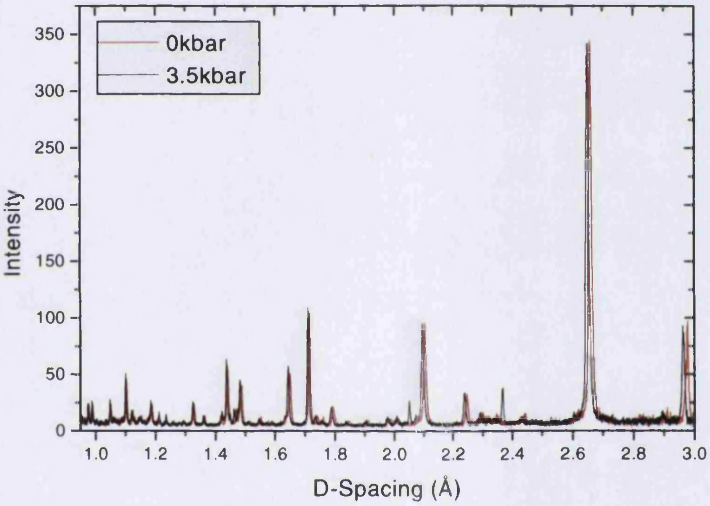

Figure 83: Difference in the observed powder diffraction pattern of $TlFeCl_3$ at ambient and 3.5kbar applied pressure.

Table 10: Structural parameters for the distorted triangular lattice antiferromagnet $TlFeCl_3$ at ambient and applied pressure.

	0 kbar			3.5 kbar		
	a	*b*	*c*	*a*	*b*	*c*
Unit cell	11.9680(1)	11.9680(1)	5.9968(1)	11.9355(1)	11.9355(1)	5.9695(1)
Tl	0.3309(13)	0.3309(13)	0.2849(42)	0.3312(11)	0.3312(11)	0.2936(35)
Fe(1)	0	0	0	0	0	0
Fe(2)	1/3	2/3	0.0560(42)	1/3	2/3	0.0642(36)
Cl(1)	0.1701	0	0.1974	0.1653(13)	0	0.2035(28)
Cl(2)	0.5032(8)	0.1667(10)	0.2589(19)	0.5024(8)	0.1594(6)	0.2661(24)

The fact that the system did not undergo a phase transition at 3.5kbar was rather interesting, as we had expected an applied pressure of this amount to have an effect on the distorted phase. It could be the case that any change in the system under pressure could not be observed using a powder diffraction technique. However, the experiment did demonstrate that any subsequent measurements to be undertaken on this system would have to be done at higher pressures to allow us the opportunity to fully establish the structural phase diagram of $TlFeCl_3$. The present high resolution data and its subsequent refinement show that it will be very difficult to obtain the low temperature phase with powder diffraction measurements. The presently deformed structure should be regarded as an 'averaged' structure. The changes from the $\beta \rightarrow \gamma$ phase must be very small and may only be obtained from single crystal diffraction data.

Recently it was shown by Visser *et al.*[151] using a Laue neutron diffraction technique that the unit cell of the γ - phase of $TlCoCl_3$ has a unit cell of size *4a x 4a x c*. The extra diffraction due to this unit cell is only visible at high Q for the layers ≥ 1. In view of this fact an experiment was carried out on the single crystal diffractometer D15, at the ILL, Grenoble in ambient and applied pressure environments.

The experiment was performed with a small single crystal (*4 x 4 x 4*mm) of $TlFeCl_3$ with the [001] – [110] plane in horizontal scattering plane. This allowed us to accurately determine the effects of the application of pressure on the lattice parameters. A hydrostatic pressure of 5.0kbar could be applied using a standard He pressure cell, Chapter 3.3.3 provides more information on this cell. The $P - T$ phase diagram was determined by scanning along a line of reciprocal space from the reciprocal lattice point Q(-4.85 –1.3 2) → Q(-4.55 –1.9 2) for various pressures up to 5kbar. Scanning this area allowed us to observe the appearance/disappearance of both the Q(1/3 1/3 0) type reflection associated with the β-phase and Q(1/4 1/2 0) type reflection associated with the γ-phase. The figures below give an example of the typical results obtained for the experiment.

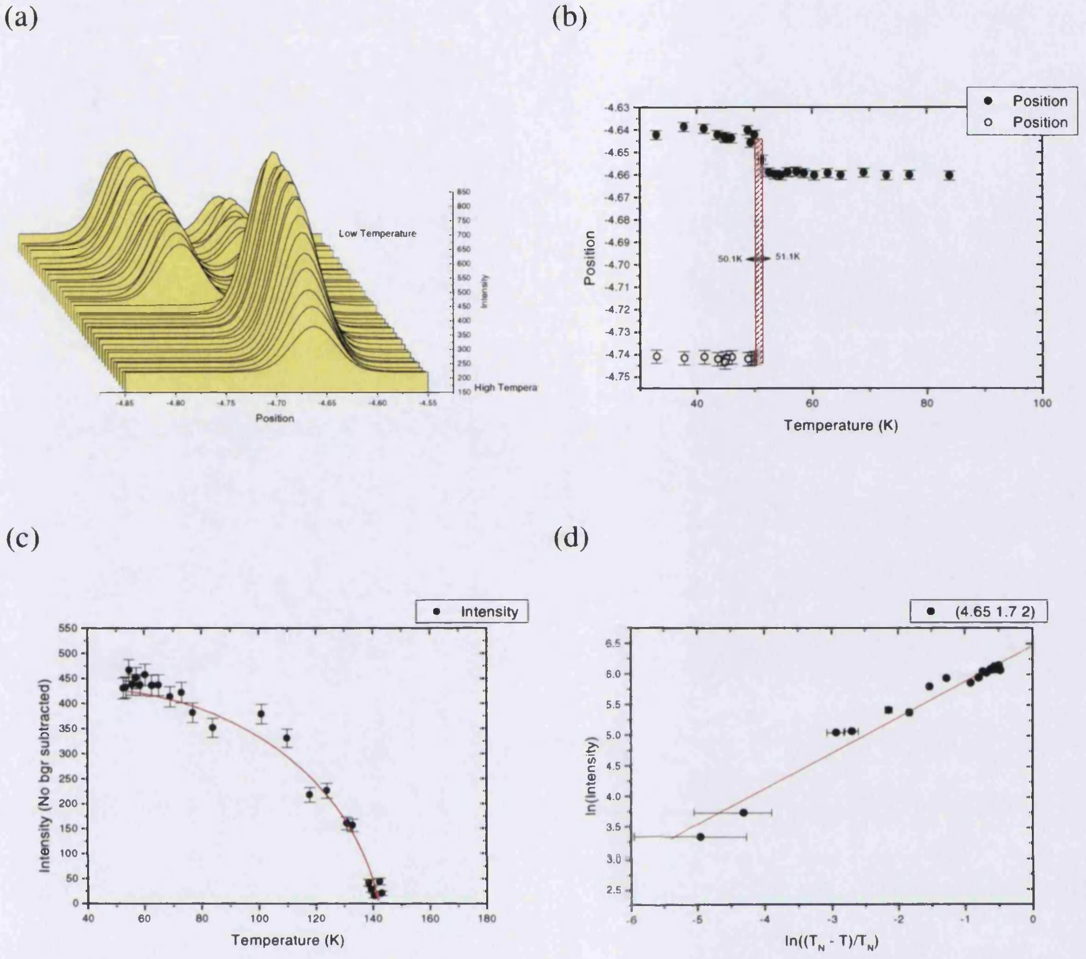

Figure 84: (a), (b) (c) and (d) show the structural phase transitions of TlFeCl$_3$, from space group P6$_3$/mmc → P6$_3$cm → unit cell *4a x 4a x c*, P = 4.0kbar.

Figure 84 (a) shows a waterfall plot of the scans taken across the structural Bragg peak (-4.667, -1.667, 2) at 4.0kbar. The plot clearly shows the structural phase transition from space group P6$_3$/mmc, at high temperature → P6$_3$cm → unit cell *4a x 4a x c*. The structural peaks were fitted to Gaussian lineshapes and it is the resultant fits that are shown in (a). Figure 84(b) shows the changing position of the Bragg peak between the space group P6$_3$cm and unit cell *4a x 4a x c* at $T_{Transition} = 50.6 \pm 0.5$K. Figure 84(c) shows the transition between space group P6$_3$/mmc and P6$_3$cm at $T_{Transition} = 141 \pm 1$K. The second order characteristics of the α - β transition is can be seen from (c), the log – log plot given in (d) shows that the critical exponent $\beta = 0.29$, a similar value to that found for RbVBr$_3$ [152]. The transition of the $\beta \rightarrow \gamma$ phase is more first order like, the region of transition being $\Delta T < 1K$, this being in strong contrast to the transition observed in similar system, $KNiCl_3$ of $\Delta T = 15K$[153].

Similar measurements to the above were taken at P = 0, 1.75, 2,2, 3,2, 4.0 and 5.0kbar. A $P - T$ phase diagram was constructed using the results of these measurements and is shown below.

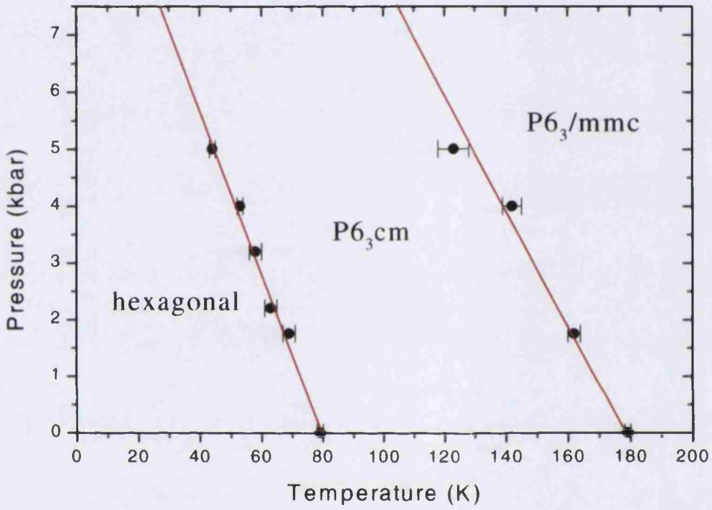

Figure 85: The structural phase diagram of $TlFeCl_3$ (lines are just guides to the eye).

It is seen that a linear dependence seems to characterise the structural phase boundaries. The α-β phase boundary has a slope ($\Delta P/\Delta T$) = -0.1435 kbar/K, and the β-γ phase boundary has a slope ($\Delta P/\Delta T$) = -0.088 kbar/K.The powder diffraction data presented and discussed earlier is now rationalised.

4.4.2 Magnetic Characterisation of $TlFeCl_3$.

The distorted triangular lattice antiferromagnet $TlFeCl_3$ orders magnetically at T_N = 2.00(5)K. Data taken by the author on the TAS, 4F1, at the LLB, Saclay shows magnetic scattering at the reciprocal lattice point Q(1/3 1/3 0). This is indicative of a

120° type magnetic ordering along the *c*-direction. This is comparable to the isostructural compound $RbFeCl_3$ which also orders with a 120° type structure at T_N = 1.90(1)K.

However, two further transitions taken place in this system, at T_{N1} = 1.55(1)K and T_{N2} = 2.35(1)K. The first structure is an incommensurate helical magnetic structure (IC_1), with $\vec{k} = (1/3 + \delta,\ 1/3 + \delta,\ 0)$. The second magnetic structure (IC_2), is sinusoidal[154]. High resolution data powder/single crystal diffraction on $TlFeCl_3$[155] shows that the magnetic structure is also slightly incommensurate with $\vec{k}$ = (0.330, 0.330, 0), adopting the IC_1 type structure.

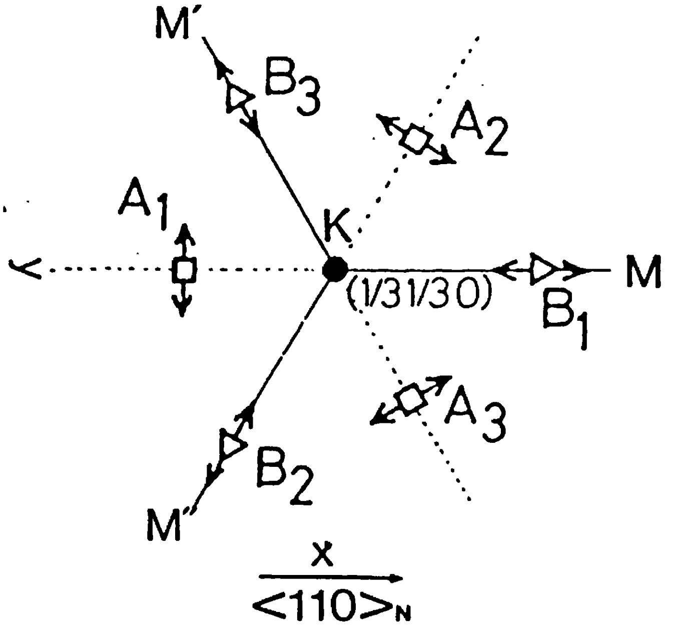

Figure 86: The position of the magnetic Bragg reflections characterising the incommensurate magnetic phases of $RbFeCl_3$[110].

As can be seen from the sublattice magnetisation plots of $TlFeCl_3$ show below, the system shows two magnetic phase transitions at P = 5kbar applied hydrostatic pressure (this data has been collected by the author and has been presented previously[148]). Due to the alignment of the crystal and to resolution limitations the characterisation of these two phases could not be completed during this experiment.

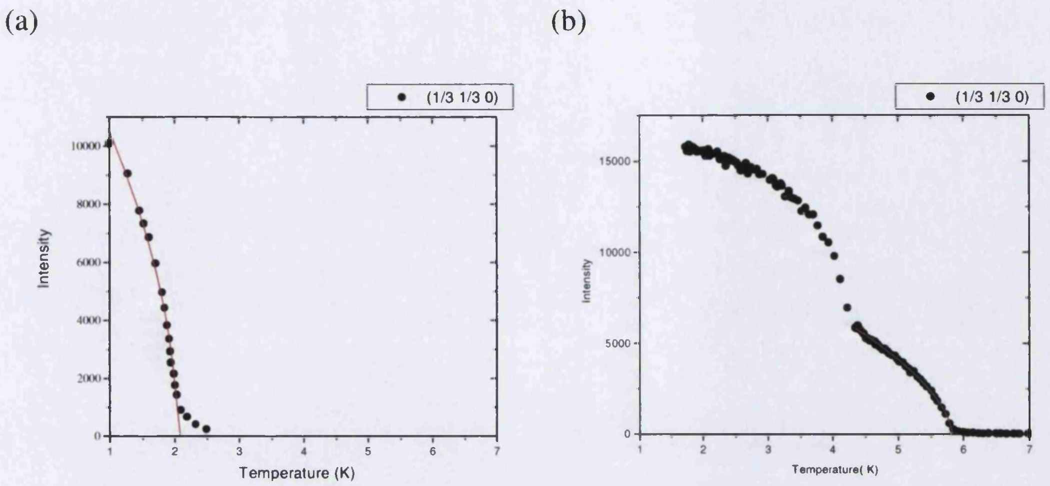

Figure 87: Sublattice magnetisation of TlFeCl$_3$ at (a) ambient pressure and (b) 5kbar applied hydrostatic pressure.(lines are best fit to power law $A\varepsilon^{2\beta}$ with β=0.28 and β=0.30 respectively).

Two scenarios are possible for the system;

- The phase is partially ordered followed by a fully ordered 120° type magnetic phase as in RbFeBr$_3$.
- The first phase is the incommensurate IC_1 as found for the ambient pressure data which locks into the 120° type magnetic ordering at T_{N2} = 4.30(5)K at 5kbar.

In order to distinguish between these two scenarios a single crystal neutron scattering experiment was performed on the diffractometer, D15, at the ILL, Grenoble. This experiment was carried out in conjunction with the structural determination measurements presented in the last Chapter. The magnetic phase diagram was established by scanning along the K- M line from Q(-0.283, -0.383, 0) → Q(-0.383, -0.283, 0). A schematic of the scan path taken, is shown below.

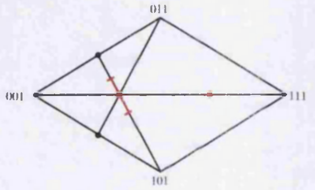

Figure 88: Scan path for the sublattice magnetisation measurements for TlFeCl$_3$.

An example of the typical data obtained is shown below in Figure 89 for an applied hydrostatic pressure of P = 3.2kbar. Scans of the same nature as these were obtained for applied hydrostatic pressures at P = ambient, 1.20kbar, 2.20kbar, 2.70kbar, 4.0kbar and 5.0kbar. The datasets were obtained with both increasing and decreasing temperatures in order to observe any hysteresis that may be present. From the data a small temperature hysteresis of approximately 1K is observed for the magnetic phase transitions.

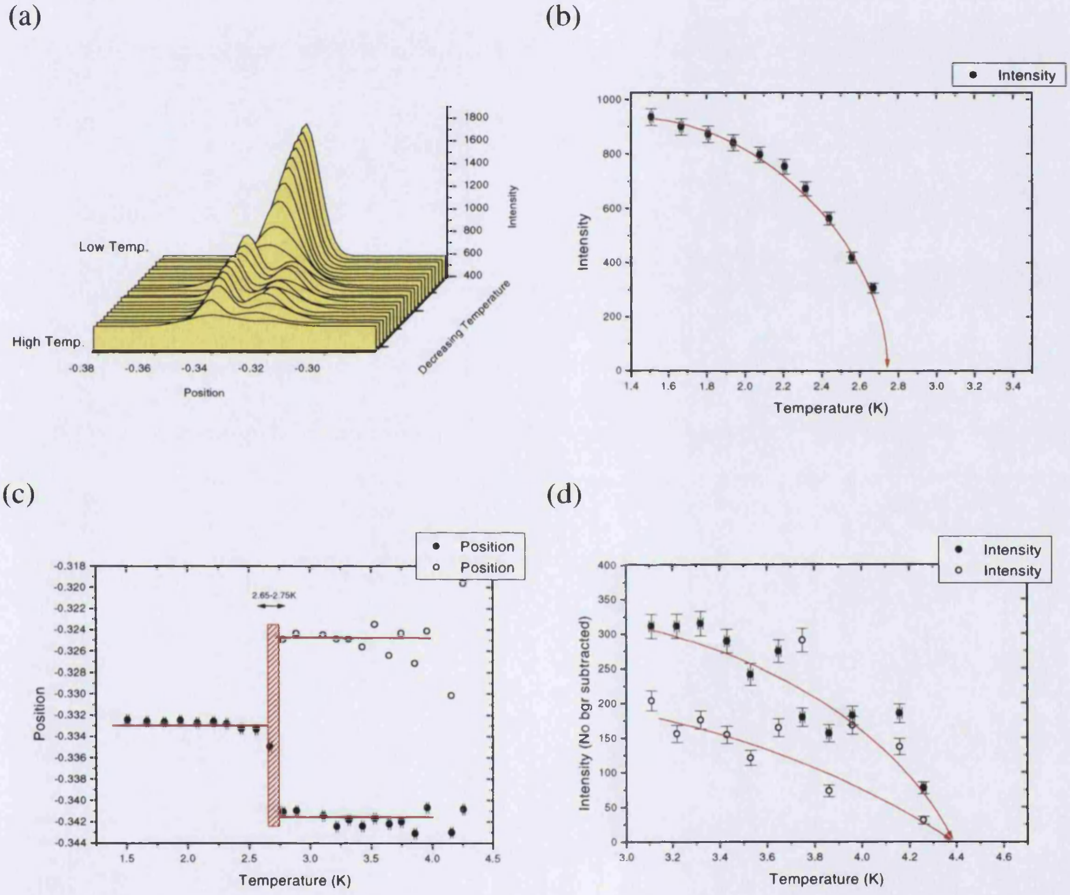

Figure 89: (a), (b) (c) and (d) show the magnetic phase transitions of $TlFeCl_3$, from the low temperature 120° type structure → incommensurate → paramagnetic, P = 3.2kbar.

Figure 89 (a) shows a waterfall plot of the scans taken across the magnetic Bragg peak (-1/3 –1/3 0) at 3.2kar. The plot clearly shows the magnetic phase transition from paramagnetic, at high temperature → incommensurate → 120° type structure. The magnetic peaks were fitted to Gaussian lineshapes and it is the resultant lines that are shown in (a). Figure 89 (b) shows the sublattice magnetisation measurements giving a $T_{Transition} = 2.7 \pm 0.1$K. Figure 89 (c) shows the same phase transition in terms of the positional parameter of the peaks. Figure 89 (d) shows the transition between the incommensurate magnetic structure and the paramagnetic type at $T_{Transition} = 4.4 \pm 0.1$K

The data obtained at the different pressures has been collated and is presented below in the form of a magnetic phase diagram.

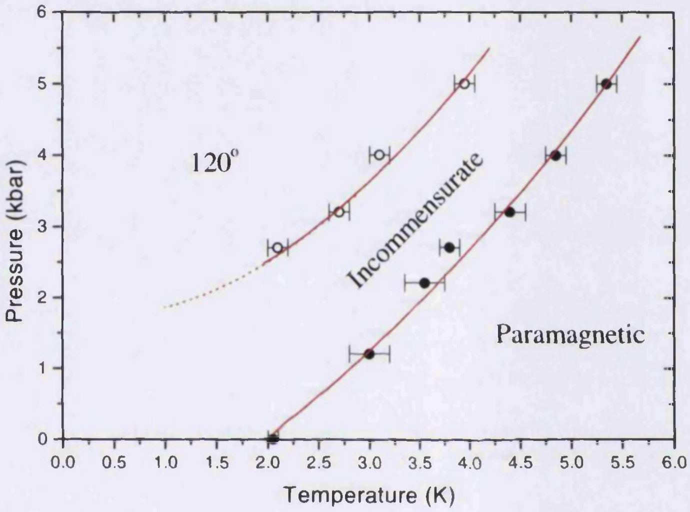

Figure 90: The magnetic phase diagram of $TlFeCl_3$, the lines are just guides to the eye.

From the experimental information we can conclude that the distorted triangular antiferromagnet $TlFeCl_3$ orders with the incommensurate IC_1 magnetic structure. The value of the critical exponent, β, observed at the transition point corresponds to a $n = 3$ chiral universality class. At higher pressures the balance in the superexchange and the magnetic dipolar forces moves the ordering towards 120° type.

4.5 $KNiCl_3$ (4F2 - LLB)

$KNiCl_3$ is a distorted triangular lattice antiferromagnet with two low temperature magnetic phases. Petrenko *et al.*[76] first reported that in different crystals of $KNiCl_3$ one may be able to observe the coexistence of different magnetic phases related to the β and γ - structural phase of $KNiCl_3$. In the β-phase of $KNiCl_3$, the magnetic moments order with a 120° type magnetic structure at $T_N = 12.5K$, while the γ-phase shows a rearranged nuclear structure with an incommensurate magnetic structure with $T_N = 8.6K$. It seems that the heat treatment during the crystal growth is of prime importance in deciding which low temperature phase may be formed. Chemical impurities also have an important effect on the stabilization of the intermediate phase, the β-phase, as can be seen from the structural phase diagram of the mixed system $Rb_{1-x}K_xNiCl_3$[156]. It was thought that these two phases came about due to different fabrication techniques and different sample histories.

Since the sequence of structural phase transitions in $KNiCl_3$ is identical to those in the distorted triangular antiferromagnet, $TlFeCl_3$, one would expect similar magnetic critical behaviour at the Neèl point. Neutron diffraction investigations were carried out on three different crystals of $KNiCl_3$ to establish the magnetic critical behaviour around T_N. Both the pure β and pure γ-phases were measured as well as a crystal where both phases were present together. The resultant values are presented below.

4.5.1 *Mixed Phase*

The first of the group of experiments was undertaken on a small single crystal sample, in which both β and γ-phases were expected to be present. As was the case for all the experiments, the sample was mounted in a standard Orange ILL cryostat with the [110] – [001] plane in horizontal scattering plane. The optimised lattice parameters on the TAS, 4F1, at the LLB were calculated at a = 6.7343Å and c = 5.9446Å. A full measurement of the [*h h* 1] was undertaken for various temperatures from 3K to 16K in order to establish the location of the magnetic Bragg peaks. The results of these scans are collated and presented below in Figure 91.

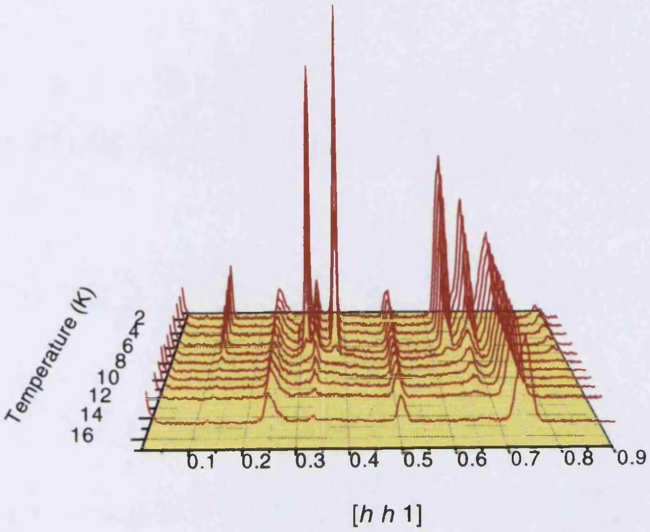

Figure 91: Temperature dependence of the magnetic Bragg peaks for the triangular antiferromagnet $KNiCl_3$ along the [*h h* 1] direction. The Bragg points at (001) and (111) have been omitted for clarity.

Magnetic Bragg peaks can be observed at the reciprocal lattice points Q(0.125 0.125 1), Q(0.31 0.31 1), Q(1/3 1/3 1), Q(0.37 0.37 1) and Q(0.628 0.628 1), Q(0.68 0.68 1) and Q(0.875 0.875 1), these are highlighted below at T =2.98K for clarity.

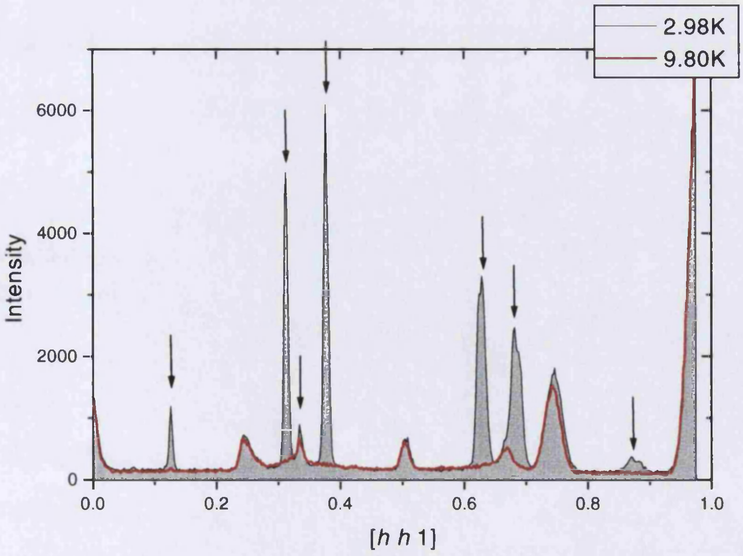

Figure 92: The magnetic (marked with arrow) and structural Bragg peaks of $KNiCl_3$ at 2.98K.

Sublattice magnetisation scans on all observable magnetic Bragg peaks at incident wavevector $k_I = 2.662$ Å^{-1} were carried out. However, time restrictions meant that we could not measure the Q(0.68 0.68 1) or the Q(0.875 0.875) peak. Each magnetic sublattice magnetization scan was recorded during a very slow temperature sweep with the detector fixed at a Q(*h* *h* 1) position. At selected temperatures a full ω–2θ scan through the magnetic Bragg reflection was made to check the validity of this method. No difference in intensity versus temperature between both methods was noted. Scans were taken for both warming and cooling of the sample in order to establish if there was any hysteresis in the sample.

According to Petrenko two types of magnetic reflections are observed, the Q(1/3 1/3 1) type reflections with $T_N = 12K$ and the Q($h/8 \pm \delta$, $h/8 \pm \delta$, l) type reflections with $\delta = 0.0183$ and $T_N = 8.6K$. The measurements of Petrenko were not of sufficient detail around the Néel points to be specific about the character of the ordering transition. The results of temperature dependence measurement of the magnetic reflection Q(1/3 1/3 1) are displayed below in Figure 93.

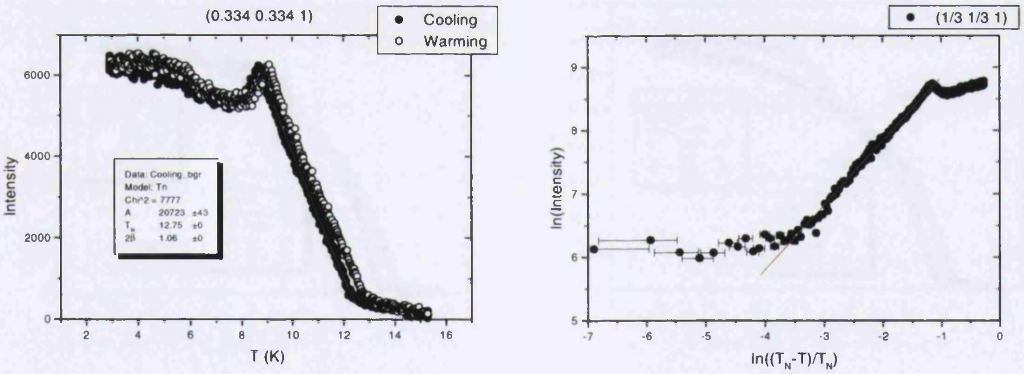

Figure 93: Sublattice magnetisation scan at Q(1/3 1/3 1), (line is best fit to power law $A\varepsilon^{2\beta}$ with β=0.545).

Sublattice magnetization measurements were taken for both warming and cooling of the sample. A hysteresis of ~0.4K was observed, indicating a possible first order transition. However, no 'jump' in intensity that would be characteristic of a first order transition is present. Therefore, this transition must have nearly a second order character. Thus a conventional analysis of the critical exponent of the sublattice magnetisation was undertaken. The average calculated value of the critical exponent was $\beta = 0.50(1)$ which is indicative of mean field behavior.

Table 11: Critical exponent β values for the triangular lattice antiferromagnet $KNiCl_3$, mixed phase.

Q		T_N	β
0.3333 0.3333 1	Cooling	8.50 ± 0.1	0.525 ± 0.025
	Warming	13.15 ± 0.1	0.475 ± 0.025

From Figure 93 it is obvious that the temperature dependant behaviour of the magnetic moment is very unusual. Around $T_N = 9.0K$ the intensity of the moment drops by about 15% which is then recovered again below 7K, at $T = 9.0K$ one also observes magnetic intensity at Q positions related to the γ-phase. The remaining sublattice magnetisation scans are presented below, a hysteresis of ~0.4K is present in these scans also.

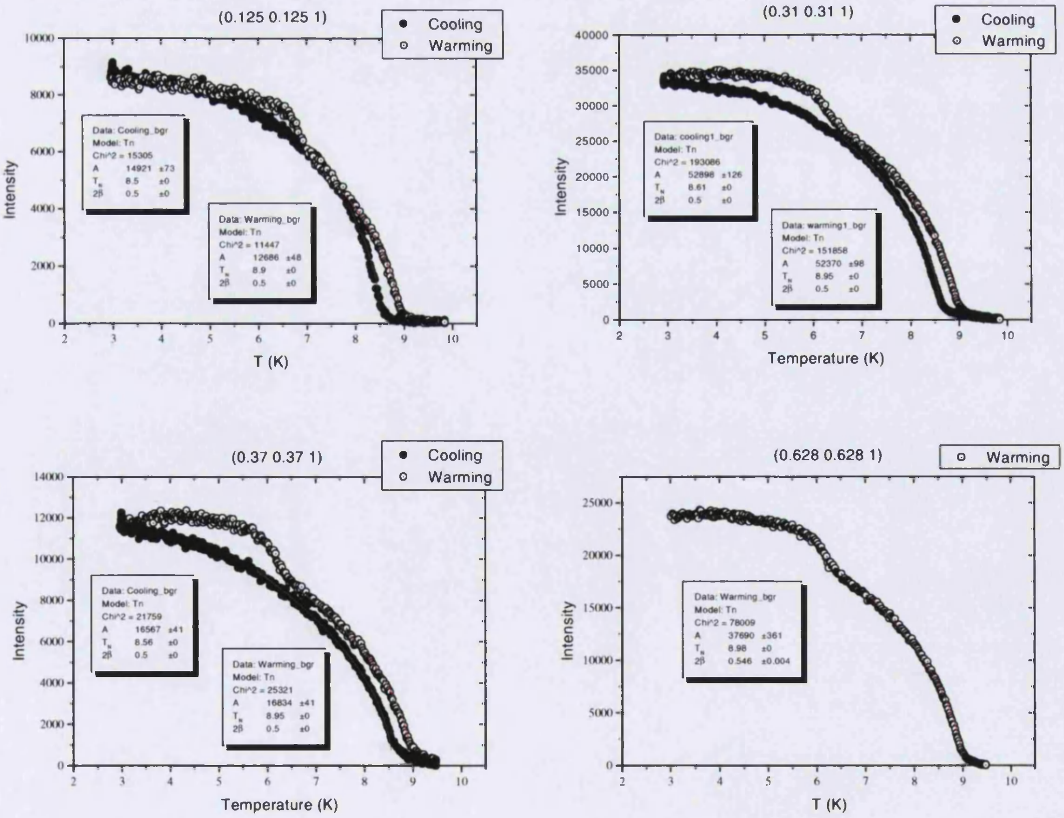

Figure 94: Sublattice magnetisation scans at various Q(*h h* 1),), (lines are best fit to power law $A\varepsilon^{2\beta}$ with β=0.25).

The values of the transition temperatures and the calculated critical exponent β are collated below.

Table 12: Critical exponent β values for the triangular lattice antiferromagnet $KNiCl_3$, mixed phase.

Q		T_N	β
0.125 0.125 1	Cooling	8.55 ± 0.1	0.30 ± 0.03
	Warming	8.95 ± 0.04	0.305 ± 0.015
0.31 0.31 1	Cooling	8.60 ± 0.05	0.270 ± 0.02
	Warming	8.95 ± 0.02	0.265 ± 0.02
0.37 0.37 1	Cooling	8.62 ± 0.1	0.25 ± 0.02
	Warming	9.00 ± 0.05	0.28 ± 0.02
0.628 0.628 1	Warming	8.98 ± 0.1	0.273 ± 0.02

The temperature dependence of all measured magnetic reflections show an anomalous behaviour on warming around T = 6 – 7K.

The total magnetic ordering behaviour becomes a little clearer when we overlay the sublattice magnetisation scan for Q(0.31 0.31 1) and Q(1/3 1/3 1). Figure 95 shows that there is a mixture of two phases in the crystal which are not independent of each other. The length scale of domains of each crystallographic phase are such that the onset of the magnetic order in the γ-phase has a distinct influence on the intensity of the β-phase. Domain wall structures may be created between the β and γ phase which rearrange themselves (diminish) below T ~7K. Warming the sample up we see that the intensity of the sublattice magnetisation is higher in intensity than upon cooling in both the β and γ-phase. Between 6K - 7K a slope change occurs and the intensity of the Q(1/3 1/3 1) reflection diminishes while its intensity rises again before the onset of the paramagnetic phase. An approximate ratio of the two domains can be obtained from a comparison of the intensity of the Q(1/3 1/3 1) reflection and the sum of the Q(0.31 0.31 1) and Q(0.37 0.37 1) reflections assuming that the 'averaged' magnetic structure of $KNiCl_3$ is identical to the helical incommensurate magnetic structure of $TlFeCl_3$.

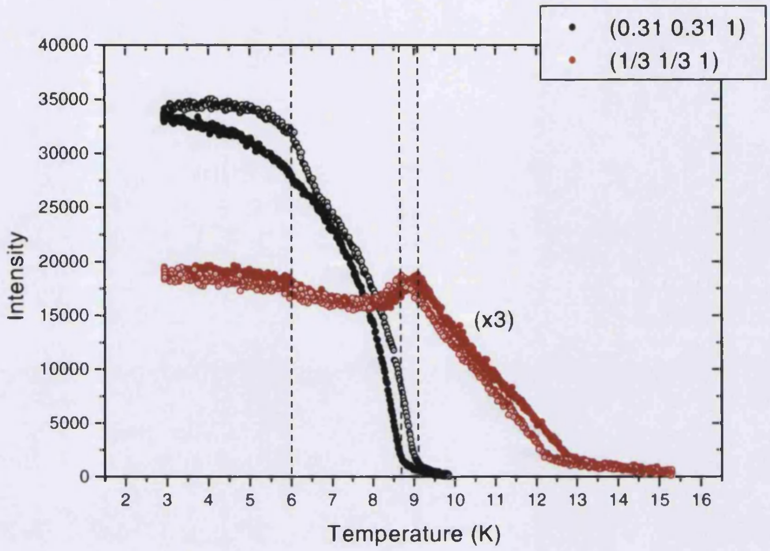

Figure 95: Comparison of the Q(1/3 1/3 1) and Q(0.31 0.31 1) magnetic Bragg peak in KNiCl$_3$.

4.5.2 **4a** *x* **4a** *x* **c** *phase*

The second experiment was performed on the same crystal of KNiCl$_3$ as the previous experiment. However, the sample had undergone a heat treatment by virtue of another experiment undertaken on the sample. The crystal had been mounted in a furnace on the PRISMA diffractometer at the ISIS facility and the temperature set to 400°C for the period of the experiment which took place over a period of 1 week. The sample was then allowed to cool slowly to room temperature. We wish to establish whether this heat treatment had any effect on the physical and magnetic structure of the system. Thus comparison measurements were carried out the TAS 4T2 at the LLB. As before, the sample was mounted in a standard Orange ILL cryostat with the [110] – [001] plane in horizontal scattering plane. A full measurement of the [*h h* 1] direction was undertaken at 8.76K and 1.55K in order to establish where the magnetic Bragg peaks were residing (shown in Figure 96). This also enabled us to compare this measurement with that in Figure 92, allowing us to see if any change had occurred in the sample due to the annealing.

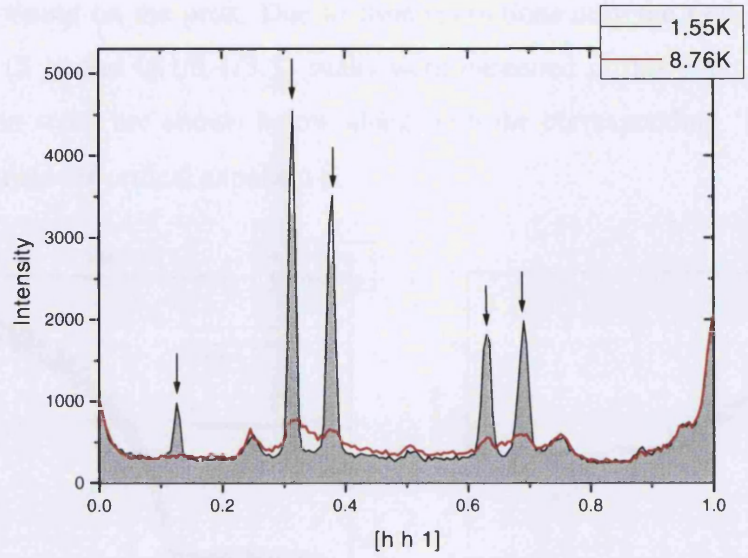

Figure 96: The difference between magnetic (marked with arrow) and structural Bragg peaks of $KNiCl_3$ at 8.76K and 1.55K.

Comparing the above with Figure 92, several points become immediately clear. The magnetic Bragg peaks at Q(0.125 0.125 1), Q(0.31 0.31 1), Q(0.37 0.37 1), Q(0.628 0.628 1) and Q(0.68 0.68 1) are still present, although the relative intensities have changed somewhat. The structural Bragg peaks at Q(001), Q(¼ ¼ 1), Q(½ ½ 1), Q(¾ ¾ 1) and Q(1 1 1) are also still present, albeit slightly swamped by the presence of the higher background count. It can be seen that these structural peaks do not have the same relative intensity as previously, this is especially true of the Q(¾ ¾ 1) and Q(1 1 1) peaks. General observation shows that the half width of the Bragg peaks has also increased slightly. The lack of a Q(1/3 1/3 1) or Q(2/3 2/3 1) peak may suggest a change in the magnetic structure of the system, however it may be that the increased background scatter has swamped these reflections. Finally, extra non magnetic scattering is present around Q(0.95 0.95 1). In order to resolve some of the uncertainties regarding the structure, sublattice magnetisation scans were undertaken on the magnetic Bragg peaks in order to ascertain both the form of the magnetisation and the critical exponent β of the system.

As before, the sublattice magnetisation scans were executed by sitting on the magnetic Bragg peak and performing a slow temperature sweep in both warming and cooling directions to check for hysteresis. Checks were carried out at various temperatures to ensure that full scans over the magnetic Bragg peak gave the same intensity as sitting on the peak. Due to time restrictions only the Q(0.125 0.125 1), Q(0.313 0.313 1) and Q(1/3 1/3 1) peaks were measured in this way. The resultant magnetisation scans are shown below along with the corresponding 'log-log' plots used to calculate the critical exponent β.

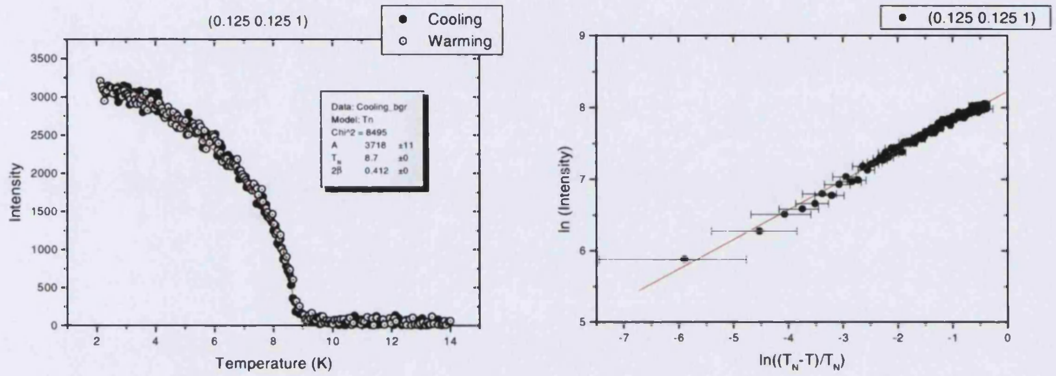

Figure 97: Sublattice magnetisation scan of annealed crystal of $KNiCl_3$ at Q(0.125 0.125 1), (line is best fit to power law $A\varepsilon^{2\beta}$ with β=0.206).

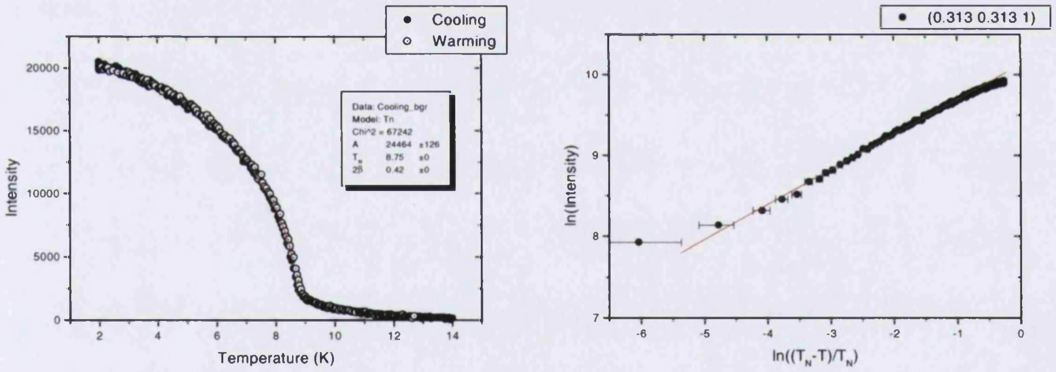

Figure 98: Sublattice magnetisation scan of annealed crystal of $KNiCl_3$ at Q(0.313 0.313 1), (line is best fit to power law $A\varepsilon^{2\beta}$ with β=0.210).

Direct comparison of the above figures and those in Figure 94 show that the hysteresis of the system between warming and cooling has been removed. The T_N of the new system does not correspond to either the warming or cooling T_N of the previous experiment (~8.9K and ~8.5K respectively) rather it sits in between them at T_N = 8.73K ± 0.03K. Again the (1/3 1/3 1) sublattice magnetisation scan has produced an unexpected result. The peak does not have a form as of the previous experiment as can be seen in Figure 93, where the peak reaches a maximum around 8.7K and stabilises at this level to low temperatures, rather it reaches a maximum around 9.0K falling off to almost zero approaching low temperature.

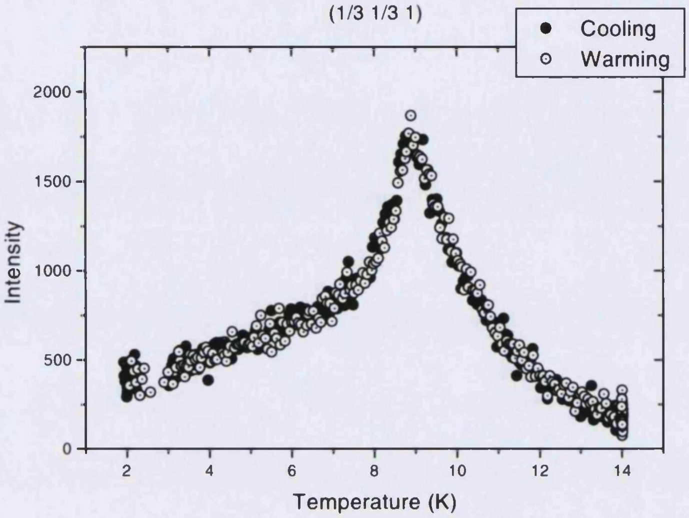

Figure 99: Sublattice magnetisation scan of annealed crystal of $KNiCl_3$ at Q(1/3 1/3 1).

A comparison of the scans taken in this experiment shows that the magnetic intensity at Q(1/3 1/3 1) does not represent magnetic Bragg scattering but corresponds to diffuse magnetic scattering from the tails of the Q(0.31 0.31 1) and Q(0.37 0.37 1) magnetic Bragg reflections. This type of scattering corresponds to short range magnetic order in the basal plane similar to that observed in $CsNiCl_3$ (Chapter 4.2.2). The most striking difference between the crystal of the mixed phase and the material after heat treatment is a change of the magnetic critical behaviour from a mean field to normal one.

In the phase which now corresponds to the 'ordered' γ phase, one observes however, a different magnetic critical exponent from that of the mixed phase crystal's γ-phase. β drops from a value of $\beta = 0.25\text{-}0.30$, corresponding to the predictions for the $n = 2$ or 3 chiral universality classes to a value of $\beta = 0.21(1)$. This value is much closer to that of the 2D-XY system. This value is also close to the one observed for $CsNiCl_3$ at T_{N2} ($\beta = 0.20$). A difference between the two different β's obtainable for the γ-phase may lie in a slightly different incommensurate magnetic structure.

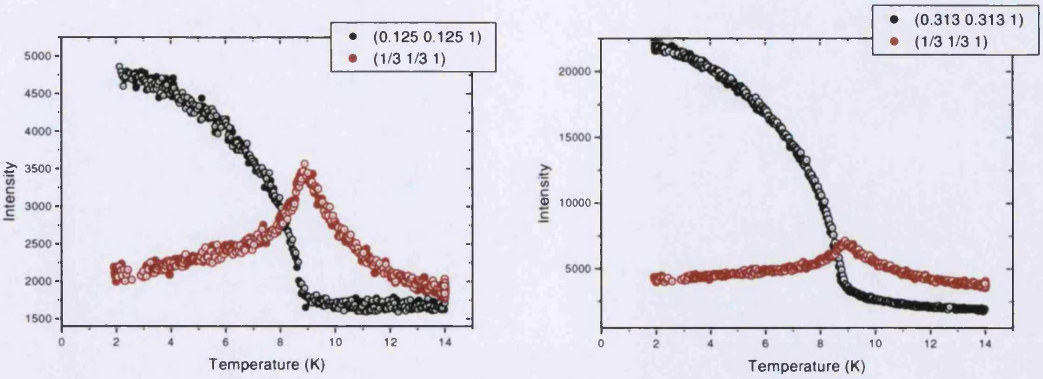

Figure 100: Comparison of the Q(0.125 0.125 1), Q(0.31 0.31 1) and Q(1/3 1/3 1) peak of the annealed crystal of $KNiCl_3$.

4.5.3 RT phase

This was the last sample to be analyzed, it had been fabricated, as is usual with virtually all the of ABX_3 halides used in this thesis, by Dr. D. Visser using the Bridgman technique and a three zone furnace. The experiment was performed on the two-axis diffractometer 3T1, at the LLB. The crystal was mounted in an ILL Orange cryostat with the [110] - [001] plane in the horizontal scattering plane. We observed magnetic Bragg reflections at the positions Q(h/3 h/3 l): $h \neq 3n$, $l = 2n+1$ which corresponds to a 120° type magnetic structure. The magnetic sublattice magnetization measurements were undertaken at Q (1/3 1/3 1), Q (2/3 2/3 1) and Q (1/3 1/3 3) using PG002 as a filter to reduce second order contamination. The positions of these magnetic Bragg positions are shown as a function of reciprocal space below.

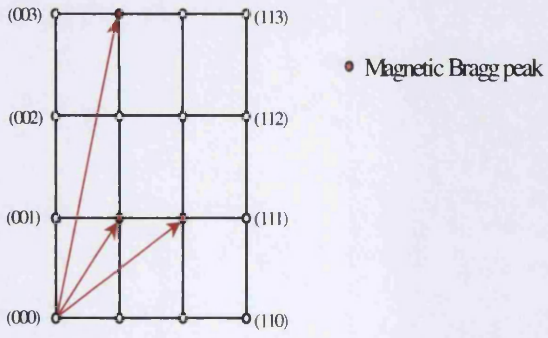

Figure 101: Reciprocal lattice positions of the magnetic Bragg peaks Q(1/3 1/3 1), Q(2/3 2/3 1) and Q(1/3 1/3 3) in the distorted triangular lattice antiferromagnet $KNiCl_3$.

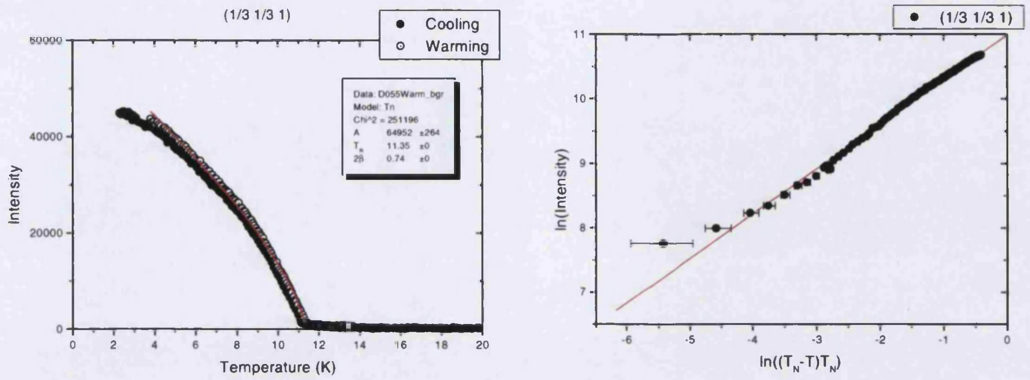

Figure 102: Sublattice magnetisation of $KNiCl_3$ at Q(1/3 1/3 1), (line is best fit to power law $A\varepsilon^{2\beta}$ with β=0.37).

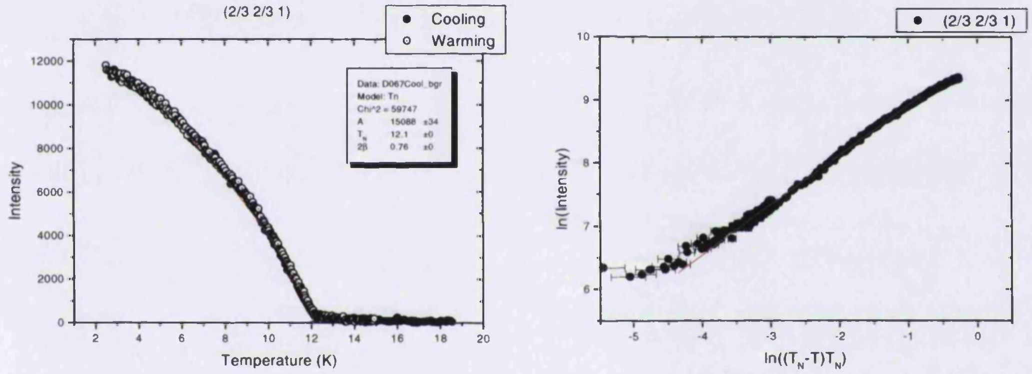

Figure 103: Sublattice magnetisation of $KNiCl_3$ at Q(2/3 2/3 1), (line is best fit to power law $A\varepsilon^{2\beta}$ with β=0.375).

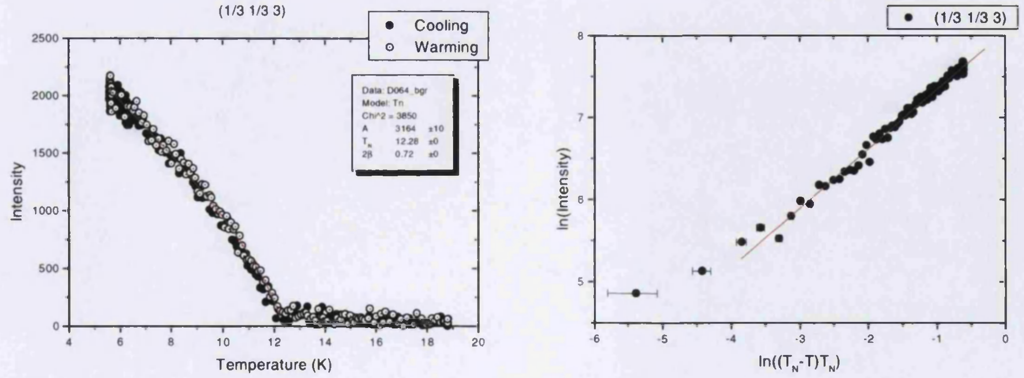

Figure 104: Sublattice magnetisation of $KNiCl_3$ at Q(1/3 1/3 3), (line is best fit to power law $A\varepsilon^{2\beta}$ with β=0.36).

Magnetization measurements were recorded for both warming and cooling of the sample. As can be seen from the figures above only a very small hysteresis was observed at the magnetic transition.

Several observations may be immediately made from the above figures. Due to the magnetic form factor, the scattering from the (1/3 1/3 3) magnetic Bragg peak is substantially lower than that from the (*h h* 1) peaks. However, a more puzzling observation is the difference in T_N between that of (1/3 1/3 1) and the other two magnetic Bragg peaks. This is unusual and may indicate that there has been a problem with the temperature regulation.

As with the previous two experiments on this system, the magnetic order parameter β was obtained by least square fitting the temperature dependent intensity of the magnetic reflections $I = M^2$ to a power law expression $\ln M \sim \ln (T_N\text{-}T/T_N)^{2\beta}$. The average values of β obtained for all three reflections are given below.

Table 13: Average critical exponent β values for the triangular lattice antiferromagnet $KNiCl_3$ (third crystal).

Q	T_N	β
1/3 1/3 1	11.25 ± 0.10	0.374 ± 0.02
2/3 2/3 1	12.10 ± 0.05	0.387 ± 0.02
1/3 1/3 3	12.20 ± 0.10	0.355 ± 0.01

It can be seen from the values of β in Table 13, that the observed values of the critical exponent are close to those of the 3-D XY and Heisenberg universality classes where $\beta = 0.3460$ and $\beta = 0.3648$ respectively. Thus we can see that the values of β for $KNiCl_3$ are far removed from those of the $n = 2$ or $n = 3$ chiral universality classes, where $\beta = 0.245$ and $\beta = 0.30$, respectively. Surprisingly the β values are also far removed from the value found for $RbVBr_3$, a system with an identical nuclear structure as the present $KNiCl_3$ crystal where $\beta = 0.28$. In order to unambiguously establish the critical exponent β and the value of T_N for the three magnetic Bragg peaks, it was decided to undertake a repeat experiment on the same crystal with the same sample environment, however this time the experiment was undertaken using the TAS 4F2, at the LLB. Thus sublattice magnetisation scans were again undertaken on the magnetic Bragg peaks (1/3 1/3 1), (2/3 2/3 1) and (1/3 1/3 3). The result of these scans may be seen below with the corresponding 'log – log' plots calculating the critical exponent β.

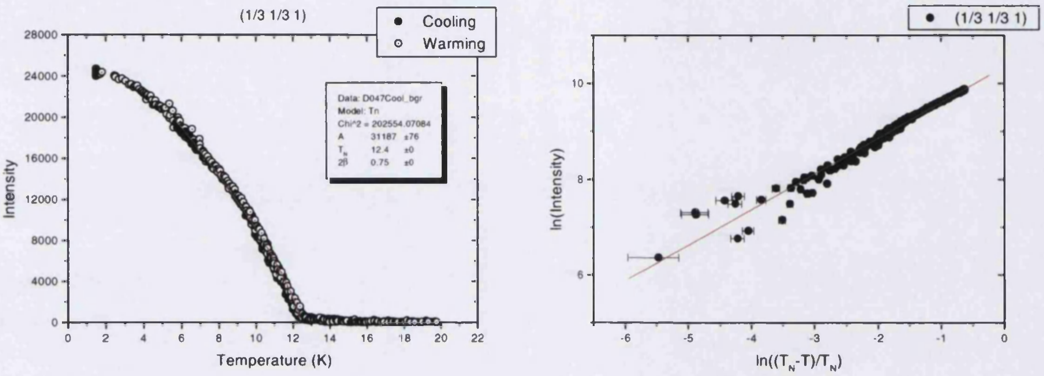

Figure 105: Sublattice magnetisation of KNiCl$_3$ at Q(1/3 1/3 1), (line is best fit to power law A$\varepsilon^{2\beta}$ with β=0.375).

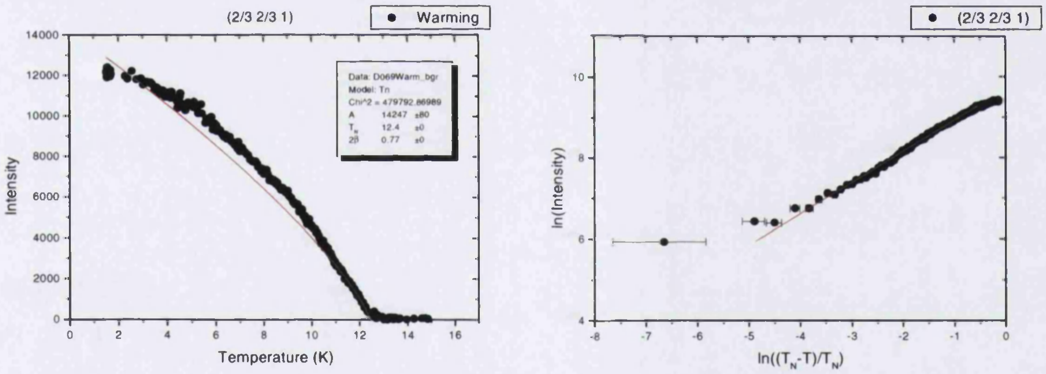

Figure 106: Sublattice magnetisation of KNiCl$_3$ at Q(2/3 2/3 1), (line is best fit to power law A$\varepsilon^{2\beta}$ with β=0.385).

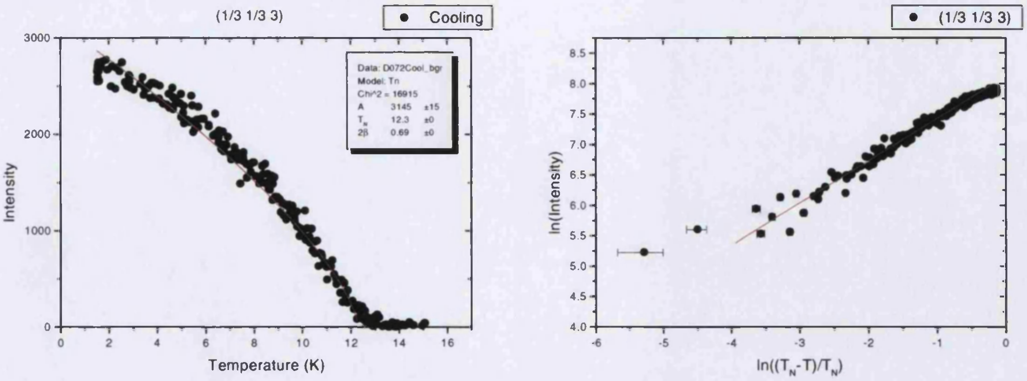

Figure 107: Sublattice magnetisation of $KNiCl_3$ at Q(1/3 1/3 3), (line is best fit to power law $A\varepsilon^{2\beta}$ with β=0.345).

The data was treated as before and is collated below,

Table 14: Critical exponent β values for the triangular lattice antiferromagnet $KNiCl_3$ (third crystal).

Q	T_N	β
1/3 1/3 1	12.40 ± 0.1	0.375 ± 0.01
2/3 2/3 1	12.40 ± 0.05	0.385 ± 0.01
1/3 1/3 3	12.30 ± 0.1	0.345 ± 0.01

It is immediately obvious that the value of T_N for (1/3 1/3 1) is now the same as the (2/3 2/3 1) and (1/3 1/3 3) magnetic Bragg peaks. This is a satisfactory result and suggests that there was some error in the previous measurements. Yet again the values of the critical exponent β are in the range 0.345 – 0.385, suggesting normal 3D XY or Heisenberg behaviour. What can be observed from a comparison of Table 13 and Table 14, is that the value of β obtained from the Q(1/3 1/3 3) reflection is lower than the critical exponent calculated for the Q(h h 1) reflections. Calculations on the Q(1/3 1/3 1) and Q(2/3 2/3 1) reflections indicate that $KNiCl_3$ represents a 3-D Heisenberg universality class while the Q(1/3 1/3 3) indicates a 3D XY universality class. If we consider the slightly different system of the weak-Ising like triangular antiferromagnet $CsNiCl_3$, we see from Figure 11 that it has two magnetic transitions. The first being at T_{N1} where the z component of the magnetic spin orders along the c-direction giving rise to a partially ordered phase, then secondly at T_{N2} where finally the xy components of the spin order out along the [110] direction. This results in largely different β's for the two components as observable from the Q(1/3 1/3 1) and Q(1/3 1/3 3) reflections. A similar scenario may be possible for $KNiCl_3$ were two magnetic transition points are very close together (with a ΔT just outside the resolution of our experiment, a close inspection of Figure 106 suggests that this is possible). In $RbVBr_3$ as well as in $RbFeBr_3$ one observes a partially ordered intermediate magnetic phase existing over a temperature range of several degrees Kelvin. The final magnetic structure is a modified 120° type magnetic structure where the canting angle of two out of the three spins of the initial triangle is larger than 120°. This results, in principle, in an orthorhombic magnetic structure where the canting angle is determined by the single-ion anisotropy of the system and the now different interchain superexchange interactions. For our present data we can conclude that $KNiCl_3$ stabilized in the β - phase and is non chiral ordering and consequently must have a modified 120° type structure.

5 Singlet Ground State AFeX$_3$ compounds

5.1 CsFeCl$_3$ (LLB)

In order to attempt to establish a correlation between the magnetic and structural behaviour of the system under pressure, it is necessary to obtain accurate measurements of the structural parameters a, c and x_{Cl} and the exchange parameters J, J' and D. The former may be obtained most accurately by means of neutron powder diffraction, these measurements are dealt with in Chapter 5.1.2. The latter, i.e. the values of D, J and J' are obtained from the dispersion curves of the magnetic excitations obtained by inelastic neutron scattering on the system and are dealt with in 5.1.1.

5.1.1 Magnon dispersion measurements on CsFeCl$_3$ under hydrostatic pressure.

The magnetic dispersion-curve measurements presented in this Chapter and in Chapter 5.2.1 deal with experiments undertaken by the author while at Loughborough University. This work was presented for the degree of MPhil and is included here to give a full picture of the magneto-structural relationship in the singlet groundstate AFeX$_3$ systems. Where extra work has been performed on this data during the period of the author's PhD studies, this has been clearly indicated.

The measurements of the magnon dispersion curves were undertaken on the TAS, 4F1 at the LLB, Saclay. (Chapter 4.4.2). A 1cm^3 single crystal, grown by Bridgeman technique and having a mosaic width of 0.2° was mounted in a He-pressure cell (Chapter 3.3.3), placed into a modified 'Orange' cryostat. The system was pressurised and then cooled to T=1.5K. The process of pressurising at room temperature and cooling to 1.5K took about 7 hours, the majority of this time was used in cooling the mass of the pressure cell. The sample was mounted with the [110]-[001] plane in the scattering plane of the instrument. Measurements were made around the magnetic Bragg points along [1/3 1/3 l], [1 1 l] and [h h 0] at various pressures, during the course of several experiments, in order to obtain a full picture of the magnetic dispersion curve under hydrostatic pressure. The directions scanned are shown below.

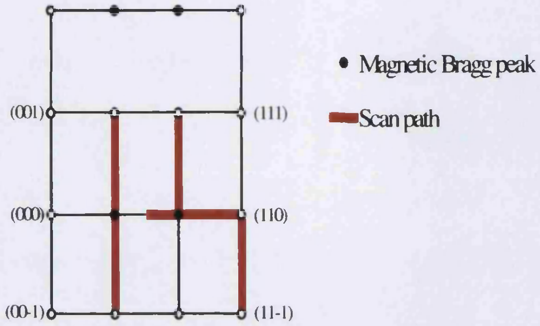

Figure 108: Scans taken through reciprocal space for $CsFeCl_3$ at 5.0kbar, 3.5kbar, and 2.0kbar.

Scans were obtained with the constant-Q method and fitted to a delta peak, modified to take into account the calibration of the instrument and the incident wavevector, thus giving a finite width to the excitation. The program used for this was called *afitv*, a fitting program developed 'in-house' by the Laboratoire Leon Brillouin specifically for analysing data from their triple axis spectrometers. Pyrolytic Graphite was used as both monochromator and analyser. A cooled Beryllium filter and a PG filter were used at k_i = 1.55 $Å^{-1}$ and at k_i = 2.662 $Å^{-1}$ respectively, to reduce the second order contamination of the neutron beam.

Through experience it was found necessary to change k_i from 2.662$Å^{-1}$ to 1.55$Å^{-1}$ when the magnetic excitation transfer energy fell below 0.4THz. This improved the resolution of the TAS but reduced the intensity of the measured peaks. At very low energy transfers such as at (2/3 2/3 0) at 5.0kbar, k_i was reduced further to 1.4$Å^{-1}$ in order to resolve the excitations very close to the incoherent peak at E = 0 THz. This of course reduced the intensity even further and could only be undertaken for a few critical points.

The observed excitations were modelled during the author's PhD work with greater accuracy than previously using the dispersion relations of Lindgård[157] and Villain[158].

$$\hbar\,\omega(q) = (\,D\,[D - 2J(q)\cdot R(T)\,]\,)^{1/2} \tag{57}$$

where $J(q) = 4\,[\,J\cos(\pi q_c) + J''\cos(2\pi q_c) + J'\gamma(2\pi q_\perp)\,]$

and $\gamma(2\pi q_\perp) = \{2J\cos(\pi q_y)[\,\cos(2\pi q_x) + \cos(2\pi q_y)\,] - 1\,\}$

J'' is a factor introduced to account for the next nearest neighbour interaction, this allowed a more accurate fitting to be undertaken in some circumstances.

q_c is the vector in the chain direction, in reciprocal space units [$2\pi / c$],

q_x is the vector in the [100] direction, in reciprocal space units [$4\pi / \sqrt{3}a$],

q_y is the vector in the [110] direction, in reciprocal space units [$4\pi / a$].

$R(T)$ is the renormalisation factor which is introduced to correct for temperature effects, it is defined by the equation:

$$R = R' / R'_o = \left(n_1 - \frac{n_2 + n_3}{2} \right) \Big/ R'_o \qquad (58)$$

where n_1 is the occupation factor for the ground state and n_2 and n_3 describe the Zeeman split states m = ±1, the $\lim_{T \to 0} R(T) = 1$.

The three directions, [1 1 *l*], [1/3 1/3 *l*] and [*h h* 0], measured were all simultaneously fitted to the equation above producing an accurate description of the magnon dispersion curves. The results for each pressure are presented below.

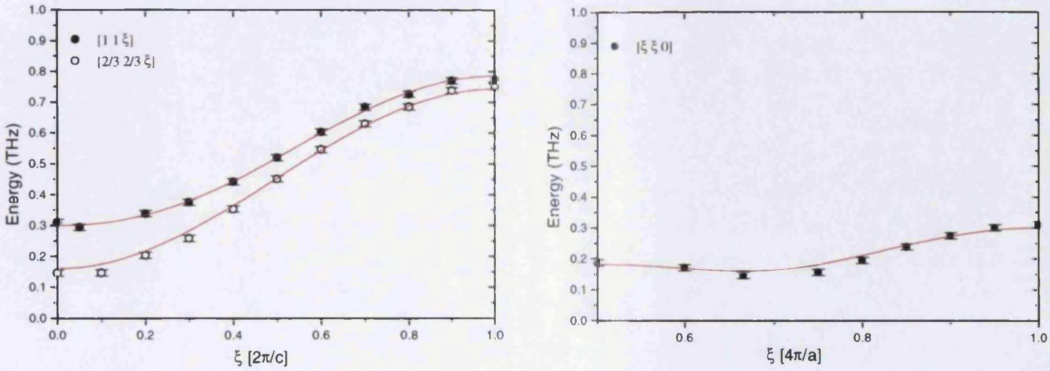

Figure 109: Magnetic dispersion of $CsFeCl_3$ at 0 kbar along [1 1 *l*], [2/3 2/3 *l*] and [*h h* 0].

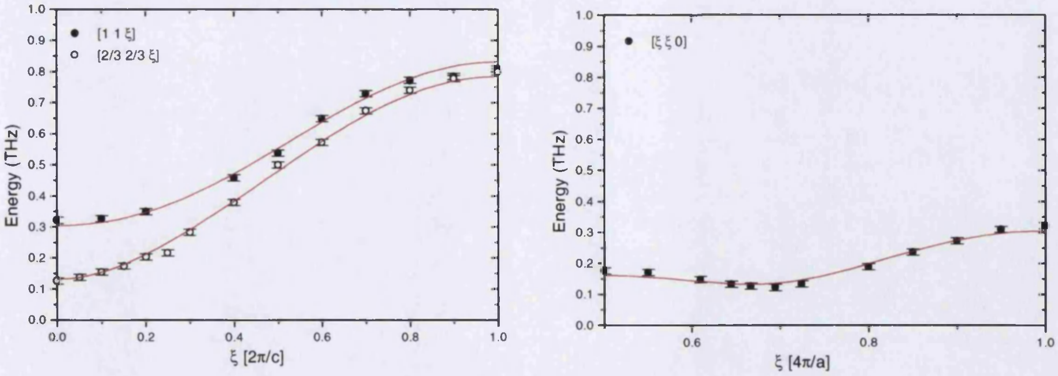

Figure 110: Magnetic dispersion of CsFeCl$_3$ at 2.0 kbar along [1 1 *l*], [2/3 2/3 *l*] and [*h h* 0].

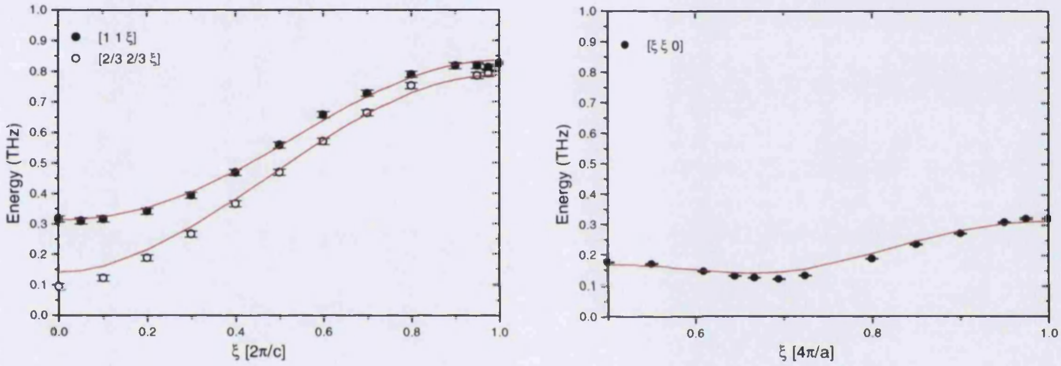

Figure 111: Magnetic dispersion of CsFeCl$_3$ at 3.5 kbar along [1 1 *l*], [2/3 2/3 *l*] and [*h h* 0].

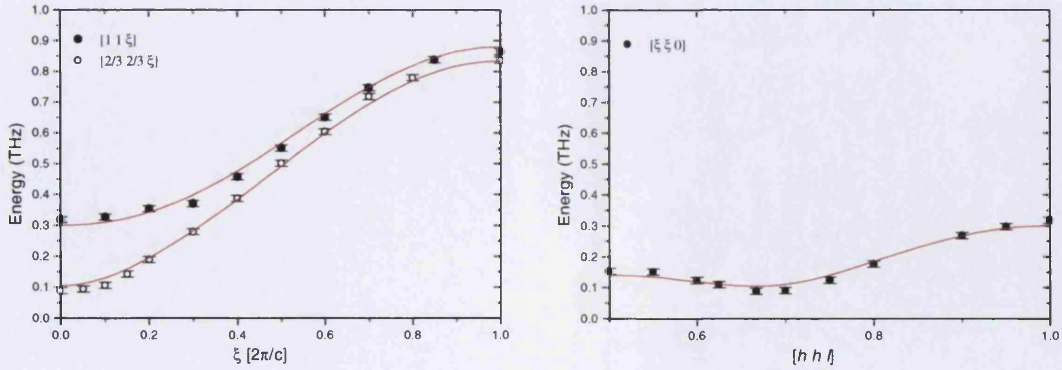

Figure 112: Magnetic dispersion of CsFeCl$_3$ at 5.0 kbar along [1 1 *l*], [2/3 2/3 *l*] and [*h h* 0].

Applying equation 57 to the magnetic dispersion curves shown above we obtain the following values for single ion anisotropy (D), *intra*chain superexchange energy (J), *inter*chain superexchange energy (J') and next nearest superexchange energy (J'').

Table 15: Values obtained for the single ion anisotropy (D), *intra*chain exchange energy (J), *inter*chain exchange energy (J') and next nearest exchange energy (J'') for $CsFeCl_3$.

P(kbar)	D	J	J'	J''
0.0	0.5185(23)	0.0634(67)	-0.0034(2)	-0.00999(73)
2.0	0.5463(59)	0.0677(15)	-0.0038(5)	-0.00958(180)
3.5	0.5484(55)	0.0683(13)	-0.0039(4)	-0.0103(150)
5.0	0.5692(50)	0.0750(17)	-0.0038(4)	-0.01211(160)

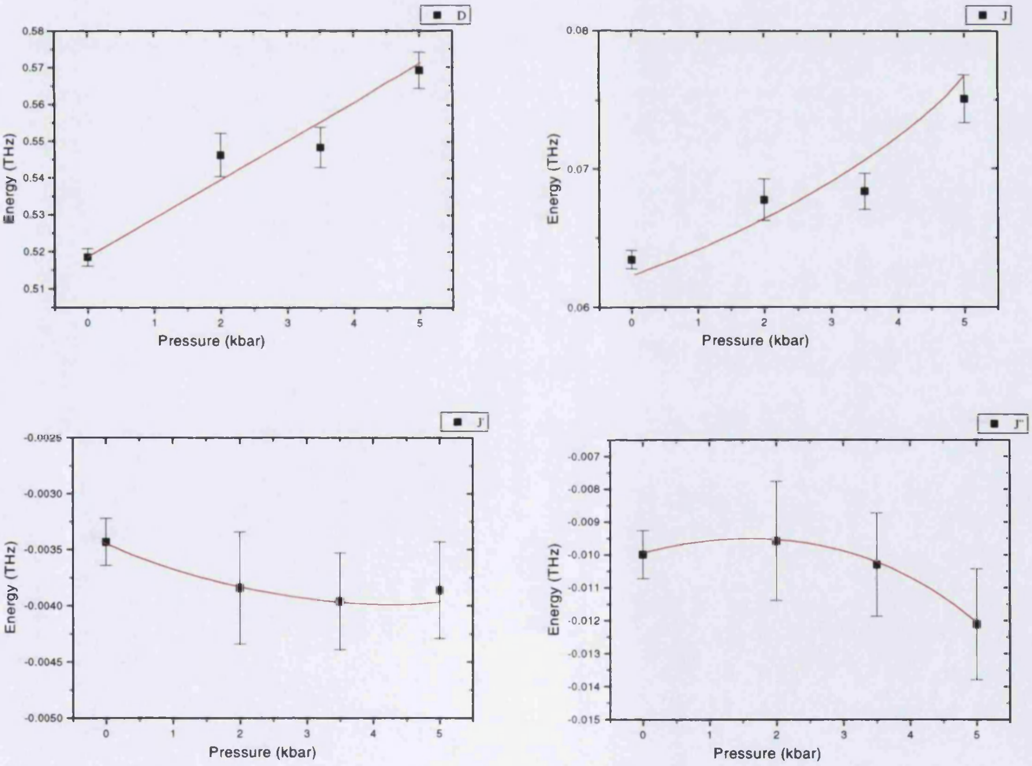

Figure 113: Values obtained for the single ion anisotropy (D), *intra*chain exchange energy (J), *inter*chain exchange energy (J') and next nearest *intra*chain exchange energy (J'') for $CsFeCl_3$.

It can be seen that the value of D increases linearly upon the application of hydrostatic pressure, this is due to the physical deformation of the BX_6^{2-} octahedra under pressure. The value of the interchain interaction also increases, again due to the physical deformation of the BX_6^{2-} octahedra. Both J' and J'' increase/decrease due to the physical distortions of the intrachain Fe-Cl-Fe and interchain Fe-Cl-Cl-Fe superexchange pathways.

5.1.2 Structural studies on $CsFeCl_3$ under hydrostatic pressure. (ISIS)

In order to fully understand the correlation between magnetic behaviour and structure it is necessary to undertake a full evaluation of the physical deformation of the crystal structure under hydrostatic pressure. Experiments of this type have been undertaken by Visser and Harrison[159] on the single crystal diffractometer D15.

The optimised lattice parameters of the system, obtained for each pressure, are shown below in tabular and graphical format. The data given here is machine specific and not of sufficient quality to undertaken calculations on the magneto-structural relationship in $CsFeCl_3$. The data in Table 16 can be compared with the optimised parameters for $CsFeCl_3$ calculated for a powder sample using the POLARIS diffractometer at the ISIS facility in Table 17.

Table 16: Optimised parameters for $CsFeCl_3$ under pressure[159].

P(kbar)	a(Å)	c(Å)	α(°)	X_{Cl}
0	7.1764	5.9706	74.19	0.1588
1	7.1681	5.9575	73.89	0.1595
2.2	7.153	5.9247	73.74	0.1609
5	7.1213	5.9198	73.42	0.1609

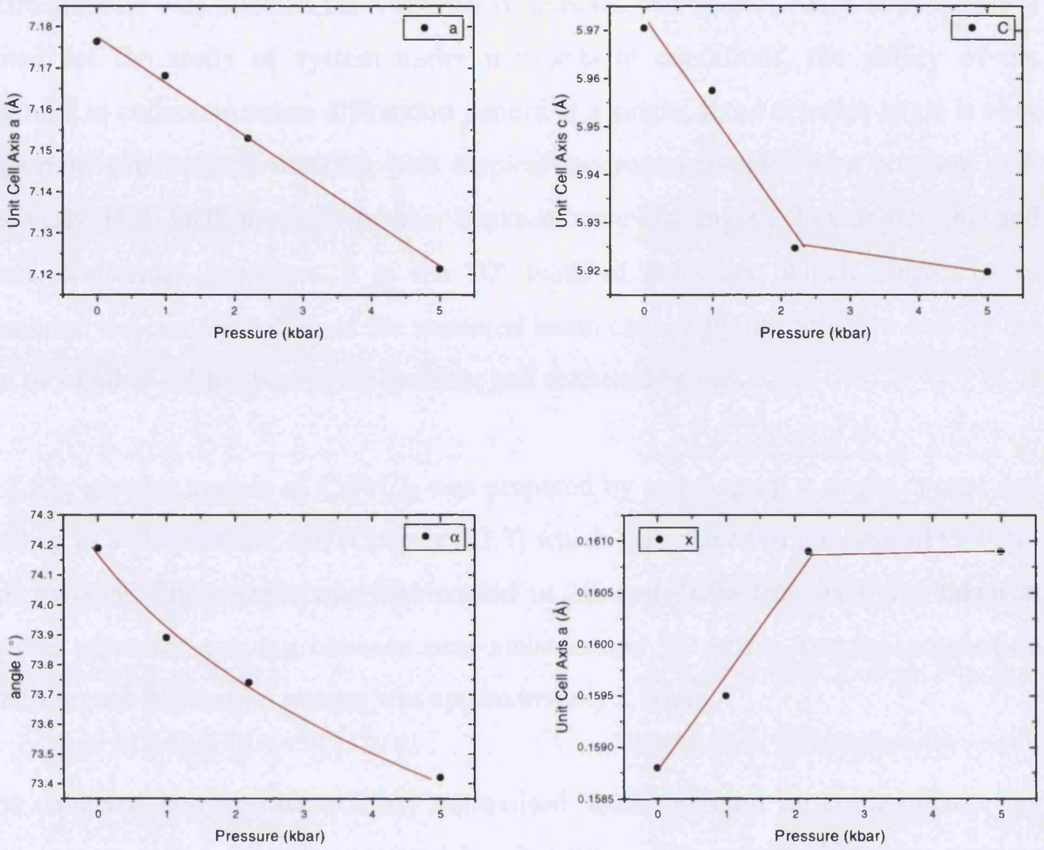

Figure 114: Optimised parameters for $CsFeCl_3$ under pressure by Visser and Harrison, lines are only a guide to the eye.

It is interesting to note the unit cell axis (*a*), has a linear compression with increasing pressure, whereas the *c*-axis undergoes an non-linear compression. However, these results may be spurious due to the experimental conditions under which they were obtained. The available resolution of the D15 diffractometer is a factor of 2-3 less in the vertical direction than the horizontal. The crystal in this experiment was orientated with the *ab* plane in the scattering plane and thus the errors in the *z* direction may be rather large.

As was described in Chapter 3.2.2, powder diffraction provides a powerful means of establishing the physical structure of a system with a high degree of accuracy. It was decided therefore to undertake the characterisation of the system using the medium resolution, high intensity powder diffractometer POLARIS at the ISIS facility. This diffractometer was selected for a number of reasons, Firstly POLARIS is particularly suited for the study of system under non-ambient conditions, the ability of the machine to collect an entire diffraction pattern at a single, fixed detector angle is very important when one is working with atypical environments such as a pressure cell. Secondly, POLARIS has four detector banks at ‘very low angle’, ‘low angle’, 90° and ‘back scattering’ positions. It is the 90° bank of detectors, which allows us to eliminate the contamination of the scattered beam caused by the pressure cell by the use of suitable collimation in the incident and scattered beams.

A 2.83g powder sample of $CsFeCl_3$ was prepared by grinding up a single crystal and loading in a He pressure cell (Chapter 3.3.3) which was placed in a modified Orange-ILL cyrostat. The sample was then cooled to 2K and diffraction data was taken at several pressures varying between near-ambient and 5.0 kbar. Average acquisition time for each diffraction pattern was approximately 2 hours.

The collected raw data were firstly normalised, then corrected for contamination by the pressure cell and finally corrected for absorption. The treated diffraction patterns were then refined using the Rietveld method outlined in Chapter 3.2.2, using the Cambridge Crystalographic Subroutine Library (CCSL). A typical fit for the obtained data is given below for P = 3.48 kbar

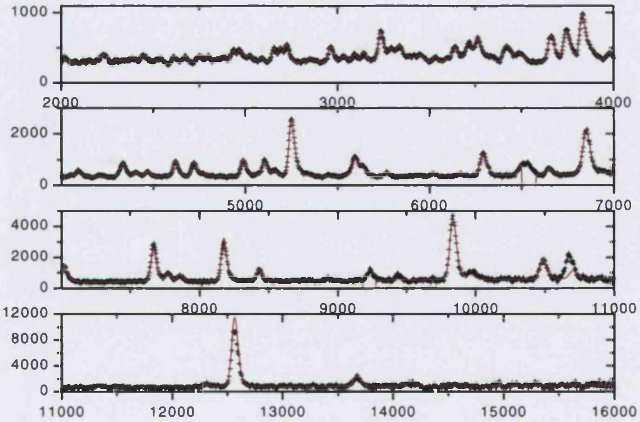

Figure 115: Sample of the Rietveld refined data for the powder sample of $CsFeCl_3$ (P = 3.48 kbar).

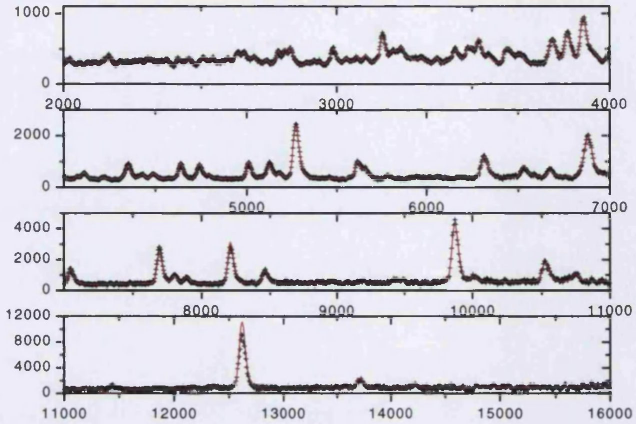

Figure 116: Sample of the Rietveld refined data for the powder sample of $CsFeCl_3$ ($P = 0.48$ kbar).

The calculated values for the unit cell parameters under pressure are given below.

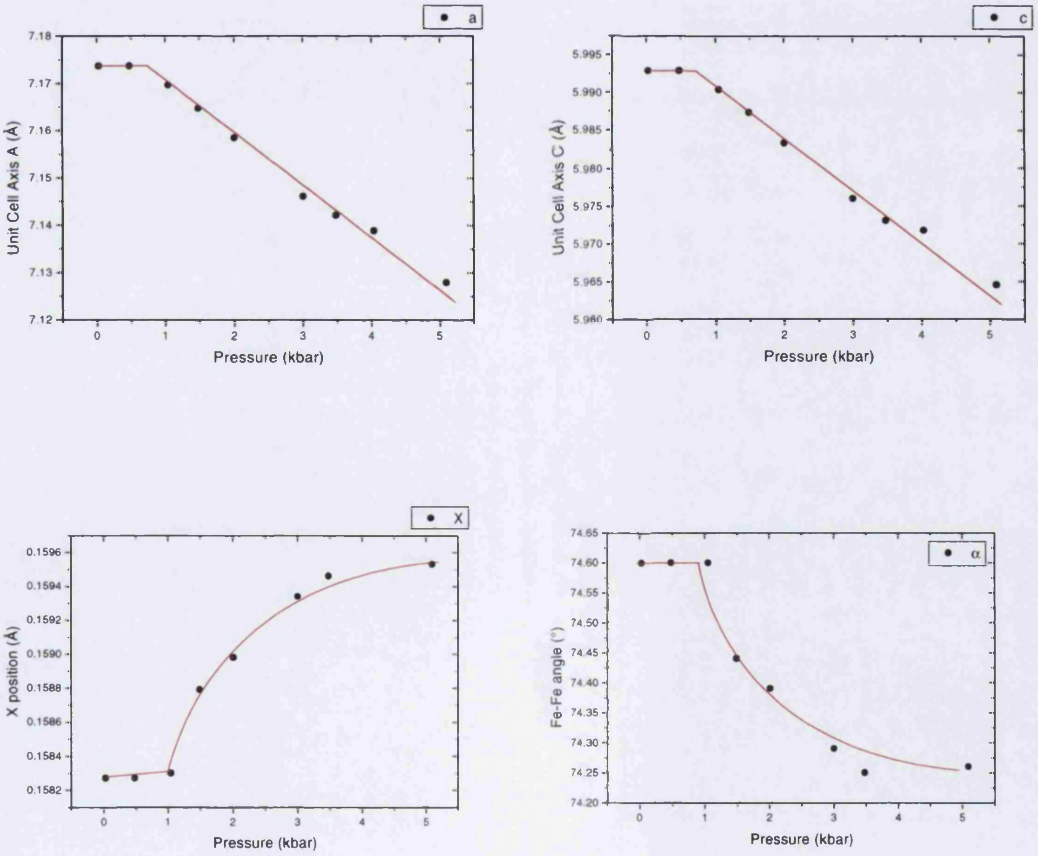

Figure 117: Structural parameters a, c, x and α for $CsFeCl_3$, obtained at the POLARIS diffractometer, ISIS.

It is seen that the system remains stable for pressures upto 0.5 – 1.0 kbar and that both parameters decrease linearly upon application of further pressure. This is in contrast to the data obtained by Visser and Harrison on the single crystal diffractometer D15 at the ILL. This single crystal data, seen in Figure 114, clearly shows an non-linear compression in the *c*-axis. However the data obtained on the POLARIS instrument is certainly more accurate and reliable.

Table 17: Optimised parameters for $CsFeCl_3$ under pressure on the powder diffractometer POLARIS at the ISIS facility, Oxford.

P(kbar)	*a*(Å)	*c*(Å)	α(°)	x_{Cl}
0.03	7.17371(12)	5.99286(19)	74.60	0.15827(10)
0.48	7.17370(12)	5.99287(19)	74.60	0.15827(10)
1.05	7.16962(15)	5.99041(19)	74.60	0.15828(10)
1.49	7.16469(11)	5.98738(15)	74.44	0.15873(9)
2.01	7.15844(12)	5.98333(20)	74.39	0.15898(10)
3	7.14621(12)	5.97589(19)	74.29	0.15932(12)
3.48	7.14236(15)	5.97288(19)	74.25	0.15946(12)
4.03	7.13884(12)	5.97171(19)	74.25	0.15867(12)
5.09	7.12795(12)	5.96453(19)	74.26	0.15953(12)

The value of the *x* parameter shows similar behaviour as the *a* and *c* axes up to 1.0kbar, however these have a decreasing linear behaviour with increasing pressure, which is not the case for *x*, as can be seen above. One of the first points which is obvious upon study of the structural parameters, superexchange angles and anisotropy values is that a pressure of 5.0kbar does not change the balance of *D* versus *J*(*Q*) sufficiently to induce magnetic ordering in the system. The compression of the crystal structure changes *D* as well as ΣJ such that the change in *D* is compensated by a similar change in the superexchange *J*(*Q*). The compression of the BX_6^{2-} octahedra (*c*-axis compression), increases the value of *D* and this is directly related to the reduction in the *c* and α parameters, resulting in x_{Cl} becoming larger. The decrease in the value of α also results in *J* becoming larger. The compression in the *a*-axis gives rise to a larger value of the intrachain superexchange value J' due to the shortened distances along the Fe-Cl-Cl-Fe pathways. The non linear change in these values of x_{Cl} and α is reflected in the non-linear change in the superexchange pathways. A surprising fact to come out of the magnetic excitation data was that the next nearest neighbour interchain superexchange does exist. The value of this parameter increase as one approaches an applied pressure of 5kbar due to the increasing overlap of the Cl-Cl ions. Data was taken at 1.0kbar but unfortunately poor statistics meant that we had to exclude this data from our analysis. The results of such a measurement should confirm the very small change in value of parameters a, c, x_{Cl} and α up to an applied pressure of 1.0kbar. Figure 117 also indicates that a further increase of pressure should not result in a large increase of the constituent parameters.

5.2 $CsFeBr_3$ (LLB)

This Chapter will be used to describe the magneto-structural relationship in $CsFeBr_3$ under hydrostatic pressure conditions. Chapter 5.2.1 will deal with the magnetic dispersion curves of the system, work undertaken at Loughborough University by the present author and presented for the degree of MPhil. Chapter 5.2.2 deals with structural studies undertaken during the author's PhD work on the POLARIS diffractometer at the ISIS facility.

5.2.1 Magnon dispersion measurements on $CsFeBr_3$ under hydrostatic pressure.

The measurements in this Chapter follow exactly the same routine as for the measurements on the system $CsFeCl_3$ expounded on in Chapter 5.1.2. The same TAS, 4F1, at the LLB, Saclay was used for the experiment. A 1cm^3 single crystal of $CsFeBr_3$ was mounted in the He-pressure cell available at the LLB, placed in a modified 'Orange' cryostat, pressurised and cooled to T = 1.5K. Constant-Q scans were then performed along the paths shown below.

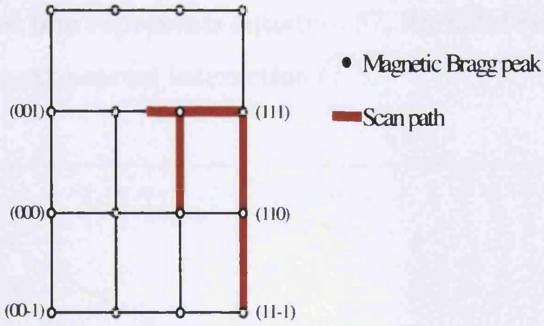

Figure 118: Scans taken through reciprocal space for $CsFeBr_3$ at 5.0kbar, 3.5kbar, and 2.0kbar.

As with $CsFeCl_3$, Pyrolytic Graphite was used as both monochromator and analyser. A cooled Beryllium filter and a PG filter were used at k_i = 1.55 Å^{-1} and at k_i = 2.662

Å^{-1} respectively, to reduce the second order contamination of the neutron beam and k_i was change from 2.662Å^{-1} to 1.55Å^{-1} when the magnetic excitation transfer energy fell below 0.4THz.

The observed magnetic dispersion curves were fitted to equation 36, modified slightly to take account of the antiferromagnetic *intra*chain interaction of the system. It was noted that in the absence of the next nearest neighbour term (*J''*), equation 36 still adequately described the magnon dispersion curves, apart from the case where P = 1.0kbar where the inclusion of *J''* gave a more accurate description of the observed curve. The resulting dispersion curves obtained for P = 5.0kbar, 3.5kbar and 2.0kbar are shown below.

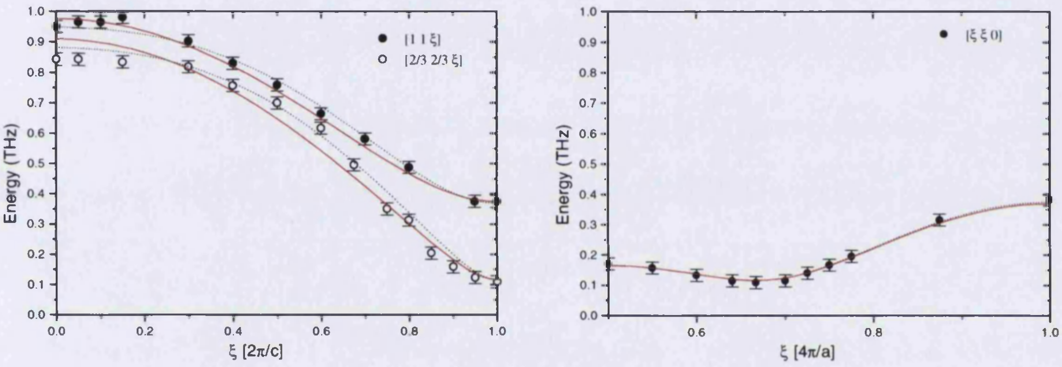

Figure 119: Magnetic dispersion of CsFeBr$_3$ at 1.0 kbar along [1 1 *l*], [2/3 2/3 *l*] and [*h h* 0], the dotted line represents equation 57, the solid red line represents equation 57 with no next nearest interaction (*J''*).

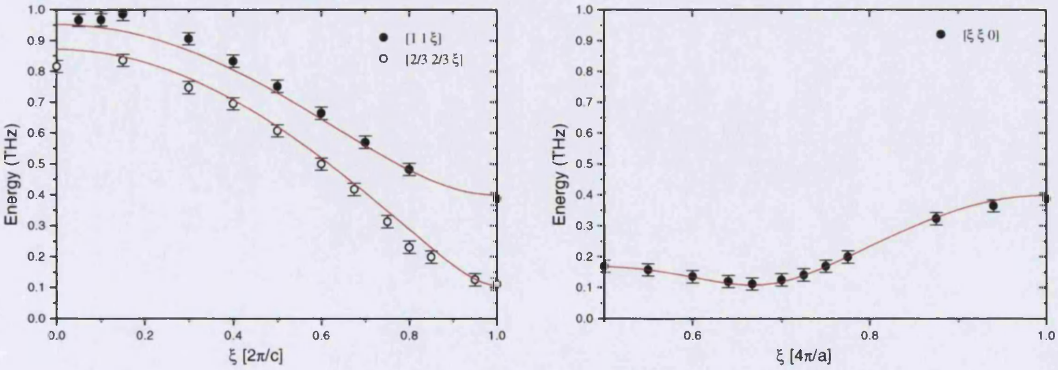

Figure 120: Magnetic dispersion of CsFeBr$_3$ at 2.0 kbar along [1 1 *l*], [2/3 2/3 *l*] and [*h h* 0].

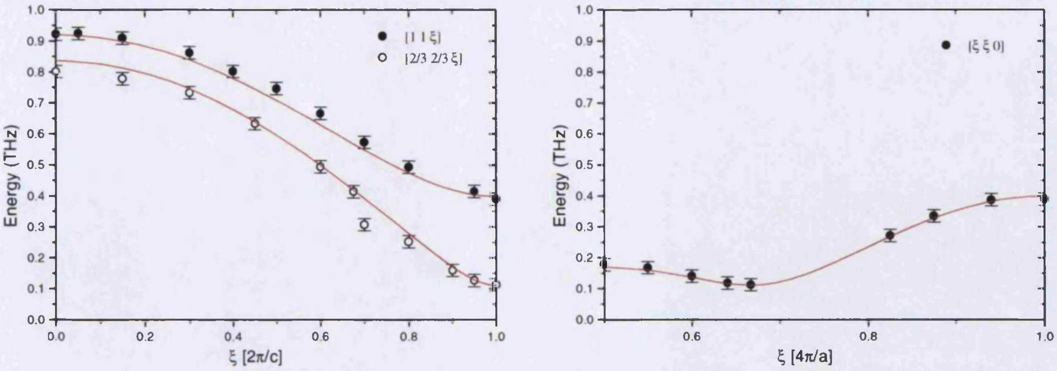

Figure 121: Magnetic dispersion of CsFeBr$_3$ at 3.5 kbar along [1 1 *l*], [2/3 2/3 *l*] and [*h h* 0].

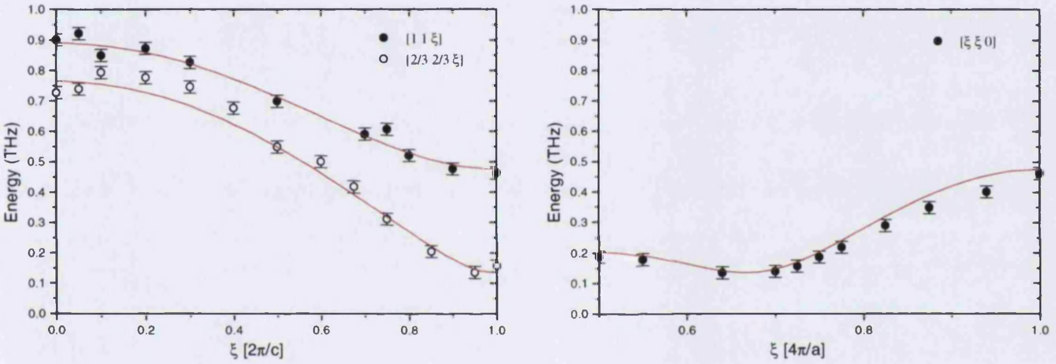

Figure 122: Magnetic dispersion of CsFeBr$_3$ at 5.0 kbar along [1 1 *l*], [2/3 2/3 *l*] and [*h h* 0].

The values obtained from equation 57 are given below.

Table 18: Values obtained for the single ion anisotropy (*D*), *intra*chain exchange energy (*J*) and *inter*chain exchange energy (*J'*) for CsFeBr$_3$.

P(kbar)	*D*	*J*	*J'*	*J''*
0.0	0.620(10)	-0.066(5)	-0.0067(5)	
1.0	0.67738(779)	-0.0737(157)	-0.00566(64)	
1.0	0.6903(112)	-0.06909(175)	-0.00494(43)	0.00735(140)
2.0	0.65901(938)	-0.07088(152)	-0.00622(52)	
3.5	0.65308(1791)	-0.06993(277)	-0.00621(52)	
5.0	0.61288(700)	-0.05915(150)	-0.00930(52)	

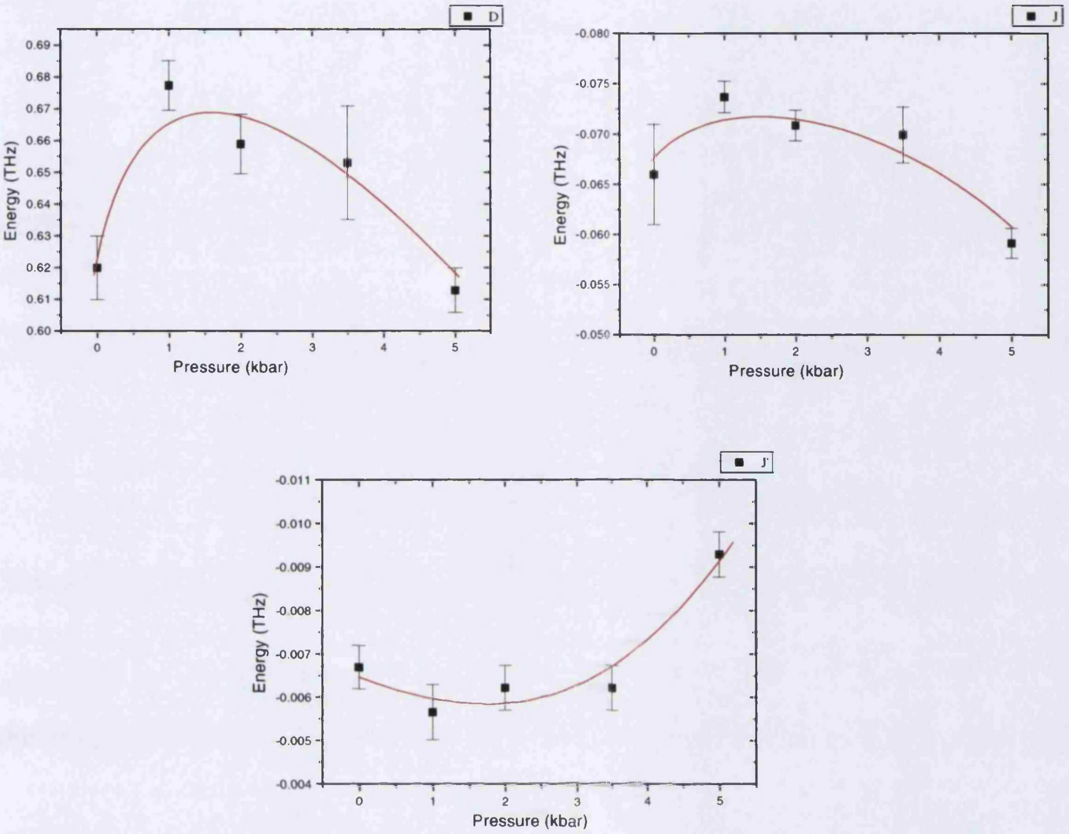

Figure 123: Values obtained for the single ion anisotropy (*D*), *intra*chain exchange energy (*J*) and *inter*chain exchange energy (*J'*) for $CsFeBr_3$. (Lines are guide to the eye only).

As can be seen from the figure above, *D* increases upon the application of hydrostatic pressure reaching a maximum around 1kbar and decreasing thereafter. This is the same for the *intra*chain interaction *J*, the interchain interaction *J'* follows a different trend, seeming to increase in value at 5kbar.

The behaviour of the structural, magnetic superexchange and single ion anisotropy parameters under applied pressure is completely different to that in $CsFeCl_3$. As can be seen in Figure 123, it looks like the chain has restored itself to ambient pressure conditions except for *J'* which is a factor 50% larger at 5kbar applied pressure, it should be noted however, that *J'* is of very small value. It is also of interest to note from Figure 119 that the interchain next nearest neighbour superexchange, *J''*, becomes significant at an applied pressure of 1.0kbar. Unlike in the isostructural compound $CsFeCl_3$, where ferromagnetic dispersion of the nearest neighbour along the c-axis has a period of π/c and the next nearest neighbour dispersion has a period of $\pi/2c$. One would not expected to observe this next nearest neighbour dispersion in the antiferromagnet dispersion of $CsFeBr_3$ as both the nearest and next nearest neighbour dispersions have a period of $\pi/2c$. It seems that some sort of contact is established between the Br ions when the Fe-Br-Br-Fe pathway becomes activated through applied pressure.

5.2.2 Structural studies on $CsFeBr_3$ under hydrostatic pressure.

The measurements contained herein were performed during the same experimental period as those taken in 5.1.2. Thus all experimental parameters such as machine, apparatus etc. are identical. The reader is refer to this Chapter for more information on the experimental aspects.

A powder sample of 2.95g was prepared by crushing a single crystal of $CsFeBr_3$. This was mounted in a clamp cell, which was placed in a modified 'Orange' cryostat and cooled to T = 4.70K. As with $CsFeCl_3$, full powder diffraction patterns were taken from ambient to 5.0kbar applied pressure. The raw data was then normalised, corrected for the presence of the pressure cell and finally corrected for absorption. A typical refinement is shown below for P = 1.39kbar

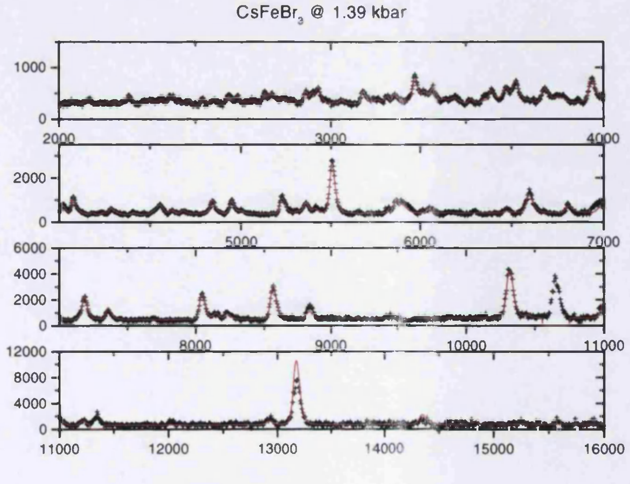

Figure 124: Sample of the Rietveld refined data for $CsFeBr_3$ (P = 1.39kbar).

The resultant values for the unit cell axes *a* and *c* were collated and are given below.

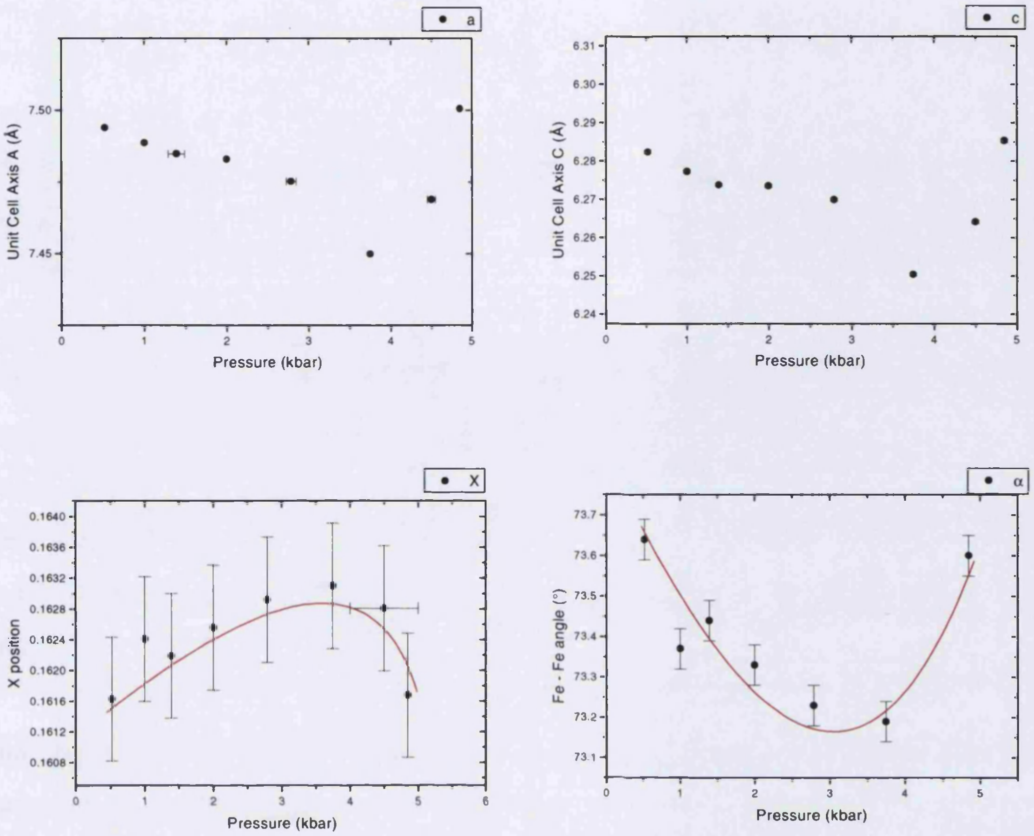

Figure 125: Structural parameters *a, c,* α and X for $CsFeBr_3$, obtained at POLARIS, ISIS (the lines are a guide to the eye only).

Table 19: Optimised parameters for $CsFeBr_3$ under pressure on the powder diffractometer POLARIS at the ISIS facility, Oxford.

P(kbar)	*a*(Å)	*c*(Å)	α(°)	X_{Br}
0	7.507	6.291	73.43(5)	0.1608
0.52	7.49391(45)	6.28247(38)	73.64(5)	0.16163(20)
1.0	7.48859(39)	6.27773(33)	73.37(5)	0.16241(20)
1.39	7.48484(48)	6.27377(38)	73.44(5)	0.16219(22)
2.0	7.48304(49)	6.27357(38)	73.33(5)	0.16256(21)
2.79	7.47556(44)	6.26976(37)	73.23(5)	0.16292(23)
3.75	7.44994(44)	6.25043(37)	73.19(5)	0.16310(26)
4.85	7.50056(57)	6.28543(48)	73.60(5)	0.16168(22)

The magnetostructural correlations in $CsFeBr_3$ can be best described as 'peculiar'. In the initial stages of pressurisation up to 1.0kbar the value of the parameters of D, J and J' increase as one would expect, due to the decrease in the cell parameters. Thereafter the values of D and J decrease whilst the J' remains more or less constant up to 4kbar increasing rapidly thereafter. The neutron powder diffraction data shows that the length of the a-axis and c -axis decrease non-linearly and seem to reach a plateau between 1-3kbar. Upon application of a further pressure up to 5.0kbar we see that the value of the *a* and *c* axes increase again and approximate the values at ambient pressure. An inverse trend is followed by the *x* parameter which increases in value up to 4.0kbar and decreases upon an application of further pressure. However, the *x* parameter does not return to the ambient pressure value as with the values of *a* and *c*, rather it seems to remain at a slightly higher value. The change in the magnetic behaviour of the system can thus be related to the change in the structural parameters.

The origin of this bizarre compressibility may be related to a pressure induced phase transition. At ambient pressure $CsFeBr_3$ adopts the highest possible symmetry space group: $P6_3/mmc$ and no indications of a phase change have been observed thus far from either powder or single crystal diffraction data at ambient pressure. The trend of the data seen in Figure 125 above 3.0kbar indicates a non-physical effect. Under applied pressure the volume of the unit cell should not increase relative to the unit cell volume of the material below 3.0kbar. No evidence of a structural change is observed from the powder diffraction data for $P \geq 3.0$kbar. Experimental conditions were such that the pressure was seen to remain stable at the chosen value during the measurements thus we can rule out a pressure 'leak'. For T = 5K and $P > 3.0$kbar the powder sample was encased in solid Helium, thus the pressure should be homogeneous throughout the sample. In the single crystal inelastic experiments no physical changes to the sample were observed, i.e. shearing of the crystal whilst under pressure etc. If this would have happened one could think of a $h \rightarrow hc$ type of phase transition as a possible cause of the behaviour. It is clear that these points need further investigation.

5.3 CsFeBr$_3$ (V2)

As was mentioned in Chapter 2.3.1, studies on the singlet ground state antiferromagnet CsFeBr$_3$ have mainly concentrated on the magnetic excitations of the system. In this section further elastic and inelastic neutron scattering studies on CsFeBr$_3$ in an applied field at very low temperature (<1K) are presented. The experiments were performed on the TAS, V2 (FLEX), at the HMI, Berlin. In conjunction with a dilution insert and the Horizontal Magnet HM1, temperatures below 100mK and fields above 5T could be reached simultaneously, allowing us to extend the map of the magnetic phase diagram of CsFeBr$_3$.

Chapter 5.3.1 presents measurements on the magnetic phase boundary of the system in the mK temperature range and Chapter 5.3.2 deals with measurements carried out on the magnetic excitations of the system with $H_{//c}$ upto 6.0T at T = 100mK.

Due to technical difficulties it was necessary to perform the experiment during two separate periods. The first period was used not only to ascertain the critical exponent β of the system at mK temperature and high field, but also to establish what measures needed to be undertaken in order to perform the experiment successfully. Several aspects of the first experiment were cited as cause for concern. It was noted that the high magnetic field emanating from the magnet HM1, caused a failure of the magnetic switches which controlled the pneumatic shielding surrounding the sample. In order to overcome this, a temporary fix was administered by taping small individual magnets to each switch to override this effect. It was also noted that the large amount of cabling, vacuum tubing, etc. attached to the dilution stick caused it to rotate within the magnet, thus ruining the alignment of the crystal. This was temporarily overcome with the use of the crane in the guide hall to lift the cabling into a position directly above the stick, this minimised rotational stress on the stick. Both of these problems had a permanent fix by the time of the second experiment. Due to a small heat leak we were unable to attain temperatures below 100mK during the first experiment, this was again remedied by the time of the second experiment.

5.3.1 Elastic Scattering.

Each experiment proceeded in the same manner whereby an approximately 1cm^3 single crystal (mosaic width 0.3°), was mounted and aligned with the [001] - [110] plane in the experimental field. This allowed access to the magnetic Bragg points (1/3 1/3 1), (2/3 2/3 1) etc. In both experiments constant-Q scans were performed across the magnetic Bragg peak (-2/3 -2/3 -1). This was the magnetic peak calculated to be on the focussed side of the analyzer and also within the available 'window' of scattering of the magnet. The phase boundary at the onset of magnetic ordering was established by scanning the peak at fixed temperature and varying the field. These 'sublattice magnetisation' scans were taken for T = 100mK, 350mK, 600mK and 900mK for the first experiment and for T = 50mK and 350mK for the second experiment. The resultant phase boundary is shown below.

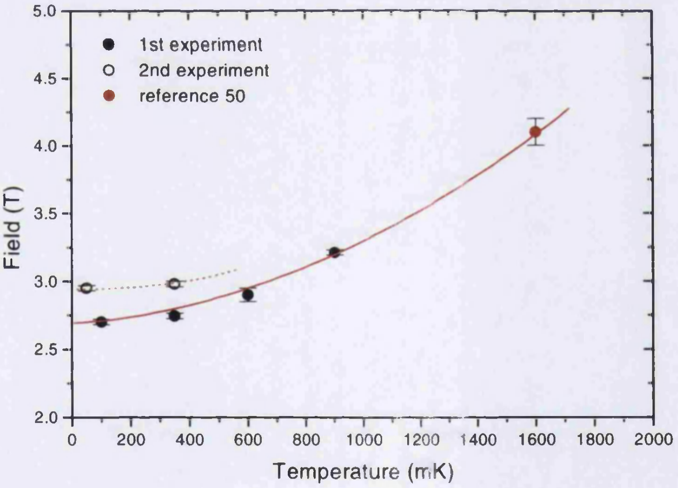

Figure 126: Magnetic phase boundary for the singlet groundstate antiferromagnet CsFeBr$_3$ at millikelvin temperatures (Line is a guide to the eye only).

It can be seen from Figure 126 that the first and second experiment give different phase transition boundaries. It is assumed that this difference is caused by the misalignment of the c-axis of crystal with respect to the horizontal magnetic field. It is estimated that the c-axis of the sample was rotated by approximately 4° to the direction of field in the second experiment, consequently altering the phase boundary.

Of course it is not only the phase boundary which can be determined by 'sublattice magnetisation' measurements, the primary use of these measurements is the determination of the critical exponent β. The measurements and calculated values of β are given below.

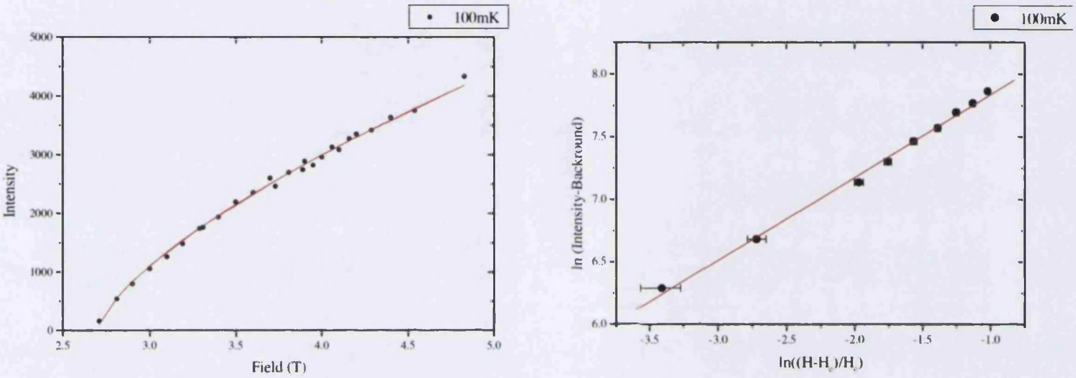

Figure 127: Sublattice magnetisation scan for the SGS system $CsFeBr_3$ taken at 100mK during the first experiment.

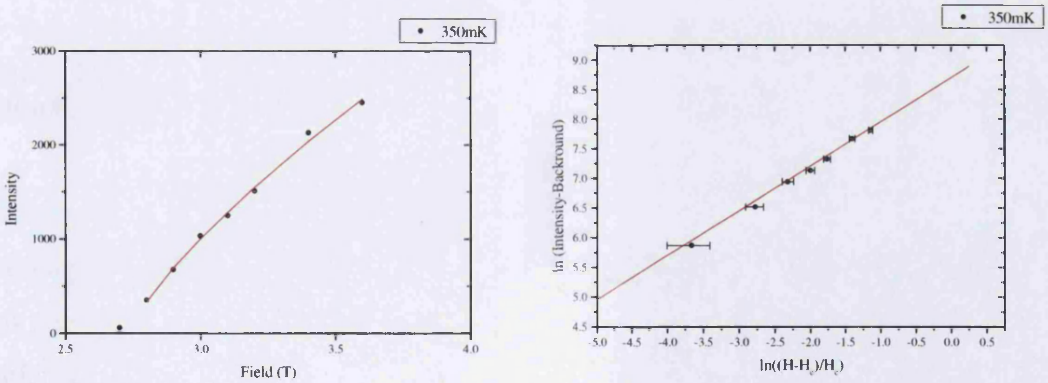

Figure 128: Sublattice magnetisation scan for the SGS system $CsFeBr_3$ taken at 350mK during the first experiment.

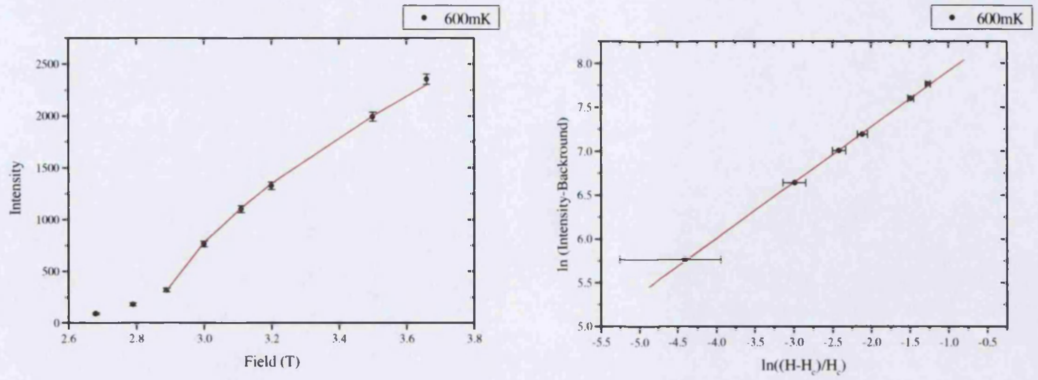

Figure 129: Sublattice magnetisation scan for the SGS system CsFeBr$_3$ taken at 600mK during the first experiment.

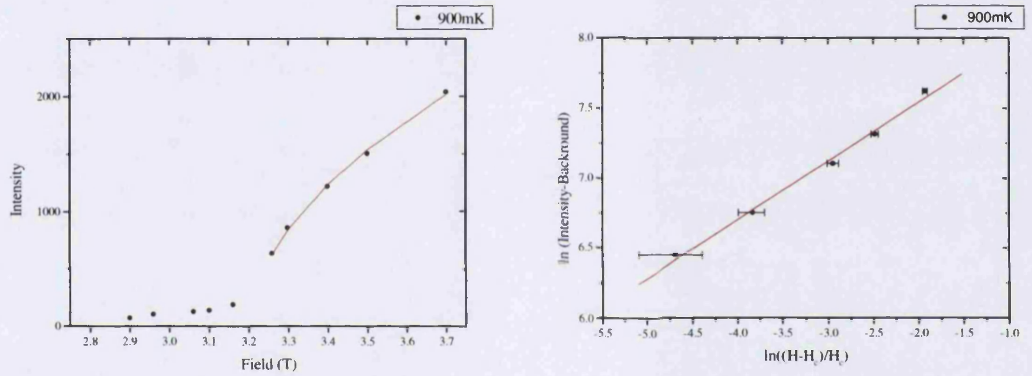

Figure 130: Sublattice magnetisation scan for the SGS system CsFeBr$_3$ taken at 900mK during the first experiment.

As can be seen from the above, the obtained data is of rather poor quality and although it was deemed of sufficient quality to determine the critical exponent β, it was decided to verify these results during the second experiment. Thus further sublattice magnetisation scans were performed during the second experiment at T = 50mK and 350mK. The results of which can be seen below.

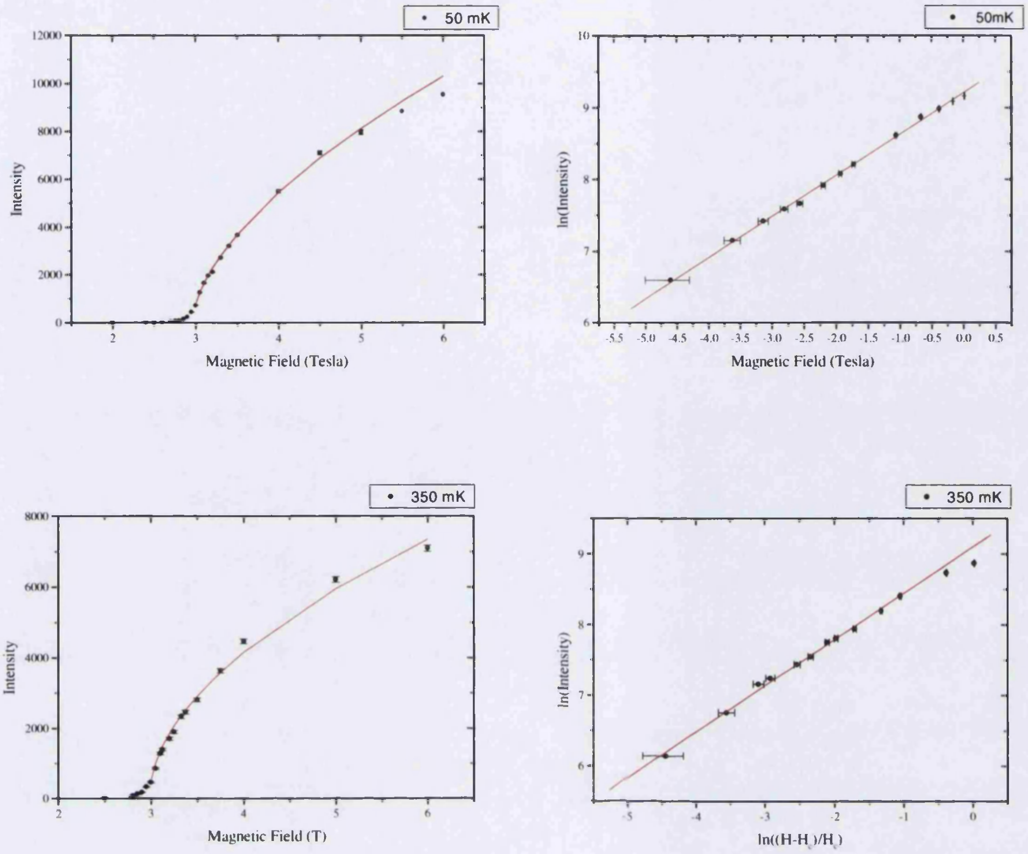

Figure 131: Sublattice magnetisation scans for the SGS system $CsFeBr_3$ taken at millikelvin temperatures taken during the second experiment.

The data obtained from the second experiment are of better quality and go some way to validating the results obtained during the first experiment. It can be seen that the resulting values of the critical exponent are slightly lower than previously, it is speculated that this is due to the fact that the crystal was misaligned by 4° during the second experiment. A similar pattern can be seen for measurements of the phase boundary in Figure 126.

Collating the results of the value of the critical exponent β from the first and second experiments produces some interesting results, as can be seen below.

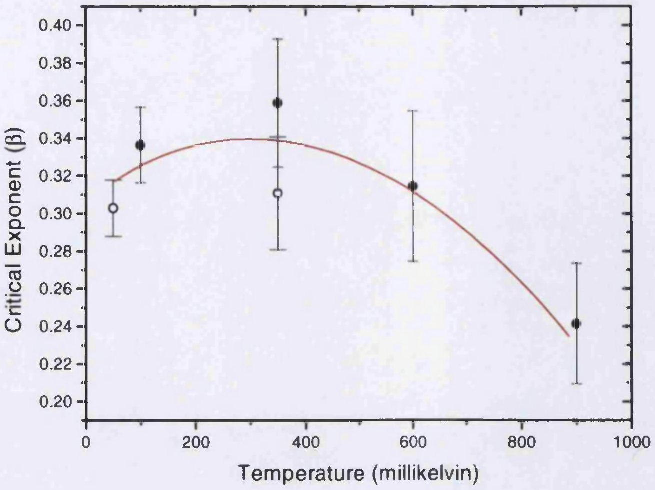

Figure 132: Value of the critical exponent β in the TLA system $CsFeBr_3$ at millikelvin temperatures.

These results suggest that as one moves along the phase boundary the critical exponent changes value. The exponent changes from β = 0.34(1) at T = 100mK, via a value of β = 0.36(2) at T = 350mK to β = 0.25(2) at T = 900mK. Previous measurements by Schmid have shown that β = 0.25 at T = 1.6K[160].

It is well known that the path followed in approaching a critical point may influence the obtained value of the critical exponent and reduce it to an effective exponent. In the case of this type of phase diagram only the pathway at T = 0K with increasing *H*, will give a valid critical exponent. Therefore an unambiguous interpretation of the values of β at the different T and *H* cannot be given. We attempted to establish the possible difference in pathway by running a T dependent scan at fixed *H*. However, this proved ineffective due to the small induced moment and the large amount of critical scattering present just above T_N. It has to be stated that the critical exponents, β, γ, ν quoted by Schmid for $CsFeBr_3$ at T = 1.6K do vary and are not consistent with the *n* = 2 chiral system. As in the case of $CsNiCl_3$ (Chapter 4.2.1), the application of an applied magnetic field under an oblique angle reduces the value of the 'effective' exponent.

5.3.2 Inelastic Scattering.

During the second experiment we also performed full magnon dispersion curve mapping for the system at base temperature (50mK) at various fields. Scans were performed along [*hh*1] and [2/3 2/3 *l*] for B = 1.5T, 3.0T and 6.0T. Typical scans at 3T and 6T are shown below for visualisation purposes.

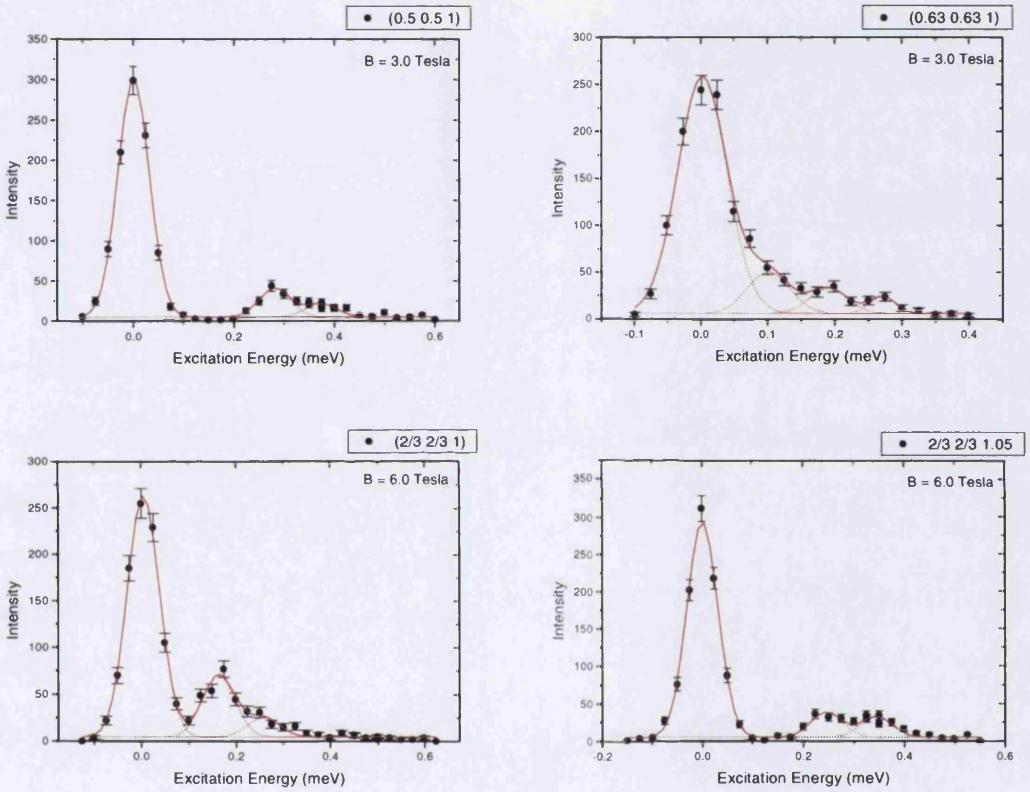

Figure 133: Typical scans performed on $CsFeBr_3$ at T = 50mK and B = 3T and 6T.

The resultant dispersion curves of the [2/3 2/3 *l*] and [*h h* 0] directions are given below. It can be seen that the original single modes have been split by the application of magnetic field along the *z* – axis. known as Zeeman splitting. The dispersion of the split modes have been derived from equation (10)[157,161], giving us an equation similar to that shown in Chapter 5.1.1.

$$\hbar\omega(q) = \{ D\,[D - 2J(q)\cdot R(T, H^z_{ex})] + J^2(q)\cdot(g\mu_B m M_z)^2 \}^{1/2}$$
$$-g\mu_B m\{ H^z_{ex} + [2J_o - J(q)]\, M_z \} \qquad (59)$$

where $J(q) = 4\,[\,J\cos(\pi q_c) + J''\cos(2\pi q_c) + J'\gamma(2\pi q_\perp)\,]$

and $\gamma(2\pi q_\perp) = \{2J\cos(\pi q_y)[\,\cos(2\pi q_x) + \cos(2\pi q_y)\,] - 1\,\}$

$R(T,\ H^z_{ex})$ is a renormalisation factor first introduced by Lindgård[161] in order to account for the temperature renormalisation and later calculated by Knop and Lindgård[162,163] for the field dependence. It is equal to the negative of the quadrupole moment. If one neglects the dispersion of the magnetic excitations in a SGS system, R is given by

$$R = R'/R'_o = \left(n_1 - \frac{n_2 + n_3}{2}\right)\Big/ R'_o \qquad (60)$$

where n_1 is the occupation factor of the ground state $m = 0$, and n_2 and n_3 are the occupation factors for the Zeeman split states $m = -1$, $m = +1$ respectively. We can see that as the external field increases, so R will decrease. This is due to the asymmetric splitting of the $m = \pm 1$ states, such that, n_2 will increase quicker than n_3 will decrease. M_z is the induced magnetic moment, which is negligible in the present case.

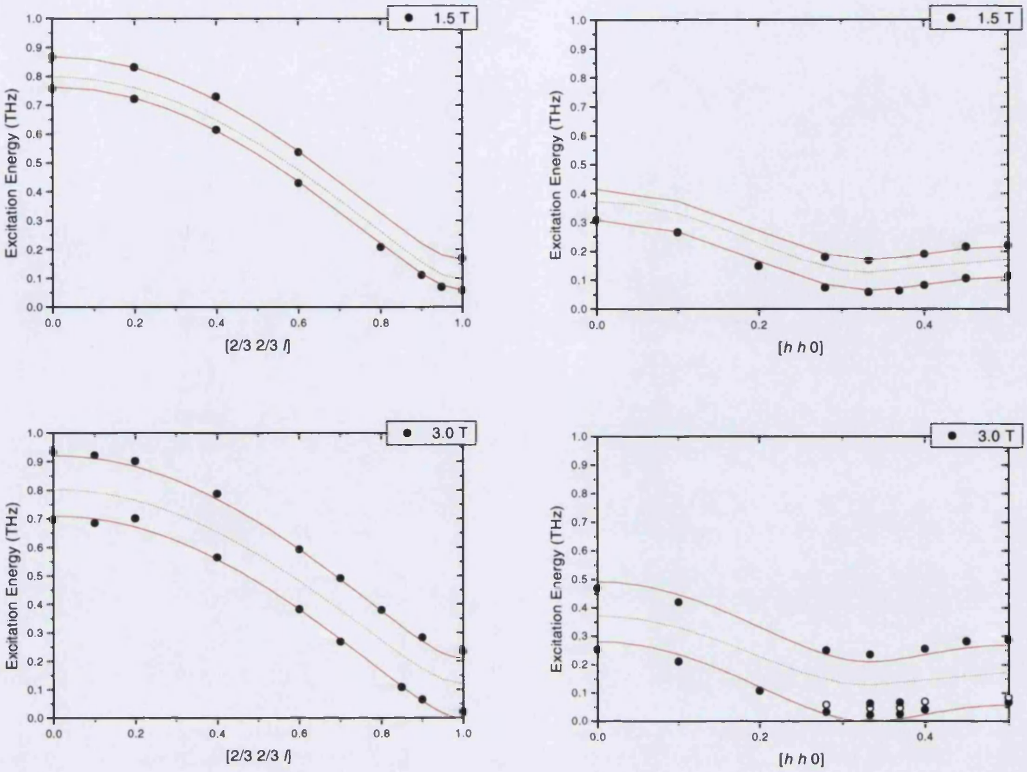

Figure 134: Magnetic excitations under external magnetic field for *B* = 1.5 Tesla and *B* = 3.0 Tesla. The solid curves are calculated using (59) and are explained below, the dotted line represents magnetic dispersion at 0 field.

Below in Figure 135a we present the Zeeman splitting at various points in reciprocal space. It can be seen that the splitting is independent of **q**, it is not so easy to discern from the graph below but the splitting is also asymmetric, with the higher frequency mode splitting more quickly than the lower one. At each field we determined the Zeeman splitting by taking the average over the available data, see Figure 134. The field dependence is linear with field and the slope of Figure 135b gives a value of the Zeeman splitting.

$$\nu_+ - \nu_- = \Delta\nu_{\text{Zeeman}} = 0.071 \pm 0.001 \left[\frac{THz}{Tesla}\right] \cdot H_{ex}^{z}$$

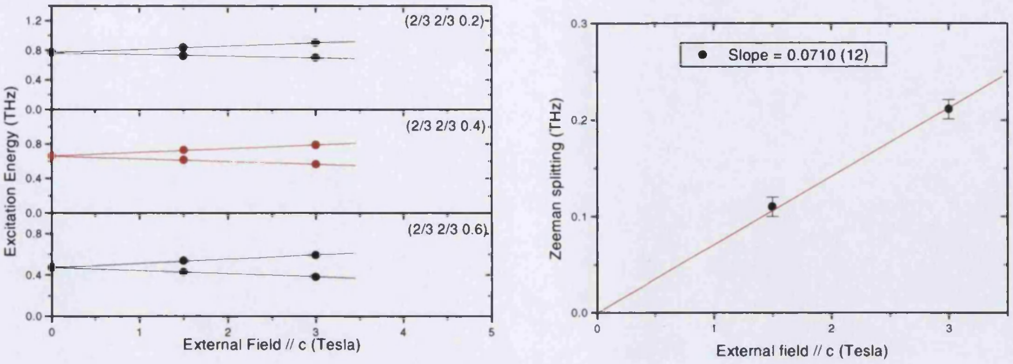

Figure 135: Zeeman splitting of the m = ±1 modes in an external field.

From this slope one can calculate the Landé factor g, of the excited state by using the relation,

$$\tfrac{1}{2}\,\Delta\nu_{\text{Zeeman}} = g \cdot \mu_B m \cdot H^z_{ex}$$

Thus we can calculate the value of g to be,

$$g = 2.5,$$

This is in good agreement with the value obtained by Dorner *et al.*[81] for $CsFeBr_3$ of $g = 2.4$ and is the same value as that obtained by Steiner *et al.*[78], of $g = 2.5$. for the SGS system $CsFeCl_3$.

Together with this value of the Landé factor, we took the values of the renormalisation factor at various field derived in ref. 81 and the determined values of D, J and J', from work by Dorner, Visser *et al.*[164], ($D = 0.62(1)$ THz, $J = -0.066(3)$ THz and $J' = -0.0067(5)$ THz). Using these values we compared the calculated and observed magnetic dispersion curves. The agreement between observed and calculated is very good as can be seen in Figure 134.

However, we see that at the onset of magnetic order at around $B = 3.0$T the situation changes and the lower branch splits into three separate branches. This splitting is further enhanced at B = 6.0T and as can be seen below, the theory of Lindgård and Villain no longer accurately describes the measured dispersion curves in the ordered phase.

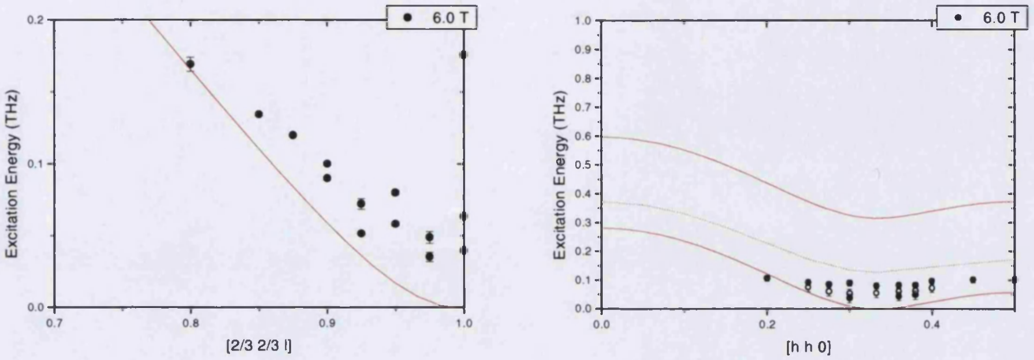

Figure 136: Magnetic excitations under external magnetic field for B = 6.0 Tesla. The solid curves are calculated using (59) and the dotted line represents the calculated magnetic dispersion at 0 field.

As can be seen from the above, the magnetic excitations at B = 6.0T could only be obtained in the vicinity to the Q(2/3 2/3 0) point, due to vanishing excitation intensity. This is due, as has been calculated by Dorner and Visser[81], to the large reduction in the dynamical structure factor with increasing field. They found that the dynamical structure factor was reduced by a factor of 3 at B = 5T compared to that at 0T for the Q(1/3 1/3 0) point.

In principle one should observe six excitation branches due to the six sublattices of the antiferromagnetic 120° type triangular structure. However, the induced moment character of $CsFeBr_3$ complicates this picture. In the pure singlet ground state case one would observe only one excitation from the singlet ground state to the excited doublet state. In the case of a magnetically ordered induced moment system with the magnetic moments in the basal plane the internal exchange field splits the doublet state, as is shown in the schematic below.

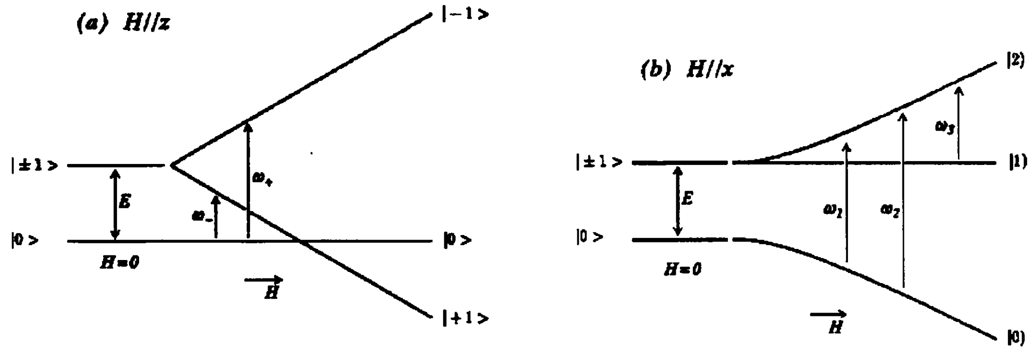

Figure 137: Effect of the application of magnetic field parallel and perpendicular to the *c*-axis in CsFeBr$_3$.

The magnetic excitation can then be understood on the basis of the pure exciton picture. Thus one should observe three single-ion excitation, those being, ω_1: 0 → 1, ω_2: 0 → -1, ω_3: 1 → -1. This, in principle, gives rise to eighteen branches for a six sublattice system. However, the transition, ω_3, will be of very small energy ~ 0.01THz, and is unable be resolved easily with neutron scattering measurements. The six highest order branches are to be observed around 0.8-1.0THz and the remaining branches will occur between these two extremes at around 0.125-0.5THz. It is these branches which can be seen in the figures above.

An alternative approach to the understanding of the magnetic excitations in singlet ground state and induced moment systems, can be obtained via the dynamical correlated effective field approach by Suzuki[26-28]. Suzuki and Makino[83] have applied DCEFA theory to the SGS system CsFeCl$_3$ accurately modelling the magnetic excitations of the system with no applied external field. A brief outline of the DCEFA theory applied is given below.

The magnetic properties of the AFeX$_3$ systems at low temperature are well described by the Hamiltonian:

$$\begin{aligned}\mathscr{H}_0 = \sum_i D S_{iz}^2 - \sum_{\langle ii'\rangle} 2\left\{J_1^{\perp}\left(S_{ix}S_{i'x} + S_{iy}S_{i'y}\right) + J_1^{/\!/} S_{iz}S_{i'z}\right\} \\ + \sum_{\langle ij\rangle} 2\left\{J_2^{\perp}\left(S_{ix}S_{jx} + S_{iy}S_{jy}\right) + J_2^{/\!/} S_{iz}S_{jz}\right\}\end{aligned} \tag{61}$$

where the first term represents the easy plane type anisotropy energy and $J_1^{\perp}$ and $J_1^{//}$ denote the nearest neighbour intrachain interaction and $J_2^{\perp}$ and $J_2^{//}$ the nearest neighbour intrachain interaction. The essence of DECFA theory lies in the approximation of the spin product S_iS_j with:

$$S_i[\langle S_j\rangle+\alpha(S_i-\langle S_i\rangle)]+S_j[\langle S_i\rangle+\alpha(S_j-\langle S_j\rangle)] \tag{62}$$

where α is the correlation parameter and $\langle S_i\rangle$ denotes the spontaneous spin moment or the spin moment induced by a magnetic field. If we consider the paramagnetic phase with no external field, then $\langle S_i\rangle$ vanishes and the effective single ion Hamiltonian for equation 61 can be expressed as:

$$\mathscr{H}_i^{eff}=ES_{iz}^2 \tag{63}$$

with,

$$E=D+\alpha\left(J_0^{\perp}-J_0^{//}\right) \tag{64}$$

where J_0^{γ}, ($\gamma = \perp$, $//$) represents the $q = 0$ component of the Fourier transform J_q^{γ} of the exchange integral. In DCEFA the dynamical susceptibility $\chi^{+-}(q, \omega)$ of the paramagnetic phase is expressed in the following form:

$$\chi^{+-}(q,\omega)=\frac{4E\rho}{\omega^2-\omega_q^2} \tag{65}$$

where ω_q represents the energy of the magnetic excitation and is given by the expression:

$$\omega_q=\left[E^2-4E\rho\left(J_q^{\perp}-\alpha J_0^{\perp}\right)\right]^{1/2} \tag{66}$$

The Fourier transform of the exchange integral $J_q^{\perp}$ takes the maximum value at q = ***K***, where ***K*** is the wave vector of the ***K***-point in the Brillouin zone. Thus the magnon energy is at a minimum value at $q = \boldsymbol{K}$.

If we consider an applied field $H \parallel z$, the Hamiltonian is expressed in the form:

$$\mathcal{H} = \mathcal{H}_0 - \sum_i g^{\parallel} \mu_B H S_{iz} \tag{67}$$

where $\mathcal{H}_0$ is the Hamiltonian for zero external field given as equation 61. In a similar manner the effective single ion Hamiltonian for equation 67 can be expressed as:

$$\mathcal{H}_i^{eff} = E S_{iz}^2 - B S_{iz} \tag{68}$$

with

$$B = g^{\parallel} \mu_B H + 2 J_0^{\parallel} (1 - \alpha) \langle S_z \rangle \tag{69}$$

where $\langle S_z \rangle$ denotes the uniform spin moment induced by the applied field. The dynamic susceptibility $\chi^{+-}(q, \omega)$ is expressed as a function of α, J_q and the single ion susceptibilities. The *static* susceptibility $\chi^{+-}(\boldsymbol{K}, 0)$ will diverge at a critical temperature T_N, between H_{c1} and H_{c2} and the system will order in a conical spin structure.

However, the approach above has not been extended to the prediction of the dispersion of the magnetic excitations in the presence of a magnetic field. Therefore, unfortunately, at present only a qualitative interpretation of our data can be given and a comparison with the magnetic excitations of the induced moment system $RbFeBr_3$ made.

The magnetic excitations in the induced moment system $RbFeBr_3$ have been studied by means of inelastic neutron scattering by Harrison and Visser[91,94]. The system undergoes a structural phase transition at T = 108K to a distorted hexagonal structure (isostructural to the RT phase of $KNiCl_3$), which relieves the magnetic frustration of the 120° type magnetic structure due to the introduction of two different intraplanar superexchange constants, see for example Figure 17. The transition is traceable through the lifting of the degeneracy of several branches of the magnetic excitations in the fully ordered magnetic phase the system. The observed magnons and associated calculated dispersion curves for $RbFeBr_3$ at T = 4.5K are reproduced below. The calculated model is based on the 120° type magnetic ordering.

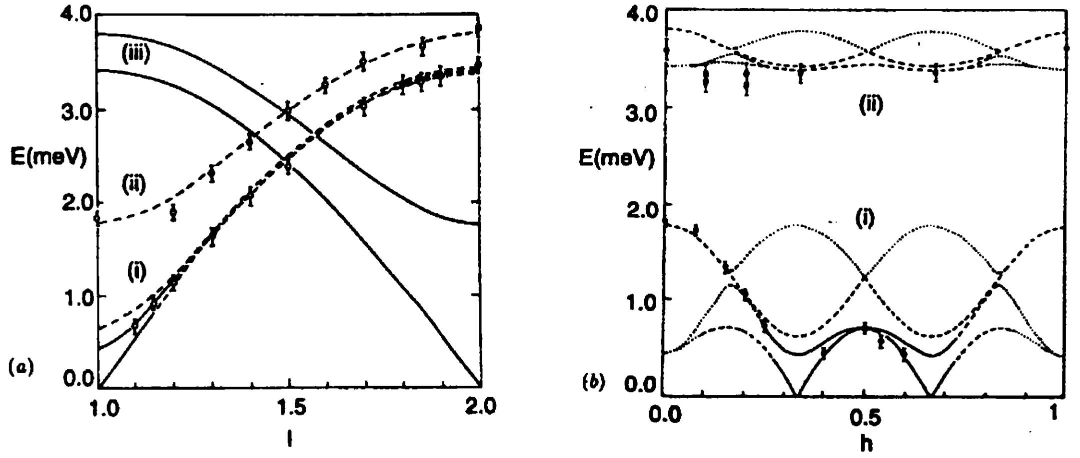

Figure 138: Magnetic Dispersion curve of (a) [2/3 2/3 *l*] and (b) [*h h* 1] of $RbFeBr_3$, the lines are best fit to DCEFA theory[94].

Visser and Harrison[165] also performed a cold, inelastic neutron scattering experiment on the sister compound RbFeBr3. Measurements were made on the magnetic excitations of the system at T = 1.35K and the lifting of the degeneracy of certain branches is obviously visible in the reproduced data below. In this system, several branches which have zero structure factor for the 120° type magnetic structure show intensity for the modified 120° structure.

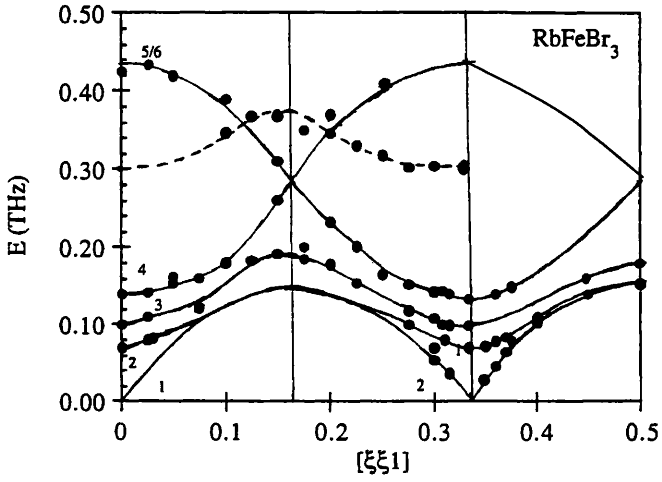

Figure 139: Magnetic Dispersion curves for $RbFeBr_3$, lines are best fit to DECFA theory.

In our present experiment for $CsFeBr_3$ at T = 60mK and H = 3.0T, one observes four branches around the magnetic Bragg point Q(2/3 2/3 1) for E < 0.15THz. As one moves away from this point along the [2/3 2/3 l] and [h h 1] directions, the branches merge quite quickly. In comparison with the calculations for the pure 120° type magnetic structure we observe the same intensity behaviour for the magnetic excitations as a function of Q at H = 3.0T. However, we observe an extra branch at the soft mode point Q(2/3 2/3 1), detecting four, rather than three, branches. This may be due to the applied field inducing a conical magnetic structure which possibly induces symmetry breaking in the system.

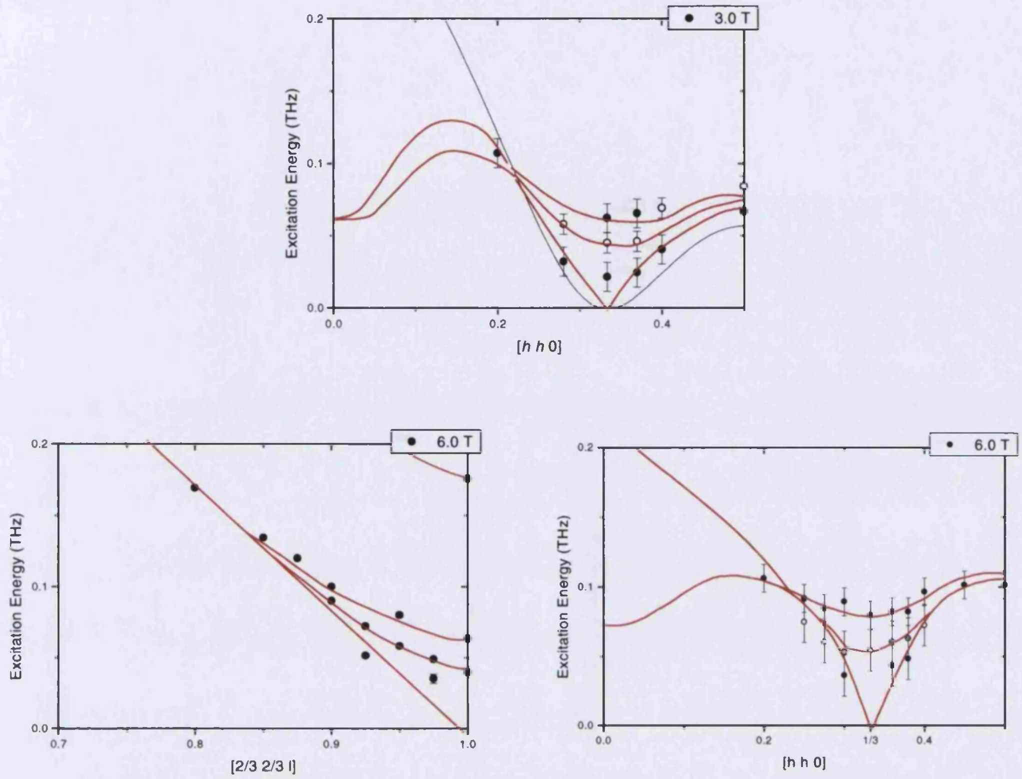

Figure 140: Possible magnon branches of SGS system $CsFeBr_3$ at T = 60mK and H = 6.0T.

At H = 6.0T, a similar picture emerges, however, the intensity of the magnetic excitations drops considerably as one moves along the [*h h* 1] direction towards the zone boundary. Although the single crystal used for the experiment was large (~$1cm^3$), it may be that the use of a larger crystal would allow us to extend the measurements to larger Q. The energy of the magnetic excitations at 6.0T are slightly more displaced than those at 3.0T, as one would expect for a larger applied field.

From this experiment one can conclude that the magnetic field induced moment phase with a 'conical' 120° type magnetic structure behaves in a similar manner to that observed for induced moment systems such as $RbFeCl_3$ and $RbFeBr_3$. Both the intensity and dispersion of the magnetic excitations can be explained by the DCEFA approach. Further development of this theory is required to accommodate the applied magnetic field and a conical 120° type magnetic structure.

6 Conclusions, Outlook

In this thesis a series of experiments have been presented which investigate:

- The possible occurrence of chiral magnetic ordering in the triangular ABX_3 antiferromagnets.
- The magnetic excitations in quasi one-dimensional quantum $S = 1$ spin systems.

Since the conjecture by Kawamura that the order parameter of frustrated stacked triangular lattice antiferromagnets includes, along with the ordinary spin variable $\vec{S}_R$, a spin chirality $\vec{C} = \left[\vec{S}_{R1} \times \vec{S}_{R2}\right]$, a relevant variable that indicates whether the helically polarised spin structure is a right handed or left handed one, giving rise to new universality classes. This conjecture has been a hotly debated topic.

Experimental investigations to verify this conjecture have been undertaken with specific heat and neutron scattering techniques. The main body of experimental evidence has been provided by the hexagonal ABX_3 halides and the BX_2 di-halides. For $CsMnBr_3$ the measured critical exponents α, β, γ, ν compare well to the predicted new chiral universality class of Kawamura. The spinflop phase of $CsNiCl_3$ also has a triangular magnetic structure. Specific heat measurements indicate that this phase displays chiral critical behaviour also.

We have attempted to obtain further experimental evidence for chiral critical ordering by trying to verify Plumer's and Kawamura's prediction for the occurrence of a magnetoelectric effect in the frustrated triangular lattice and the occurrence of chiral critical scattering in the deformed triangular lattices.

A proof of the existence of a magnetoelectric effect in $CsMnBr_3$ has been obtained for elastic neutron scattering experiments. The magnetic order parameter, β, indicated that for a sufficiently high electric field, applied parallel to the [110] direction, magnetoelectric coupling occurs and that an Ising like magnetic phase is formed. The diffuse magnetic scattering is also strongly affected, indicating that the formation of the different types of chiral domains are influenced in the presence of an electric field. The magnetic phase diagram of $CsMnBr_3$ in the presence of an applied electric field is expected to remain identical to the $E = 0$ case. However, measurements suggest that the boundary of the transition to spinflop phase moves to higher temperatures.

For the weak Ising triangular antiferromagnet, a chiral critical behaviour has been predicted for the spinflop phase. Specific heat data indicates that a $n = 3$ chiral phase is present at the critical temperature evolving into a $n = 2$ chiral phase. Neutron scattering experiments in applied magnetic field $H \,//\, c$, show a similar behaviour for the magnetic order parameter. It has also been demonstrated that the order parameter is strongly influenced by the direction of the magnetic field. A similar effect has been observed for the induced moment phase of $CsFeBr_3$. Chiral like magnetic order parameters have also been found for the weak Ising triangular antiferromagnets $CsNiCl_3$ and $RbNiCl_3$. In these systems the partially ordered phase which is formed between $T_{N1} - T_{N2}$ has an xy component remaining in it. Evidence have been found that indicates that the parameters D, J, and J' in $RbNiCl_3$ may also influence the chiral class selection or provide a mechanism for crossover between two classes.

Evidence has also been obtained for deformed triangular lattice structures which indicates that the 120° type or helical magnetic symmetry must be preserved before chiral ordering occurs. Thus the modified structures of the α and β-phase of $KNiCl_3$ are non-chiral, whereas, the helical magnetic structure in $TlFeCl_3$ gives a $n = 3$ chiral order parameter.

Further evidence for chiral magnetic order has recently been obtained from polarised neutron scattering experiments. The predicted average chiral critical exponents β_c and γ_c have been obtained from the chiral critical crossover exponent, $\phi_c = \beta_c + \gamma_c$. The results were accomplished by investigation of the fluctuations of the chirality above T_N. Because the chirality vector $\vec{C}$ is expressed through the spin pairs at the different lattice sites, the chiral fluctuations are related to four spin correlations and their direct study is impossible. Thus, Maleyev[166] proposed the study of the projection of the chiral fluctuation on the field-induced magnetisation, also called the Dynamical Chirality (DC). The DC results in a polarisation-dependant, completely inelastic part of the neutron scattering cross-section, which may be defined as[166,167]:

$$\left(\frac{d\sigma}{d\omega d\Omega}\right)_{P_0} \propto P_0 \left|F(Q)^2\right| \frac{k_f}{k_i}[1-\exp[-\omega/T]]^{-1} \times \left\{(\vec{Q}\vec{h})^2 \operatorname{Im} S_1(Q,\omega) + (\vec{h}\vec{Q})(\vec{Q}\vec{c})(\vec{c}\vec{h}) \operatorname{Im} S_2(Q,\omega)\right\} \tag{70}$$

where $\vec{Q}, \vec{h}, \vec{c}$ are the unit vectors along the momentum transfer, external field and hexagonal axis respectively. For an isotropic Heisenberg system $S_2 = 0$,while for an XY system such as $CsMnBr_3$, $S_1 = 0$. This results in a polarisation dependent, energy spectrum of the neutron, $\Delta I^{(\uparrow\downarrow)}\omega$, from which ϕ_c can be deduced. A detailed description of this theory can be found in reference 168. Similarly the value of β_c can be obtained independently from the polarisation dependence $\Delta I^{(\uparrow\downarrow)}$ of the sublattice magnetisation in the presence of unequal chiral domain population for $CsMnBr_3$.

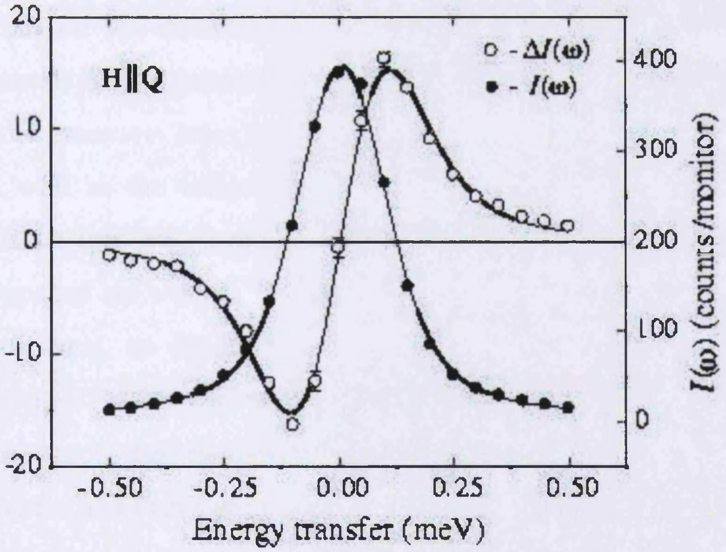

Figure 141: Polarisation dependence of the sublattice magnetisation of $CsMnBr_3$[168].

Presently, the weight of experimental evidence supports the existence of chiral magnetic ordering. However, a further generalisation is required with test experiments on model materials with different magnetic anisotropies and crystal classes (structures). Specific heat and polarised neutron scattering experiments will play a vital role in these studies.

Further evidence of the magnetoelectric effect in different ABX_3 halides is required. Direct evidence could be achieved with specific heat measurements on the magnetoelectric effect in $CsMnBr_3$.A theoretical evaluation of the form of the magnetic phase diagram of the system in the presence of an electric field should be carried out. In order to further enhance our knowledge on the different sub-groups within the ABX_3 family, it will be necessary to carry out neutron diffraction studies on the small easy plane anisotropy system ($D < 3J'$). These studies should also be carried out on the deformed triangular lattice material such as $RbMnBr_3$, $RbFeBr_3$, $KVCl_3$ and $KNiCl_3$.

A further investigation of the VX_2 compounds, followed by the hexagonal ABO_3 and ABO_2 oxide family may enhance our knowledge of chiral ordering.

As early as 1969 the hexagonal ABX_3 perovskites attracted attention as model magnetic materials for one-dimensional magnetism. Since the spin value of the first row transition metals B^{2+} is spread from the quantum $S = 1/2$ to the classical $S = 5/2$ state, the effects of crossover from the quantum to classical on the 1-D spin chains can be analysed as well as the influence of 3D magnetic ordering on such systems. Haldane's conjecture that integer spin chains would exhibit different behaviour to half integer chains opened up a wide range of experimental routes for these systems. However, as is normal, no ideal physical models could be synthesised to test the theoretical predictions, in this case one looks for isomorphous materials with which to test the conjectures. In this thesis, an unusual route has been taken to vary the structural parameters and thus vary the magnetic superexchange pathways and single ion anisotropy. Structural deformations have been induced in several of the $S = 1$ quasi one-dimensional ABX_3 materials by means of applied hydrostatic pressure.

The SGS materials $CsFeCl_3$ and $CsFeBr_3$ were investigated by means of inelastic neutron scattering techniques, due to the singlet ground state properties of the materials no magnetic order is observable. However, a sufficiently large, externally applied, magnetic field // c-axis will produce an induced magnetic moment and long range order will occur in the system. A similar process occurs upon the application of a symmetry breaking pressure // *a* or if the anisotropy and superexchange parameters are varied sufficiently i.e. by structural deformation. The magnetostructural studies elaborated upon in Chapter 5 set out to establish the compressibility behaviour of the physical structures and the corresponding magnetic dispersion curves of the singlet groundstate materials in order to obtain the anisotropy and exchange parameters under applied hydrostatic pressure. Although it is seen that hydrostatic pressure induces an anisotropic compression, these systems are not sufficiently deformed to induce magnetic ordering. The changes in crystal structure have been related to the change in the magnetic parameters. The studies contained in Chapter 5, give for the first time a basis for a rigorous magnetostructural correlation and also a foundation for further theoretical calculations of the superexchange parameters.

The determination of the magnetic excitations of $CsFeBr_3$ in higher magnetic fields than previous reported showed that, for T = 50mK and H = 3.0-6.0T, the features of the magnetic excitations resembled those of the induced moments systems e.g. $RbFeCl_3$. This gives a basis for extending the present DCEFA theory to the calculation of the magnetic excitations in field induced systems and distorted-triangular induced moment magnets. Verification of subsequent theories could be obtained by studying $CsFeCl_3$ and $CsFeBr_3$ in an applied magnetic field both // and ⊥ to *c*. Further magnetic characterisation of $TlFeCl_3$ under applied pressure would also provide insight into the ordering process. Other candidates which would prove useful to investigate include $TlFeBr_3$, ND_4FeCl_2, ND_4FeBr_2, $CsFeI_3$ and $TMFeCl_3$.

A similar study of the Haldane, $S = 1$ systems, $CsNiCl_3$ and $RbNiCl_3$ was started during the same period. The systems have been investigated previously at ambient pressure and have been shown to exhibit characteristics commensurate with the Haldane conjecture. Comparable studies have been undertaken by the author for the systems under a hydrostatic pressure environment in order to obtain the values of the exchange parameters and single ion anisotropies and 'create' extra Haldane systems. This was done in order to test the conjecture in materials with modified values of D, J and J'. This undertaking could not be completed within the allotted time as no beam time was forthcoming for the comparative structural study of the materials. From the inelastic data, acquired at 5.0kbar applied hydrostatic pressure, we see that the changes in the excitation spectrum are less pronounced than in the $CsFeX_3$ materials. This is most probably due to the fact that the $ANiCl_3$ compounds have smaller r_B/r_X ratios and are less compressible. Nevertheless differences in the longitudinal mode energies are observable. A full interpretation and magnetostructural correlation or these materials awaits experimental completion.

The influence of a change in the sign of the single ion anisotropy, D, on the gap behaviour of the $ANiCl_3$ materials has been obtained for a pilot experiment on $KNiCl_3$. The magnetic excitations have been measured in the β and γ-phases at the softmode point and show that a system with positive D also possesses a gap. Unfortunately there are no theoretical predictions for such systems and a detailed analysis of the present data would require the introduction of the correct crystallographic structure.

In the near future theoretical studies are required to include different types of anisotropy in the calculation of the 1-D properties of a $S = 1$ chain system. Experimental realisation of different D, J and J' models can be obtained by looking at a vast number of Ni coordination complexes and further study of the ABX_3 halides.

Appendix A

This section describes inelastic neutron scattering experiments performed on some $ANiCl_3$ compounds at ambient and applied hydrostatic pressure conditions. Measurements were made on the distorted triangular lattice antiferromagnet $KNiCl_3$ and the easy axis anisotropy stacked triangular lattice systems $CsNiCl_3$ and $RbNiCl_3$. All experiments were performed using the TAS, 4F1 at the LLB, Saclay, and in the case of the $CsNiCl_3$ and $RbNiCl_3$ samples, in conjunction with the 'in-house' He-pressure cell. Further information on these can be found in Chapters 3.2.1.3 and 3.3.3, respectively. Using this setup enabled us to apply hydrostatic pressures of up to P = 5.0kbar at a temperature T < 2K to the systems. The data are presented in this appendix as no treatment of the dispersion curves has yet been carried out and thus the values of the single ion anisotropy D, and the inter and intrachain energies (J and J' respectively) are not yet available. In all cases the data is incomplete and detailed information about the nuclear and magnetic structure is lacking. No beamtime has been made available thus far to carry out these studies. Unfortunately the He pressure cell at the LLB, Saclay fractured and had to be fixed thus preventing further study of these systems under applied pressure environments.

The interest in the $ANiCl_3$ compounds is still substantial more than 15 years after Haldane argued that the integer spin Heisenberg antiferromagnets have an unusual excitation spectrum; they should exhibit an excitation gap above a singlet ground state. Evidence for such a gap has been presented by Buyers *et al.* for $CsNiCl_3$[55] and $RbNiCl_3$[56]. Neutron scattering experiments at $T \cong 2T_N$ indicate the existence of a gap in the pure one-dimensional case. In the ordered phase below T_N = 4.8K, the anomalous behaviour is also observed. The Goldstone modes predicted by spin wave theory were observed but another excitation branch with a finite gap was detected. Affleck and Wellmann[21] presented a thorough discussion of the theory for the triangular antiferromagnets $CsNiCl_3$ and $RbNiCl_3$. Since only a few systems are available for experimental work the route of applied pressure has been followed to induce changes in the interactions of D, J and J' in the systems. The influence of the change of the anisotropy in such systems has yet to be investigated. The distorted lattice compound $KNiCl_3$ has *XY* anisotropy and Affleck and Wellmann predict that such a system should have a gap in its excitation spectrum at the soft mode point Q(1/3 1/3 1). Therefore it is necessary to study $KNiCl_3$ in order to resolve this point. However, the details of the magnetic structure of the β and γ-phases of $KNiCl_3$ may lead to complications.

Section A-1 presents magnetic excitation measurements on two different structural phases of $KNiCl_3$ and provides a rationalisation for the differences in the form of the magnon dispersion curves. In Section A-2 the magnon dispersion curves of $CsNiCl_3$ under applied hydrostatic pressure conditions are presented and comparisons are made between this and ambient pressure data. Finally in Section A-3 data are given showing the magnon dispersion curve of the $RbNiCl_3$, again under applied hydrostatic pressure conditions and comparison is made to ambient pressure data.

Appendix A-1.

As was mentioned in Chapter 4.5, $KNiCl_3$ is a distorted triangular lattice antiferromagnet with two low temperature magnetic phases first reported on by Petrenko *et al.*[76]. In the β-phase of $KNiCl_3$, the magnetic moments orders with a 120° type magnetic structure at $T_N = 12.5K$, while the γ-phase shows a rearranged nuclear structure with an incommensurate magnetic structure with $T_N = 8.6K$. Measurements were undertaken on the magnon dispersion curves of the β and γ-phases in order to ascertain to what extent the form of the dispersion curves varied between the phases. These measurements were carried out in conjunction with the critical exponent measurements elaborated upon in Chapter 4.5, thus experimental conditions will be identical to those and the reader is referred to these sections for more detailed information.

For both the β and γ-phase samples measurements were carried out along the [0 0 *l*] and the [1/3 1/3 *l*] directions, as well as the perpendicular direction [*h h* 1]. For the γ-phase sample measurements were taken at both T = 8.75K and T =2.00K in order to observe any softening of the modes with decreasing temperature. The resultant magnon dispersion curves for the different phases are displayed below.

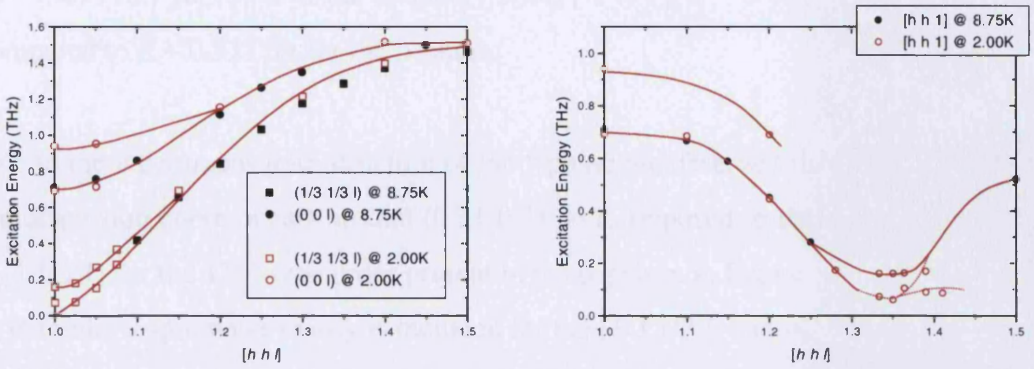

Figure 142: Magnetic dispersion of the β-phase of $KNiCl_3$ at ambient pressure along the [0 0 *l*], [1/3 1/3 *l*] and [*h h* 1] directions, lines are a guide to the eye only.

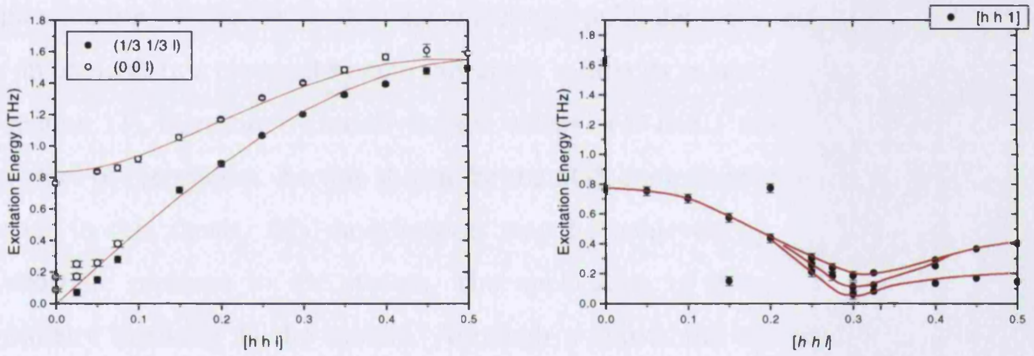

Figure 143: Magnetic dispersion of the γ-phase of $KNiCl_3$ at ambient pressure along the [0 0 *l*], [1/3 1/3 *l*] and [*h h* 1] directions, lines are a guide to the eye only.

Comparing the magnon dispersion curves of the two phases several features are immediately obvious. In the β-phase, between (0 0 1) → (0 0 1.15), it is seen that there are two branches to the upper mode of the [0 0 *l*] curve. This is not apparent in the γ-phase where only one mode may be observed. For both phases, the [0 0 *l*] and [1/3 1/3 *l*] modes converge towards a value of E ~ 1.5THz at the zone boundary. However there is a difference in the gap between the energy of the [0 0 1] and [1/3 1/3 1] excitations for the different phases, this suggests that the β and γ-phase have different values of J'. Along the perpendicular direction the excitation energy of zone boundary point [0 0 1] in the γ-phase ($E \sim 0.76$THz) is higher than that in the β-phase ($E \sim 0.69$THz) yet lower at the boundary point [½ ½ 1], $E \sim 0.40$THz for the γ-phase compared to $E \sim 0.52$THz for the β-phase.

Due to the incommensurate structure of the γ-phase we observed that the minimum of the dispersion curve occurs around (0.31 0.31 1) as opposed to the expected value of (1/3 1/3 1) for the 120° type order present in the β-phase. In Figure 143 a fit according to Petrenko's spin wave theory is included for the [1/3 1/3 l] and [0 0 l] directions.

Appendix A-2.

As has been mentioned in Chapter 2.2.1, $CsNiCl_3$ orders with a slightly distorted 120° type structure, where the weak Ising anisotropy pulls the spins out of the basal plane by an angle θ. In a classical system this angle is directly related to the value of $D / 6J'$ (equation 11), therefore by modifying the values of D and J' one will deform the spin structure of the system. As was shown for the SGS compounds $CsFeCl_3$ and $CsFeBr_3$, earlier in this thesis, this modification may be achieved by the application of a hydrostatic pressure to the system. The application of pressure may also induce symmetry breaking in the system. Although a substantial amount of experimental work has been performed on $CsNiCl_3$, very little has been done to characterise the distorted system. Recent heat capacity measurements done on another Haldane gap material NENP[59] has shown an increasing gap mode with increasing applied pressure. Thus it would be of interest to observe the magnon dispersion curve and gap mode of $CsNiCl_3$ under applied hydrostatic pressure conditions to see if the same trend exists.

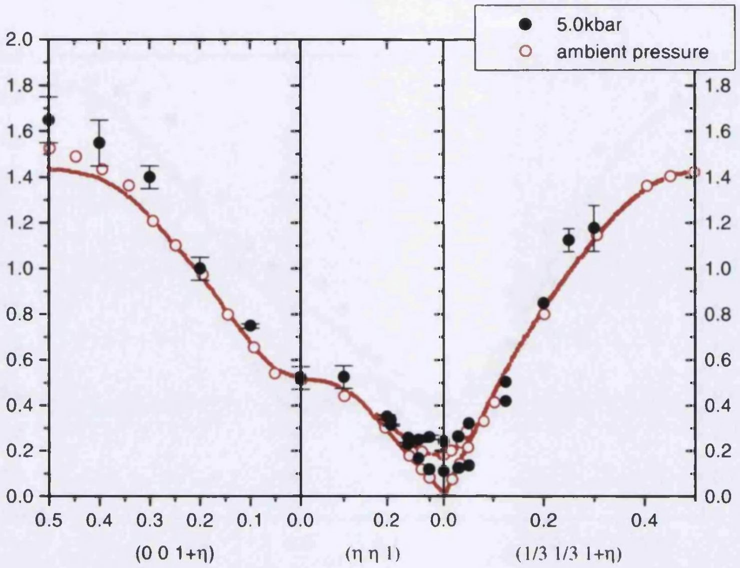

Figure 144: Comparison of the magnon dispersion curves of $CsNiCl_3$ at ambient pressure and 5.0kbar applied hydrostatic pressure, line is best fit to ambient data.

No dramatic changes in the dispersion curve are visible in Figure 144, however, the change in excitation energies is evident whereby the excitations have repositioned to a higher energy due to the applied pressure environment, this normally leads to a larger value of the single ion anisotropy parameter, *D*, *J* and *J'*.

Appendix A-3

Measurements were carried out on the similar system $RbNiCl_3$, for similar reasons as those outlined in A-2. The magnon dispersion curves are shown below with ambient pressure data for comparison purposes.

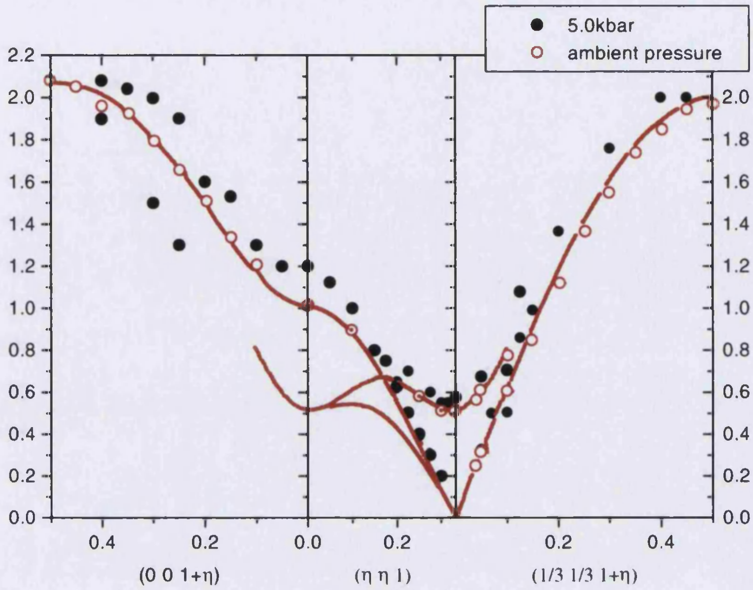

Figure 145: Comparison of the magnon dispersion curves of $RbNiCl_3$ at ambient pressure and 5.0kbar applied hydrostatic pressure, line is best fit to ambient data with the theory of Affleck and Wellmann[21].

As with $CsNiCl_3$, there is no drastic change in the magnon dispersion curve of $RbNiCl_3$ under applied hydrostatic conditions. The energies of the excitation again move to higher energy due to physical deformation of the crystal. In Chapter 5 it was demonstrated that the applied hydrostatic pressure induces only small changes in the structure of the $CsFeX_3$ systems. A similar conclusion can already be made for our present experimental data. Nuclear and magnetic structure determination under applied pressure conditions are required to obtain the full magnetostructural correlation of these two systems an will aid to a better understanding of the Haldane gap phenomena in the quasi one-dimensional triangular lattice antiferromagnets.

References

---

[1] de Jongh, L.J., Miedema, A.R., Adv. Phys., **23**, 1-260,(1974).

[2] Carlin, R.L., Magnetochemistry, Springer Verlag, Berlin, (1986).

[3] Carlin, R.L., van Duynevela, A.J., Magnetic Properties of Transition Metal Compounds, Springer Verlag, Berlin, (1977).

[4] Willet, R.D., Gutteschi, D., Kahn, O., Magneto-Structural Correlations in Exchange Coupled Systems, NATO ASI, C140, Ridel Dondrecht, (1983).

[5] de Jongh, L.J., Magnetic Properties of Layered Transition Metal Compounds, Kleuwer Academic Press, (1994).

[6] Itoh, S., Endoh, Y., Kakurai, K., Tanaka, H., Phys. Rev. Lett. **74**, 12, (1995).

[7] Weltz, D., Physica B., **213&214**, 185, (1995).

[8] Engelfriet, D.W., Doctor Thesis, The University of Leiden, Leiden, (1980).

[9] Delhoes, P., Dillion, M., Organic and Inorganic Low Dimensional Crystalline Materials, NATO ASI, B168, Plenum Press New York, (1986).

[10] Kahn, O., Magnetism: A Supramolecular Function, NATO ASI, C484, Kluwer Dordrecht, (1996).

[11] Ramirez, A.P., J. Phys.: Condens. Matter, **9**, 8171, (1997).

[12] Rao, C.N.R., Raveau, B., Transition Metal Oxides, VCH Cambridge, (1996).

[13] Ramirez, A.P., Ann. Rev. Mat. Sci., **24**, 453, (1994).

[14] Diep, H.T., Magnetic Systems with Competing Interactions, World Scientific, Singapore, (1994).

[15] Riemers, J.N., Greedan, J.E., Bjorgvinsson, M., Phys. Rev. B, **45**, 13, (1992).

[16] Halperin, B.I., Hohenberg, P.C., Phys. Rev., **177**, 952, (1969).

[17] Wilson, K.G., Phys. Rev. B, **4**, 3177, (1971).

[18] Ofenty, P., Toulouse, G., Introduction to the Renormailsation Group and Critical Phenomena, J. Wiley, (1978).

[19] Plumer, M.L., Kawamura, H., Caillé, A., Phys. Rev. B, **43**, 13786, (1991).

[20] Plumer, M.L., Caillé, A., Kawamura, H., Phys. Rev. B, **44**, 4461, (1991).

[21] Affleck, I., Wellman, G.F., Phys. Rev. B, **46**, 8934, (1992).

[22] Enderle, M., Tun, Z., Buyers, W.J.L., Steiner, M., Phys. Rev. B, **59**, 4235, (1999).

[23] Monteith, A., Thesis MPhil., Loughborough University, (1994).

[24] Renard, J.P., Regnault, L.P., Verdagnet, M., J. Phys. (Paris) Colleque, **C8**, 1425, (1988).

[25] Visser, D., Harrison, A., J. Phys. (Paris) Colleque, **C8**, 1467, (1988).

[26] Suzuki, N., J. Phys. Soc. Japan, **45**, 1791, (1978).

[27] Suzuki, N., J. Phys. Soc. Japan, **52**, 1002, (1983).

[28] Suzuki, N., J. Phys. Soc. Japan, **52**, 3907, (1983).

[29] Villain, J., J. Phys. C: Solid State Phys. **10**, 4793 (1977).

[30] Kawamura, H., J. Phys. Soc. Japan, **56**, 474, (1987).

[31] Kawamura, H., J. Phys. Soc. Japan, **58**, 584, (1989).

[32] Miysahita, S., Shiba, H., J. Phys. Soc. Japan, **53**, 1145, (1995).

[33] Collins, M. F., Petrenko, O. A., Can. J. Phys., **75**, 605, (1997).

[34] Kawamura, H., J. Phys.: Condens. Matter, **10**, 4707, (1998).

[35] Beckmann, D., Wosnitza, J., von Löhneysen, Visser, D., Phys. Rev. Lett., **71**, 2829, (1993).

[36] Enderle, M., Schneider, R., Matsuoka, Y., Kakurai, K., Physica B, **234**, 554, (1997).

[37] Enderle, M., Furtuna, G., Steiner, M., J. Phys.: Condens. Matter, **6**, L385, (1994).

[38] Haldane, F. D. M., Phys. Lett.,**93A**, 464, (1983).

[39] Haldane, F. D. M., Phys. Rev. Lett., **50**, 1153, (1983).

[40] Affleck, I., J. Phys: Condens. Matter, **1**, 3047, (1989).

[41] Affleck, I., Phys. Rev. Lett., **57**, 1048, (1986).

[42] Affleck, I., Phys. Rev. Lett., **56**, 408, (1986).

[43] Lieb, E. H., Schultz, T., Mattis, D. J., Ann. Phys., NY, **16**, 407, (1963).

[44] Affleck, I., Leib, E. H., Lett. Matt. Phys., **12**, 57, (1986).

[45] Affleck, I., Kennedy, T., Leib, E. H., Tasaki, H., Phys. Rev. Lett., **59**, 799, (1987).

[46] Affleck, I., Kennedy, T., Leib, E. H., Tasaki, H., Commun. Math. Phys., **115**, 477, (1988).

[47] Botet, R., Juillen, R., Phys. Rev. B, **27**, 613, (1983).

[48] Botet, R., Juillen, R., Kolb, M., Phys. Rev. B, **28**, 3914, (1983).

[49] Bonner, J., J. Appl. Phys., **61**, 8, (1987).

[50] Moses, D., Shechter, H., Ehrenfreund, E., Makovshy, J., J. Phys. C., **10**, 433, (1977).

[51] Clark, R.H., Moulton, M.G., Phys. Rev. B, **5**, 788, (1972).

[52] Johnson, P.B., Rayne, J.A., Friedberg, S.A., J. Appl. Phys., **50**, 1853, (1979).

---

[53] Rayne, J.A., Collins, G.J., White, G.K., Solid State Commun. **33**, 39, (1980).

[54] Almond, D.P., Physica (Amsterdam) **86-88B+C**, 651, (1977).

[55] Buyers, W.J.L., Morra, R.M., Armstrong, R.L., Hogan, M.J., Gerlach, P., Hirakawa, K., Phys. Rev. Lett., **56**, 4, (1986).

[56] Buyers, W.J.L., Tun, Z., Harrison, A., Rayne, J.A., Nicklow, R.M., Physica B, **180**, 222, (1992).

[57] Enderle, M., Ph.D. Thesis, University of Mainz, Germany, (1993).

[58] Lu, W., Tuchendler, J., Vonortenberg, M., Renard, J.P., Phys. Rev. Lett., **67**, 3716, (1991).

[59] Ito, M., Yamashita, H., Kawae, T., Takeda, K., J. Magn. Magn. Mater., **177**, 673, (1998).

[60] Mason, T.E., Collins, M.F., Gaulin, B.D., J. Phys. C: Solid State Phys., **20**, L945, (1987).

[61] Mason, T.E., Collins, M.F., Gaulin, B.D., Phys. Rev. B, **39**, 586, (1989).

[62] Ajiro, Y., Nakashima, T., Unno, Y., Kadowaki, H., Mekata, M., Achiwa, N., J. Phys. Soc. Japan, **57**, 2648, (1988).

[63] Kadowaki, H., Shapiro, S.M., Tnami, T., Ajiro, Y., J. Phys. Soc. Japan., **57**, 2640, (1988).

[64] Way, J., Belanger, D.P., Gaulin, B.D., Phys. Rev. Lett., **66**, 3195, (1991).

[65] Deutschmann, R., von Löhneysen, H., Wosnitza, J., Kremer, R.K., Visser, D., Europhys. Lett. **17**, 637 (1992).

[66] Mason, T.E., Collins, M.F., Gaulin, B.D., Larese, J.Z., Phys. Rev. Lett., **62**, 1380, (1989).

[67] Kawamura, H., Caillé, A., Plumer, M.L., Phys. Rev. B, **41**, 4416, (1990).

[68] Wang, J., Belanger, D.P., Gaulin, B.D., Phys. Rev. Lett., **66**, 3195, (1991).

[69] Plumer, M.L., Caillé, A., Hood, K., Phys. Rev. B: Condens. Matter, **39**, 4489, (1989).

[70] Feile, R., Kjems, J.K., Hauser, A., Güdel, H.U., Falk, U., Furrer, A., Solid State Commun., **50**, 435, (1984).

[71] Kadowaki, H., Ubukoshi, K., Hirakawa, K., Belanger, D.P., Yoshizawa, H., Shirane, G., J. Phys. Soc. Japan, **55**, 2846, (1986).

[72] Visser D., Verschoor, C.G., Ijdo D.J.W., Acta. Crystallogr., **B36**, 28, (1980).

[73] Suzuki, N., Shirai, M., Physica **138B**, 346, (1986).

[74] Zhang, W.M., Saslow, W.M., Gabay, M., Benakli, M., Phys. Rev. B, **52**, 3511, (1995).

[75] Machida, K., Mitsui, T., Kato, T., Iio, K., Solid State Commun., **91**, 17, (1994).

[76] Petrenko, O., Collins, M.F., Stager, C.V., Collier, B.F., Tun, Z., J. Appl. Phys., **79**, 6614, (1996).

[77] Petrenko, O., Lumsden, M.A., Lumsden, M.D., Collins, M.F., J. Phys.: Condens. Matter, **8**, 10899, (1996).

[78] Steiner, M,. Kakurai, K., Knop, W., Dorner, B., Happek, U., Day, P., McLeen, G., Solid State Commun., **38**, 1179, (1975).

[79] Schmid, B., Dorner, B., Visser, D., Steiner, M., Z. Phys. B: Condens. Matter, **86**, 257, (1992).

[80] Schmid, B., Dorner, B., Visser, D., Steiner, M., J. Magn. Magn. Mater., **104-107**, 771, (1992).

[81] Dorner, B., Visser, D., Steiner, M., Z. Phys. B: Condens. Matter, **81**, 75, (1990).

[82] Lindgård, P-A., Schmid, B., Phys. Rev. B, **48**, 13636, (1993).

[83] Suzuki, N., Makino, J., J. Phys. Soc. Japan, **64**, 2166, (1995).

[84] Schmid, B., Dorner, B., Petitgrand, D., Regnault, L. P., Steiner, M., Z. Phys. B, **95**, 13, (1994).

[85] Shiba, H., Solid State Commun., **41**, 511, (1982).

[86] Haseda, N., Wada, N., Hata, M., Amaya, K., Physica B, **108**, 841, (1981).

[87] Baines, J. A., Johnson, C. E., Thomas, M. F., J. Phys. C: Solid State Phys., **16**, 3579, (1983).

[88] Chiba, M., Ajira, Y., Adachi, K., Morimota. T., J. Phys. Soc. Japan, **57**, 3178, (1988).

[89] Ohta, H., Makita, N., Yoshida, K., Nanba, T., Motokawa, M., Int. J. Infrared Millimeter Waves, **13**, 457, (1992).

[90] Eibschütz, M., Davidson, G. R., Cox, D. E., AIP Conf. Proc., **18**, 386, (1973).

[91] Harrison, A., Visser, D., Phys. Lett., **137A**, 79, (1989).

[92] Mitsui, T., Machida, K., Kato, T., Iio, K., J. Phys. Soc. Japan, **63**, 839, (1994).

[93] Adachi, K., Takeda, K., Matsubara, F., Mekata, M., Hatsada, T., J. Phys. Soc. Japan, **52**, 2202, (1983).

[94] Harrison, A., Visser, J. Phys.: Condens. Matter, **4**, 6977, (1992).

[95] Davidson, G. R., Eibschütz, M., Cox, D. E., Minkiewicz, V. J., AIP Conf. Proc., **5**, 436, (1971).

[96] Yoshizawa, H., Kozukue, W., Hirakawa, K., J. Phys. Soc. Japan, **49**, 144,(1980).

[97] Yoshizawa, H., Axe, J. D., Shirane, G., Solid State Commun., **38**, 241,(1981).

[98] Wada, N., Ubukoshi, K., Hirawkawa, K., J. Phys. Soc. Japan, **51**, 2833, (1982).

[99] Wada, N., Sumiyoshi, K., Watanabe, T., Amaya, K., J. Phys. Soc. Japan, **52**, 1893, (1983).

[100] Shiba, H., Suzuki, N., J. Phys. Soc. Japan, **51**, 3488, (1982).

[101] Dorner, B., Schmid, B., Kakurai, K., Petitgrand, D., Can. J. Phys., **73**, 800,(1995).

[102] Achiwa, N., J. Phys. Soc. Japan,**27**, 561, (1969)

---

[103] Montano, P. A., Cohen, E., Shecter, H., Makovsky, J., Phys. Rev. B: Solid State, **7**, 1180, (1973).
[104] Eibschütz, M., Lines, M.E., Sherwood, R.C., Phys. Rev. B: Condens. Matter, **11**, 4595, (1975).
[105] Lines, M.E., Phys. Rev. B: Solid State, **11**, 1134, (1975).
[106] Coad, S., Ph.D. thesis, The University of Warwick, UK, (1997)
[107] http://www.isis.rl.ac.uk/ess/
[108] Egelstaff, P., Thermal Neutron Scattering, Academic Press, (1965).
[109] Halpern, O., Johnson, M.H., Phys. Rev., **55**, 898, (1939).
[110] Harrison, A., D.Phil., Oxford, (1986).
[111] http://www.hmi.de/bensc/instrumente/e1/e1.html
[112] http://www.hmi.de/bensc/instrumente/e1/e1-pic.html
[113] http://www.hmi.de/bensc/instrumente/v2/v2-pic.html
[114] http://www-llb.cea.fr/spectos/spectro/4f1.eps
[115] http://www.ill.fr/YellowBook/D15
[116] http://www.hmi.de/bensc/instrumente/e2/e2-pic.html
[117] Rietveld, H. M., J. Appl. Cryst., **2**, 65, (1969).
[118] http://www.isis.rl.ac.uk/Crystallography/HRPD_figs.htm
[119] http://www.isis.rl.ac.uk/Crystallography/HRPDguide.htm
[120] http://www.isis.rl.ac.uk/crystallography/images/POLguide_fig1.JPG
[121] http://www.hmi.de/bensc/instrumentation/instrumente/e2/e2-pic.html
[122] http://www.hmi.de/bensc/sample-env/orange.html
[123] http://www.hmi.de/bensc/sample-env/dilution.html
[124] http://www.hmi.de/bensc/sample-env/vm3_cross-section.html
[125] http://www.hmi.de/bensc/sample-env/hm.html
[126] Plumer, M.L., Kawamura, H., Caillé, A., Phys. Rev. B, **43**, 13786, (1991).
[127] Nakanishi, O., Solid State Commun., **35**, 995, (1980).
[128] Bak, P., Jensen, M.H., J. Phys. C, **13**, L881, (1980).
[129] Shirane, G., Phys. Rev. B, **28**, 6251, (1983).
[130] Freeman, A.J., Schmid, H., Magnetoelectric Interaction Phenomena in Crystals, Gordon and Breach, New York, (1975).
[131] Siratori, K., J. Phys. Soc. Japan, **48**, 1111, (1980).
[132] Visser, D., Coldwell, T.R., McIntyre, G.J., Graf, H., Weiss, L., Zeiske, Th., Plumer, M.L., Ferroelectrics, **162**, 147, (1994).
[133] Azaria, P., Diep, H.T., Phys. Rev. B, **39**, 745, (1989).
[134] Visser, D., McIntyre, G., ILL Report, (1986).
[135] Plumer, M.L. Caillé, A., Phys. Rev. B, **41**, 2543, (1990).
[136] Maegawa, S,. Goto, T., Ajiro, Y,. J. Phys. Soc. Japan, **57**, 1402, (1988).
[137] Bramwell, S.T., Holdsworth, P.C.W., J. Phys.: Condens. Matter, **5**, L53, (1993).
[138] Bramwell, S.T., Holdsworth, P.C.W., Phys. Rev. B, **49**, 8811, (1993).
[139] Weber, H., Beckmann, D., Wosnitza, J., von Löhneysen, Visser, D., Int. J. Mod. Phys., **9**, 1387, (1995)
[140] Zaliznyak, I., Phys. Rev. B, **50**, 15824, (1994).
[141] Weltz, D,. J. Phys. Condens. Matter, **5**, 3643, (1993).
[142] Minkiewicz, V.J., Cox, D.E., Shirane, G., Solid State Commun., **8**, 1001, (1970).
[143] Yelon, W.B., Cox, D.E., Phys. Rev. **B6**, 204, (1972).
[144] Collocott, S.J., Rayne, J.A., J. Appl. Phys., **61**, 4404, (1987).
[145] Oohara, Y., Kadowaki, H., Iio, K., J. Phys. Soc. Japan, **60**, 393, (1991).
[146] Oohara, Y,. Iio, K., Tanaka, H,. Nagata, K., J. Phys. Soc. Japan, **60**, 4280, (1991).
[147] Visser, D., McIntyre, G.J., (to be published).
[148] Visser, D., Monteith, A.R., Harrison, A., Petitgrand, D., High Pressure Research, **14**, 29, (1995).
[149] Rutherford Appleton Laboratory Report, RAL-93-009
[150] http://www.isis.rl.ac.uk/opengenie/
[151] Visser, D., Wilkinson, C., McIntyre, G.J., Cowan, J., (to be published).
[152] Tanaka, H., Kakurai, K,. J. Phys. Soc. Japan, **63**, 3412, (1994).
[153] Matchida, T., Mitsui, T., Kato, T., Ito, K., Solid State Comm., **91**, 17, (1994).
[154] Wada, N., Ubukoshi, K., Hirakawa, K., J. Phys. Soc. Japan, **51**, 2833, (1982).
[155] Visser, D., Harrison, A., (to be published).
[156] Tanaka, H,. Hasegawa, T., Nagata, K., J. Phys. Soc. Japan, **62**, 4053, (1993).
[157] Lindgård, P.A., Physcia **120B**, 190, (1983).
[158] Villain, J., J. de Physique, **35**, 27, (1974).

---

[159] Visser, D., Harrison, A., (to be published).

[160] Schmid, B., Ph.D. Thesis, University of Regensberg, Germany, (1995).

[161] Lindgård, P.A., J. Phys. C, **8**, L178, (1975).

[162] Lindgård, P.A., J. Magn. Magn. Mater., **54-57**, 1227, (1986).

[163] Knop, W., Thesis, Technische Universität, Berlin, (1985).

[164] Dorner, B., Visser, D., Steigenberger, U., Kakurai, K., Steiner, M., Z. Phys. B.: Condens. Matter, **72**, 487, (1988).

[165] Visser, D., Ph.D. Thesis, University of Loughborough, (1996).

[166] Maleyev, S.V., Phys. Rev. Lett., **75**, 4682, (1995).

[167] Maleyev, S.V., Plakhty, V.P., Smirnov, O.P., Wosnitza, J., Visser, D., Kremer, R.K., Kulda, J., J. Phys. Condens. Matter, **10**, 951, (1998).

[168] Plakhty, V.P., Maleyev, S.V., Kulda, J., Wosnitza, J., Visser, D., Moskvin, E., Europhys. Lett., **48**, 215, (1999).